In situ characterisation of batch and continuous crystallisations

Raphael Joseph Stone

Submitted in accordance with the requirements for the degree of Doctor of Philosophy.

The University of Leeds

School of Chemical and Process Engineering

School of Chemistry

January 2024

The candidate confirms that the work is their own, except where work which has formed part of jointly authored publications has been included. The contribution of the candidate and the other authors to this work has been explicitly indicated below. The candidate confirms that appropriate credit has been given within the thesis where reference has been made to the work of others.

Acknowledgements

I'd like to start by acknowledging and thanking my funding source, the EPSRC Centre for Doctoral Training in Molecules to Product, as well as Elaine, Angela, the rest of the management board, and everyone else involved in the CDT, for giving me the opportunity to do this PhD. A key driving principle of the CDT is that collaborative, cross-disciplinary work is better than working in isolation, and this has proven to be very true during my PhD, as evidenced by the many, many individuals who have helped me during the past four years. As such, there are plenty of other people I'd like to acknowledge who have helped me complete this PhD.

I'd like to thank my three supervisors: Nikil Kapur, Richard Bourne, and Fiona Meldrum. Nik has been a superb PI to me, acting as a source of broad wisdom and creative solutions to problems. Rich, in a similar vein, offered poignant advice throughout my PhD, despite the project not quite reaching his specialist area. Fiona took me into her labs during a difficult time in late 2020, which allowed me both the human and physical resources to complete this project. Speaking of, I'd like to thank the members of the Meldrum group for functioning as a laboratory-based 'family' for the last three years: Xuefeng, Zhao, Yilin, Xiaoyue, Tom D, Steph, Olly, Maxime, Liam, Joe, Jo, Ilaria, Cedrick, Charlotte, Bidisha, Ashmita, and Adrianna. Whether at social events such as weekly cake, Friday pub trips, office parties, or country walks, I've been so privileged to have met some wonderful scientists and friends. They have enabled some of the greatest highs I've experienced during my time here, and they have also picked me up at my lowest.

I'd like to give special thanks to Tom Turner, the instrument scientist for the Flow-XI facility, who commissioned the XRD instrument which has been such a big part of my PhD. Furthermore, he acted as somewhat of a fourth supervisor to me, offering countless pieces of advice on the subjects of crystallisation and XRD analysis. I'd also like to give a special thanks and acknowledgement to Nina Patel, an MChem student with whom I worked on many of the studies covered as part of this PhD. She was an outstanding student, and I'm sure she will be both successful in and greatly enjoy her own PhD journey.

During this project, I have received a lot of help with characterisation instruments that I've needed to use, and there have been a number of people who have helped in this regard: Alex Kulak, Chris Pask, Algy Kazlauciunas, Mary Bayana, and Ben Douglas. I've also had help from several workshop-based technicians: Sam Flint, James Barnes, and Matt Broadbent. I'd also like to thank Ricardo Labes and other members

of the IPRD lab for getting me started in the labs early on in my PhD. I've been privileged to go on several trips to beamlines as part of my PhD, and I'd like to acknowledge the staff at Diamond Light Source and the European Synchrotron Research Facility (ESRF) for this opportunity, as well as Cedrick, Zhao, and the group in Nottingham for the invites.

It was a privilege to be invited for an industrial placement at Syngenta's Jealotts Hill research site, for which I would like to thank Jennifer Webb, John Hone, Neil George, and everyone else in the process studies group. I was made to feel so welcome and received so much help and support there, which made the trips so successful and enjoyable. I look forward very much to starting my new role there following the conclusion of my PhD. I'd also like to thank my industrial supervisors from AstraZeneca – Anna Jawor-Baczynska and Lauren Agnew – for their input and advice during this PhD.

I was very lucky to be part of a cohort of CDT students with whom I developed a strong friendship during the first parts of our PhDs: Sam, Harrison, Anthony, Janine, and Amna. In the case of the first two, I couldn't have asked for better housemates during a difficult winter of being locked up in the house. Thanks as well to the members of other cohorts of the CDT for their friendship and collaboration at CDT events and conferences. Thank you as well to my family - Mum, Dad, and Theo – for their help and support during this journey. I love you all very much. Last, but certainly not least, thank you Josh. You've been the most amazing, inspirational, and loving person I could ever ask to have in my life, and I'm so glad for your help during this journey. I've look up to you every day as an ideal to strive towards.

Abstract

Crystallisations are a ubiquitous class of phase-change processes and have an importance that spans industrial and natural processes. Being able to control and understand crystallisation processes is vital for the acquisition of desired properties for high added-value particulate products. X-ray diffraction (XRD) techniques remain the gold-standard method of determining crystal structure, which is intricately connected to the resultant crystal properties. Determining structure (and therefore properties) during the crystallisation process has traditionally been performed by taking samples of crystals and determining structure *ex situ*, which is slow and may induce inaccuracies. *In situ* application of XRD has, in recent years, shown promise for accurate, real-time characterisation of crystallisation processes in batch and continuous-flow devices, although this has largely been carried out using synchrotron sources. It is only recently that the next-generation of laboratory-based XRD instruments has facilitated these capabilities previously constrained to the beamline.

This report presents first a detailed literature review, covering crystallisations, the concepts underpinning continuous-flow operation and synthesis, and the scientific theory of XRD. Next, a detailed study of the crystallisation of calcium sulfate in a batch reaction vessel coupled with *in situ* laboratory-based XRD characterisation is reported across different operating conditions. This allowed for a probing of the effects of reactant concentrations, additives, and solvent selection on the crystallisation kinetics and structural outcomes. Subsequently reported is the use of a millifluidic device, which is studied as a continuous crystallisation platform. This was coupled with the XRD instrument to enable steady-state characterisation, representing a first-of-its-kind combined crystallisation and characterisation platform. Experiments from the batch crystallisation study were replicated on this continuous-flow platform, which showed utility. Finally, a study of the antisolvent crystallisation of a small organic molecule in the same continuous crystallisation platform is reported, which showed the flexibility of the platform across crystallisation systems. Overall, the project marks a significant step towards demonstrating the application and utility of *in situ* characterisation of crystallisations with a laboratory X-Ray diffraction instrument, in both batch-mode and continuous-flow.

Table of Contents

Table of Figures

Table of Tables

1. Background and Literature Review

1.1. Introduction to the Report

Crystallisation is one of the most common phase change processes encountered in natural environments and industrial settings. It is important as a phase-separation and purification step in the manufacture of high-value particulate products, such as pharmaceuticals, electronics, and consumer goods. The properties of a solid formed during a crystallisation process are intimately connected to the physio-chemical conditions present during the crystallisation. From the perspective of controlling key crystal properties (shape, size, and structure), techniques that enable these properties to be rapidly and accurately determined across multiple conditions are desirable. Traditionally, crystal properties were characterised ex situ by extracting crystals at different time-points during the reaction. Changes in the samples can also be induced during filtration, drying, and processing of these samples for analysis.

In situ characterisation techniques are therefore being increasingly explored to overcome these problems. This is particularly beneficial for transient or rapid crystallisation processes. Continuous monitoring of crystallisation processes can therefore allow more accurate kinetic models to be fitted, leading to greater understanding of how to control of crystallisation processes to deliver the desired properties. There are still issues with *in situ* techniques in terms of cost, accessibility, and the quality of the data is often inferior to that obtained from *ex situ* techniques (due to background noise or the need for operational flexibility in different operating environments). However, great strides have been made in recent years to upgrade the capabilities of *in situ* analysis equipment, leading to their increased suitability for studying crystallisation.

Powder X-ray diffraction (PXRD) is undoubtedly the ‘go-to’ method of determining the crystal structure of a bulk powder. PXRD is easy to perform and analysis of the results is both intuitive and trivial. PXRD may be carried out with a laboratory-based instrument or at specialist synchrotron facilities, where the latter can provide incomparable levels of analytical resolution relative to the former. Recently, *in situ* studies of crystallisation processes have been carried out using synchrotron facilities. This has allowed for processes such as the earliest stages of crystallisations to be characterised, as well as the accurate characterisation of transient crystallisation processes. However, synchrotrons are heavily over-subscribed, and the limited time available during a single beamtime constrains the number and complexity of

experiments that can be performed. This has partially driven the development of laboratory-based sources to the point where the X-ray brilliance and detection capabilities of modern instruments is approaching the threshold where more detailed *in situ* experiments are increasingly viable.

In this report, a state-of-the-art custom-designed PXRD laboratory instrument is used to study crystallisation processes *in situ* in batch and continuous-flow environments, and to explore the capabilities of this technique. Two different crystallisation systems were studied: the reactive precipitation of calcium sulfate and the antisolvent crystallisation of ROY. In the case of the former, the effects of supersaturation, inorganic additives and solvent conditions were screened across batch crystallisations, and time-resolved kinetic analysis was enabled by calibration of diffraction intensities against the solid content. Continuous-flow reactions were carried out in a millifluidic device (the *fReactor*), which showed good solids-handling and the ability to effectively mix reactants resulting in precipitation. Furthermore, the integration of X-ray transparant 'windows' at different points along the length of the reactor enabled novel steady-state *in situ* characterisation across the length of the cascade, allowing the progress of the crystallisation to be monitored. This work provides the first example of an actively-stirred continuous-flow device being used in this manner with a laboratory-based XRD instrument. The antisolvent crystallisation of a small organic molecule (ROY) was also carried out using the fReactor at a variety of different conditions, and demonstrated the versatility of platform. Together, these studies show that *in situ* laboratory PXRD can be used to understand the effects of processing conditions on crystallisation phenomena.

1.2. Crystallisation Science

1.2.1. Crystal Structure

Crystals are solids in which atoms, ions, or molecules are arranged in a repeating, periodic lattice, which exhibits long-range order [1]. Solids not exhibiting this long-range order can be described as amorphous or non-crystalline [1]. Studying the internal structure of crystals is of interest, as the properties of the crystalline material are intrinsically dependent on the crystal structure [2]. Crystals possess symmetry, whereby planes, axes or points exist in the structure about which the crystal can be rotated and appear to reach its original structure before a full 360° rotation has been accomplished [3]. There are 32 different combinations of state of symmetry (including

an asymmetric state), which are referred to as the different point groups. The 32 different point groups can be classified into seven different crystal systems of point groups: cubic, tetragonal, orthorhombic, monoclinic, triclinic, trigonal, and hexagonal. This classification is performed on the basis of relative angles between axes of the points in the point lattice and the distance between points – the lattice parameters (Figure 1) [1]. A single cell constructed using the lattice parameters is referred to as a unit cell, which when repeated over and over again builds up a larger crystal with a regular repeating pattern – the Bravais lattice. There are 14 different Bravais lattices which are shown in Table 1. These are generated by combining 7 different crystal systems with centering types (face centred, body centred, base centred, or primitive).

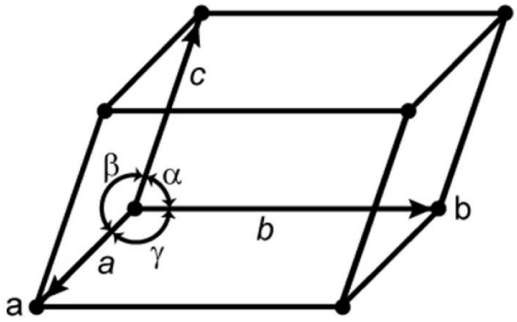

Figure 1 - An example of crystal axes applied to a unit cell. The crystal parameters are shown on the exes, with a, b, and c being the lengths of each of the corresponding axes, and the angles α, β, and γ representing the angles between the axes b-c, a-c, and a-b respectively.

Table 1 – The 14 Bravais lattices and their corresponding crystal system. Their relative axis lengths and axis angles are shown.

Crystal System	Bravais Lattice	Axis Lengths	Axis Angles
Cubic	Cube	a=b=c	α=β=γ=90°
	Body-Centred Cube		
	Base-Centred Cube		
Hexagonal	Hexagonal Prism	a=b≠c	α=β=90°, γ=120°
Rhombohedral	Rhombohedron	a=b=c	α=β=γ≠90°
Tetragonal	Square Prism	a=b≠c	α=β=γ=90°
	Body-Centred Square Prism		
Orthorhombic	Rectangular Prism	a≠b≠c	α=β=γ=90°
	Body-Centred Rectangular Prism		
	Rhombic Prism		
	Body-Centred Rhombic Prism		
Monoclinic	Monoclinic Parallelepiped	a≠c	α=γ=90°, β≠90°
	Clinorhombic Prism		
Triclinic	Triclinic Parallelepiped	All other cases	

The combination of the 14 Bravais lattices, the lattice transformations and symmetries described by point groups, and other symmetry elements such as rotation or screw axes results in 230 different space groups, with the arrangement of atoms or molecules in a unit cell being described by one of these space groups [4]. Effectively, the space groups describe the symmetry of a crystal pattern [5]. Identification of the unit cell and space group can be achieved using XRD [4]. A point in the Bravais lattice can represent, in a physical crystal system, either one atom or molecule, or multiple atoms or molecules. The packing arrangement of the molecules or atoms that make up the points in the lattice depends on the intermolecular bonds between the atoms or molecules that make up the lattice. According to the close-packing theory proposed by Kitaigorodski, atoms will be arranged in the lattice in such a manner as to minimise free space in the lattice [6]. More free space occurs in crystal structures where hydrogen bonding is present.

Directions from any point on the lattice can be described using indices of direction, which are in turn described by directions of travel relative to the 3 different axes. For

example, going from a point (0,0,0) to a point (1,1,1) returns an indices of direction of [1,1,1]. Negative directions (e.g. (0,0,0) to (-1,1,0)) can be described using a bar above the number: [$\bar{1}$,1,0]. A family of directions is represented by the <1,1,1> notation, which covers all combinations of negative and positive directions relative to each of the three axes. Miller indices with the notation {h,k,l} are used to represent planes within a crystal lattice. The parameters h, k, and l represent the reciprocals of where the plane crosses the axes x, y and z respectively. If a plane runs parallel to an axis, the parameter becomes zero. Miller planes are used to describe real crystals through the use Miller indices of the crystal faces which appear in the crystal habit (shape) [1]. Examples of planes and Miller indices are shown in Figure 2.

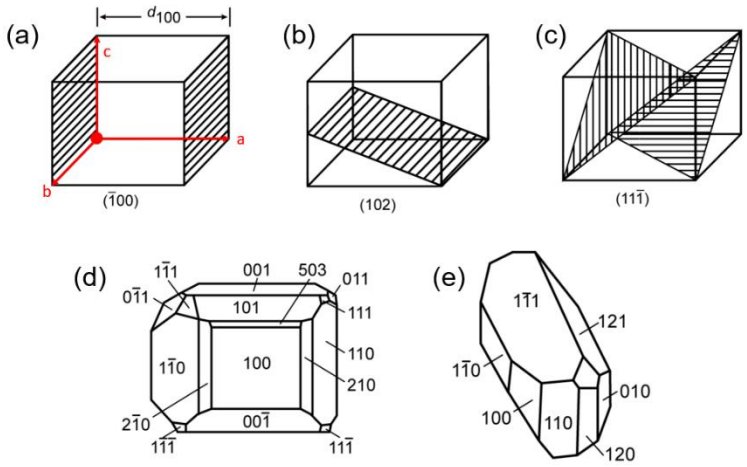

Figure 2 – (a)-(c) Planes in relation to axes a,b and c, and the Miller indices of the planes. (d)(e) Crystal habits of two different crystals and the Miller indices of the faces [2].

1.2.2. Crystal Nucleation

Crystallization is the process by which a solute in solution, a liquid, or a gas is transformed to a crystal [7]. Crystallization can be described as a two-stage process: the *nucleation* of a new crystalline phase, and its subsequent *growth*. The first step in the nucleation of a new phase is the formation of a supersaturated phase, wherein it is thermodynamically favourable to form a new crystalline phase (the spontaneous appearance of a new phase can only occur at such non-equilibrium conditions) [8]. Supersaturated phases, in the case of a solute in solution, are those that contain more dissolved solute than would otherwise be expected at thermodynamic equilibrium with the solid phase [3]. This does not necessarily mean that a solid phase will appear spontaneously, as there are other kinetic barriers to be overcome to transform the

solute into an ordered solid phase [9]. The solubility refers to the maximum amount of solute that can be dissolved into a solution at a given state [3].

The fundamental driving force for crystallization to occur is the difference in chemical potential (Δμ) of a solute molecule in a supersaturated solution (μ_s) and in the crystal state (μ_c), as shown in equation 1.

$$\Delta\mu = \mu_c - \mu_s \quad (1)$$

The dimensionless thermodynamic expression for supersaturation can be defined in terms of the chemical potential of a solute molecule in solution (μ_2) and a solute molecule at equilibrium conditions (μ_1), as shown in the dimensionless expression equation 2 [10].

$$\sigma = \frac{\mu_2 - \mu_1}{RT} = ln\left(\frac{\gamma_2 x_2}{\gamma_1 x_1}\right) \quad (2)$$

Where γ and x refer to the activity coefficients and mole fractions respectively, and subscripts 1 and 2 refer to saturated (thermodynamic equilibrium) and supersaturated conditions, respectively. Commonly, the ratio of activity coefficients (γ_2/γ_1) is assumed to be unity (for a system close to ideal), and the ratio of mole fractions is approximated to the equivalent concentrations in solution [11]. The latter ratio is referred to as the supersaturation ratio, S, shown in equation 3. These approximations generally hold at low supersaturations, and can be inaccurate at high supersaturations [10]. A common simplification is shown in equation 4, which neglects the requirement for the activity coefficients to be known.

$$S = \frac{c_2}{c_1} \quad (3)$$

$$\sigma \approx ln(S) = ln\left(\frac{c_2}{c_1}\right) \quad (4)$$

Although supersaturation is required for crystallization to occur, it does not necessarily occur instantly – the existing phase is metastable at sufficiently low supersaturations, and a kinetic barrier still needs to be overcome [9, 12]. Empirically, the rate of nucleation is heavily related to supersaturation through a power law dependency [13]. Nucleation is typically divided into two categories: primary and secondary nucleation, with primary nucleation typically further divided into homogeneous and heterogeneous nucleation.

Primary Nucleation – Homogeneous Nucleation

Primary nucleation is nucleation that occurs in a previously crystal-free environment [14]. Primary nucleation is further divided into two categories: homogeneous and heterogeneous nucleation. Homogeneous nucleation occurs exclusively in the bulk fluid that contains only solvent and solute, without the presence of other crystals, surfaces, or impurities [15]. Although the process by which homogeneous nucleation takes place is not fully understood, one theoretical description of homogeneous nucleation is classical nucleation theory (CNT). The new, small crystalline structures that form the bulk of the new supersaturated phase must have a free energy that is lower than that of the old phase [13]. However, because of the effect of the surface atom's positive contribution to the free energy of the new nucleated phase (from the interfacial surface energy), these nuclei are not necessarily stable. An interfacial energy gap is present between the bulk atoms and the surface atoms, which results in an energy barrier being present that must be overcome to form the new crystalline phase [13]. When there are a low number of atoms which have joined to form a cluster, as is the case initially in the supersaturated phase, the contribution of the surface atoms to the free energy dominates, dissolution is energetically favourable, and the nucleus is unable to grow and dissolves. When the clusters become sufficiently large the contribution of the surface atoms to the free energy becomes small enough that the bulk dominates, and a reduction in free energy can be achieved though the growth of the nucleus, and thus the nucleus is stable [13]. There exists a critical size where the nucleus is large enough to continue growing spontaneously, as any growth will result in a reduction in free energy. This trade-off between the free energy change for the formation of a surface and the change associated with the phase transformation forms the basis of CNT [8]. This process is depicted graphically in Figure 3 [8]. This shows the free energy change associated with the creation of new surface (ΔG_S) and in the creation of the bulk phase crystalline structure (ΔG_V) as the radius of a nucleus increases.

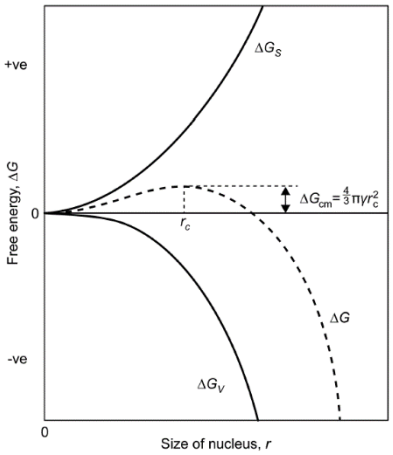

Figure 3 – Change in free energy in the creation of new surface (ΔG_s) and phase transformation (ΔG_v). The combined effects over a range of nucleus sizes are shown by the dashed line. The critical nucleus size beyond which an increase in nucleus size results in a reduction of free energy is shown by r_c [8].

The activation barrier for crystallization is the maximum value of free energy change and is shown in equation 5 in terms of the critical radius (r_c) and the surface tension (σ).

$$\Delta G_{crit} = \frac{4}{3}\pi {r_c}^2 \sigma \qquad 5$$

To calculate the predicted steady state rate of nucleation, J, an Arrhenius relationship can be used, as shown in equation 6. This is derived from the dependence of the nucleation rate on the critical free energy change associated with the critical nuclei size [8].

$$J = Aexp\left[-\frac{16\pi\sigma^3 v^2}{3K^3T^3(lnS)^2}\right] \qquad 6$$

where A is a pre-exponential factor, σ is the surface tension, v is the molecular volume, k is the Boltzmann constant, T is the temperature and S is the relative supersaturation. Clearly, the rate of nucleation is heavily dependent on supersaturation within CNT. Furthermore, the pre-exponential factor, which is related to the rate of attachment of molecules to the critical nucleus, is thus dependent on the mobility of molecules, and therefore changes with the temperature of the system.

The operating region where the system is supersaturated but nucleation does not occur spontaneously is referred to as the metastable zone, which can be visualised on a graph of concentration against temperature (Figure 4). At a sufficiently high

supersaturation, the critical radius is reduced to the point where it's is smaller than the units of growth – in the presence of an initiating site, nucleation occurs then occurs and is limited only by the transport of growth units to the nucleus [13]. At this point, the process is in the labile zone, and the system is undergoing spinodal decomposition. Experimentally, the metastable zone width (MSZW) is determined based on the point at which nuclei are first detected by analytical equipment, such as a focused beam reflectance measurement (FBRM) probe [16]. The true size of a critical nucleus, however, is often below the detection limit of most analytical equipment, and as such there is a large amount of uncertainty as to what happens between nuclei formation and detection [17]. It is thought that homogeneous primary nucleation rarely occurs through spinodal decomposition in industrial operations due to the presence of impurities and foreign surfaces [8]. These have a catalysing effect on the crystallization process, resulting in nucleation at much lower supersaturations than in the case of spinodal decomposition [18].

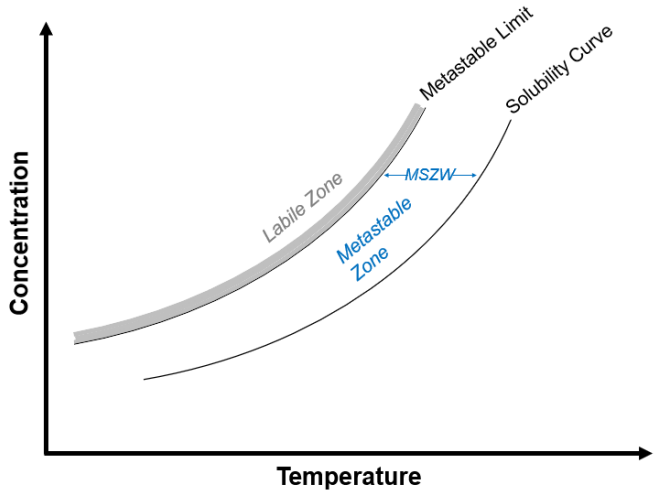

Figure 4 – Phase diagram for a crystallization process showing the metastable zone and the labile zone. A solution to the right or below the solubility curve is undersaturated. Entering the metastable zone, the solution is supersaturated, but nucleation is not necessarily observed instantaneously due to the requirement for a critical nucleus size for nuclei to become stable. At the Labile zone, nucleation takes place near instantaneously, as the critical radius is less than the radius of the growth units.

This derivation of a critical nucleus size is based on many assumptions, such as the nuclei being spherical and the surface tension being independent of curvature effects (capillarity assumption), which affect the change in free energy associated with the creation of surface. These assumptions mean that CNT does not accurately describe nucleation in many systems, resulting in experimental discrepancies in predicted

nucleation rates [8, 19]. CNT often gives too high a predicted nucleation rate at high temperatures, and too low a rate at low temperatures [12], which is explained by the lack of consideration of the effect of curvature and size on surface tension, and the lack of consideration of the vanishing of the nucleation barrier once the region of spinodal decomposition has been reached [8].

A number of alternate theories have therefore been developed that in particular aim to address the capillarity assumption [8]. CNT assumes a single-step process; several recent theories have proposed two-step nucleation processes, which involve the creation of a metastable dense liquid-like phase of solute particles within which the solute molecules can order into a crystalline phase [8, 20]. The two-step theory has been successful in explaining observations not covered by CNT, such as the much lower than predicted observed nucleation rate of Lysosome crystals [20]. Initially applied to protein crystallization, two-step nucleation theories have been developed and applied to a number of systems, including small-molecule organic and inorganic compounds and biominerals [20].

Primary Nucleation - Heterogeneous Nucleation

Heterogenous nucleation is nucleation that takes place on the surface of foreign microparticles or substrates that provide an active centre for nucleation to take place [15]. The foreign particles and surfaces reduce the activation energy required for nucleation to occur by reducing the surface excess energy of nucleation clusters [8]. As such, a crystallizing system will experience a higher nucleation rate when undergoing heterogeneous nucleation than homogeneous nucleation at the same supersaturation [21]. The decrease of the activation barrier and thus the rate of heterogeneous nucleation is dependent on the contact angle between the pre-nucleation cluster and the substrate on which it is adsorbed. A lower contact angle, and thus a higher degree of substrate wetting by the cluster, reduces the free energy change associated with nucleation by a contact angle factor, Φ.

Secondary Nucleation

Secondary nucleation refers to nucleation that takes place because of the presence of existing crystals of the same compound [22]. Secondary nucleation has a lower activation barrier, and as such occurs at lower supersaturation [16]. Secondary nucleation often occurs in industrial crystallization processes where crystallisation reactions are performed at supersaturations where there is little primary nucleation

[21, 23]. Typically, in a starting solution free of existing crystals of the solute, primary nucleation will initially dominate, but once a sufficient number of particles have been generated, secondary nucleation will dominate the rest of the crystallization process [16]. Several theories have been proposed regarding the origin of secondary nuclei, including the shearing- or breaking-off of the non-crystalline solute layer on a growing crystal, and the attrition of smaller crystalline particles from a larger particle [16].

1.2.3. Crystal Growth

The second step in the crystallization process following nucleation is crystal growth. This involves the addition of growth units to the stable nuclei to increase their size and develop a crystalline product. Both the nucleation and growth stages control the final particle properties, such as size, purity, and crystal habit (shape) [1]. This is a result of not just the rate of growth in mass or volumetric sense, but in terms of the relative growth of different crystal faces, which grow at different rates as a result of internal structure and bonding, crystallization conditions, interfacial attachment kinetics, and the presence of impurities [7]. The differences in growth rates of different faces results in different morphologies, as faces with relatively slow growth rates will have a larger surface area in the product crystal, and vice versa [24, 25].

Theories of Crystal Growth

The growth of a face of a crystal can be assumed to grow in a layer-by-layer fashion, with growth units undergoing desolvation from solution and adsorbing onto the surface of the crystal [1]. This can occur at different sites on the crystal surface, where the number of bonds the growth unit forms with the surface is dependent on the nature of the surface and the available sites for bonding. A schematic of a crystal surface where growth units are represented cubically is shown in Figure 5.

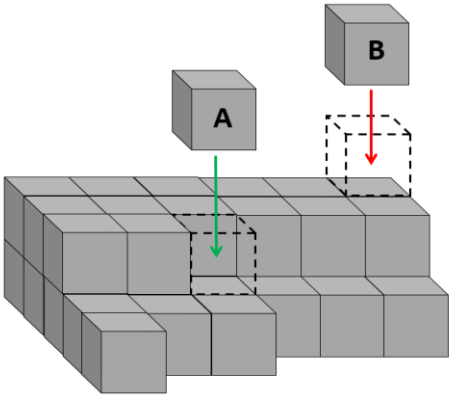

Figure 5 - Kink site model for crystal growth. 'Molecule' A will be less likely to detach from the bulk, as it is coordinated on more sides than B.

A growth unit that has attached to the growing crystal face can do one of two things: remain on the face or detach back into the solution. The chance of either happening is dependent on the strength of the bonding between the growth unit and the number of bonds the growth unit can form with other atoms [13]. Molecule 'A' on figure 7 has bonds with three other molecules, whereas molecule 'B' is only bonding with one other molecule. Assuming all bonds are the same strength, this means that molecule A is much more likely to remain on the growing crystal face, and molecule B is more likely to detach and go back into solution. Thus, molecule A is more energetically stable than molecule B. A site where two bonds can form is referred to as a 'step' and a site where three bonds can form is referred to as a 'kink' site [1]. The energetically favourable kink and step sites mean that growth can be modelled by the units initially adsorbing onto the surface, then diffusing across to a kink or step site, resulting in growth by steps [1]. Importantly, growth by kink site addition does not change the overall effective surface area, conveying less of a surface tension penalty. The rate of the step advancement is given by the difference in the rate of detachment and attachment, in terms of molecules per unit time. From this, a speed of step advancement (v) can be derived, being the product of the rate of step advancement and depth of the kink (units of length). The equation for speed of step advancement is given by equation 7 for the assumption of a rough step with a high density of kink sites [13].

$$v = \Omega\beta(C - C_e) \qquad 7$$

where C is the concentration and subscript e refers to equilibrium concentration, Ω is the volume of the molecule and β is a parameter called the kinetic coefficient. For

smooth surfaces without kink sites, the speed of step advancement is described as equation 8.

$$v = \Omega\beta[(C - C_e) - C_e f(n_1)] \quad (8)$$

where f(n_1) is a function for a kink site density that varies with absolute supersaturation. It increases in a linear manner at low concentrations and reaches a constant value at high concentrations. Because equation 10 and 11 both imply that step speed increases with absolute supersaturation, step speed also scales with solubility, and thus a more soluble molecule will have a faster step speed than a less soluble molecule [13]. A number of different growth theories have been developed to explain in more detail how steps form (as opposed to just propagate) and what the rate-limiting factor is in the growth of faces [1].

The first such theory is two-dimensional growth theory, which considers the growth units as two-dimensional spheres nucleating on the surface of a growing crystal and uses much of the same logic as CNT (in regards to critical radius) [26]. Using CNT, rate equations for the formation of critical nuclei per unit surface area per unit time can be found and reveal a strong dependence on temperature and supersaturation. But to predict how the nuclei spread to form a new layer, two models have been suggested: mononuclear, where nuclei spread instantaneously to form a new layer at infinite velocity; and polynuclear, where nuclei do not spread at all and instead a new layer is formed by the accumulation of enough nuclei to cover the surface. Issues with both models exist, as the mononuclear model suggests that growth rate is directly proportional to surface area (which is not experimentally true) and the polynuclear model predicts that at a certain supersaturation the growth rate will reach a maximum value beyond which growth rate will decline (which has not been experimentally observed) [26]. A third model (the birth and spread model) considers the spreading velocity to exist as a non-zero finite value and has shown slightly more usefulness compared to the previous two, although it can struggle to accurately predict growth rates at low values of supersaturation [26].

The second proposed theory is the Burton-Cabrera-Frank (BCF) theory of crystal growth, which has had some success in alleviating issues with two-dimensional growth theory. This is achieved by considering growth as a continuous, self-perpetuating process, with screw dislocations resulting in spiral growth [27]. The theory of growth from screw dislocations helps to explain how crystals can grow even under low levels of supersaturation (in contrast, two-dimensional growth theory suggests that nucleation of the two-dimensional islands should not be able to occur

at low supersaturations [28]). A schematic showing how spiral growth occurs from screw dislocations is shown in Figure 6. A subset of the BCF model useful for describing solution growth (where diffusion of the growth units through a boundary layer is likely to be the rate-limiting step) is the bulk diffusion model proposed by Chernov [29]. An important element of the BCF model and Chernov's diffusion model is the consideration of the effects of hydrodynamic conditions on the growth rate [26]. Both models predict that growth rate will initially increase as the relative velocity between the crystal and solution increases, in a process referred to as mass transfer limited growth. Eventually, it will reach a maximum growth rate, which represents the point at which surface diffusion limits the growth rate. This is referred to as growth limited by interfacial attachment kinetics.

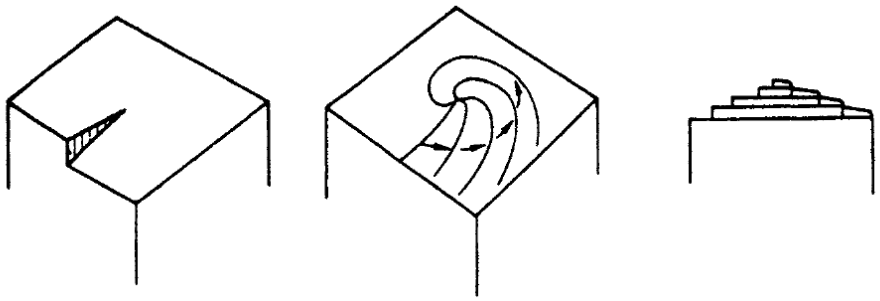

Figure 6 - Propagation of spiral growth from a screw dislocation (shown on the left) in BCF theory [29].

Crystal Growth Kinetics

Measuring the kinetics of crystal growth is of vital importance for the design and operation of industrial crystallizer units such that crystals with the desired properties are produced. To describe crystal growth, one can describe how a particular dimension changes with time through a description of *linear growth rate* [26]. This can be described by the rate of growth perpendicular to a particular face. The linear growth rate of a characteristic dimension of a crystal can also be specified, where this is typically the second longest dimension [26]. This dimension can be related to a shape factor to describe both the surface area and volume of the crystal. A second way of measuring crystal growth is in terms of the change in mass of a crystal with time, which can be related to the characteristic length, L, as per equation 9.

$$R_G = \frac{1}{A}\frac{dM}{dt} = 3\frac{\alpha}{\beta}\rho G = 3\frac{\alpha}{\beta}\rho\frac{dL}{dt} \qquad 9$$

where R_G is the increase of mass per unit time per unit surface area, A is the surface area of the crystal, ρ is the crystal density, and α and β are volume and area shape features respectively. The shape features must be known or estimated to calculate crystal growth in terms of mass. Often, a spherical crystal shape can be assumed, and the equivalent spherical shape features used, although naturally this may be inaccurate for crystals which are not roughly spherical [26].

As in nucleation, crystal growth can only occur in a state of supersaturation [30]. The rate of cooling or addition of antisolvent is crucial in determining the supersaturation and can be used to control the rate of nucleation and growth and therefore the properties of the product crystals [31]. Following nucleation, if the crystals are of a sufficient size, then the contribution of the surface (or interfacial) energy is negligible, and the difference in bulk free energy of both the crystal and the solution represents the difference in chemical potential [32]. For different types of crystal growth, the growth is limited by the rate-limiting step, which can be one of three steps (the slowest being the rate-limiting step) [32]:

1. The introduction of atoms or molecules to the crystal phase across the interface between crystals and a growth medium (the interface kinetic process)
2. The supply of atoms or molecules to the interface (the volume diffusion process)
3. The removal of latent heat from the growth interface from crystallization

During solution growth in industrial settings, the rate of growth is typically determined by both the interface and diffusion kinetics, operating in a mixed diffusion-kinetic regime [30]. As the relative motion of the crystals compared to the solvent molecules increases, the diffusion step becomes less controlled as the local concentration of solute around crystals increases, and the interface kinetics play a larger role in determining the rate of growth [33]. Mass transfer, and thus the rate-limiting step, is heavily controlled by the convection of the solute molecules relative to the solvent molecules, which is in turn influenced by the degree of agitation and mixing in the crystallization vessel [34]. A useful model for the consideration of mass transfer from the bulk to the crystal is the boundary layer model [34].

To express crystal growth as a function of supersaturation, two different equations can be used for both linear growth velocity in terms of unit length per unit time (G,

equation 10) and mass rate of crystal growth in terms of mass per unit area per unit time (R_G, equation 11).

$$G = k_g \Delta C^g \quad (10)$$

$$R_G = K_g \Delta C^g \quad (11)$$

where k_g and K_g are constants, ΔC is the supersaturation (=C-C_{sat}) and g is a power usually between 1 and 2. The two constants are temperature-dependent, and as such can be fitted to Arrhenius relationships (with pre-exponential constant A) [1], as shown in equation 12 for the linear crystal growth velocity constant k_g. A complete representation of crystal growth velocity can then be derived by consideration of supersaturation ΔC, as shown in equation 13. The value of the activation energy E_a can be used to determine whether the rate-limiting step is diffusion or surface integration. Activation energy values of diffusion controlled processes are generally in the range 10-20 kJ mol^{-1} and 40-60 $kJ.mol^{-1}$ for surface integration controlled processes [3]. Reactions tend to be diffusion controlled to a higher degree at higher temperatures, as the rate of integration of molecules into crystals increases more than the rate of diffusion [3].

$$k_g = Aexp(-E_G/RT) \quad (12)$$

$$G = Aexp(-E_G/RT)\Delta C^g \quad (13)$$

Growth rates can be measured in a number of ways, roughly categorised as single crystal, or suspensions of crystals measurements [1]. Techniques for measuring the growth rates of single crystals include using a single-crystal growth cell and a travelling microscope to measure face-specific growth rates (as shown in Figure 7) [3]. A small (order of mm) crystal is mounted on a tungsten wire in the desired orientation, and exposed to a flowing solution of known temperature, velocity and supersaturation, and the rate of advance of the face of interest is measured by observing it with a travelling microscope. The overall growth rate can also be calculated by growing seed crystals with specified sizes under carefully controlled hydrodynamic conditions and constant supersaturation, and measuring the mass deposited on the crystals [21]. From this, the overall linear growth rate, G ($m.s^{-1}$) can be expressed as per equation 14 [3].

$$G = \frac{M_i^{1/3} - M_f^{1/3}}{(\alpha \rho N)^{1/3} t} \quad (14)$$

where M_i and M_f are the initial and final mean masses respectively, α is the volume shape factor of the crystals, ρ is the density, and t is time. This can then be related to the supersaturation via equation 15 [3].

$$G = \frac{\beta}{3\alpha\rho} K_G \Delta c^g \qquad 15$$

where β is a crystal surface shape factor and Δc^g is the mean supersaturation over the course of the experiment.

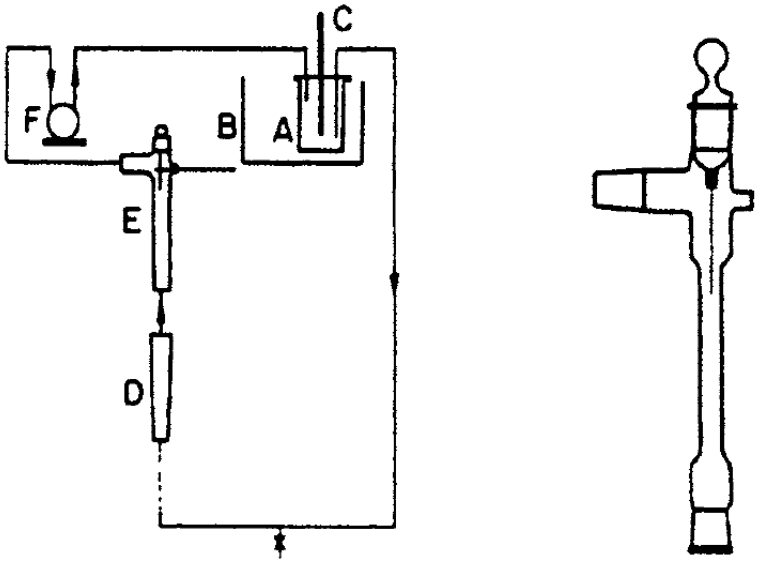

Figure 7 – Apparatus used for the measurement of face specific growth rate of a single crystal. On the left is the complete circuit, showing (A) solution reservoir, (B) thermostat bath, (C) thermometer, (D) flow meter, (E) cell, (F) pump. Shown on the right is a more detailed view of the cell in which the single crystal is suspended [114].

Size Dependent Growth and Growth Rate Dispersion

Differences in solubility exist between particles of a sufficiently small size and slightly larger particles, where smaller particles experience a higher solubility in solution [26]. Smaller particles therefore experience a smaller supersaturation – and therefore slower growth rate – than larger particles. This is generally true for particles below 1µm in size. For larger sized crystals, several mechanisms of size-dependent growth have been proposed by Garside and co-workers. These are based on the assumption that growth occurs via the BCF theory of crystal growth, where screw dislocations facilitate self-perpetuating growth. It is proposed that as the crystal grows, its surface area increases, and so does the chance of dislocations being present. A higher number of screw dislocation sites means that there are more sites for self-perpetuating growth to occur [35, 36]. Garside and co-workers also proposed a

mechanism for situations in which bulk diffusion as opposed to interfacial attachment is the limiting factor [37].

Although size-dependent growth explains how particles of different sizes can grow at different rates, there have been observations of particles initially of the same size growing in identical operating conditions, but at different rates, resulting in a range of final particle sizes. This observation is termed growth rate dispersion [23] two different mechanisms have been proposed to explain it [1]. The first is that the growth rate of a single crystal is determined at the point of nucleation, and each crystal then grows at that constant rate such that a population of crystals will possess a range of constant growth rates. The second proposed mechanism is that the growth rate of the crystals fluctuates over time, although the time-averaged growth rate is identical for the population of crystals. This could result in two different crystals exhibiting two different growth rates, although their average growth rates over a sufficiently long time are identical. Growth rate dispersion again originates from BCF growth theory. It is proposed that the random appearance of screw dislocations could result in a stochastic range of growth rates across a range of crystals [22]. The movement of dislocations from one face of a crystal to another could result in a change in growth rate of that face on the order of 5 to 6 orders of magnitude [22]. The number and density of dislocations could also be affected by collisions with the crystallizer wall, impeller, or other crystals, changing the growth rate of that crystal [1].

Crystal Habit

The crystal habit refers to the external shape or morphology of a crystal and is determined by the growth rates of the individual faces [1]. To describe the geometry of the crystal habit, one can make use of a characteristic dimension, L, which typically refers to the second longest dimension of the crystal and is used to describe its volume (V, equation 16) and area (A, equation 17).

$$V = \alpha L^3 \quad (16)$$

$$A = \beta L^3 \quad (17)$$

where α and β refers to the volume and area shape factors respectively. Crystals with the same crystal structure and thus faces will not necessarily exhibit the same habits if the areas of the crystal faces are different [1]. There are many factors that can affect the crystal habit by altering the relative rates of growth of different faces. The supersaturation can affect the morphology of the resultant crystal, as different faces

will grow at different rates at different supersaturations, resulting in a different crystal habit [38]. The degree of mixing can also affect the transfer of mass to the growing crystal faces, affecting the growth and thus habit [38]. Considering the Arrhenius nature of the growth rate equation, temperature can affect the growth rates of different faces in different ways if the faces each possess different activation energies [38]. Solution pH can also affect the growth rates of different faces resulting in a modification of habit, where the pH may affect the nature of the solute molecules in a solution [30].

The differing interactions of different solvents with the crystal faces can also change the morphology of crystals. For example, polar solvents such as acetone can preferentially absorb on more polar crystal faces, inhibiting their growth (the same is true for non-polar solvents) [39]. The presence of impurities in a crystallizing system can affect both the nucleation and growth of solutes, serving to both increase or decrease the rates of each [3]. Impurities change the growth rates in a variety of ways, for example by changing the supersaturation [3]. Impurities can also be absorbed preferentially onto different crystal faces, slowing their growth and thus modifying the overall morphology. In particular, adsorption at kink sites may be particularly effective in slowing the step velocity and thus the growth of the crystal face [40]. Adsorption of impurities at step sites can lead to a rounding of growth layers, which also modifies the morphology [41].

Control of morphology is an important consideration in industrial crystallization, as the morphology of a crystal can impact unit operations (such as filtration and centrifugation), product handling (dust formation, agglomeration, and breakage), and product properties (and therefore product performance) [38]. One manner of controlling the morphology is through the use of tailor-made additives. These modify the crystal habit by having one part of the molecule that bonds to the crystal lattice and a second part that does not. The part that does not can cause significant interatomic stresses and also repel growth units, resulting in disruption of the crystal structure and modification of face specific growth rates [38].

Temperature cycling is a common method of crystal size and shape modification and relies on repeated heating and cooling of crystals [1]. This can exploit the Ostwald ripening effect, whereby smaller particles will dissolve and deposit on the surface of larger particles (owing to their higher solubility), resulting in a narrowing of the crystal size distribution (CSD) as the system aims to minimise surface free energy [1]. Likewise, it can cause smaller particles to dissolve whilst larger particles grow,

resulting in control over the number of smaller particles and thus control of size [42]. Selection of the cycling temperature and number of cycles is key to making sure that dissolution is controlled to the correct degree [43]. The heating and cooling rates, end temperatures, and the inclusion of an aging period at a higher temperature are other factors that can be modified to get the desired crystal sizes [1]. Control of particle size using heating and cooling cycles has been achieved recently through the use of process analytical technology (PAT) to monitor the onset of nucleation and control the number of particles in solution, typically using FBRM for this purpose [44].

Seeding

Seeding is a strategy used in crystallization processes to control the final size and properties of crystals [21], and is achieved by adding heterogenous or homogeneous crystals with specific characteristics to a crystallization solution to nucleate or grow new crystals [45]. Seeding works by separating the nucleation and growth stages of the crystallization process, ensuring that the process operates exclusively within the metastable zone where growth of the crystals will occur. Within this operating zone, primary nucleation is effectively suppressed, and the system is dominated by the growth of seeds, resulting in a more uniform and controlled distribution of crystal sizes [46]. To make seeding more effective, supersaturation can be monitored in situ and maintained at a constant value [47].

A number of factors have to be controlled if seeding is to be effective. Seed loading refers to the amount of seed that is added to a crystallization process and can be expressed in terms of mass or surface area [45]. An increase in the mass of seed loading results in a smaller difference in the mean sizes of the seed and product crystals, as the same supersaturation (and thus growth) is spread out over more particles [48]. Using the same mass of seeds, but with smaller sizes results in smaller final crystals, and small differences between the size of the seed crystals and the product crystals [49]. Thus, the characteristics of the seeds are also important. Another characteristic to be considered is the size distribution of the seeds, where a broad dispersion of seeds will result in a broader size distribution of the products [50]. In terms of operation, identifying the point of seeding is key in a crystallization process [45]. Typically, this requires knowledge of both the solubility curve and MSZW. Seeding then typically takes place approximately mid-way through the metastable zone, to ensure growth whilst suppressing primary nucleation. A typical temperature curve shown within the metastable zone is shown in Figure *8* [45].

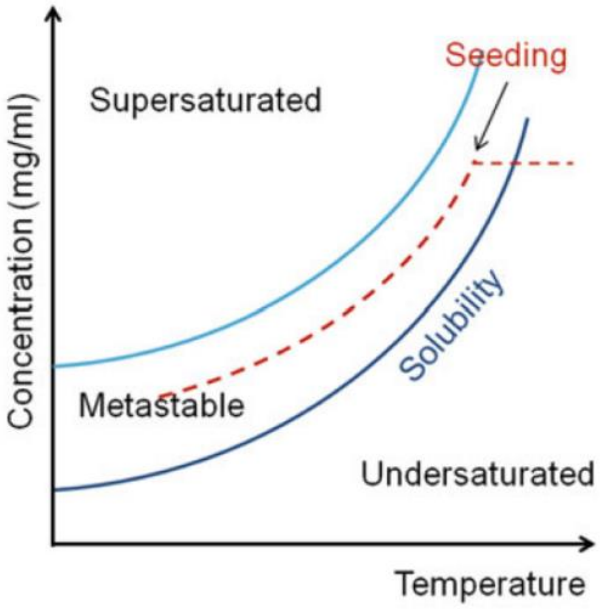

Figure 8 – A typical operating curve for a seeded crystallization process (shown with the dashed red line). The point of adding seed crystals is shown to be midway through the metastable zone, in order to supress nucleation whilst maintaining growth.

1.2.4. Polymorphism and Crystal Morphology

Polymorphism is the ability of a chemical species to adopt more than one crystalline packing arrangement [1]. The molecules within two different polymorphs will be arranged differently in the solid state but will be identical in terms of composition within the liquid or vapour state [51]. Polymorphs can exhibit different shapes due to differences in the lattice. This can cause changes in physical properties such as hardness, density, melting point, solubility and reactivity [3]. This does not imply, however, that all changes in morphology are a result of polymorphism – as mentioned before, the relative growth rates of different faces results in a change in morphology, but this will not change the crystal structure itself. The differences in properties can be useful for industrial purposes, where it is often desirable to selectively produce one polymorph that has the physical properties best suited to processing (e.g. filterability) or performance (e.g. bioavailability) [52]. A good example is that of paracetamol, where form II has superior compressibility and solubility than the more common form I, but is difficult to produce [53]. Solvates are a form of crystal structure closely related to polymorphs, where solvents can be incorporated into the crystal lattice in different amounts [1]. Where the solvent incorporated is water, these are referred to as hydrates These are often found in natural environments [54].

Thermodynamics and Kinetics of Polymorphism

Different polymorphs have different thermodynamic stabilities, and their formation (and the transformation between them) is dependent on kinetic (and other) factors [1]. At any temperature (except for a transition temperature) one polymorph is thermodynamically stable, and any other polymorphs are thermodynamically metastable such that they are capable of transforming into a more stable polymorph [3]. The stability of a polymorph can be assessed using the chemical potential of a species in each polymorphic form – in the case of two polymorphic forms (I and II), form I will be more stable if it fulfils the criteria in equation 18.

$$\mu_I < \mu_{II} \qquad 18$$

where μ represents chemical potential and subscripts I and II represent forms I and II respectively. From this, one can deduce that the more stable phase will always have a lower solubility in any solvent [3]. It is important to assess the number of different polymorphic forms that can be obtained from a crystallization process, the relative stabilities of each polymorph, and the conditions under which different polymorphs are obtained. The relationship between temperature and the stability of polymorphs can be described as either monotropic or enantiotropic, where these thermodynamic behaviours are shown in Figure 9 [3]. Within a monotropic relationship (for the example of two polymorphic forms), one form is always more stable than the other, whereas in an enantiotropic relationship, there exists a point at which the most stable polymorph switches from one form to another. Another caveat is how the natures of monotropic and enantiotropic relationships affects the reversibility of a polymorphic transformation. Monotropic relationships imply an irreversible change in form, whereas enantiotropic relationships allow reversible changes in form [1].

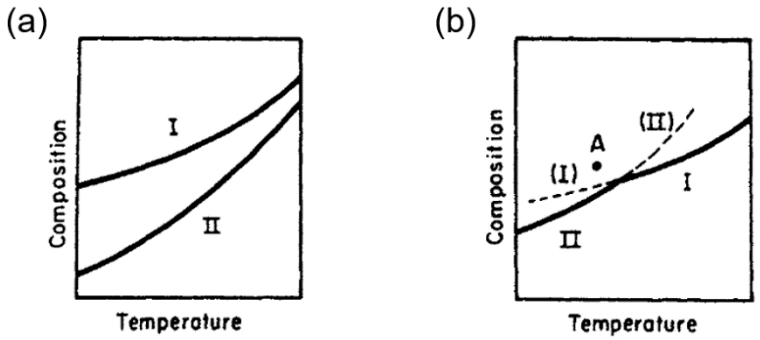

Figure 9 – (a) Monotropic relationship between two polymorphs (I and II). Form II is more stable at all temperatures. (b) Enantiotropic relationship between two polymorphs I and II, showing the solubility curves of the metastable forms above and beyond the transition temperature. Below the transition temperature, form II is more stable, and above it form I is more stable [1].

Ostwald's rule of stages describes the successive production of different forms and the order in which they appear. The rule states that in any phase change, the state that is initially obtained is not the most stable state, but the least stable state that is closest to the original state in terms of free energy [1]. This does not necessarily mean that all metastable states will be observed before the stable form is obtained. In the case of paracetamol, the stable form I is almost always obtained, with metastable forms dissolving and re-nucleating as the stable form I, suggesting a low kinetic barrier to interconversion between forms [55]. At the opposite end of the scale to paracetamol, the existence of a metastable form does not necessarily mean that conversion to a stable form will be readily observed – for carbon, conversion from metastable diamond to stable graphite will only occur in detectable amounts at extreme conditions [56]. A diagram demonstrating Ostwald's law of stages, showing how the free energy of different polymorphs changes, is given in Figure 10 [57].

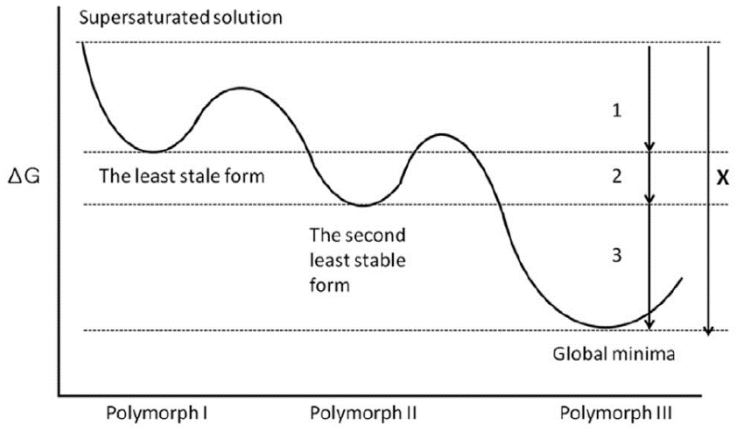

Figure 10 – The relative stabilities of different polymorphs in terms of free energy. The transition from a supersaturated solution to the least stable form (I) through to the most stable form (III) is an example of Ostwald's law of stages. Taken from [57].

Equation 19 describes the rate of nucleation J,

$$J = Aexp\left[-\frac{16\pi\gamma^3 v^2}{3k^3T^3(\ln S)^2}\right] \qquad 19$$

where A is the pre-exponential constant (the attachment frequency), γ is the interfacial tension, v is the molecular volume, k is the Boltzmann constant, T is the temperature and S is the supersaturation. For a metastable form, the attachment frequency will likely be higher than the stable form, which favours a faster rate of nucleation. However, the supersaturation of a metastable form is lower than a stable form, and

so a balance is struck between the two variables [57]. The observed rate of nucleation of the stable form is often higher than the metastable form at low temperatures due to higher relative supersaturations. This also results in a lower critical free energy for nucleation of the less stable forms, which increases their nucleation rates [58].

Although Ostwald's rule of stages suggests that the nucleation rate of the metastable form should be higher than the stable form across all temperatures, this kinetic nucleation theory suggests that this is not always the case [57]. In short, although the relative stabilities of different forms at a given temperature can be specified, the forms that will crystallize within a process are governed by kinetics (through competitive kinetics and growth rates) [59]. One important result of the competitive kinetics of polymorphic formation is concomitant polymorphism, where several different polymorphs crystallize at once [1]. This is a result of the balance between the kinetic factors that favour the formation of metastable forms, and thermodynamics that favour the formation of stable forms [60]. The polymorph(s) that form(s) are a complex function of the conditions within the crystallization unit (temperature, presence of impurities, mixing etc), and it can (especially for crystallizing systems that can readily form multiple polymorphs) be difficult to reliably produce a given polymorph. This is highlighted by the observance of so-called 'vanishing' polymorphs [61].

Thermodynamics favour the transformation of a metastable polymorph to a more stable polymorph. The most common method of polymorphic transformation is solution-mediated transformation, whereby a metastable solid is in contact with a saturated solution [1]. This has three steps: nucleation and growth of the more stable form; dissolution, evaporation or melting of the less stable phase; and mass transfer in the medium [62]. The driving force for this process to occur is the difference in Gibb's free energy between the forms (i.e. the difference in the solubilities of the two forms) [62]. Solution-mediated phase transformations can be promoted or hindered by changing the conditions (temperature, agitation etc) [1], as well as the choice of solvent, which affects the solubility, viscosity, and solute-solvent interactions [62]. Impurities and additives can also be used to modify the rate of phase transformation through inhibition of the growth of the stable form or by increasing the viscosity of the solution [63, 64]. Solution mediated phase transformations can be either growth or dissolution limited, which can be discerned by tracking the supersaturation profile [62]. As well as solution mediated, other phase transformation methods involve melt and interface mediation, and solid-state transitions, where the latter is significantly slower than the other three methods [62].

The heterogeneous nucleation of solutes on a template surface can result in the preferential nucleation of a polymorph [65]. Template-induced nucleation is affected by a number of factors, including the surface topography, chemistry, supersaturation, hydrodynamics, and solvent [65]. It is also affected by the similarity in structure between the nucleating crystal and the surface, and can affect the polymorph that is produced [66]. The more traditional method of polymorphic control is by seeding with the desired polymorphic form [1]. This works through the suppression of spontaneous nucleation of the undesired form, and promoting the growth of the form that matches the seed crystals; this is able to grow below the metastable limit [67]. Secondary nucleation can also function as an important source of nuclei of alternative polymorphs [68, 69]. Above all else, a thorough screening of conditions at which polymorphs form is required to discern how operating conditions affect the polymorphs that form. A particular goal is to identify the thermodynamically stable form, which is often preferred for pharmaceutical products [70, 71]. The polymorphs present can be identified through the use of off-line or in situ characterization techniques.

1.2.5. Types of Crystallisations

Crystallisation from solution can only take place when the solution is supersaturated. There are a number of different ways of generating supersaturation. A solution can be cooled, which often results in a reduction in solubility and thus the generation of supersaturation. This approach is commonly used for the crystallisation of large amounts of products in a cheap and efficient way, particularly when there is a large difference in solubility of a solute between high and low temperatures [72]. Evaporative crystallisation involves the direct evaporation of solvent and concentrates the solute until supersaturation is reached. Although this is encountered in natural environments, it is rarely applied in industrial settings, due to the lack of control over crystal products and the high energy requirements for evaporating solvents.

Cooling Crystallisations

Cooling crystallisations utilise differences in solubility at higher temperatures relative to lower temperatures to generate supersaturation and thereby induce crystallisation. Cooling crystallisations are frequently used to facilitate crystallisation unit operations in industrial settings, owing to their ease of operation, good control of supersaturation, and well-defined seeding points [[72]. Where a large difference exists in solubility between two temperatures (such as large solubility at high temperatures and low

solubility at low temperatures), then cooling crystallisations are attractive due to ability to isolate large yields. Solubility naturally changes with solvents, so solvent choice is key to obtaining desired yields. Cooling crystallisation processes have been demonstrated in both batch crystallisers and continuous-flow [73].

The operating principles behind cooling crystallisations can be neatly illustrated graphically on an example solubility graph (temperature vs concentration), as shown in Figure 11(a). At position A, the solution is undersaturated, and thus the solute in solution is stable. As a constant linear cooling gradient is applied, the system will move to position B on the solubility curve, meaning saturation is achieved. Following further cooling, the system enters the metastable zone, where, in the absence of heterogeneous crystallization surfaces or seeding, no crystallization occurs initially despite the presence of supersaturation. Eventually, the metastable limit is reached at position C, where nucleation spontaneously occurs. Following this, the system enters a growth stage, where supersaturation is consumed by the growing crystals, resulting in a drop in solution-phase concentration. Eventually, at the end of the cooling, the system will reach a state of equilibrium, where a saturated solution remains along with the newly formed crystalline phase. Figure 11(b) shows the same time points over time for the batch cooling crystallization, in relation to supersaturation, temperature, and solute concentration. Seeding can also be effectively applied to cooling crystallisations, due to the relative ease of operation with the metastable zone. This in turn can help to crystal properties such as size and polymorphic form [74].

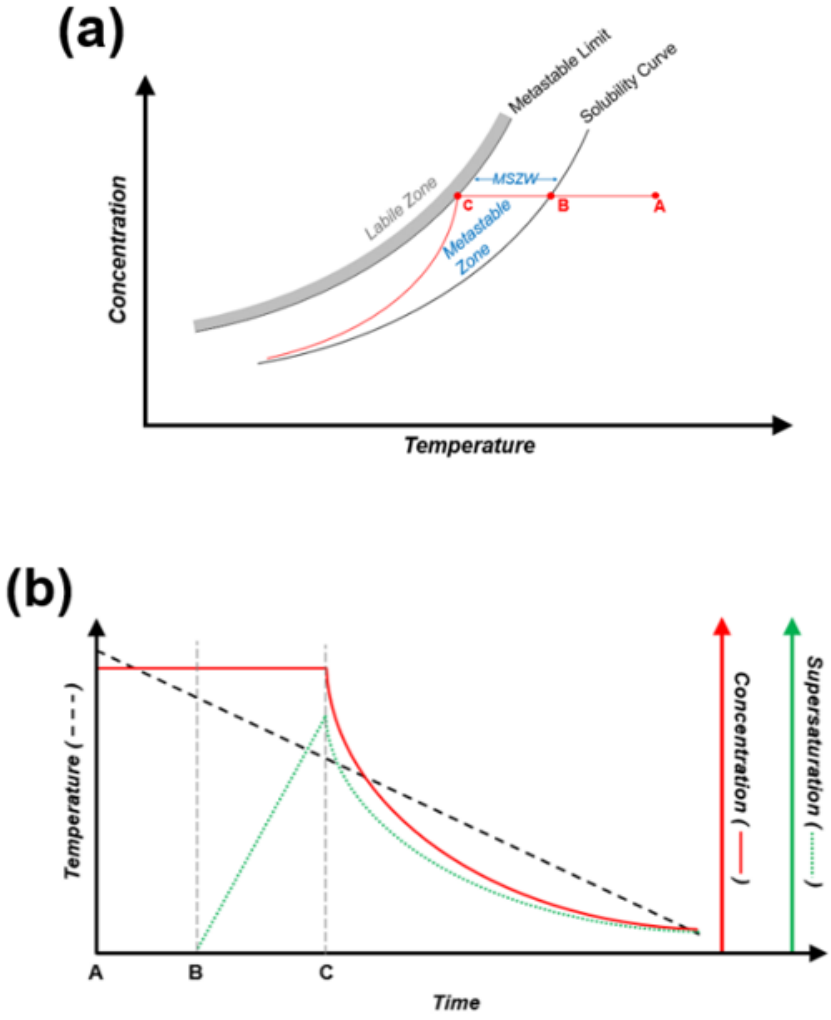

Figure 11 - Phase diagrams for a batch cooling crystallization. (a) Concentration variations relative to the metastable limit and solubility curves as the temperature is decreased. (b) Effect of concentration, temperature, and supersaturation over the time the crystallization takes place.

Reactive Crystallisations

Reactive crystallisation involves a reaction between two or more species that are dissolved in solution to give a product that has a much lower solubility in the solvent than the precursors, causing it to crystalise. This is sometimes referred to as precipitation. Reactive crystallisation is frequently encountered in natural systems for the formation of inorganic solids (including biomineralization and in natural geological formations) [75]. Reactive crystallisation is sometimes utilised during the industrial production of small-molecule, high value organic products [76] and can be used to isolate a chemical intermediate product and prevent its subsequent conversion to an undesired product [77].

Reactive crystallisation is inherently complex and is driven by the balance between the driving force for the reaction and the supersaturation. The relative supersaturation itself is complex, owing to the change in the solubility with the changing amounts of reactants and impurities within the reaction mixture [78]. Mass transfer and mixing also play important roles in dictating the overall rate of crystallisation [79], particularly when mixing times are comparable to or shorter than the time taken for crystallisation [80]. Reactive crystallisation can be broadly sub-divided into those processes that form crystals that primarily comprise ionic bonds and those with covalent bonds, with the former tending to proceed with much greater spontaneity and at a higher rate, without the requirement for a catalyst [78].

Antisolvent Crystallisations

Although the establishment of a cooling gradient is perhaps the most common and well-studied way of generating supersaturation, antisolvent crystallization is also used frequently in industry [81]. Antisolvent crystallization involves the mixing of another miscible solvent (the antisolvent) within which the solute is poorly soluble at the temperature(s) at which the crystallization is taking place [30]. The rate of creation of supersaturation and the MSZW are related to the rate of addition of antisolvent [82]. There are several reasons for the use of antisolvent crystallization in industry. It is useful for temperature sensitive materials, as supersaturation can be generated at a low operating temperature [31]. The low or ambient operating temperature also has economic advantages owing to the lack of requirement for heating. It is also useful for processes where solubility does not show a steep relationship with temperature, and is rapid and typically gives high yields (if sufficient mixing of antisolvent and solute can be achieved) [83].

There are disadvantages to the use of antisolvents, however. For example, there is a risk of impurities being incorporated into the final crystal product [83] and the high degree of sensitivity of antisolvent crystallization to mixing is an issue on scaling to industrial volumes, where inhomogeneities in mixing and thus supersaturation can result in a broadening of product properties [83]. The requirement to remove the antisolvent following crystallization (and, possibly in the case of non-aqueous antisolvent, recycle it) means that antisolvent crystallizations are typically only viable for high-value chemical products such as pharmaceuticals [84]. A key consideration of antisolvent crystallization not required for cooling crystallizations is the reduction in solution concentration upon the addition of antisolvent, which can increase the

complexity of the process. Antisolvent crystallization can also be combined with a cooling gradient to give added control of crystallization [31].

Antisolvent crystallization typically results in a localised area of large supersaturation close to the antisolvent inlet where nucleation occurs. The growth then occurs in the bulk solution [85]. The inhomogeneities in processing conditions associated with such addition points in a batch can result in difficulties in controlling product properties with antisolvent batch crystallization. Controlling the mixing of antisolvent and solution (which affects the resultant supersaturation and thus product properties) is difficult, as mixing is sensitive to numerous processing variables, such as agitation speed, addition mode and addition rate [86]. This can cause problems in scaling-up as it is difficult to predict how the mixing will be effected [86]. The use of impinging jets to mix antisolvent and solution has been shown to be useful in obtaining small, highly-uniform particles that are valuable for pharmaceutical purposes [86]. Detailed analysis of the time scale of turbulent mixing enables the kinetics of nucleation and growth to be compared, which ensures that mixing is not limiting the crystallization process [87]. A lack of sufficient mixing relative to the kinetics of the crystallization process can cause a broadening of product properties such as size and morphology, which is often undesirable [88]. Continuous antisolvent crystallization using static mixing devices to rapidly mix the solvent and antisolvent can give intense and well controlled processing environments. These also promote the formation of a plug flow regime that can give increased control of the product [88].

1.3. Continuous Crystallisation

1.3.1. Basic Principles and Modelling

Continuous crystallization reactions consist of a continuous process (that is, with an input and an output), where the input is a particle-free, undersaturated solution, and the output is a slightly supersaturated particulate crystalline suspension [68]. Unlike batch crystallization processes, continuous crystallizations operate at a 'steady-state', where conditions do not change with time at a given point within the crystallizer (batch crystallization operates to a state of equilibrium, with the state-composition of the crystallizer constantly changing until this point). Several designs of continuous crystallizers have been described in the literature, with the most common being mixed suspension mixed product removal (MSMPR), continuous tubular crystallizers, segmented flow crystallisers, and Continuous Oscillatory Baffled Crystallizers (COBC) [89]. Within each category, there are further design refinements and operational variables considered, including supersaturation generation, scale, flow regime, and control mechanisms.

Traditionally, industries have performed crystallization in batch reactors and have not made use of continuous crystallization, [90]. This is because better defined 'batches' of product can be obtained from batch crystallizers, such that the product can be readily assessed against specifications and safety requirements (something that is particularly important for the manufacture of pharmaceuticals). In recent years, continuous processing of high value chemical products has been a subject of increased interest [91-97], with a number of potential benefits over traditional batch processing techniques. These include higher efficiency, increased product yields, safety, and product selectivity [98]. Furthermore, continuous processing facilitates ease of integration of in-line PAT, with the two forming a powerful combination for the accurate and representative real-time monitoring and investigation of reaction progress and performance [99]. Continuous processing is a manufacturing technique widely used within high-volume chemical industries (such as the petrochemical industry) but has found less use within fine chemical industries, such as the pharmaceutical industry [100]. Such industries have been hesitant to implement continuous flow processes, owing to lack of process understanding (and, on the flipside, familiarity with batch processing), uncertainty over the required investment, reactor fouling, and the typically complex reactions involved in Active Pharmaceutical Ingredient (API) synthesis [91, 92, 101]. Despite a great deal of progress being made

to facilitate continuous flow in synthetic reactions, little attention has been paid to crystallization processes.

Economic drivers are resulting in considerations of continuous processing of high-value products at both the synthesis and downstream stages, motivated by potential ease of scale-up, the ability to meet fluctuating market demands, to downsize the equipment footprint and the easing of transport of manufacturing equipment as demand requires [89]. The increased robustness of product quality afforded by continuous flow manufacturing could also be a factor in fighting competition with competing generics, which provides a key selling point [102]. For crystalline products, the greater assurance of desired morphology could have benefits with regards to downstream processes such as filtering [88]. For greater industrial use, continuous crystallizers need to show operational flexibility and robustness without encountering blockages or requiring downtime due to cleaning requirements. Furthermore, as production volumes of some high-value crystalline products (such as pharmaceuticals) trend downwards [89], continuous crystallizers need to show that they can be operated at low flow rates without compromising product quality due to poor mixing (something particularly true for continuous tubular crystallizers).

In operating a continuous crystalliser, it is critical to establish the nature of the flow of material through the crystalliser. This can be characterised as a residence time distribution (RTD), which captures the range of residence times of material flowing through the crystalliser. There are a number of ways in which the RTD behaviour can be modelled for a continuous crystalliser. In the case of plug flow behaviour, the RTD is effectively zero, as there is no axial dispersion of material taking place. In other words, all the material has exactly the same residence time. Naturally, this is an idealised scenario, although some systems can effectively approximate plug-flow behaviour, such as segmented-flow reactors (which will be discussed in the next section).

Another model commonly used is the continuous stirred-tank reactor (CSTR). This can be thought of as a well-mixed stirred vessel with an inlet and outlet stream running at a constant, equal flow-rate. By well-mixed, we assume that the conditions within the vessel are homogeneous, and the vessel is at a steady state. CSTRs can also be modelled as multiple units (N) in series, where the output of one unit flows into the next as the input. The normalised RTD is referred to as the exit distribution or an E-curve (E, units time^{-1}). Dimensionless time (θ) is commonly used to express the ratio

of time (t) over the mean time per tank for *N* tanks ($\bar{t}$), as shown in equation 20. The E-curve for *N* tanks in series is given by equation 1 [103].

$$\boldsymbol{E_\theta} = (N\bar{t}_i)\boldsymbol{E} = N\frac{(N\theta)^{N-1}}{(N-1)!}e^{-N\theta} \qquad 20$$

The equivalent cumulative frequency distribution (the F-curve) is given by equation 21 [103].

$$\boldsymbol{F} = 1 - e^{-\theta_i}\left[1 + \theta_i + \frac{{\theta_i}^2}{2!} + \cdots + \frac{{\theta_i}^{N-1}}{(N-1)!} + \cdots\right] \qquad 21$$

Plots of the variation of E_θ with θ and F with θ_i (the dimensionless time per unit) for different numbers of tanks in series (*N*) are shown in Figure 12. For plug-flow behaviour, the E-curve is represented by a curve of zero width and infinite height at θ = 1, and for the F-curve a vertical frequency distribution curve at θ_i = 1. Note that as the number of tanks in series increases, it more closely begins to approximate plug-flow behaviour. For the F-curve, the mean residence time of material in the reactor is given by the point where F = 0.5.

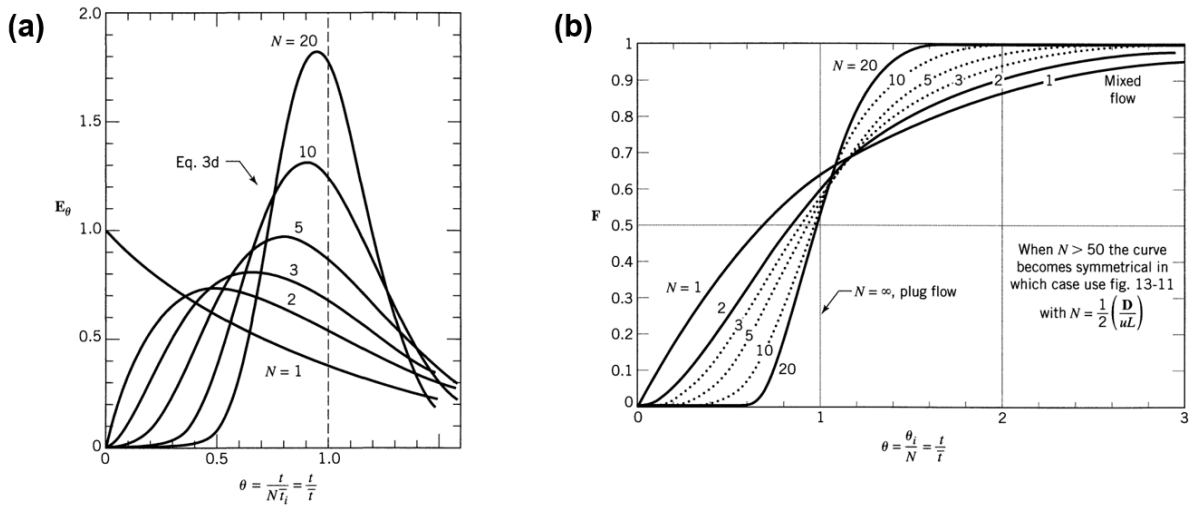

Figure 12 - (a) E-curves for N tanks in series for different values of N. (b) F-curves for N tanks in series for different values of N. Adapted from [103].

1.3.2. Examples of Continuous Crystallisations

Tubular

Perhaps the simplest design of a continuous crystalliser is a tubular crystalliser, wichh consists of a tube through which the reaction slurry flows. The key design variables for this system are the length and the inner and outer diameters, as well as the material (a particular consideration for heat transfer for non-isothermal crystallisations). In the field of chemical synthesis, such reactors have enabled multiphasic reactions to be carried out in continuous flow. However, the crystallisation of solids presents new challenges, and careful operation is required to minimise the potential for uncontrolled nucleation and growth which can result in blockages. Early examples for cooling [104] and antisolvent [88] continuous crystallisation demonstrated the potential of such devices to deliver crystals of well-controlled sizes and polymorphs. Tubular crystallisers can also be operated with an inlet flow of seed crystals, which may supress uncontrolled nucleation and therefore help to control particle size and reduce the chances of blockages and encrustation occurring [48, 49]. Tubular crystallisers may be spread over different temperature-controlled 'zones' in order to confer flexibility of cooling profile during cooling crystallisation [105]. Similarly, for the case of antisolvent or reactive crystallisation, different addition points may be present across the length of crystalliser to simulate different addition rates [88].

Due to the small-diameter tubing that is often used for continuous tubular crystallisers, blockages and encrustation may occur, which can limit their performance. This is in direct contrast to the desire to use lower diameters of tubing to maintain a turbulent mixing regime, as per Reynold's law. Static mixers [88] and ultrasonication [106] can also be used to induce mixing in tubular mixers. However, the static mixer provides additional surface on which for solids to nucleate (risking blockages and encrustation), while ultrasonication presents safety issues at higher (industrially relevant) scales, and is difficult to model. Coiled-flow inversion, where coils of the tubes are arranged in different orientations, make use of Dean vortices to induce additional mixing in the slurry. The addition of different orientations of the helical coils has been shown to improve control of crystal size distribution, a result of increasing homogeneity of mixing and a reduction in residence time distribution [107].

Segmented Flow

Segmented flow crystallisers make use of an immiscible 'carrier' phase to separate the crystallisation solution into multiple discrete slugs or droplets within the reactor. An immediate benefit of such a technique are the typically narrow residence time distributions, as crystallising material is confined to the length of the slug. The use of segmented flow can also be beneficial in alleviating blockages and encrustation, particularly when the segmenting phase preferentially contacts the wall of the crystalliser [108, 109]. Segmented flow crystallisers can be operated on a variety of scales, from nanolitre-sized droplets [110] to litres per hour range of operation [111]. The immiscible segmenting phase is typically either air or an immiscible liquid, with the choice of carrier phase impacting the contact angle between the phases and thus determining the phase in contact with the walls of the crystalliser [109]. Cooling [112], antisolvent [113], and reactive [108] crystallisation processes have all been performed in continuous segmented crystallisers.

A continuous segmented crystalliser using two segmenting phases (air and an immiscible carrier fluid) – the KRAIC – was presented by Robertson et al. [109]. The use of two phases ensured that the crystallising solution did not contact the walls of the crystalliser, as the perfluoropolyether carrier fluid preferentially contacts the fluorinated polyether tubing used. The non-slip boundary between the carrier fluid and solution generates 'bolus' flows within the solution, inducing consistent and homogeneous mixing of the solution. The use of air as a secondary segmenting phase ensures that solution slugs don't combine, providing additional operational stability. Adjusting the air flowrate can also confer operational flexibility, as the residence time of the slug can be changed without modifying the mixing behaviour of the solution (determined by the slug size). Original designs of the KRAIC to enable cooling crystallisation made use of discrete, single-temperature cooling baths to provide a cooling gradient. A more recent iteration makes use of a tube-mounting with a counter-current cooling liquid inside, which enabled a higher degree of control over the cooling gradient [112]. Figure 13 is a schematic of the KRAIC system, showing the tri-segmented operation.

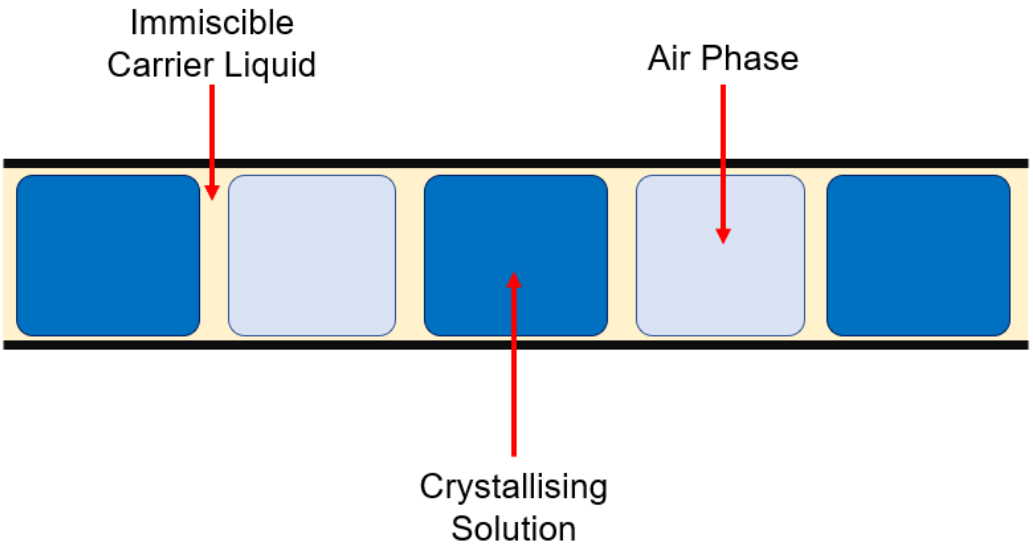

Figure 13 – Operation of the KRAIC system, a tri-segmented continuous crystallisation platform. Carrier liquid and air segments the crystallising solution, ensuring it does not contact the walls of the reactor, helping to alleviate blockages and encrustation.

Continuous Oscillatory Baffled Crystallisers

Continuous Oscillatory Baffled Crystallizers (COBC) consist of a tube in which baffles are periodically placed perpendicular to the direction of net flow and induced oscillatory forces. The combination of the baffles and the oscillations induces eddies and vortices in the flowing suspension that results in a high degree of mixing and enhanced heat and mass transfer [114]. The induction of vortices also serves to continuously, vigorously remove particles from the walls of the crystallizer, helping to reduce encrustation. The mixing present in a COBC is shown in Figure 14(a) [115]. A key feature of COBC is the decoupling of mixing (which is enhanced by the use of oscillations) from the net flow rate, which is not the default case in tubular crystallisers [116]. This means that efficient mixing approaching plug flow behaviour can be achieved without the use of impractically high flow rates and thus long crystallizer lengths. The combination of COBC with PAT techniques can enhance control of particle size, polymorphic purity, crystal size and yield [117]. A number of different industrially-relevant crystal products have been manufactured using COBC, including APIs [118], as well as more complex crystal forms such as co-crystals [119]. A representation of the growth of crystals in a COBC of a given inlet concentration, flowrate and molar composition is shown in Figure 14(b).

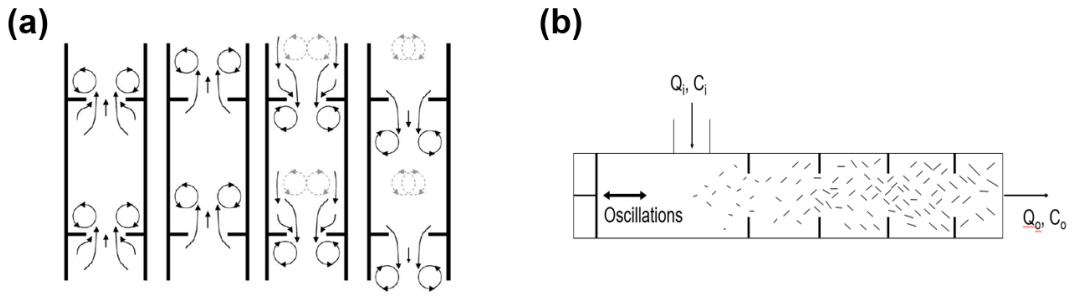

Figure 14 - (a) Flow patterns encountered in COBC between baffles, from left to right: start of up stroke, maximum velocity in up stroke, start of down stroke, maximum velocity in down stroke [115]. (b) Depiction of a typical COBC showing inlets and outlets, and crystal growth occurring. Supersaturation could be generated either through separate antisolvent addition, or through a cooling fluid pumped through a jacket surrounding the vessel.

Mixed Suspension Mixed Product Removal (MSMPR)

Mixed-Suspension Mixed Product Removal (MSMPR) continuous crystallisers consist of a stirred tank with an input of solution and an output of crystalline suspension, which are assumed to be perfectly mixed [120]. Typically, the product withdrawal stream consists of an overflow system, where withdrawals are performed intermittently and in a high-throughput manner to prevent size classification [121]. The molecular composition of the withdrawal stream was assumed to be identical to the input stream in an idealised MSMPR [122]. Like most crystallizers, supersaturation is generated by cooling or the addition of antisolvent; for the former, a temperature-controlled jacket is typically used [123], and for the latter a separate antisolvent addition stream can be used [124].

Of all the methods of continuous crystallization, MSMPRs are most similar to traditional batch crystallizers. This can result in a number of operational benefits, such as ease of conversion of a batch process to a MSMPR, easier maintenance and operation, and ease of control [89, 90, 121]. However, their similarity to batch processes results in many of the same drawbacks, such as poor operational efficiency [90]. The typically large residence time distributions (RTD) encountered in MSMPRs can result in a wide CSD, as well as a low degree of homogeneity of critical quality attributes of the crystal products [89]. Furthermore, MSMPRs can be difficult to scale-up, such that it can be difficult to predict heat transfer behaviour. The low degree of efficiency of a single MSMPR, which is often worse than the equivalent batch process, has prompted operation of multi-stage cascaded MSMPRs, which could improve performance [122]. The residence time distribution of multiple MSMPRs can be effectively modelled as a series of continuous stirred-tank reactors (CSTRs) [125].

Because of their similarity to batch processes (favoured for industrial manufacturing), they are the continuous crystallisation device most frequently used for studies involving the crystallisation of industrially-relevant compounds such as pharmaceuticals [95]. As such, they are often used for volumes of production on the order of hundreds of millilitres to litres. Reports at lower millilitre or microfluidic scales are lacking. A schematic representation of an MSMPR is shown in figure Figure 15.

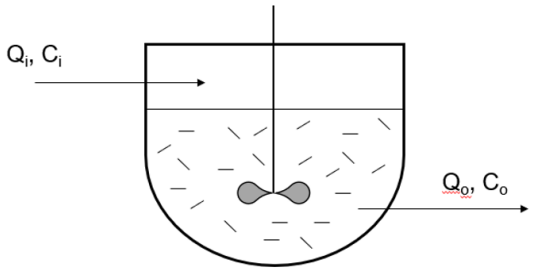

Figure 15 - Diagram of an MSMPR crystallizer. The input is continuous, and is at a certain flowrate (Q), concentration (C).

Small-Scale CSTRs

There are a few common reasons for using continuous flow reactors for homogeneous chemical reactions, but also those specific to those for use with crystallisations. Rapid, intense mixing, irrespective of the flow-rate used, is required to ensure that mixing time is not a rate-limiting step during synthesis. Furthermore, its often desired for continuous-flow reactors to be able to handle multi-phasic processes (making use of solids, liquids and gases). Operation on a small-scale may also be desired to minimise material usage, and to facilitate studies of scale-up. In striving to incorporate these desirable traits, the fReactor (‘free-actor’) system was recently developed at the University of Leeds [126]. This consists of a series of continuous stirred tank reactors (CSTRs) arranged in series, with each containing a magnetic flea for stirring. The total free volume of the cascade neglecting the volume taken up by the magnetic flea is approximately 7.8mL. Each fReactor unit consists of a Polyether Ether Ketone (PEEK) base with a circular cylindrical chamber, 4x1/4-28” threaded ports leading to the chamber, and a glass lid, rubber o-ring, and PEEK top which can all be screwed down onto the base to form a sealed chamber. A diagram showing a fReactor unit is displayed in Figure 16. The inclusion of the magnetic fleas allows the cascade to be placed on a hot-plate stirrer, resulting in actively induced

mixing being decoupled from the flow-rates used, making the fReactor suitable for a wide-range of flow-rates and residence times.

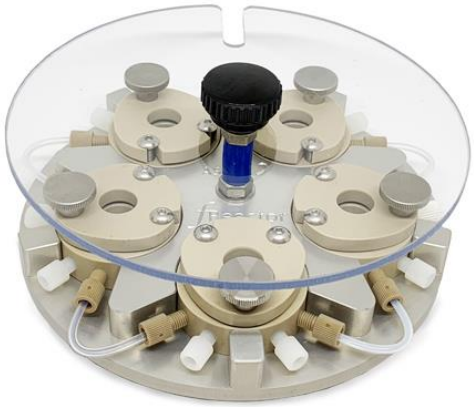

Figure 16 - 5-unit fReactor cascade on a custom-made stainless steel heating block. Image courtesy of Asynt Ltd [126].

Originally, the use of the fReactor was demonstrated for a variety of different multiphasic reactions, including the synthesis of a N-Chloroamine and for an electrocyclization (both liquid-liquid biphasic), a hydrogenation (solid-liquid-gas) and a continuous crystallisation (solid-liquid). For the latter, diastereomeric crystallisation of rac-salsolidine was carried out with mandelic acid, with the two reacting from a mixed Ethyl Acetate / methanol solution to form diastereomerically resolved co-crystals. An high selectivity to the R form of salsolidine was achieved (de = 91%), an improvement on the equivalent batch process (de = 83%) at a similar yield (24% for the former, 30% for the latter). This is an excellent example of the intense, homogeneous mixing present in the fReactor cascade.

Similar designs have been reported by the group of Jensen and co-workers at the Massachusetts Institute of Technology. An early design showed utility in enabling a continuous-flow solids-forming reaction of isoprene and maleic acid anhydride [127]. RTD behaviour of this platform showed a close approximation to the idealised behaviour of CSTRs in series. A millifluidic platform consisting of 5 x CSTRs in series was also realised for well-controlled photo-redox reactions with solid-phase reactants (Figure 17) [128]. A unique piston-based slurry pump was developed for delivering the solid reactants, and active stirring within the reaction chambers led to a wide operational range. Solid-phase RTD behaviour again approximated the idealised CSTR in series behaviour for particle sizes on the order of 10s of microns. The same design was later combined with at-line HPLC analysis, which facilitated the automated

optimisation of a solids-forming reaction [129], which shows it's applicability to a wide range of reaction conditions. Similar designs have also been utilized for the production of nanoparticles in continuous flow [130, 131].

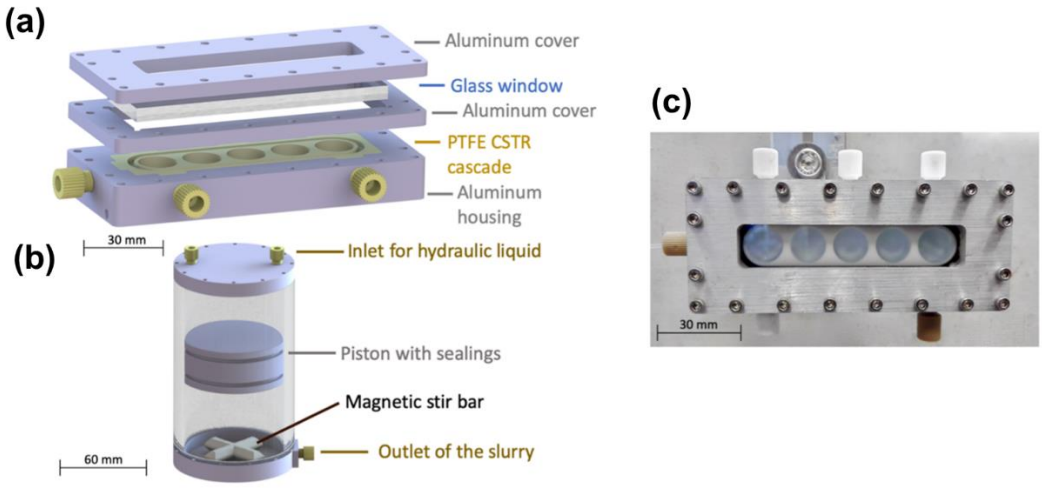

Figure 17 – Miniature CSTR cascade developed by Jensen and co-workers. (a) Schematic of 5xCSTR PTFE reaction chamber with aluminium housing. (b) Piston pump used for slurry delivery to the cascade. (c) Photograph of the CSTR cascade showing stirrer bars in the chambers. Adapted from [128].

1.3.3. Coupling Continuous Crystallisations with in-line analysis

Considering the wide-spread use of crystallisations in the manufacturing and purification of solid products, it is of vital importance to determine how different crystallisation conditions affect crystal properties critical to their performance (such as size, structure, purity and shape) [44]. Traditionally, samples would be taken at different times throughout the crystallisation to determine solute concentration and / or crystal structure, average size, and size distribution. Not only is this laborious, but the requirement for sampling reduces accuracy, as crystals will have to be filtered and dried, which may induce changes in the solid samples. Furthermore, there may be a selection bias in taking the sample, wherein a non-representative size range may be obtained. To improve both accuracy and the ability to rapidly optimise crystallisation processes, in situ analysis techniques have recently been applied to crystallisations in both batch and continuous flow in order to characterise both solute and solid phases during crystallisations. Within the context of crystallisations, *in situ* characterisation refers to where acquisitions are made of a sample during crystallisation, in the crystallisation environment [132]. This has been achieved for a

number of different characterisation techniques: Raman [133, 134] and IR spectroscopy [124, 135], UV-vis [136, 137], HPLC [138], imaging and particle tracking techniques [139-142], and X-Ray diffraction [143, 144]. The use of *in situ* monitoring of crystallisations has enabled rapid, real-time evaluation of the state of a crystallisation process, which in turn has allowed for control techniques to be implemented to optimise crystallisation processes [44, 145].

Because continuous crystallisations operate at a steady-state with respect to time, the position along the length of a continuous crystallisation device represents a single extent of reaction (i.e. a single point in reaction time-space). This is illustrated in Figure 18 for the example of a tubular continuous crystalliser of length *L* with a single input and output. The variation in an example measured parameter (P) with the length of the crystalliser is shown by the coloured dots in both the graph and the figure. At steady-state, the values of *P* are not changing with real time (as long as a constant supply of inlet material is maintained and the conditions of the crystalliser are not modified). Applying an *in situ* analysis technique to a single point along the length of a continuous crystalliser thus allows for the acquisition time to be decoupled from the reaction time. Such a technique – referred to as an in-line characterisation – thus yields excellent time-resolution, and has found use for characterising rapid crystallisation processes or the early stages of crystallisations [146].

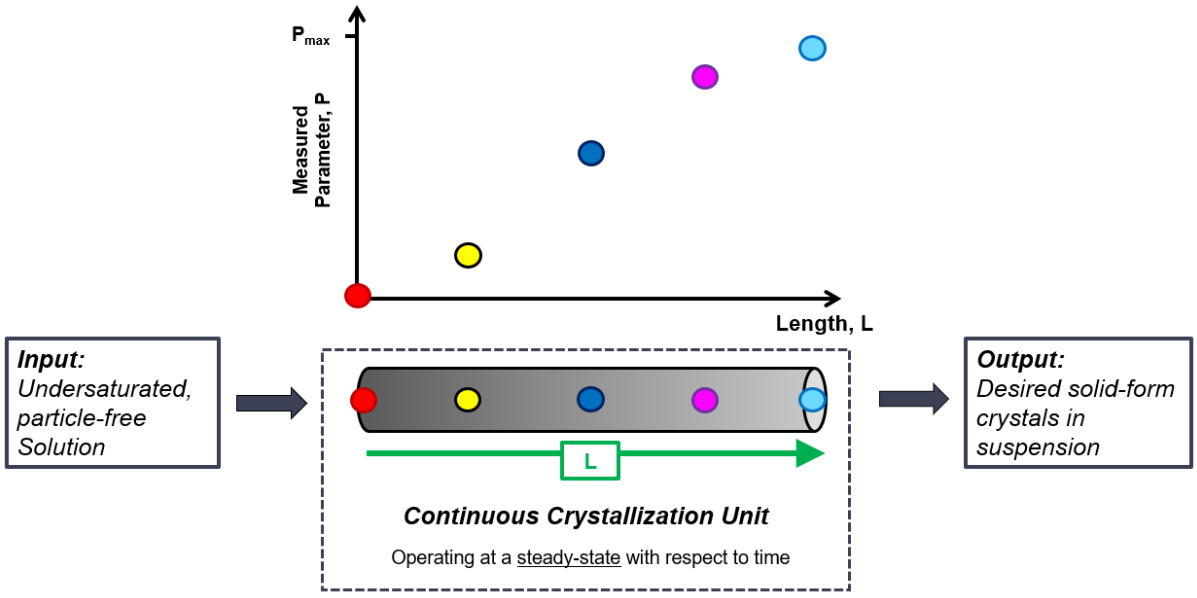

Figure 18 – Illustration of a continuous crystallisation unit operating at a steady-state with respect to time. The variation in an example measured parameter, P*, over the length of the crystalliser, is shown in the graph.*

1.4. X-Ray Diffraction

XRD techniques are a group of analysis techniques that can give information about the crystallographic structure and properties of a solid sample [147]. XRD describes the phenomenon of elastic scattering of X-rays incident on a periodic lattice [148]. Information about the structure of the crystal lattice can be obtained from these scattered X-rays. One such piece of structural information is the interplanar spacings, which allow the unit cell metrics to be determined [149]. For incident X-ray energy radiation at a monochromatic wavelength, the interplanar spacing (d) can be related to the wavelength of light which is scattered (λ), as well as by the angle of the incident radiation on the sample (θ) by Bragg's law, shown in equation 22.

$$\lambda = 2d\ sin\theta \qquad 22$$

Thus, angles at which radiation is intensely scattered correspond to interplanar spacings, and can be used for structural characterization [1]. The scattering is considered to occur through the reflection of incident radiation off scattering planes. A description of this process, showing how equation 3 can be derived in practice, is shown in Figure 19. Constructive interference of waves reflecting off of sequential scattering planes results at a particular incidence angle (θ) because waves from lower scattering planes have to travel a whole-number of wavelengths (λ) extra compared to scattering from higher planes (Figure 19(a), (b)). A trigonometric relationship can then be derived for this scenario (Figure 19(b), (c)) wherein the distance d (representing the interplanar spacing) can be calculated. The high intensity of constructively-interfered X-rays can be detected as a bright-spot at a particular angle, allowing one to calculate the interplanar-spacing d. Repeating this process for every scattering plane in the crystal allows for all interplanar-spacings to be calculated, thus rendering the dimensions of the unit cell.

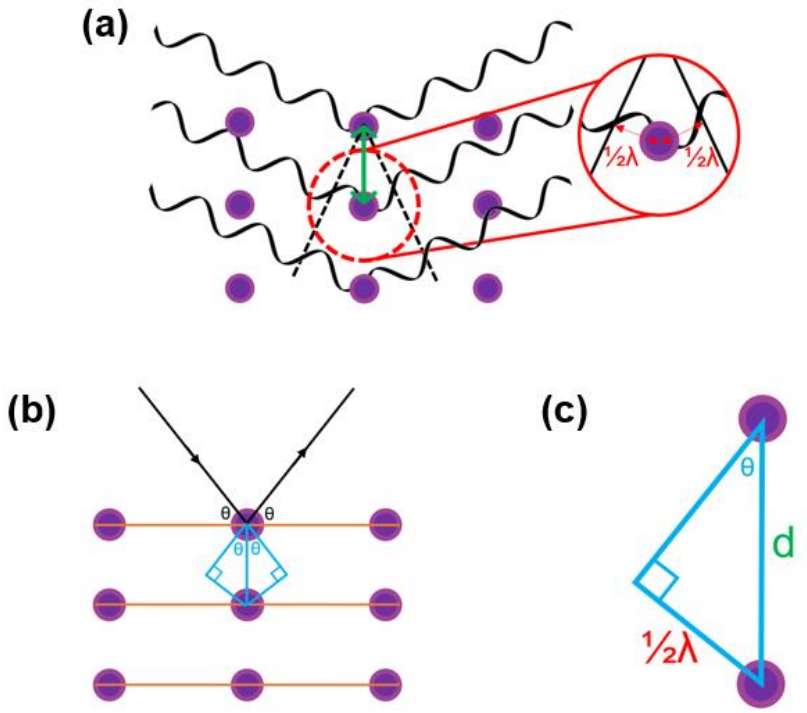

Figure 19 – Reflection of parallel X-ray radiation of a wavelength λ off multiple scattering planes in a crystal sample. If the path length difference is a multiple of λ, then constructive interference of the waves will occur, resulting in intense scattering. Relating this to the angle of incidence and the wavelength through Bragg's equation allows one to calculate the interplanar distance.

When diffraction occurs within a 3-dimensional structure of scattering planes, the *Laue* equations must be satisfied, which are shown in equations 23 to 25

$$a.(\vec{s} - \overrightarrow{s_0}) = h\lambda \quad 23$$

$$b.(\vec{s} - \overrightarrow{s_0}) = k\lambda \quad 24$$

$$c.(\vec{s} - \overrightarrow{s_0}) = l\lambda \quad 25$$

where a, b, and c are the dimensions of the unit cell, $\vec{s}_0$ and $\vec{s}$ are the unit vectors in the direction of the incoming and outgoing wave respectively, and h, k, and l are integers [150]. Because diffraction can only occur when all three equations are satisfied, the integers h, k and l can be assigned to a diffracted beam in a unique manner, helping the diffracted beam to be to indexed in the resultant spectra [150]. The integers h,k, and l are known as the reflection indices, and represent the whole number multiples of wavelength that an incident beam must travel in order to go from one scattering plane to the next in the direction of the beam. For every reflection (h,k,l) there is an associated Bragg scattering plane which intersects the unit cell of the crystal (described by axes (a,b,c)) at points (a/h, b/l, c/k). The distance between

scattering planes d can be related to the unit cell dimensions (for a unit cell at which all angles are 90°) by equation 26.

$$\frac{1}{d} = \frac{h^2}{a^2} + \frac{k^2}{b^2} + \frac{l^2}{c^2} \quad (26)$$

For the cubic system, this simplifies to equation 27.

$$d = \frac{a}{\sqrt{h^2 + k^2 + l^2}} \quad (27)$$

With the spacing between scattering planes found, relations can be drawn between the angle of scattered radiation (using the Bragg equation) and reflection indices [150].

1.4.1. X-Ray sources and instrumentation

Single-crystal XRD (SC-XRD), as the name implies, involves an XRD study of a single crystal. The crystal is mounted on the instrument, and rotated, and diffraction patterns are recorded for each orientation until all orientations have been accounted for. The structure of the crystal is then solved using software based on the positions and intensities of the diffraction events, knowing the chemical composition of the sample [151]. SC-XRD offers high accuracy in determining crystal structure, and it is typically used for *ab initio* crystal structure determination [152]. However, it does require a single crystal of a sufficient size to be grown, which may not always be possible.

For routine structural determination, particularly in the identification of known polymorphs, PXRD is more commonly performed [153]. A powder of fine particles will present all possible reflection planes at once when radiation is incident on it, allowing for rapid assessment of the crystal structure, as well as identification of impurities and the degree of crystallinity [1]. PXRD can also be used for the determination of crystal structure of new crystals when a single high-quality crystal cannot be grown, as facilitated through the use of advances in computational methods for PXRD indexing [154]. A common practical method of PXRD assessment is through the use of an X-Ray Diffractometer, which consists of an X-Ray Tube, moveable sample stage (goniometer), and an X-ray detector, as shown in Figure 20. A powder sample is dispersed on the stage as flat and as even as possible. To ensure that all the different orientations are captured in a representative manner during the PXRD acquisition, the powder crystals should be orientated randomly on the sample disc. However,

crystals will typically orient themselves on flatter, larger sides, leading to preferential orientation [153]. This may mean that not all crystal reflections are captured in the acquisition, with some intensities being smaller (or larger) than those predicted by simulations using known unit cell dimensions [155]. For an angle of rotation of the stage θ, the detector is moved through an angle of 2θ, allowing detected x-ray intensity to be plotted as a function of angle. The resultant diffraction pattern can be compared to reference databases to find matches in crystal structure, allowing the powder sample to be identified [156]. An example of indexed peaks for a pure powder sample of the pharmaceutical API Acetaminophen (Paracetamol) is shown in Figure 21 [157].

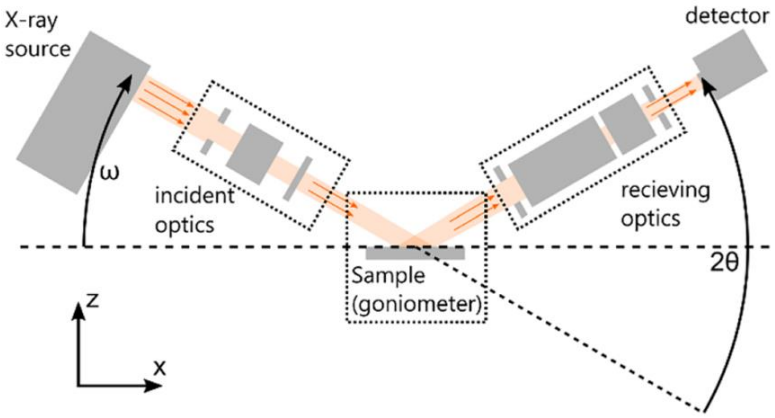

Figure 20 – X-ray diffractometer used in power X-ray diffraction analysis of a sample.

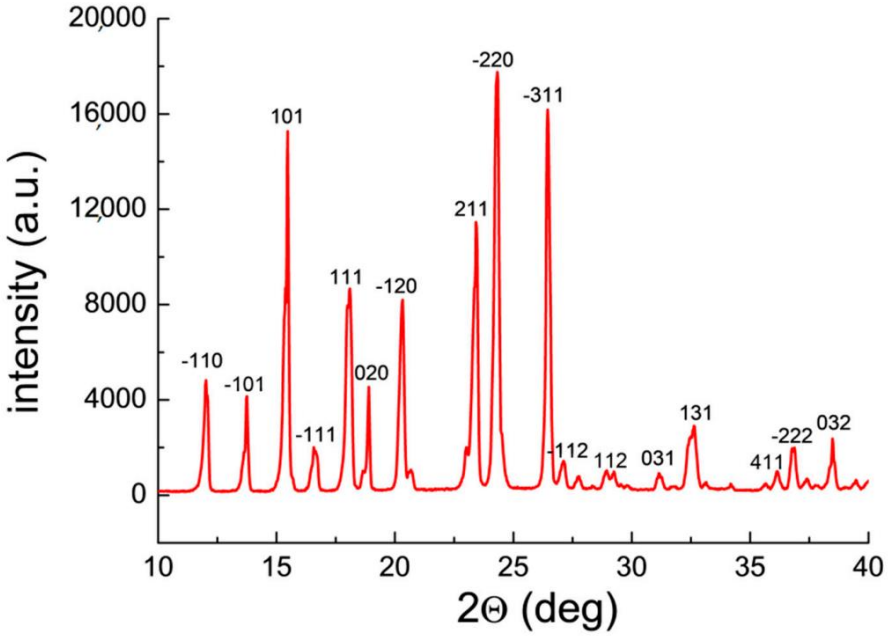

Figure 21 - Powder XRD spectra of the stable form I of Acetaminophen. Different scattering planes are identified for the major peaks, allowing the crystal structure to be determined. Adapted from [157].

X-rays are typically generated by accelerating electrons from a heated cathode filament towards a metal anode target by a high-voltage potential. Most metal anodes used are copper, where incident electrons knock inner shell electrons out, with the resultant vacancies filled by outer-shell electrons, resulting in the generation of X-rays [158]. A slit is used to specify the width of the beam – a wider beam gives more energy, but at the expense of resolution. Filters are then used to remove unwanted radiation – Cu-Kβ radiation is most often filtered out, along with Cu-Kα2 in some more sophisticated machines, leaving Cu-Kα1 to interact with the sample [158]. Very powerful sources of radiation are found at synchrotrons, where electrons are accelerated to close to the speed of light using powerful magnets and a circular vacuum chamber, resulting in the emission of X-ray photons [156]. Synchrotron radiation sources facilitate the tailoring of beam parameters (such as photon flux, energy bandwidth, pulse length) to a higher degree than systems using X-ray tubes, and facilitate higher resolution investigation of samples [159]. The unrivalled nature of synchrotron radiation sources does lead to them being oversubscribed and offering a very short amount of experimental time within the facility [160].

1.4.2. X-Ray Diffraction – examples of *in situ* analysis

Within the context of crystallisations, *In situ* X-ray diffraction experiments refer to those where acquisitions are made of a sample during crystallisation, in the crystallisation environment [132]. Like other *in situ* techniques, this offers the benefits of increased accuracy and time-resolution, allowing for rapid optimisation of processes . *In situ* X-ray diffraction may take place using a synchrotron or laboratory-based source of X-rays. Examples have been reported for both sources under a number of different sample environments.

Synchrotron Radiation – Batch and Stopped-Flow

A common method of synchrotron-based *in situ* analysis of crystallisation processes is through the use of a stopped-flow device. Such a device facilitates the remote, automated mixing of reactants by flowing them into a mixing chamber, followed by stoppage of the flow. With the flow stopped, *in situ* studies of the reaction products may be undertaken [161]. Stopped flow apparatus has shown to be useful for capturing the early stages of a reaction (down to the micro-/millisecond scale), allowing for the study of short-lived transient species [162] [163]. The combination of stopped flow devices and *in situ* X-ray diffraction studies has been extensively demonstrated for a number of crystallisation processes, including for the formation of nanoparticles [164], biominerals [165], Metal-Organic Frameworks (MOFs) [166, 167], and proteins [168]. The combination of stopped-flow with in situ SAXS / WAXS has shown to be particularly useful in observing early-stage evolution of both particle size (SAXS) and structure (WAXS), allowing for the elucidation of crystallisation mechanisms and pathways [165, 169]. Stawski and co-workers made use of a commercial stopped-flow device [170] with *in situ* SAXS to identify a multi-stage non-classical mechanism for the formation of the stable form of $CaSO_4$ (Gypsum) from aqueous solution [171]. Initially, sub 3nm particles were shown to nucleate, which subsequently underwent densification and aggregation, before final self-assembly and growth of crystalline Gypsum particles. This is an excellent demonstration of the power of such devices and *in situ* characterisation to identify the earliest stages of crystallisation even at the nanoscale. Stopped flow devices, however, can suffer from blockages of feed-lines and back mixing, reducing the accuracy of measurements [172, 173].

A novel sample environment that has also been demonstrated for *in situ* studies of crystallisations is the acoustic levitation device. A small droplet (typically in the

microlitre scale) is trapped between pressure nodes of a standing wave field generated by the device, and radiation is emitted incident to the droplet, allowing for transmission-mode diffraction data to be gathered [174, 175]. Acoustic levitation provides a contact-free environment within which homogenous (as opposed to heterogeneous) crystallisation may be favoured. Wolf and co-workers demonstrated this for the $CaCO_3$ crystallisation system, which underwent diffusion-controlled homogeneous nucleation upon evaporation of the aqueous droplet [176]. It was found that crystallisation of $CaCO_3$ proceeded via an amorphous liquid-like phase, which subsequently formed the stable form Calcite. Gnutzmann and co-workers studied the crystallisation of a highly polymorphic small organic molecule within similar apparatus using both synchrotron X-Ray diffraction and Raman spectroscopy [177]. They identified the influence of solvent choice on the resultant polymorph following evaporation, and proposed a set of mechanisms underpinning phase transformations for this system. Crucially, a previously unidentified transient amorphous form was observed, highlighting how such novel sample environments may result in unexpected phenomena. Such a unique experimental environment, however, may lack applicability to real-world crystallisation conditions, which invariably occur in contact with a surface.

Synchrotron Radiation – Continuous-Flow Environments

An early example of the use of a continuous flow was reported by Alison and co-workers, who made use of both *in situ* SAXS and WAXS to monitor the antisolvent crystallisation of 2-dibromo-4-nitroaniline (DBA) in a basic plug-flow reactor (PRF) [173]. The PFR consisted of an aluminium mixing section followed by a 250µm-thick Melinex window wherein *in situ* XRD measurements were performed. The very initial nucleation stage of the crystallisation was tracked by scanning across the 15cm length of the reactor, with approximately 1s of reaction time being captured at the flow-rates used. Combined with the rapid mixing induced by the PFR, this meant that the early nucleation stages were captured in the device. The SAXS data indicated a new phase which appeared prior to the first observation of diffracting species on the WAXS data, although the relative sensitivity of the two different detectors was not reported. Nevertheless, it serves as a demonstration of the excellent time-resolution afforded by continuous-flow reactors, and shows their potential to access the early stages of crystallisation processes.

The use of droplet-based or segmented-flow reactors with *in situ* XRD has been demonstrated recently at a number of scales from the nanolitre [110] to millilitre scale [178]. The first report of the use of *in situ* XRD applied to a droplet-based continuous crystallisation device involved the screening of protein crystallisation [179]. Crystals of Thaumatin and Lysozyme 50-200µm were analysed within the nanolitre-scale droplets, allowing for an accurate measurement of structure and unit-cell dimensions. Techniques such as SAXS and SANS have also been used with droplet-based reactors [180-182]. Robertson and co-workers have previously demonstrated the use of a tri-segmented tubular system (the KRAIC), with *in situ* PXRD, to study the cooling crystallisation of a pharmaceutical API (Carbamazepine) and a co-crystal system (Urea – Barbituric Acid) [178]. The KRAIC system has previously shown excellent solids handling and applicability across reaction conditions [109, 183], alongside the aforementioned benefit of a segmented flow environment in enabling tight residence time distributions and, consequently, studies of transient crystallisation processes [184]. For both crystallisation systems, the time dependent crystallisation pathways were studied, with metastable to stable transformations tracked across different mixing and seeding regimes. This demonstrated the flexibility of the KRAIC to enable time-resolved studies of industrially-relevant crystallisations, and the coupling with *in situ* XRD enabled accurate identification of crystallisation mechanisms. Despite its benefits, the KRAIC does suffer from high material usage (~100mL volume) and operational complexity.

The coupling of such reactors with *in situ* X-Ray techniques provides an analysis problem in so far as the contribution from the segmenting phases (be they liquid or gas) needs to be removed. An elegant way of demonstrating this was reported by Levenstein and co-workers for the analysis of crystallisations in a millifluidic droplet device (Figure 22) [146]. The short acquisition times used (20ms) were much lower than the time period that a droplet or segmenting oil phase was in the beam, meaning the frames with a contribution from only oil could be automatically identified and discarded in post-processing. The remaining diffraction patterns were then combined and integrated to give excellent final signal to noise. Because of the serpentine design of the millifluidic reactor and the use of droplets, XRD could be carried out across the length of the reactor to give excellent time-resolution. The authors exploited this to quantitatively screen nucleants for $CaCO_3$. In a subsequent publication, the authors demonstrated that the use of a droplet-based (as opposed to simply solution-based) operating protocol was crucial for both alleviating encrustation and in minimising

residence time distribution. This ensured that for each position along the device the residence time matched the reaction time.

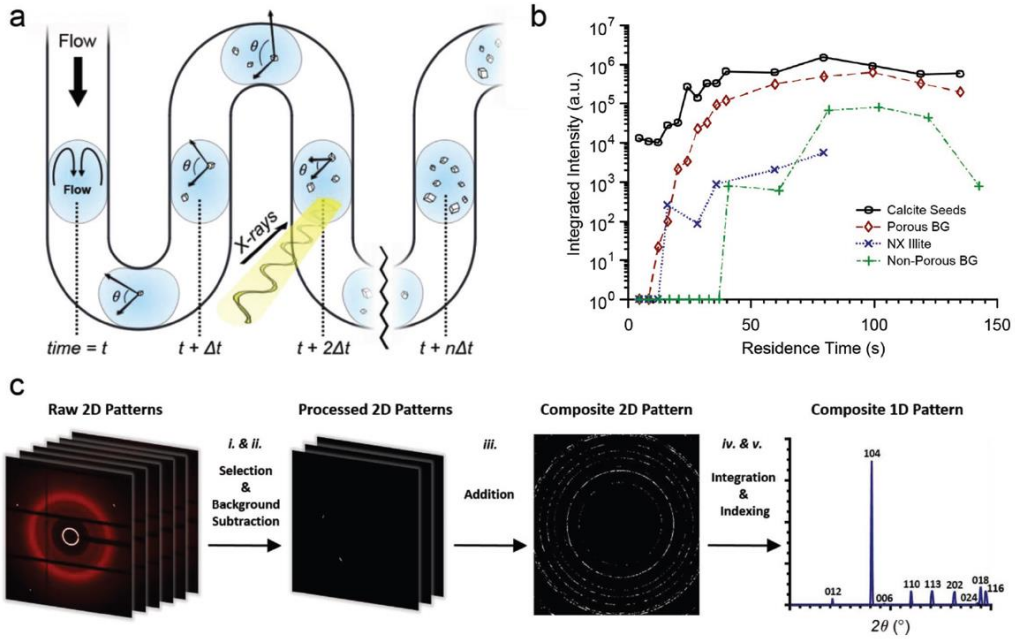

Figure 22 – Screening of nucleants for the crystallisation of CaCO3 within a droplet microfluidic reactor. (a) Diagram of the serpentine design of the reactor, showing X-rays incident on a position along the channel. (b) Intensity of CaCO3 diffraction over residence time for different nucleants. (c) Automated data analysis technique: selection of diffraction patterns, addition to make a composite pattern, and 2D to 1D azimuthual integration. Adapted from [146].

Laboratory-Based X-Ray Sources

Because synchrotron facilities are often oversubscribed, it may be difficult to secure enough (or any) experimental time at these facilities. Even if one does secure a valuable slot at the synchrotron, researchers typically only have a matter of days to carry out their experiments [185]. Laboratory-based equipment may allow for experiments to be optimised or 'practiced' in an environment with less time-pressure than a synchrotron visit, gathering preliminary data that would allow researchers to use their synchrotron time effectively and for more complex experiments [186, 187]. Although the brilliance of the X-rays produced through synchrotron has resulted in previously unrivalled performance, advances in laboratory-based X-Ray sources have shown their potential to supplement or replace synchrotron-based experiments [144, 188]. Improvements in photon flux in lab-based sources have been achieved through advances in X-ray generation methodology. Micro-focus sources, introduced commercially in the early 21st-Century, can produce powerful, highly-focussed beams, with low power requirements and maintenance costs [186]. The combination

of a micro-focussed beam with a liquid- or rotating-anode allows for photon fluxes approaching synchrotron levels (8-25KeV) [186, 189]. Concomitant developments in detection capabilities have been achieved by the now widespread use of 2D hybrid photon counting (HPC) detectors, initially in synchrotrons and now widely available for lab sources [190, 191].

The combination of a laboratory X-ray source and flow-through cell has been demonstrated to be useful for assessing *in situ* the evolution of crystal structure over time. Such flow-cells were originally developed for use with synchrotron radiation sources, and subsequently extended to use with lab-based sources. For use with cooling crystallisations, flow-cell loops may be temperature controlled the ensure no non-representative crystallisation occurs within the loop [192]. Hammond and co-workers reported the use of a flow-cell set-up to monitor polymorphic forms during batch crystallisations of several compounds [143]. In particular, for the case of L-Glutamic Acid, only the stable polymorph was identified for a slow cooling rate, but a mixture of metastable and stable polymorphs could be identified for a fast cooling rate. The minimum solids concentration required for a signal to be registered was around 1 wt.% for these compounds. The same instrument was subsequently used to characterise the transformation of the metastable α-form of L-GA to the stable β-form [193, 194]. A linear relationship was found between solids concentration and diffraction peak area, allowing for quantification of the relative amounts of the two forms. This in turn allowed for the kinetics of dissolution of the α-form and growth of the β-form to be plotted, with zeroth order and first order showing the best respective fits [194].

This work was subsequently expanded upon by Turner et al., who made use of an improved flow-cell design to monitor the phase transformation between two enantiotropically related polymorphs of *para*-Aminobenzoic Acid (PABA) [195]. The improved flow-cell, shown in Figure 23(a), which made use of a thin-walled borosilicate glass capillary, allowed for a lower limit of detection (0.6 wt.%) compared to the previous design. The transition between the metastable β-form to the stable α-form was monitored at four different temperatures above the enantiotropic point, with the same zero-order dissolution (Figure 23(b)) and first-order growth (Figure 23(c)) kinetics being applied. By extrapolating the relationship between rate constants (for dissolution and growth) and temperature to the equilibrium case (Figure 23(d)), an estimate of enantiotropic transition temperature was made. *In situ* UV-vis spectroscopy was also used to monitor solute concentration during the transition. This concentration data was used to indicate that the dissolution of the metastable form

was the rate-limiting process in the transformation, as opposed to the nucleation and growth of the stable form. This highlights the utility of a combination of *in situ* monitoring techniques to account for both solid- and solute phase material during a crystallisation process, which can lead to a greater degree of understanding of the processes occurring. The acquisition time of this instrument, however, was on the order of minutes, rendering it suitable only for slow processes.

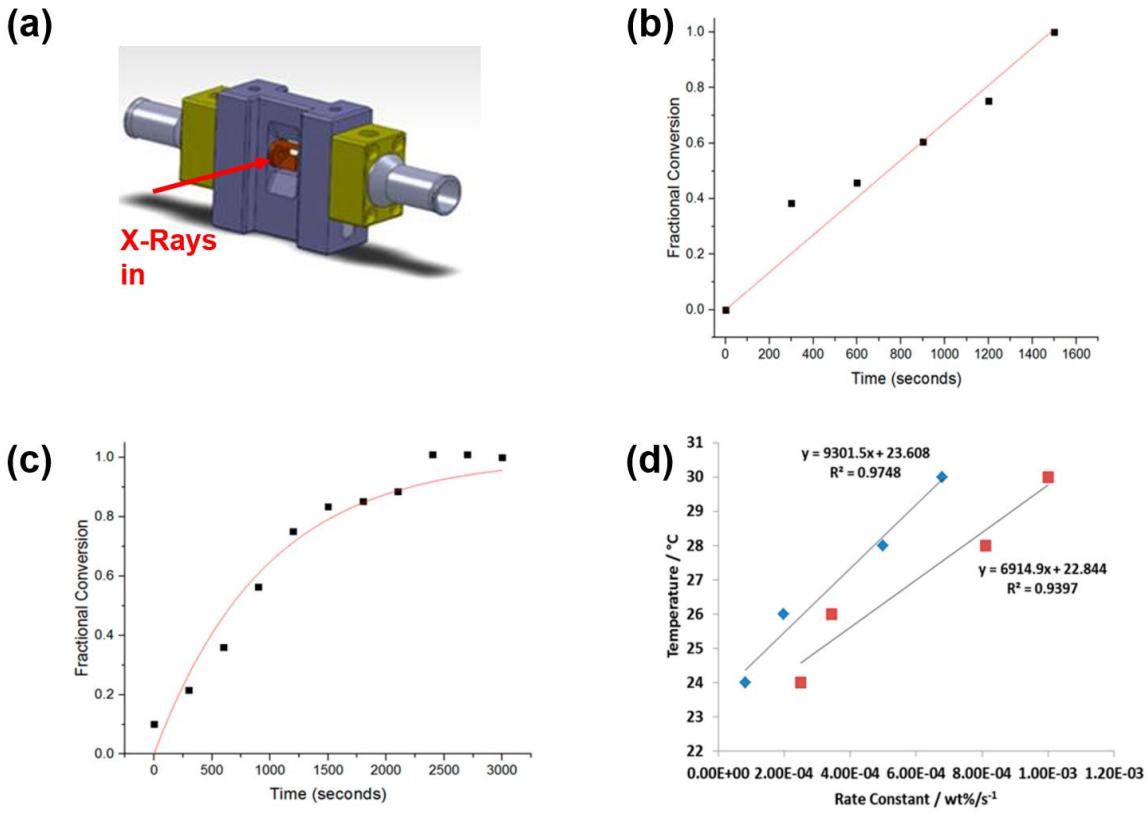

Figure 23 - Study of polymorphic transformations of enantiotropically related forms of PABA by Turner et al. [195]. (a) Improved flow-cell design facilitating transition-mode in situ XRD characterisation. (b) Zeroth order fit to the dissolution of the metastable form. (c) First order fit to the growth of the stable form. (d) Dissolution- and growth-rate parameters across temperatures used to predict enantiotropic transition temperature.

The use of laboratory X-ray diffraction instruments has recently been extended to the monitoring of crystallisations within continuous-flow environments. Polte and co-workers reported the coupling of a microfluidic mixing device with in-line SAXS to elucidate the mechanisms of growth of gold nanoparticles in solution [196]. This was the first example of the application of in-line SAXS to a continuous flow platform to monitor the formation of nanoparticles in solution that did not rely on synchrotron radiation. It was also an example of the detailed (i.e. millisecond) time-resolution afforded by the use of continuous-flow with in-line analysis, which was useful for

monitoring the early stages of crystallisation. Chen et al. subsequently performed a more detailed study on the gold nanoparticle system using a stopped flow device and lab-based SAXS/WAXS and UV-vis [169]. Such a combination allowed for a systematic investigation of reaction parameters on both nucleation and growth rates, highlighting how different analysis techniques can be used simultaneously to monitor different scales (particularly as SAXS and WAXS capture diffraction from different features at different size scales). A subsequent, similar study was reported for the production of ZnO nanoparticles [197].

A recent report demonstrated the use of the microfluidic droplet continuous crystalliser discussed earlier [146] with different laboratory-based SAXS and WAXS instruments [144]. Although mixed results were obtained with the former instrument, the latter gave better signal to noise ratios, allowing the intense (1 0 4) peak of calcite to be observed during the reactive crystallisation of $CaCO_3$. However, other peaks could not be resolved, limiting the applicability of the microfluidic chip with the lab-based source for detailed structural resolution. Noting the existence of an optimum path length at which maximum transmitted intensity occurs, the authors made use of a larger (1mm) path length analysis cell and an adapted-version of the segmented-flow KRAIC system [109]. Slurries of both $CaCO_3$ and paracetamol were studied *in situ* with the lab-based XRD, with much improved signal to noise. This demonstrates the importance of considering scale and path length for optimising signal to noise during *in situ* XRD monitoring.

1.5. Aims and Objectives

The broadest aim of the project is to assess new methodologies for the characterisation of crystallisation processes in an accurate and time-resolved manner, avoiding the unintentional modification of samples. Characterisation in an *in situ* manner shows great promise to facilitate this, and as such will be explored. Whilst this has been achieved for crystallisations in the past, there are several areas of potential improvement which have not yet been realised. The next-generation of laboratory-based X-Ray diffraction instruments has not yet been utilised for *in situ*, time-resolved studies of crystallisation phenomena for the important class of crystallisations of mineralisations. Furthermore, the coupling of such instruments with a continuous crystallisation route has not yet been realised. More broadly, *in situ* probes for monitoring crystallisations (such as FTIR probes, often demonstrated for batch crystallisations) remain under-utilised for continuous crystallisations.

Continuous crystallisations carry benefits in terms of providing an intense and consistent mixing environment. Furthermore, analysis of continuous flow reactors at a steady-state has benefits in terms of reproducibility and accuracy for time-resolved processes, and can allow for ease of interfacing with automation and optimisation software, as has previously been demonstrated with homogeneous chemical reactions. The ability to demonstrate steady-state analysis of a continuous crystallisation is thus the next step towards realising the extension of automated analysis to crystallisation processes.

The novelty of the project is thus primarily in the realm of physical processing and crystallisation route development, and the coupling of this with both a novel *in situ* PXRD analysis technique and an *in situ* FTIR probe. Secondary to this is the knowledge to be gained from the study of example crystallisation systems. These were chosen due to gaps in the understanding of how these crystallisations occur under different experimental conditions (e.g. supersaturation, solvent mixture, additive concentration). Initially, the reactive crystallisation of Calcium Sulfate was studied under different supersaturations, additive concentrations, and solvent mixtures, under a simpler, batch environment. This allowed for the development of the *in situ* PXRD analysis technique, allowing for a flexible operational environment wherein the kinetics of crystallisation could be studied. This reaction was then transferred to a continuous-flow platform (the *fReactor*), which in turn was integrated into the PXRD instrument resulting in a completely novel crystallisation analysis platform. A different class of crystallisations (the antisolvent crystallisation of a small organic compound, ROY) was then studied in the fReactor platform. Finally, continuous seeded crystallisations are demonstrated under isothermal conditions, in an attempt to track crystallisation growth rates in the fReactor platform. This showed the flexibility of the continuous crystalliser for use with different supersaturation generation methods and model systems.

2. Batch Reactive Crystallisation of $CaSO_4$

2.1. Introduction

2.1.1. Background Science

Calcium Sulfate

Calcium Sulfate is a mineral of industrial and natural significance. Within the solid state, a number of different structural forms exist with varying degrees of hydration: gypsum ($CaSO_4.2H_2O$), bassanite ($CaSO_4.½H_2O$), and the anhydrous form anhydrite. Within a purely aqueous environment, gypsum is the most stable form below ~40-60°C, and above this temperature range anhydrite is the most stable. However, anhydrite, despite being thermodynamically stable, does not typically form from aqueous solutions until around 120°C, due to kinetic inhibition [198]. Bassanite is metastable within these temperature ranges in a purely aqueous solution, and will undergo a rapid, exothermic hydration reaction to gypsum upon the addition of water [199]. As a result of this, gypsum exists as the dominant structural form within natural environments, being the most abundant sulfate mineral on earth [200]. Anhydrite can exist in three different polymorphs (AI, AII, AIII), the formation of which is temperature and pressure dependent [200]. A phase diagram showing the aqueous temperature dependent solubility of the three aforementioned hydrates (anhydrite form I) is given in Figure 24.

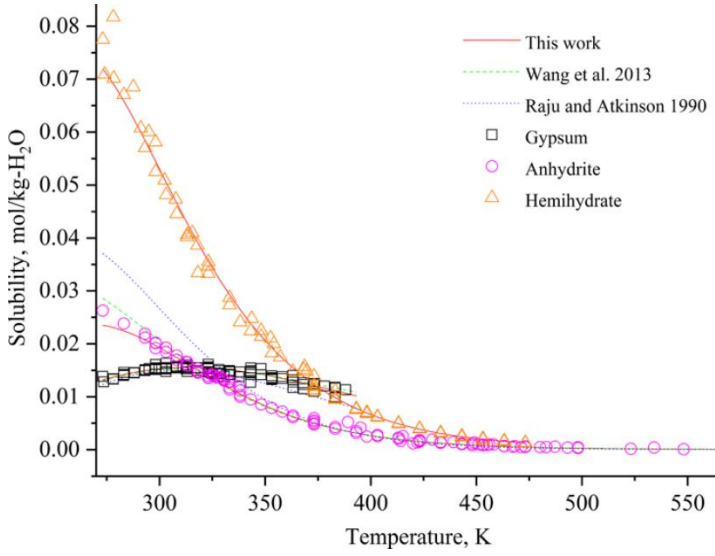

Figure 24 – Solubility of different hydrate of CaSO4, reproduced from [201]. Experimental measured values are given by the symbols, and thermodynamic modelling was undertaken to fit to the solubilities, as indicated by the red lines. These values were compared with previous fits from the literature [202, 203]. The hemihydrate (bassanite) is found to be metastable at all temperatures. A crossover in solubility between gypsum and anhydrite (AI) occurs at ~320K.

Solid gypsum has a monoclinic structure and spacegroup $P2_1/m$, and the anhydrite forms possess orthorhombic and cubic forms. Bassanite is typically sub-divided into two different forms: α- and β-hemihydrate. Despite some disagreement as to the exact structure, it is thought that these two forms differ only in morphology and crystal size, perhaps as a result of different preparation methods [204]. The former is typically produced through aqueous reactions in the presence of electrolytes or at elevated temperatures (80°C) [205], and the latter finds industrial use as the building material *plaster of Paris*, and is produced from the heating of solid gypsum, resulting in dehydration [206]. As well as the form of bassanite with a water content of $0.5H_2O$, forms with higher water contents (xH_2O, $x>0.5$) have been reported, which can form in highly humid environments [207]. The water molecules in the bassanite form are arranged in channels, which provides a relatively low energy barrier to hydration to the gypsum form upon contact with bulk water [207]. The structures and unit cells of gypsum, bassanite and anhydrite (form AII) are shown in Figure 25. An amorphous form of $CaSO_4$ has also been reported [208], which can occur within confined environments [209, 210] or in the presence of polymeric additives [211].

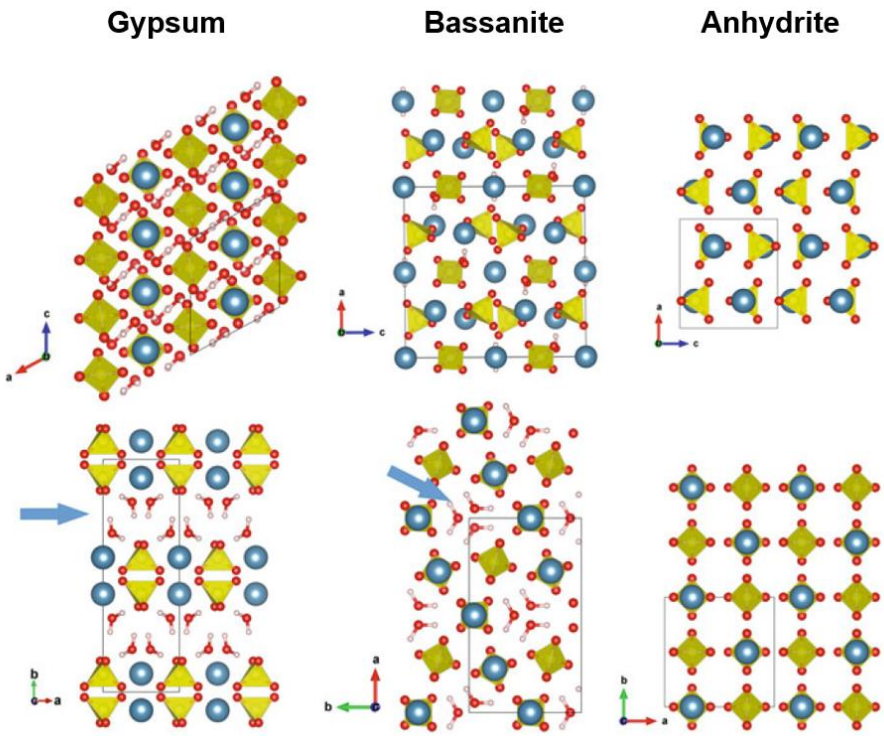

Figure 25 - Structures of CaSO4 hydrates (gypsum, bassanite, anhydrite form AII), constructed by Van Driessche et al. [212]. The yellow tetrahedral represent sulfate ions, the blue spheres represent Ca2+ ions, and the interstitial water molecules are indicated by the arrows. Two different angles are shown to indicate the structural motif (top and bottom row). The unit cells are indicated by the drawn box.

Calcium sulfate formation mechanisms

The exact mechanisms of both the precipitation of gypsum from aqueous solutions at ambient conditions and the transformation of bassanite to gypsum have been the subject of recent academic interest. Wang et al. (2012) originally reported the existence of an amorphous, as well as a metastable crystalline (bassanite) precursor to gypsum during precipitation from 50mM solutions of Ca^{2+} and SO_4^{2-}, making use of cryo-cooled Transmission Electron Microscopy (Cryo-TEM) to make time-dependent structural identifications [211]. Samples were 'quenched' with ethanol, which was presumed to stop the reaction at a desired time-point without affecting it. Although it was suggested that the reaction mixture as a whole progressed through an amorphous – metastable – stable pathway, subsequent reports suggested the quenching of the precipitation process in ethanol may isolate bassanite in high yields (where, in a purely aqueous reaction mixture, only gypsum would be found) [213, 214]. Indeed, mixing 50mM aqueous solutions of Ca^{2+} and SO_4^{2-} in such a volume of ethanol and water as to reach a final water content of 33wt.% resulted in Bassanite being produced with a yield in excess of 90%. With increasing water content, the resultant hydrate selectivity begins to rapidly favour gypsum. This somewhat calls into question the validity of the observed amorphous – bassanite – gypsum pathway within purely aqueous bulk crystallisation. In terms of growth kinetics, the majority of studies have indicated a second-order relationship [215, 216], with a few studies suggesting the order can increase to between 3 and 4 at exceptionally high supersaturations [217, 218].

Evidence has been obtained, however, for a non-classical nucleation pathway of gypsum from aqueous solution. Time-resolved quenching and Cryo-TEM studies revealed that gypsum can form by the initial nucleation of bassanite nanoparticles, which subsequently self-assemble co-axially, before solid-state transformation to gypsum occurs (Figure 26(a)) [219]. Further evidence for this non-classical crystallisation was provided by Stawski et al., who reported the investigation of $CaSO_4$ nucleation with time-resolved stopped-flow *in situ* SAXS/WAXS characterisation [171]. A four-step nucleation pathway was elucidated from the scattering data, as shown schematically in Figure 26(b). Initially, non-interacting primary elongated scattering species (<3nm in length) are formed. These then begin to aggregate into loose domains, followed by densification into disordered aggregates composed of the primary units. Finally, gypsum is formed through further aggregation and reordering of the primary units. Subsequent *in situ* liquid-cell TEM studies of the transformation of bassanite to gypsum indicated that it can proceed via either a dissolution-

reprecipitation mechanism or a solid-state transformation, with the former being the predominant mechanism [220].

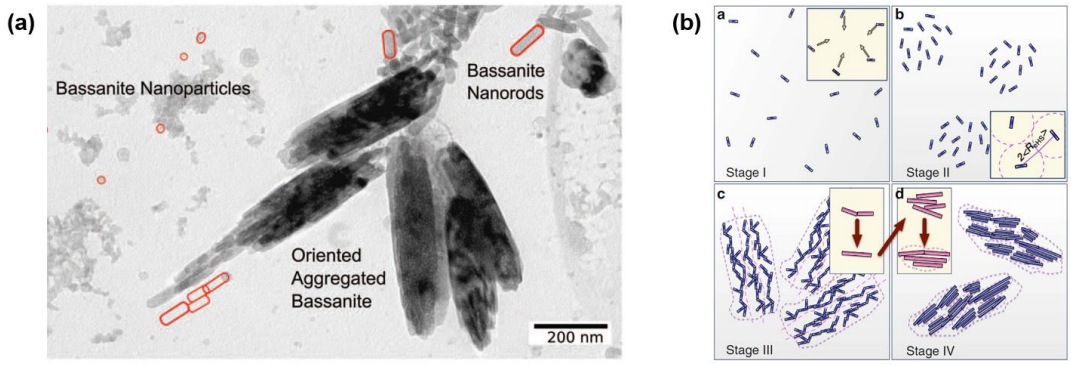

Figure 26 – Non-classical pathways to the formation of gypsum. (a) CryoTEM image showing oriented attachment of bassanite nanorods which undergo solid-state transformation to gypsum [219]. (b) 4-stage pathway to the formation of gypsum from in situ stopped-flow SAXS studies. The orientated attachment mechanism is preceded by the initial formation of bassanite nanoparticles below the bulk solubility [171].

The β-hemihydrate form of bassanite is commonly used in the construction industry as *Plaster of Paris*. The addition of water induces its reprecipitation and hardening into gypsum. The exact mechanism of this transformation has been the subject of investigation. A number of crystallisation models have been proposed for the transformation, including where small gypsum crystals are included as seeds, but there remains a disagreement as to the best kinetic model for the transformation [221]. Recently, synchrotron radiation studies of the hydration of both α- and β-hemihydrate through the introduction of water allowed for the kinetics of the transformation to be studied [204]. Both Avrami-Erofe'ev [222] and Gualtieri models [223] were reported, and showed a good fit for both forms, with the latter showing the closest agreement. The Gualtieri model allows for the probability of nucleation to be estimated across experimental conditions, which was exploited to show the effect of a commercial accelerant on the nucleation rate of gypsum.

Reactive crystallisation of $CaSO_4$ with additives

An additive within the context of a solution crystallisation process (be it a reactive precipitation, or a cooling or antisolvent crystallisation) can be described as a molecular entity present within the undersaturated liquor that is not the same as the principal (or desired) crystallising material and does not crystallise under the set crystallisation conditions. This additive may interact with the crystallising material through adsorption onto the growing facets (either uniformly or face-specifically), directing growth [224]. Having been demonstrated for both organic and inorganic systems, face-specific growth-rate hinderance may be exploited for purposes of

morphological modification [225]. Additives have also been shown to affect the nucleation process in a number of ways [226], serving potentially as heterogenous nucleation sites to lower the kinetic barrier to nucleation [227] or as nucleation inhibitors through solution complexation [228]. The role of additives in controlling nucleation processes has also been rationalised within the framework of non-classical (i.e. multi-step) nucleation processes [229]. It may also be incorporated into the crystal lattice under certain conditions, becoming occluded within the crystal structure [230]. Such incorporation of guest species in host crystals may induce changes in bulk material properties [231] and offers a route to the formation of functional materials, such as for optoelectronic materials [232] and for drug delivery [24].

For the reactive crystallisation of calcium sulfate, a number of studies have been performed to assess the role that additives play in the crystallisation, and the resultant effects on morphology and structure. Wang and Meldrum (2012) made use of three different additives, both organic and inorganic, to generate amorphous calcium sulfate as well as metastable bassanite at room temperature, both of which were able to be stabilised in solution [233]. Making use of time-resolved filtration and quenching, as well as TEM analysis, they were able to quantify the degree to which the additives slowed-down the precipitation process. As well as influencing the polymorph that formed (by slowing down the transformation of less stable forms to more stable forms), the two organic additives used had a significant effect on morphology. They found that the use of inorganic Mg^{2+} ions as an additive, however, did not yield significant morphological differences. Polymeric additives have subsequently been used to mediate the water activity of the crystallisation solution, which was shown to stabilise bassanite [234]. More recently, off-line kinetic analysis has demonstrated mechanisms by which inorganic ionic additives (Na^{+}) can influence the rate of transformation within mixed-solvent systems [235].

In terms of kinetics, recent work has suggested that the use of Mg^{2+} additives may have either an inhibitory or promotive effect on growth rates at different additive concentrations [236]. At lower concentrations, Mg^{2+} may inhibit active growth sites causing a reduction in growth rates; but at higher concentrations, the Mg^{2+} may begin to preferentially complex with the solvent (water) molecules owing to their higher hydration enthalpies than Ca^{2+}. This may cause Ca^{2+} to favourably attach to the growing lattice, resulting in a promotion at higher Mg^{2+} concentrations. The effect of inorganic additives on kinetics was investigated by the use of *in situ* turbidity measurements, which allowed for induction times to be accurately measured across different additives (K^{+}, Na^{+}, Li^{+}, and Mg^{2+}) [237]. A rationalisation of the role of each

additive was supplemented by SEM imaging and analysis of the level of incorporation of additives in the crystal structure. Only Na^{2+} (~25 wt.%) was able to be occluded within the crystal structure, with all other additives being found exclusively at the crystal surface. Mg^{2+} was shown to have the most significant impact on crystal growth, drastically slowing down both the induction time and growth rate. It also had a minor effect on morphology, resulting in the 'tips' of the needle-like gypsum crystals becoming rounded. The lack of mechanistic insight that can be gained through the use of a turbidity probe means that exact, quantitative growth rates could not be obtained.

2.1.2. Goals and Rationale

Recent improvements in X-Ray generation and detection capabilities away from synchrotron sources has led to the development of advanced, laboratory-based instruments. It has already been shown that synchrotron sources can enable *in situ* characterisation of crystallisation formation mechanisms and kinetics. The question is now to what extent are laboratory based XRD instruments a credible alternative to synchrotron sources for such studies? Specifically, can an experimental apparatus be developed that allows for *in situ* characterisation of a crystallisation process with sufficient time-resolution and signal as to gain quantitative kinetic and structural information under a variety of experimental conditions? With respect to the reactive crystallisation of $CaSO_4$, there are still unresolved questions regarding the reactive crystallisation of this important mineral system. There is still uncertainty with respect to the rate of crystal growth following precipitation from aqueous solutions, and the kinetic order with which it can best be modelled [200]. There have been conflicting reports as to whether the presence of Mg^{2+} ions can induce the formation of and stabilise the bassanite form of $CaSO_4$ following precipitation from aqueous solutions [233, 237]. There are also conflicting reports as to the mechanism of the transformation from bassanite to gypsum, specifically whether this proceeds via a more classical dissolution-reprecipitation process or a non-classical solid-state transformation [220].

To go some way to resolving these gaps, an experimental apparatus was constructed to enable the *in situ* characterisation of crystallisations in a flowing environment using a state-of-the-art laboratory-source XRD instrument. A flow-cell was used to enable *in situ* XRD characterisation of a small volume of crystallisation slurry continuously sampled from a batch reactor. Calibrations were undertaken to relate known slurry densities to the intensity of diffraction obtained, and to find the signal-to-noise limit.

This in turn allowed for studies of the effect of precursor concentration and additives (Mg^{2+}) on crystallisation kinetics, wherein the mass of crystals over time could be quantified. Finally, $CaSO_4$ crystallisations were carried out in the presence of ethanol, under both different ethanol fractions relative to water and in the presence of Mg^{2+}, in order to elucidate the effects on the $CaSO_4$ phases that form over time.

2.2. Methods

2.2.1. Apparatus

FlowXL

The FlowXL facility at the University of Leeds consists of an XRD instrument and Raman spectrometer, both of which have been designed to enable *in situ* experiments [238]. In particular, the goal of the instruments is to facilitate time-resolved studies of crystallisation processes in flowing (or otherwise novel and well-controlled) sample environments. At the heart of the facility is the XRD enclosure, approximately 1.86 x 1.42 x 1m in size, wherein crystallisation experiments take place. Approximately half the volume of the enclosure is taken up by the diffractometer, leaving the remainder for equipment for crystallisations, which allows for experimental flexibility. The enclosure must be shut, and an interlock enabled when XRD experiments take place, meaning the enclosure functions in a similar manner to the 'hutches' present at synchrotron facilities. This does mean, however, that experiments must be started, then the enclosure doors are shut and locked, and then XRD acquisitions can begin – this process can take about 20-30s, resulting in dead-time at the start of the experiments. A Raman spectrometer is also included in the facility outside the enclosure, with a 10x objective probe (connected to the spectrometer via a fibre-optic cable) positioned inside the enclosure. A diagram showing the mechanical design of the FlowXL XRD enclosure is shown in Figure 27.

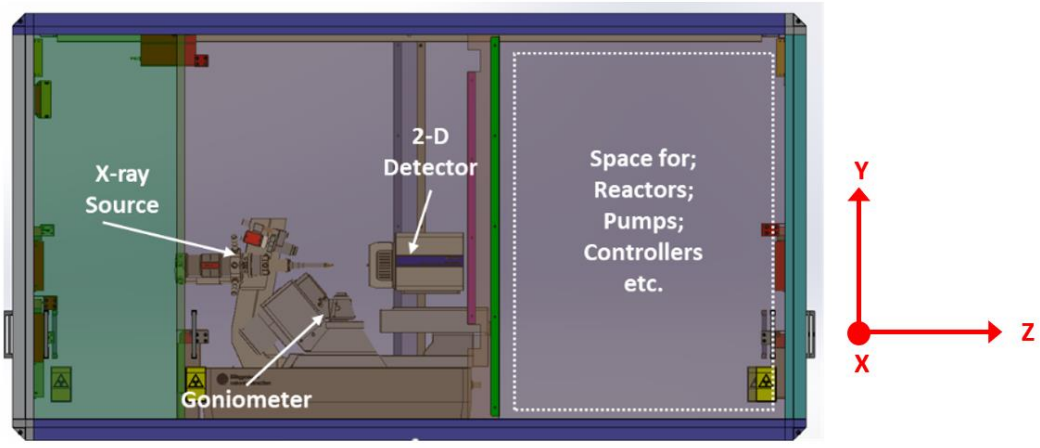

Figure 27 – Mechanical drawing of FlowXL XRD enclosure (side-view). Significant space is provided within the enclosure for equipment to facilitate crystallisations which can be monitored in situ by the XRD. The X-direction is that coming out of the plane of the page.

The diffractometer itself is a custom-made Rigaku XtaLAB Synergy Custom. This includes a MM007-HF (Cu) microfocus rotating anode with VariMAX very high flux X-

Ray optics as the source, and a Hybrid Photon Counting (HPC) 2-D detector. A typical beam size for the source is 150µm in diameter (FWHM) with a 10mrad divergence, and a high sample brightness of >2.0 x 10^{11} photons s^{-1} mm^{-2} at the detector [239]. The detector enables fast data collection with low-noise, with 100 x 100µm pixel sizes and a high dynamic range. The combination of such a source and detector leverages recent developments in the design of both to enable *in situ* low-noise data collection of samples for flowing environments [186, 239].

For XRD studies, samples are typically positioned between the X-Ray source and detector at the centre of the goniometer, and diffraction data is collected in transmission mode. A motorised stage – the XtalCheck-S – is included, which can be mounted directly above the goniometer. The stage enables movement in the X, Y and Z axes, to manipulate samples into and out of the beam in a precise manner. This was originally designed to fit samples within standard Society of Biomolecular Screening (SBS) crystallisation plates (128 x 86 x 15 mm), although custom 3D printed sample holders can also be used that fit within the plate holder. CrysAlisPro software (v42, Rigaku Corporation, Japan) was used to obtain PXRD measurements for all experiments. Upon the acquisition of a 2D diffraction pattern, the same software was used for azimuthal integration to obtain a 1D diffraction pattern.

Flow-cell Design and Usage

Transmission mode XRD studies of flowing samples within slurries were carried out within a custom-made flow-cell [195]. This consists of four parts: an inner cylindrical cartridge within which a 2mm glass capillary is mounted, a stainless-steel block within which the cartridge can be mounted, and two smaller stainless-steel blocks screwed down to either side of the main block to facilitate interfacing with tubing. The cartridge contains a 1.5mm glass capillary (10µm wall thickness), which carries the slurry and is where X-rays are incident normal to the direction of the slurry. With the cartridge positioned within the main block, the two side blocks are screwed in place with 8 x M3 bolts, sealing the cartridge. Either side of the blocks, ¼-28 ports were drilled to allow for interfacing with 3/16th inch OD tubing with flangeless fittings. Either side, an o-ring sits between the side block and main block to seal the assembly. A diagram of the flow-cell is shown in Figure 28.

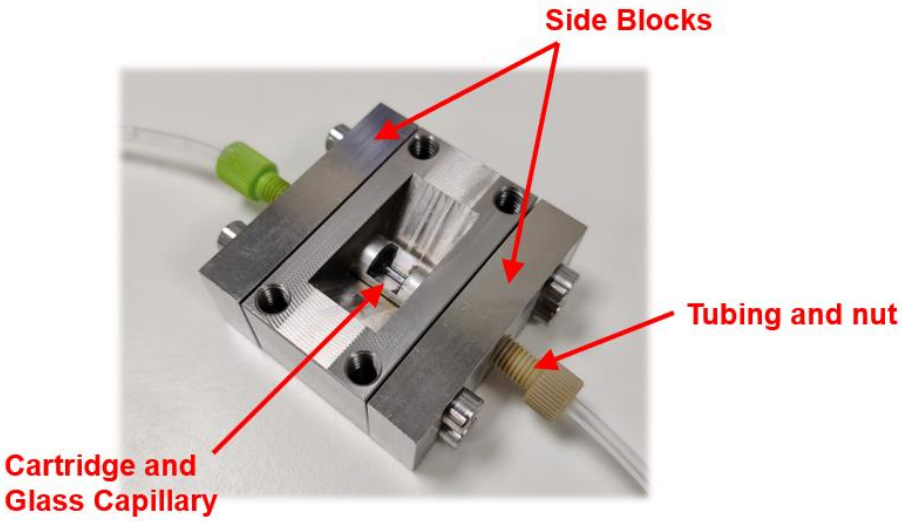

Figure 28 – Flow-cell used for in situ XRD studies. The 2mm glass capillary is indicated inside the cartridge. The side blocks are indicated, showing how they seal the cartridge in place. Tubing can be seen interfaced with the flow-cell at either side.

The flow-cell was mounted on a 3D printed holder designed to fit into the XtalCheckS motorised stage. At the ports, lengths of PFA tubing (OD = 4.76mm, ID = 3.18mm) were screwed into place with appropriately sized PEEK ferrules and nuts. One length of tubing led to a 500mL glass batch reactor with overhead stirring. The other length led to a peristaltic pump, where the PFA tubing was interfaced with flexible peristaltic pump tubing (Masterflex L/S 15, length 0.4m) with hose clips. A further length of PFA tubing led from the other end of the peristaltic pump tubing to the batch reactor, completing a loop to and from the batch reactor via the peristaltic pump and flow-cell. The total length of the loop is 2.43m, and the volume is approximately 24mL. With the peristaltic pump running at 150RPM, the slurry took approximately 5s to traverse the loop. A schematic of the sample loop used for the experiments is shown in Figure 29 and a photograph is shown in Figure 30.

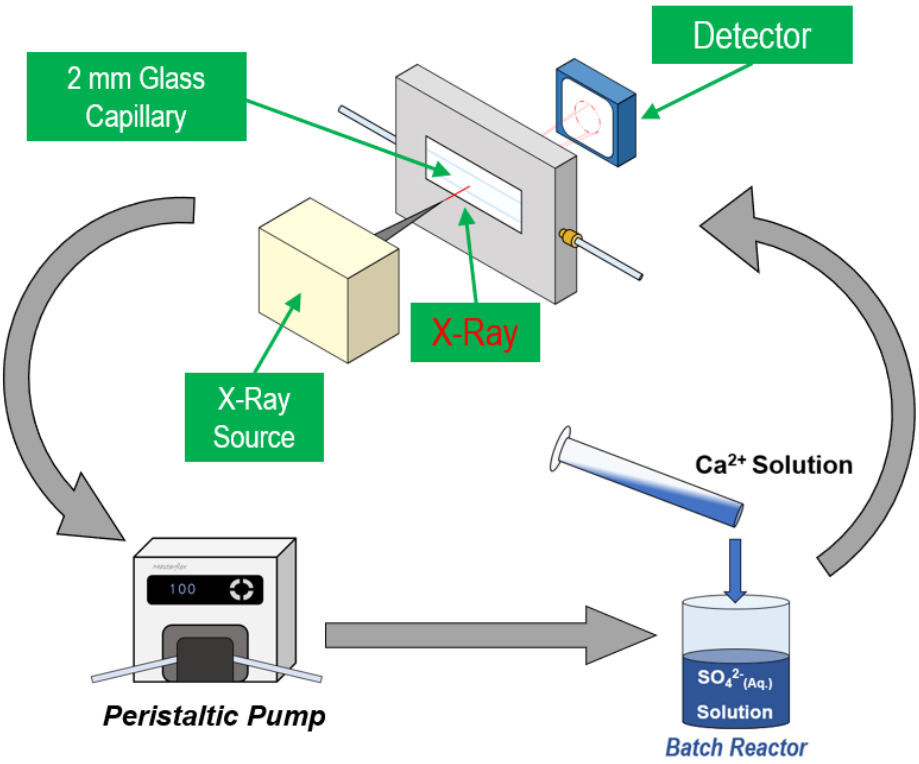

Figure 29 - Batch reactor and inline PXRD loop flow-cell apparatus. Solutions are transported between the batch reactor and the flow-cell using a peristaltic pump and 3/16" I.D. PFA tubing. The volume of the flow path and the cell is approximately 24mL.

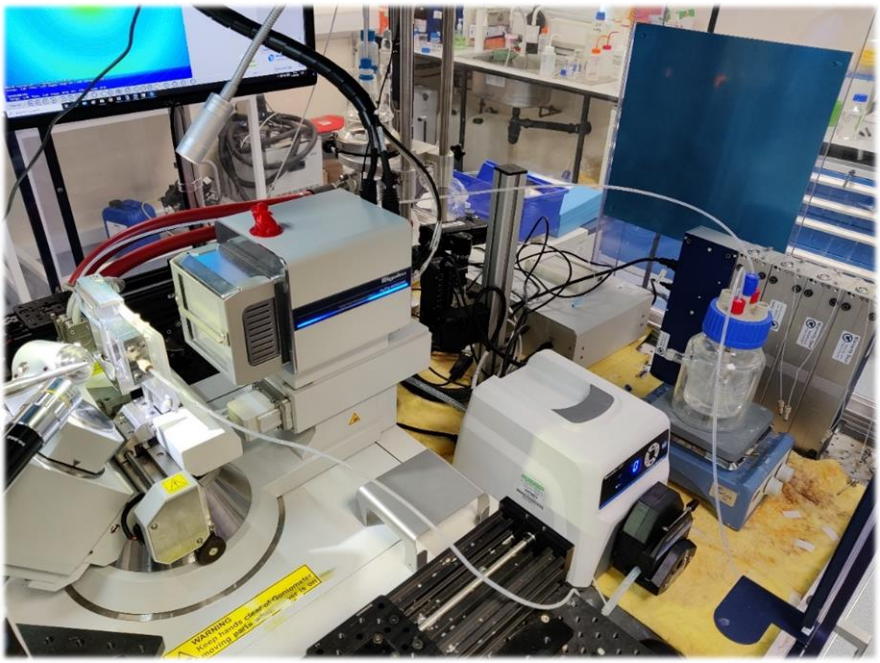

Figure 30 - Photograph of the apparatus used for the batch crystallisation experiments with in situ PXRD characterisation. The flow-cell is mounted between the X-ray source and detector, and tubing runs between the flow-cell, batch crystalliser, and peristaltic pump.

Reagents and Materials

$CaSO_4.2H_2O$ (Gypsum) was used as supplied by Fluorochem Ltd. (Glossop, UK) for off-line PXRD and calibration experiments. Na_2SO_4 (Thermo Fisher Scientific inc., Waltham, MA, USA) was used as a source of SO_4^{2-} ions, $CaCl_2.2H_2O$ (Sigma-Aldrich, Burlington, MA, USA) was used as a source of Ca^{2+} ions, and $MgCl_2.6H_2O$ (Thermo Fisher Scientific inc., Waltham, MA, USA) was used as the source of Mg^{2+} ions. Deionised water was obtained from a Milli-Q EQ 7008 water purification system (MerckMillipore, Darmstadt, Germany). Absolute ethanol (purity >99.8%) was used as supplied by VWR international (Radnor, PA, USA).

2.2.2. Off-line PXRD Characterisation of Hydrates

Off-line PXRD was carried out on samples of Gypsum and Bassanite using a Brucker D2 Phaser benchtop PXRD instrument (Brucker Corporation, MA, USA). Samples of Gypsum were deposited in ethanol and drop cast onto a silicon wafer, which was left to dry at 40°C for 3 hours. Bassanite was prepared by sintering Gypsum in a crucible at 300°C for 5 hours, before being drop cast onto a silicon wafer in the same manner. Data was collected for a 2θ range of 6-35° utilising Bragg-Bretano geometry, and the disc was rotated at a speed of ~5RPM during acquisitions.

2.2.3. Calibration of PXRD to Solids Concentration

The effect of varying $CaSO_4$ solids concentration within slurries was investigated in order to develop a calibration between $CaSO_4$ solids concentration and the resultant PXRD patterns. Slurries of varied weight fraction of $CaSO_4$ were pumped through the flow-cell apparatus, with diffraction patterns measured following the attainment of steady-state. A saturated solution of $CaSO_4$ was prepared by combining 10g of Gypsum with 500mL of de-ionised water in a round-bottom flask, leaving it to stir overnight with magnetic stirring at 300 rpm, and then filtering through 0.45µm membrane filter, retaining the filtrate and discarding the excess solid gypsum. 200mL of the saturated solution was added to the batch reactor, and a diffraction pattern was measured of the saturated solution. Known masses (in steps of 0.25 wt.%) of gypsum were added sequentially, with a diffraction pattern measured 5 minutes after each addition giving time for the solids to be well-mixed into the batch reactor. To repeat the experiment with bassanite, 10g of gypsum was left in a furnace for 5 hours at 300°C to generate bassanite. A saturated solution was created using absolute ethanol instead of water to prevent a bassanite to gypsum transformation, and the experiment was repeated as in the case of the gypsum calibration.

2.2.4. Aqueous Reactive Crystallisations of $CaSO_4$

Varying Precursor Concentration

Reactive crystallisations of $CaSO_4$ were carried out by mixing aqueous solutions containing the precursor ions - Ca^{2+} and SO_4^{2-} - at a 200mL total volume scale within a 500mL batch reactor with a magnetic overhead stirrer. Three different end (post-mixing) concentrations of precursor solutions were used (75, 100, 125mM), with three repeats of each being carried out. Initially, 100mL of the SO_4^{2} solution was added to the batch reactor. Then 100mL of the Ca^{2+} solution was added, the stirring (300RPM) and peristaltic pump (150RPM) were started, the doors to the enclosure were sealed, and the acquisitions began. XRD acquisitions were completed with a 20s acquisition time, and were run consecutively, with a short down-time between acquisitions. Experiments were run until a state of equilibrium was assessed to have been reached by consistent PXRD peak intensities between several acquisitions (typically at least 5).

Varying Mg^{2+} Additive Concentration

To explore the effect of an additive on the crystallisations, $CaSO_4$ reactive crystallisations were carried out at a fixed post-mixing concentration of Ca^{2+} and SO_4^{2-} (100mM each) at different Mg^{2+} additive concentrations (25-250mM). $MgCl_2.6H_2O$ was dissolved in the Ca^{2+} solution prior to mixing with the SO_4^{2-} solution. XRD acquisitions were carried out in the same manner as in the case of the additive-free experiments. Three repeats of each additive concentration were carried out. Following the conclusion of the experiment, samples of the crystals formed were taken by filtering the reaction mixture through a membrane filter using a vacuum. Scanning electron microscopy (SEM) was carried out on the samples using a Nova NanoSEM 450 instrument operating at 5kV with a CBS detector. The samples were sputter coated with a 2nm layer of Iridium prior to imaging.

2.2.5. Ethanolic Reactive Crystallisations of $CaSO_4$

Varying Ethanol Volume Fraction

To explore the effect of ethanol content on the crystallisation of $CaSO_4$, reactive crystallisations were carried out wherby the Ca^{2+} was dissolved in ethanol (as opposed to water), and the SO_4^{2-} remained in an aqueous solution. Three different volume fractions of ethanol were targeted: 40, 50, and 60 vol.%, with the remainder being water. To keep the final concentration of the Ca^{2+} / SO_4^{2-} ions at 100mM, the precursor concentration was adjusted between the different volume fraction experiments to account for lower or higher volumes of the precursor solutions that

were used. A table showing the experiments carried out along with the precursor ion concentrations is shown in Table 2.

Table 2 – Batch crystallisation experiments undertaken in the presence of ethanol at different volume fractions. Different precursor concentrations were used to keep the final post-mixing ion concentration at 100mM between experiments.

Ethanol Vol. Fraction (%)	Ca^{2+} Concentration (mM)	Ca^{2+} Volume (mL)	SO_4^{2-} Concentration (mM)	SO_4^{2-} Volume (mL)
40	250	80	167.7	120
50	200	100	200	100
60	167.7	120	250	80

Varying Mg^{2+} Additive Concentration

Reactive crystallisations of $CaSO_4$ were carried out in a 50 vol.% ethanolic environment in the presence of Mg^{2+} ions at different concentrations (75-250mM). The end $CaSO_4$ concentration was fixed at 100mM. $MgCl_2.6H_2O$ was dissolved in ethanol alongside 200mM $CaCl_2.2H_2O$. The Mg^{2+} / Ca^{2+} solutions were mixed with 200mM SO_4^{2-} solutions to initiate crystallisations.

2.3. Results

2.3.1. Off-line PXRD results

Figure 31 shows the normalised off-line PXRD acquisitions of Bassanite and Gypsum, with a comparison to reference patterns for Gypsum (CCDC file: 2057-ICSD) and Bassanite (CCDC file: 92947-ICSD). The reference patterns and off-line measured patterns show a good agreement for both forms.The majority of peaks show different positions between the hydrates. This means that distinguishing between the hydrates using PXRD is trivial.

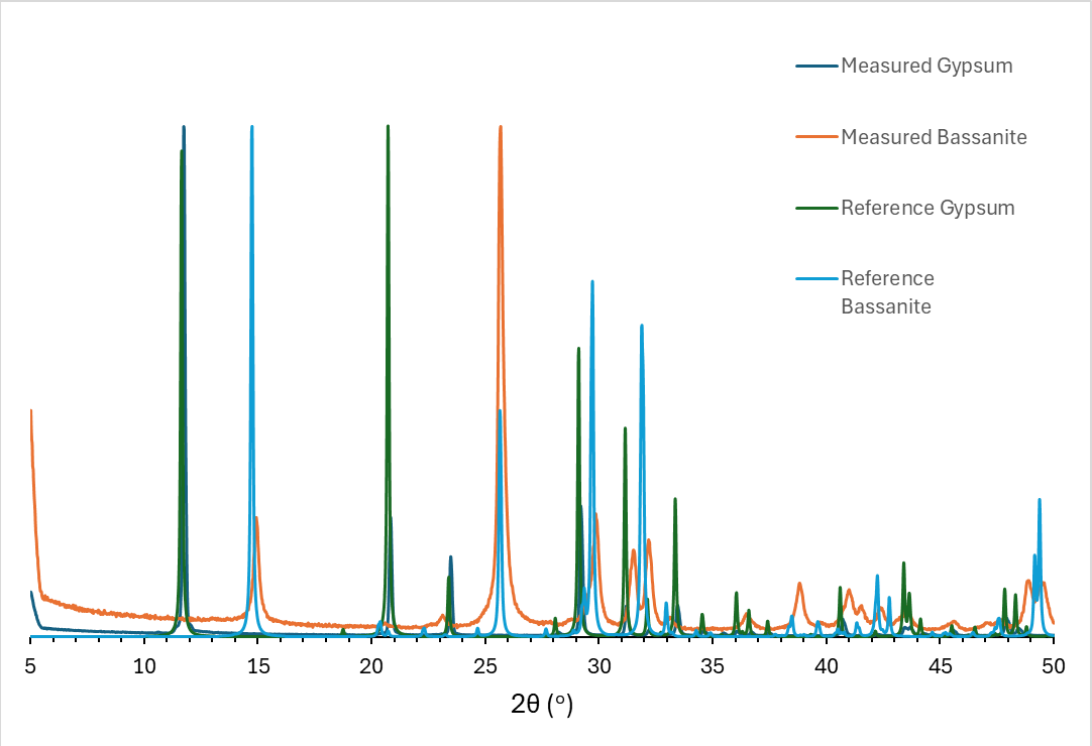

Figure 31 – Normalised off-line PXRD acquisitions of Bassanite and Gypsum for the 2θ range 5-50°, alongside reference patterns. The reference and measured patterns in each case show a good agreement.

2.3.2. Calibration of PXRD to Solids Concentration

Figure 32(a) shows a typical 1D diffraction pattern obtained from precursor concentration experiments. Four Gypsum peaks are readily seen: the (020) peak at 11.6°, the (021) peak at 20.8°, the (041) peak at 29.0°, and the (-221) peak at 31.0°. It is also noticeable that the relative sizes of these peaks, qualitatively, are similar, which is in contrast to typical off-line PXRD acquisitions of Gypsum. This is to be expected, as taking acquisitions in the flow-cell removes the limitation of preferential orientation on the disc following deposition of the power for an off-line experiment. A

significant background scattering can be observed, which can be removed through the use of background correction (asymmetric least squares, performed using OriginPro 2022 software [240]). The pattern obtained following background correction is shown in Figure 32(b), alongside the labelled peaks.

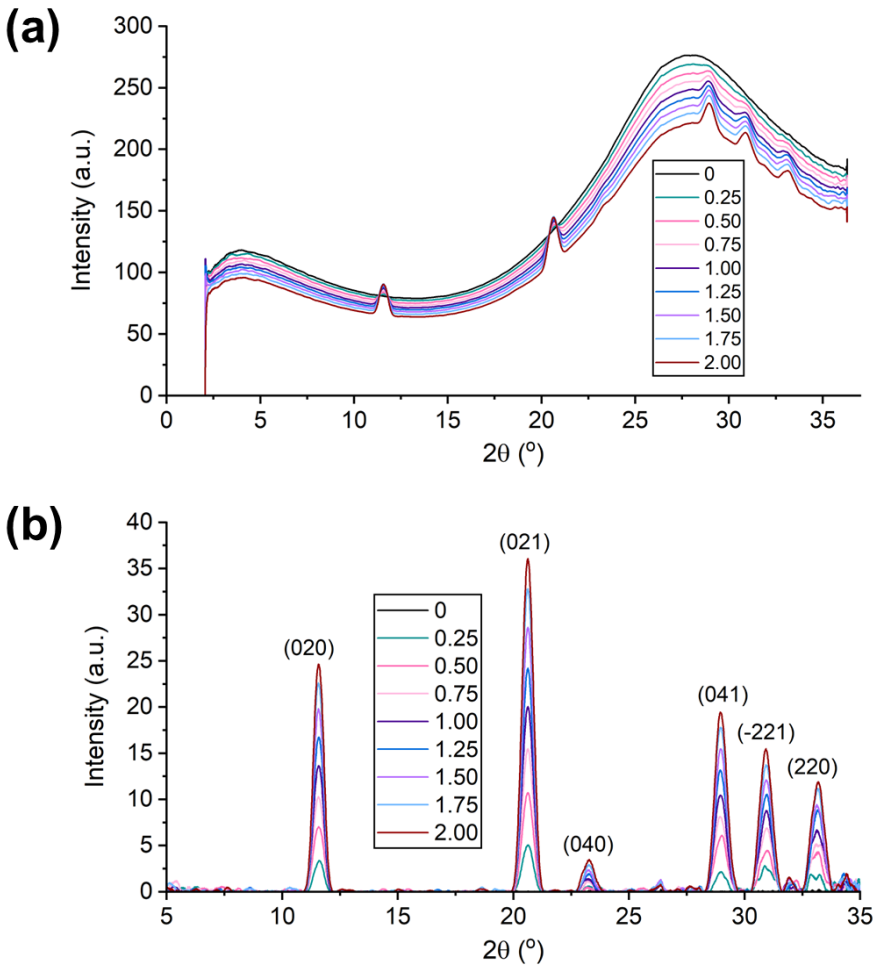

Figure 32 – (a) In Situ PXRD patterns obtained for different percentage weight fractions (shown as different coloured lines) of Gypsum during the calibration experiments. (b) Baseline correction of the data to remove the scattering from the solution phase and isolate six peaks associated with Gypsum: (020), (021), (040), (041), (-221), and (220).

Figure 33 (a) shows the results of the calibration experiment with Gypsum on the baseline-corrected (0 2 0) reflection of Gypsum present at 2θ = 11.6°. No signal was obtained at 0 weight percentage (as expected), and a small amount of signal was obtained at the lowest weight percentage studied (0.25 wt.%). Upon integration of the remaining peaks, a strong linear relationship (slope, 7.15; adjusted R^2 = 0.994; intercept forced through the origin) between (0 2 0) peak area and mass fraction of $CaSO_4$ solid was obtained, as shown in Figure 33(b)).

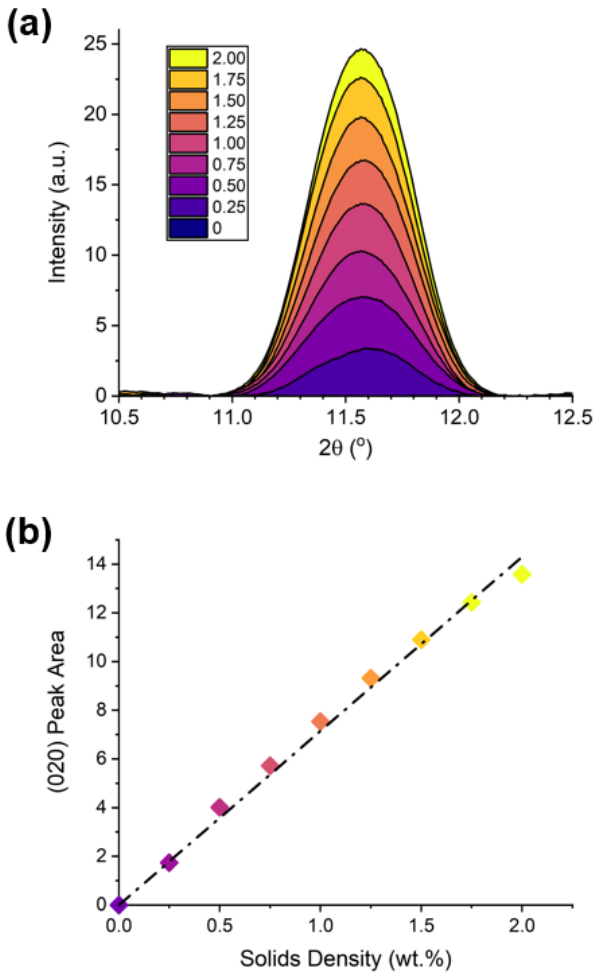

Figure 33 - (a) Baseline-corrected (020) peak of Gypsum for different added mass fractions during calibration experiments. (b) Integrated peak area of (020) peak of Gypsum across different mass fractions, with linear fit applied.

Such a linear fit was also found for the (1 0 1) peak of Bassanite (R^2 = 0.999), albeit with a different gradient (also shown in Figure 34). A key observation is the strong fit of the data to linear relationships for both reflections. This is a similar result to previous reports of the relationship between integrated peak area and mass fraction during in situ PXRD acquisitions. The relative sizes of the peaks are different – for any given mass fraction, the integrated area of the (101) Bassanite peak is higher than the (020) Gypsum peak. In both cases, the intercept was forced through the origin.

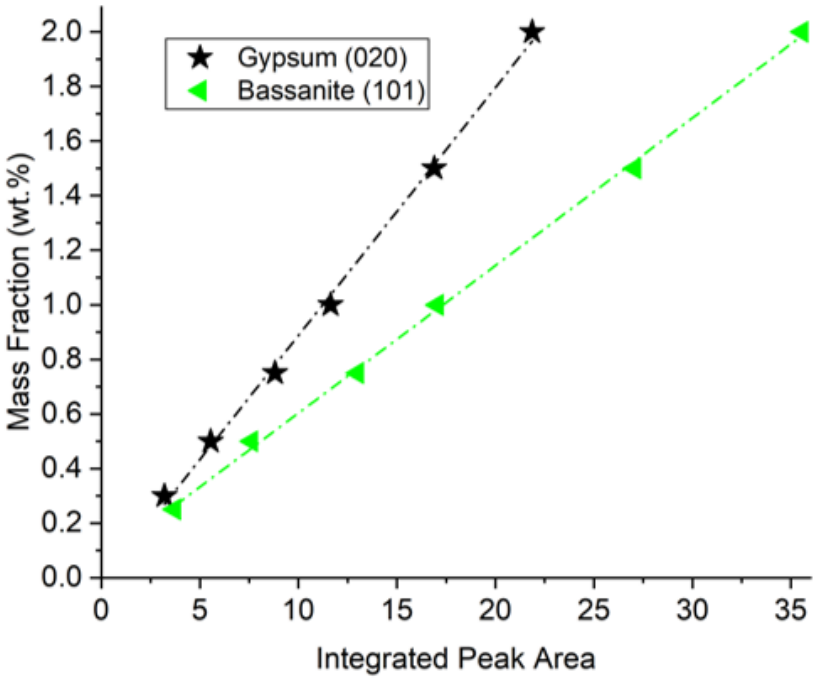

Figure 34 – Mass fraction calibrated against integrated peak area for the Gypsum (020) peak and Bassanite (101) peak.

2.3.3. Aqueous Reactive Crystallisations of $CaSO_4$

Varying Precursor Concentration

Error! Reference source not found. shows a waterfall plot of the PXRD data obtained for the experiment at 100mM $CaSO_4$ and 200mM Mg^{2+}. For this experiment and for all other repeats at different precursor and additive concentrations, only peaks associated with Gypsum were observed, with no peaks associated with Bassanite or any other form of $CaSO_4$ observed. This is in contrast to previous reports of a Bassanite precursor using synchrotron radiation [171]. This could be a result of the lower signal to noise with the laboratory-based source and detector.

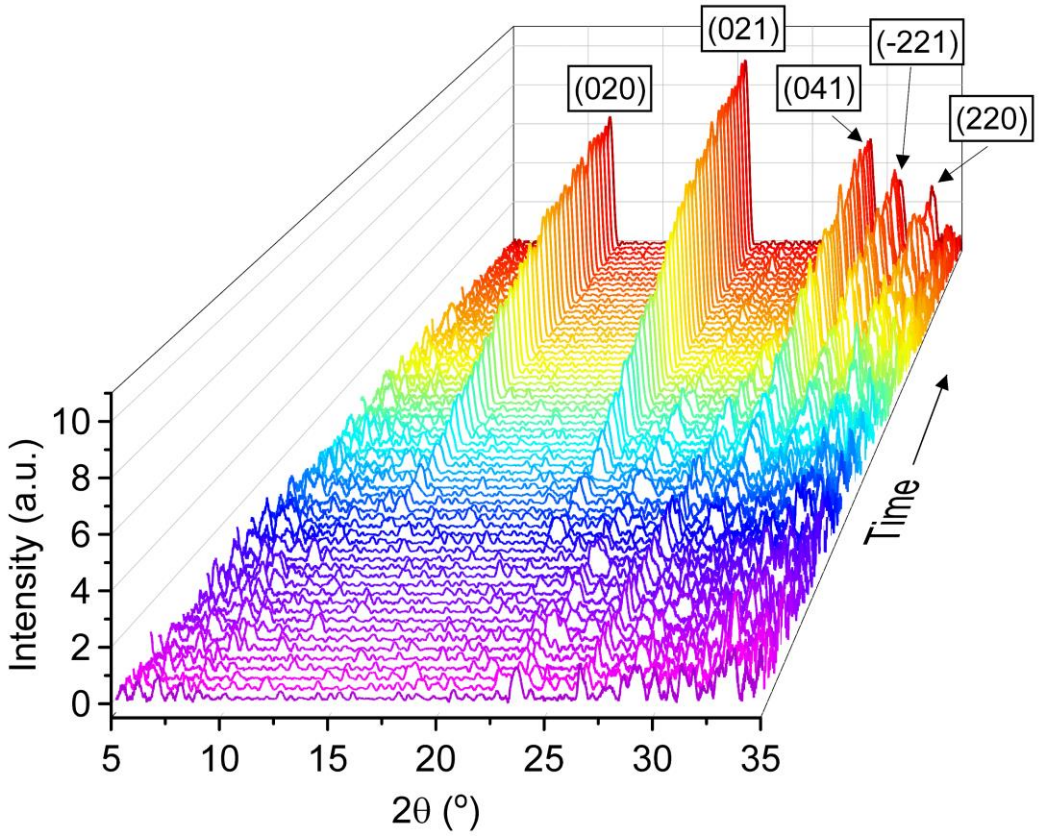

Figure 35 - Waterfall plot of PXRD acquisitions during the crystallisation of CaSO4 (what concentration) with 200 mM Mg2+. Only peaks associated with Gypsum are observed: (020) @ 11.6°, (021) @ 20.8°, (041) @ 29.0°, (-221) @ 31.2°, and (220) @ 33.4°.

Figure 36 (a)-(c) shows the time-evolved diffraction patterns in the 2θ range 11-12.5° – the location of the (020) peak of Gypsum – from the first repeat (N = 1) of 3 experiments wherein the concentration of precursors was varied. Initially, the intensity was relatively constant, with only the background scattering primarily from the solution present. Once sufficient crystallisation had occurred, the peak began to be visible over the background scattering. After some time, the size of the peak was found to have reached an equilibrium between acquisitions, wherein it was assumed that crystallisation had concluded. To estimate the extent of crystal growth, equation 28 was applied to the data, where the area of the (020) peak is calculated in the same manner as described for the calibration experiment, and where the final area was determined as the value at which no significant change in area occurred. This is valid due to the linear relationship reported for the previous calibration experiment.

$$Conversion, X_{g,G} = \frac{Area\ (020)}{Area\ (020)_{final}} \qquad 28$$

Time-evolved values of $X_{g,G}$ for the three repeats of each of the three precursor concentrations studied are shown in Figure 36(d)-(f). Conversion is seen to increase over time for each of the conditions, indicative of the growth of Gypsum. There is a variance in the induction time between both repeats of a single condition and between the conditions, as indicated by the time taken for the (020) peak to be first observed over the background. This is demonstrative of the inherent stochasticity of crystal nucleation, wherein induction times can vary between repeats of the same crystallisation process [241]. Induction times were, on average, noticeably shorter at higher concentrations (up to 10 minutes for the 75mM case but a maximum of 2 mins for the 125mM case). This is to be expected, as the higher supersaturations at higher concentrations provide a higher probability of nucleation occurring by a given time point.

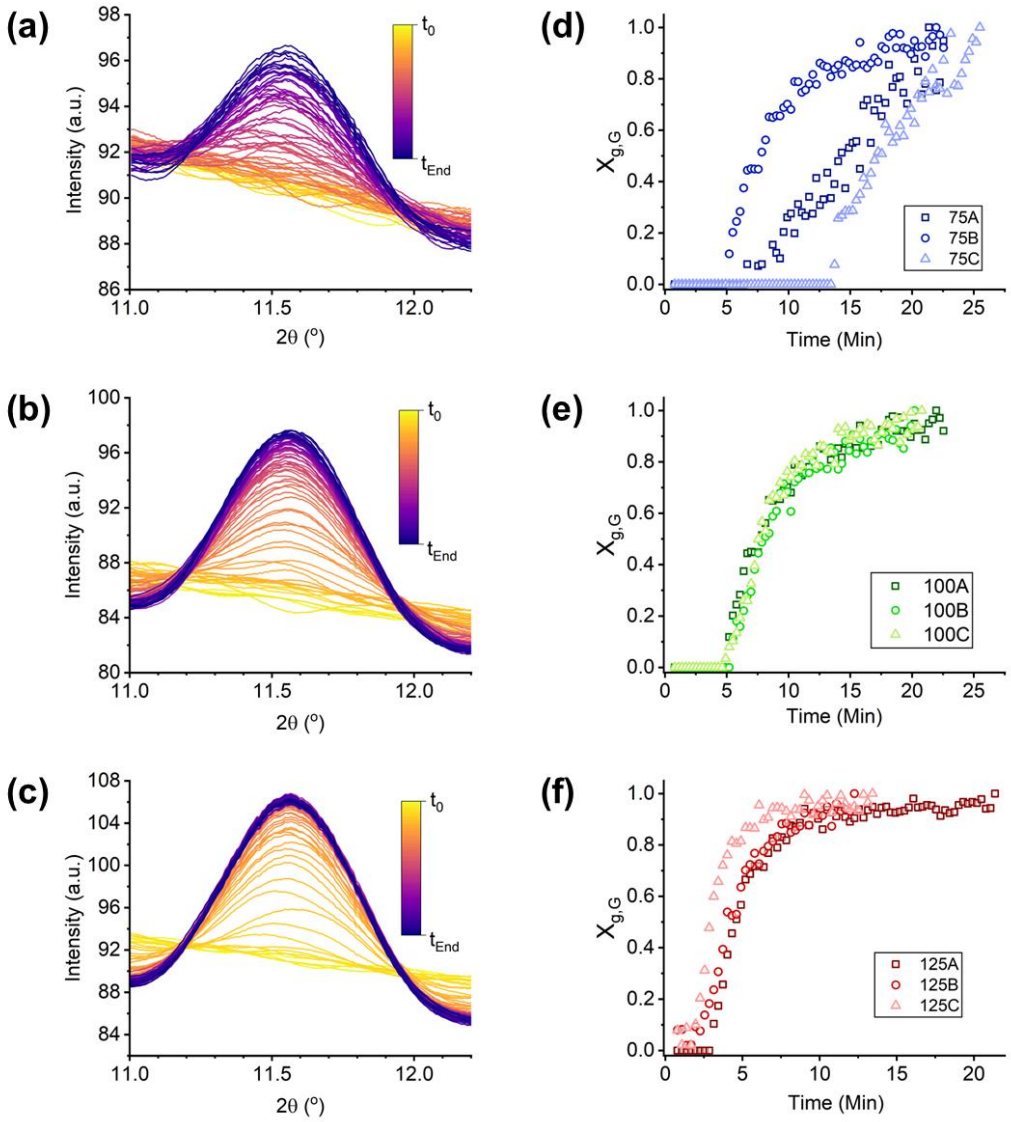

Figure 36 – Growth of Gypsum across three different precursor concentrations as monitored by in situ PXRD. The diffraction intensity over time (for the first of three repeats) is shown for the range 11-12.4° (where the (020) peak is located) for precursor concentrations of (a) 75mM (b) 100mM (c) 125mM. The resultant conversion values are shown in (d)-(f) for three repeats (A-C, with the A values being those corresponding to the diffraction patterns shown).

The integral-form first-order relationship for growth rate ($K_{G,g}$) is shown in equation 29 considering the conversion, $X_{g,G}$, over time, t (where t is relative to the induction time). Figure 37 shows first-order fits (dashed lines) to the three precursor concentration values (a) 75mM (b) 100mM and (c) 125mM. In fitting the data, only the region between $0.1 < X_{G,g} < 0.9$ was considered. At values below 0.1, nucleation is the dominant process, and as such the growth rate will not be consistent as the available nuclei on which growth can occur is not constant. At values above 0.9, the experimental error is relatively higher, as there is a fluctuation in the measured area

due to small inconsistencies in the density of slurry being pumped through the flow-cell.

$$K_{g,G}t = -Ln(1 - X_{g,G}) \quad (29)$$

Figure 37*Figure 37* (d) shows the variation in $K_{g,G}$ with relative supersaturation (S-1). Values of S-1 were calculated for the three values of concentration used in the experiments using Visual MINTEQ software. A polynomial relationship was fitted to the data, as given in equation 30. This allowed for values of $K_{g,G}$ to be predicted for intermediate supersaturations.

$$K_{g,G} = 0.43316 - 0.11114(S-1) + 0.01147(S-1)^2 \quad (30)$$

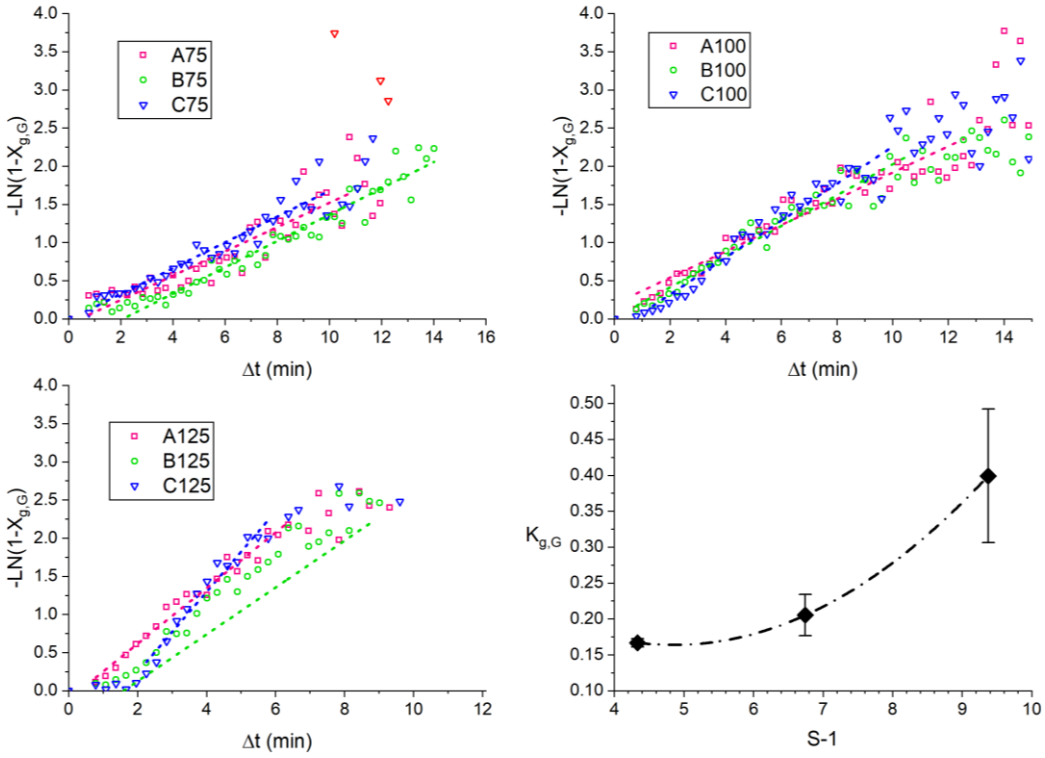

Figure 37 – First-order growth rate fits to the concentration variation experiment data: (a) 75mM (b) 100mM (c) 125mM. Dashed lines for each indicate a linear fit between 0.1 < X_g < 0.9. (d) Obtained values of $K_{G,g}$ plotted for the three concentrations, with error bars representing a standard deviation calculated from the three repeats. A second-order polynomial fit has been applied to the data.

Table 3 shows the fitted first-order growth rate parameters ($K_{g,G}$) for the different experiments, as well as averages from the three repeats, standard deviations (S.D.), and R^2 values. The mean value of $K_{g,G}$ increases across the concentrations. This corresponds to an increase in supersaturation due to the higher rate of reaction at

higher concentrations, which in turn leads to an increase in crystal growth rate. Values of R^2 are generally high, indicating a consistently good fit of the obtained data to the second-order relationship. Better fits were obtained for the higher concentration values. This could be due to a higher overall signal from the higher mass of crystals that were precipitated at higher concentrations, resulting in a lower relative experimental error.

Table 3 - First-order parameter estimates for the three repeats of the three concentrations, showing values of $K_{g,G}$ and R^2, as well as standard deviations (S.D.).

Exp.	$K_{G,g}$	Average	S.D.	R^2	R^2 Average
75A	0.159	0.167	0.0057	0.799	0.879
75B	0.172			0.940	
75C	0.169			0.898	
100A	0.172	0.218	0.0144	0.895	0.929
100B	0.201			0.927	
100C	0.242			0.915	
125A	0.307	0.399	0.093	0.956	0.960
125B	0.365			0.975	
125C	0.526			0.949	

Second order relationships have commonly been fitted to model Gypsum growth rates [200]. An integral-form second-order relationship for growth rate ($K_{G,g}.t$) is shown in equation 31 considering the conversion, $X_{G,g}$, over time, t (where t is relative to the induction time). Figure 38 shows second-order fits (dashed lines) to the three precursor concentration (a) 75mM (b) 100mM and (c) 125mM for the range $0.1 < X_g < 0.9$.

$$K_{g.G}t = (1 - X_{g.G})^{-1} \quad 31$$

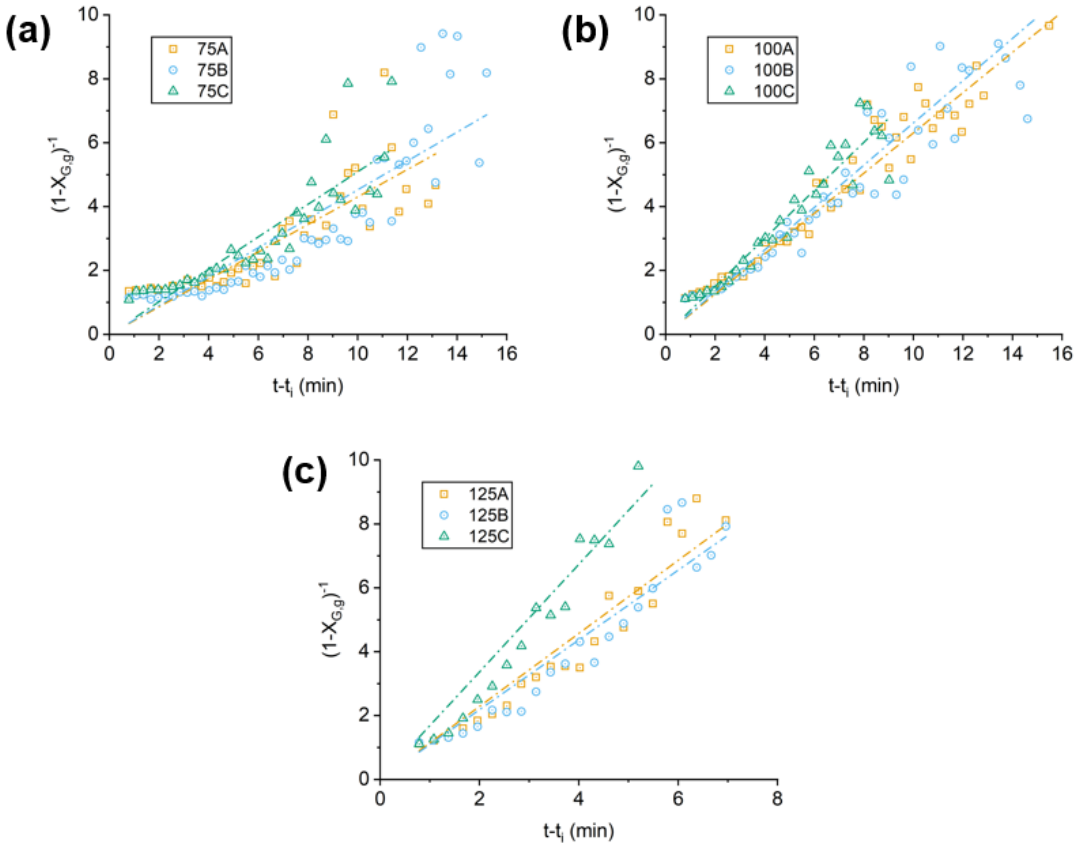

Figure 38 – Second-order growth rate fits to the concentration variation experiment data: (a) 75mM (b) 100mM (c) 125mM. Dashed lines for each indicate a linear fit between 0.1 < X_g < 0.9.

Table 4 shows the obtained values of $K_{G,g}$ and R^2 values for each fit for each experiment, as well as the averaged $K_{G,g}$ and standard deviation for each concentration value. The R^2 values are consistently lower than the equivalent first-order fits, indicating that the first-order relationship better approximates the data. Although previous experiments have indicated a second order relationship for growth rate, these were carried out at comparatively lower supersaturation and under less vigorous stirring [215]. It can be assumed that the reaction vessel is well-mixed, and with the high supersaturation presence the growth process may be limited by the surface absorption of solute onto the crystal surface [30, 242]. This results in a first-order mechanism of crystal growth [243].

Table 4 – Values of second-order growth rate parameters $K_{G,g}$ and the associated R^2 values for the three different concentrations across three repeats. The mean value of $K_{G,g}$ and the calculated standard deviation is also shown.

Exp	$K_{g,G}$	R^2	Average $K_{g,G}$	Standard Deviation	Average R^2
75A	0.3866	0.7576	0.4455	0.0431	0.7358
75B	0.4612	0.6584			
75C	0.4886	0.7914			
100A	0.7359	0.8925	0.6587	0.0646	0.8883
100B	0.5778	0.9254			
100C	0.6625	0.8470			
125A	1.9664	0.9645	1.4955	0.3339	0.9323
125B	1.2897	0.9292			
125C	1.2303	0.9033			

Varying Additive Concentration

Throughout all the crystallisations in the presence of Mg^{2+}, only Gypsum was identified, with no other phases indicated. Although this does contradict previous reports of Mg^{2+} being able to stabilise Bassanite [233], these experiments were performed with a slightly higher concentration of additive. Furthermore, the signal to noise of the instrument precludes the analysis of the earliest stages of nucleation. However, this earlier study made use of ethanol to quench the reaction, which lends evidence to the ethanol being responsible for the acquisition of Basssanite as opposed to the Mg^{2+} ions.

Shown in Figure 39 are first order plots of the growth rate of $CaSO_4.2H_2O$ under different concentrations of Mg^{2+} additives for three repeats. Linear fits have been applied to the data and the values of the obtained growth rate parameter $K_{G,g}$ and R^2 values for the first order fits are shown in Table 5. A reduction in $K_{G,g}$ values can be observed with an increase in Mg^{2+} concentration, and a change in induction times can also be observed across the Mg^{2+} concentrations, with induction time generally increasing at higher additive concentrations. Within a classical nucleation theory (CNT) framework, this could indicate that Mg^{2+} ions are reducing the likelihood of formation of a nucleus of sufficient size such that growth is favoured. With respect to non-classical Gypsum formation mechanisms previously discussed, the Mg^{2+} ions could be impacting any of the multiple steps of Bassanite nanoparticle formation, aggregation, and solid-state transformation to Gypsum. However, owing to the low signal-to-noise relative to synchrotron sources, Bassanite was not observed during these experiments, and evidence of nucleation mechanisms was thus not available.

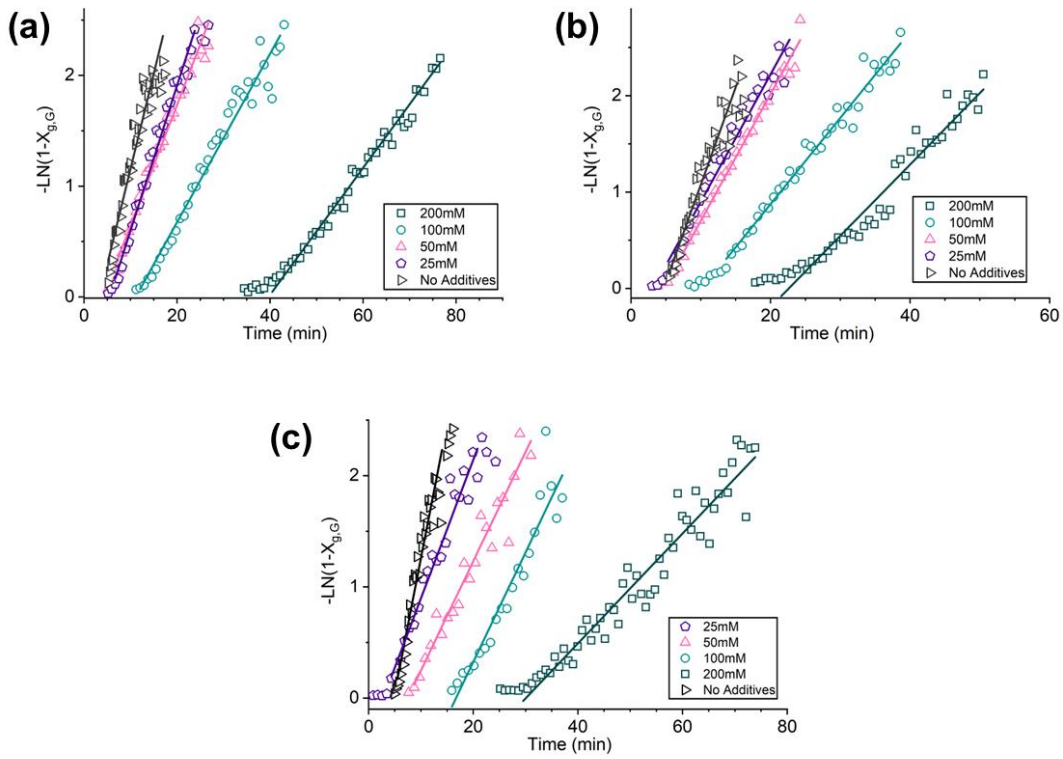

Figure 39 – First-order growth rates of CaSO4 under different concentrations of Mg2+ additives. (a) Repeat 1 (b) repeat 2 (c) repeat 3.

Table 5 – Values of $K_{g,G}$ and R^2 for the first-order fits applied to the three repeats of the experiments at different Mg^{2+} additive concentrations.

Mg^{2+} Conc. (mM)	200	100	50	25	0
$K_{g,G}$ Repeat 1	0.05733	0.07603	0.10941	0.13079	0.263
R^2	0.97212	0.96317	0.97607	0.98282	0.89543
$K_{g,G}$ Repeat 2	0.075	0.0891	0.1263	0.1321	0.2322
R^2	0.95193	0.97428	0.99052	0.96457	0.92957
$K_{g,G}$ Repeat 3	0.04945	0.09861	0.09826	0.12457	0.24209
R^2	0.93584	0.90312	0.93231	0.94934	0.91536
Average $K_{g,G}$	0.0606	0.0879	0.1113	0.1292	0.2458
Standard Deviation	0.0107	0.0093	0.0115	0.0033	0.0128

Visual MINTEQ software was used to calculate saturation indexes (SI) for $CaSO_4$ across the experimental range of Mg^{2+} concentrations used and at a fixed concentration of $CaSO_4$ of 100mM. The results are shown in Table 7, alongside values of supersaturation ($S = 10^{SI}$) and relative supersaturation (S-1). There is a clear decrease in supersaturation as Mg^{2+} concentration increases. This general

relationship matches well with experimental data from the literature, where solubility of $CaSO_4$ was observed to increase with increasing Mg^{2+} concentration [244].

Table 6 – Saturation index (SI), supersaturation (S), and relative supersaturation (S-1) of $CaSO_4$ at 100mM across various Mg^{2+} concentrations.

Mg^{2+} Conc. (mM)	SI	S (=10^{SI})	S-1
0	0.889	7.744618	6.744618
25	0.867	7.362071	6.362071
50	0.84	6.91831	5.91831
100	0.795	6.237348	5.237348
200	0.728	5.345644	4.345644

Figure 40 (a) shows the relationship between Mg^{2+} concentration and both measured and predicted $K_{g,G}$ values, and Figure 40(b) shows the same growth rate data plotted against relative supersaturation (S-1). Predicted $K_{g,G}$ values were regressed from the previously developed 2nd order polynomial relationship between supersaturation and measured growth rate (equation 31). The experimentally measured values of growth rate for experiments in the presence of Mg^{2+} are clearly lower than the expected values based purely off of supersaturation. This provides evidence that Mg^{2+} is inhibiting crystal growth by binding to the surface of the growing crystals, blocking kinks sites and providing an additional kinetic barrier to be overcome. Qualitatively, there is a lower relative decrease in growth rate for higher concentrations of Mg^{2+} compared to lower concentrations, which can be explained by considering the relative relationship between surface area and volume for the crystals. Generally, for a given increase in volume with an increase in a characteristic linear size dimension, the resultant surface area will increase by a much larger comparative amount. This results in a requirement for a much larger amount of additives that would have to be present to block kink sites and result in the same growth rate. As such, with increasing additive concentration, there is a 'diminishing return' in the ability of the additive to reduce the growth rate.

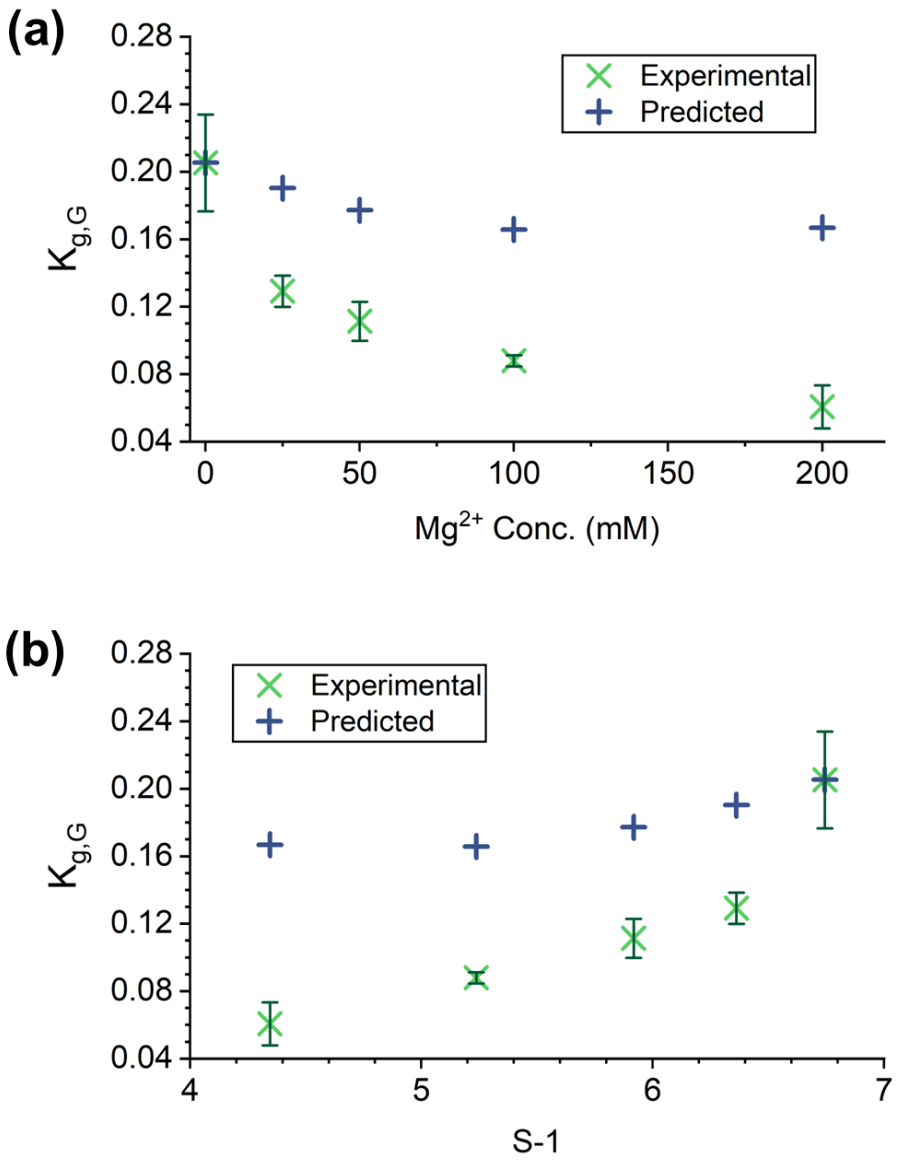

Figure 40 - Comparison of Magnesium concentration with both experimentally measured and predicted growth rate. (a) On a basis of Mg2+ concentration (b) On a basis of relative supersaturation (S-1). The error bars represent standard deviations as calculated from three repeats.

It is well known that the use of additives in crystallisations can result in a change in morphology, which in turn could change the relative sizes of the diffraction peaks for a given mass of crystals. As such, confirmation is required that the relative sizes of the observed diffraction peaks are not changing across the Mg^{2+} concentration. Figure 41 shows the ratio in area of four different observed peaks associated with Gypsum relative to the size of the (0 2 0) peak across the different Mg^{2+} content at the end of the experiment. There are no major, systematic deviations in the relative sizes across Mg^{2+} concentration. The inset table gives the corresponding mean values, standard deviations, and percentage errors. This confirms the validity of using a single peak as

a proxy for solids mass during *in situ* studies across the Mg^{2+} concentrations. Figure 42 shows SEM images of the crystals obtained from the experiments across the different Mg^{2+} additive concentrations. Again, this confirms that there is no major change in morphology. In line with previous reports, there is a slight rounding of the capping faces of Gypsum (at the short end of the rods) with increasing Mg^{2+} concentration [237].

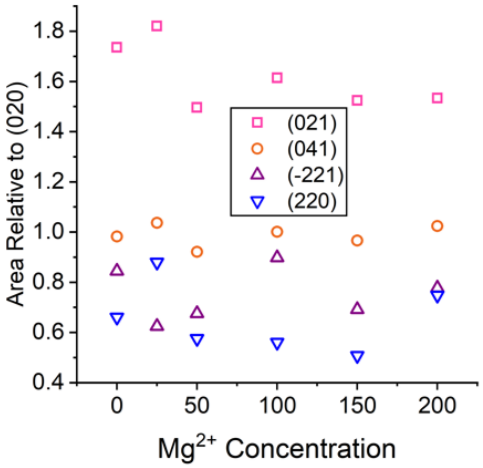

Peak	Mean	S.D.	% Error
(021)	1.581	0.087	5.50%
(041)	0.979	0.035	3.54%
(-221)	0.778	0.086	11.02%
(220)	0.610	0.084	13.84%

Figure 41 – Relative sizes of four peaks associated with Gypsum to the (020) peak from the final acquired frame across Mg^{2+} concentration. The inset table gives mean values of relative sizes, alongside standard deviation (S.D.) and percentage error. The relative sizes do not change significantly, indicating an insignificant change in morphology.

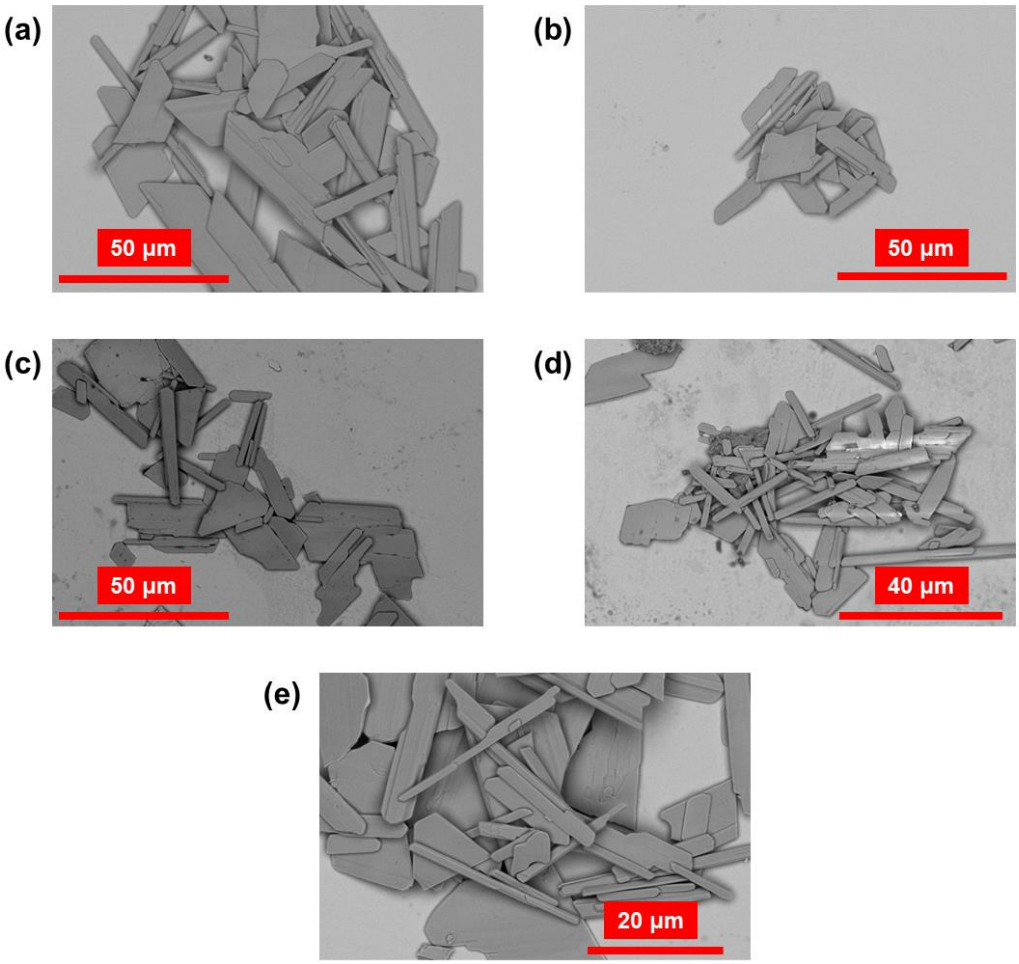

Figure 42 - SEM images of Gypsum crystals following crystallisation under different concentrations of Mg^{2+}: (a) No Mg^{2+} (b) 25mM (c) 50mM (d) 100mM (e) 200mM.

2.3.4. Ethanolic Reactive Crystallisations of $CaSO_4$

Varying Ethanol Volume Fraction

Visually, upon the addition of the second precursor solution, rapid instantaneous nucleation was observed, with the solution immediately turning a cloudy white. This contrasted with the aqueous-only experiments where an induction time of between 30s to several minutes was observed. Because of the need to start the peristaltic pump and seal the PXRD enclosure door, the first frame was only observed with an average time-point of 39s, and there was a dead-time of approximately 20s before data was acquired. Figure 43(a)-(c) shows the time-resolved diffraction patterns obtained for the three different ethanol fractions studied ((a) 40 vol.%, (b) 50 vol.%, (c) 60 vol.%). Across all three experiments, the (101) peak is present in the initial frame either dominantly or exclusively. A transformation then occurs to Gypsum, as

shown by the reduction in the size of the (101) peak and an increase in the size of the (020) peak. In the case of 40 and 50 vol.% ethanol, where the (020) peak of Gypsum is present in the first frame (albeit at a low intensity), it is unclear whether Gypsum nucleates concomitantly with Bassanite or if this is a result of transformation from Bassanite to Gypsum occurring in the 20s deadtime before the acquisition. The case of 60 vol.% does suggest the latter case, as Gypsum is not observed until several minutes have passed.

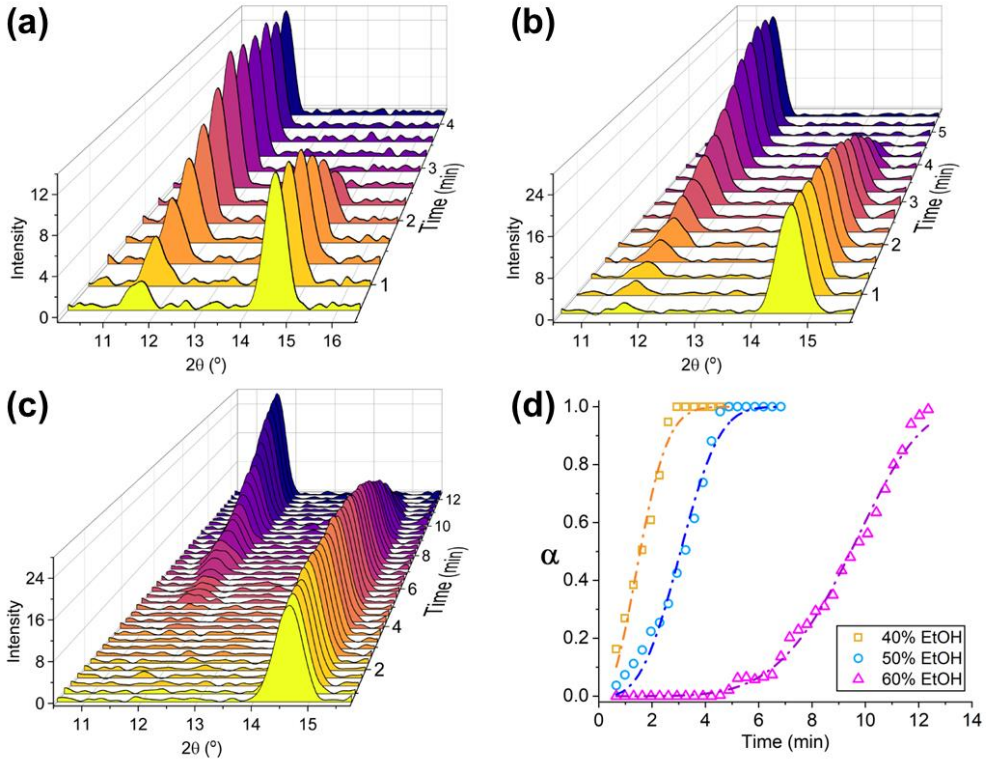

Figure 43 - CaSO4 crystallisations in varying ethanol volume fractions, as monitored using in situ PXRD. (a) Diffraction patterns from the 40 vol.% case (b) 50 vol.% (c) 60 vol.%. (d) Calculations of degree of conversion to Gypsum (α) over time, with fits to the Avrami relationship shown by the dashed lines [222].

To quantify the amount of each phase present at a given time-point, the calibration relationship previously developed (Figure 34) was employed to find the predicted mass of Gypsum present at a given time point. This was then divided by the total mass (of Gypsum and Bassanite) to give the fractional conversion, α. This is shown in equation 32. The Avrami model is commonly used to model phase transformations, including for the transformation of Bassanite to Gypsum [204, 222]. Equation 33 is the Avrami relationship adapted for use with α, where k and n are parameters to be fitted, and t is time in minutes. This relationship was fitted to the values of α for the three different ethanol volume fractions, as shown in figure Figure 43(d).

$$\alpha = \frac{Predicted\ Mass\ Gypsum}{Predicted\ Mass\ Gypsum + Bassanite} \quad (32)$$

$$\alpha = 1 - EXP(-kt^n) \quad (33)$$

Clearly, higher ethanol fractions result in both a higher stability of the Bassanite phase, as well as slower kinetics of conversion of the stable Gypsum phase. This is particularly noticeable for the case of 60 vol.%, where bassanite is exclusively observed until over 4 minutes have elapsed. The Avrami relationship showed an excellent fit to the data, with fitted values of the parameters k and n given in Table 7, alongside R^2 data. These show an excellent statistical fit to the data, as indicated by high R^2 values. The higher degree of stability of Bassanite in higher ethanol fractions is most likely caused by a reduction in solubility at higher ethanol fractions [245], meaning there is a kinetic barrier to the dissolution of the metastable phase.

Table 7 – Parameter values for k and n for the Avrami fits of the phase transformation data for different ethanol volume fractions. R^2 values are also shown.

Ethanol Vol. %	k	n	R^2
40	0.2655	2.18	0.999
50	0.02238	3.06	0.999
60	7.06E-06	5.12	0.993

Varying Mg^{2+} concentration

Figure 44 shows the conversion (α) results obtained for different Mg^{2+} concentrations at a fixed value of $CaSO_4$ concentration (100mM) and ethanol content 50 vol.%. Qualitatively, the transformation to Bassanite appears to be delayed with an increasing concentration of Mg^{2+} additive. This holds true for all values except between 75 and 100mM Mg^{2+}, wherein the transformation is similar, but the 75mM is slightly delayed. This most likely represents an inherent stochasticity in the transformation times, and multiple repeats of the same experiments would most likely show that, on average, the 100mM case is delayed relative to the 75mM case. In the case without additives, the transformation begins on the second frame just after 1 minute, where a small amount of Gypsum is present. In contrast, the transformation begins after approximately 3 minutes for the highest additive concentration of 250mM. For all the cases, the solution turned a cloudy white immediately after combination of the two precursor solutions, indicating rapid nucleation of the Bassanite form. The

use of increasing Mg^{2+} additive did not have an effect on the observed Bassanite nucleation rate, which was rapid and immediate for all concentrations. An Avrami fit was applied to each of the datasets, as indicated by the dashed lines in Figure 44. This showed a good fit to the datapoints, although a small deviation was observed at the highest and lowest values of α. This is most likely down to the relatively large error associated with the measurement of the smallest Gypsum or Bassanite peaks. Parameters of the Avrami fits as well as R^2 values are shown in Table 8.

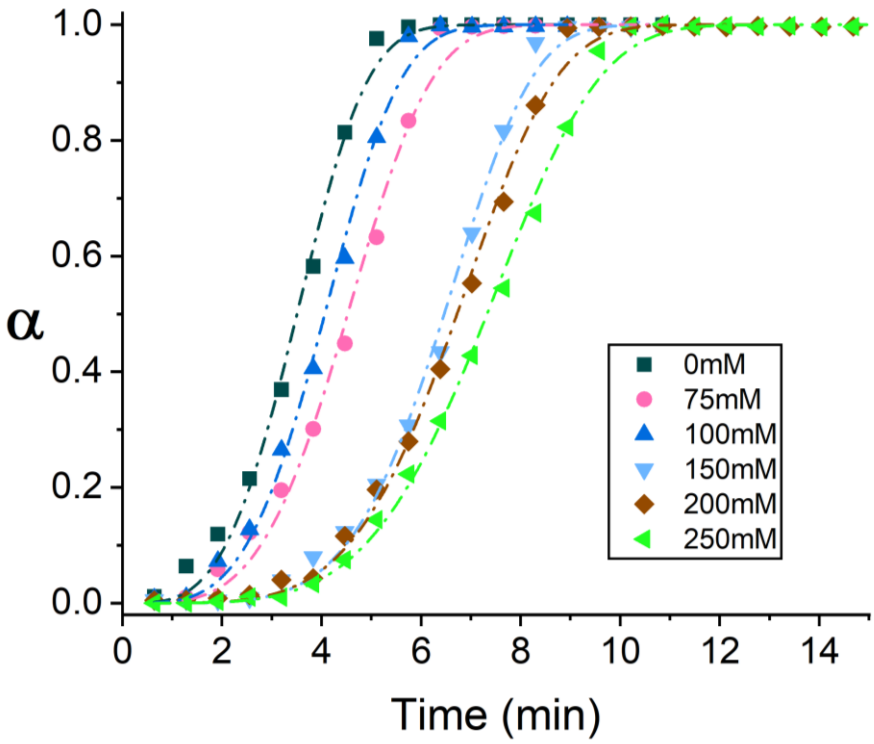

Figure 44 - Values of conversion (α) from Bassanite to Gypsum across Mg2+ concentrations for a fixed ethanol fraction of 50 vol.% and a fixed CaSO4 concentration of 100mM.

Table 8 – Parameters for Avrami fits for the Bassanite to Gypsum transformation data across Mg^{2+} additive concentrations. R^2 values are also shown.

Mg^{2+} Concentration	k	n	R^2
0	0.00785	3.572	0.997
75	0.00207	3.850	0.995
100	0.00328	3.81851	0.997
150	4.82912E-5	5.12937	0.997
200	7.96417E-5	4.76128	0.998
250	7.48386E-5	4.58751	0.998

To gain an insight into the exact mechanism of the transformation, the total mass of solids present can be calculated throughout the transformation, as is plotted in Figure 45. For all the experiments, there is a non-equilibrium solids density during the transformation, with the overall trend of an increasing amount of solids as the transformation progresses. This makes sense within the framework of a classical dissolution – reprecipitation process, as the higher solubility of metastable Bassanite results in a lower yield from solution compared to the eventual yield of Gypsum. There is a slight decrease in the yield of Gypsum following the completion of the transformation, which can be explained by a decrease in the pumping efficiency of the peristaltic pump at high solids densities as material may begin to settle in the pump tubing.

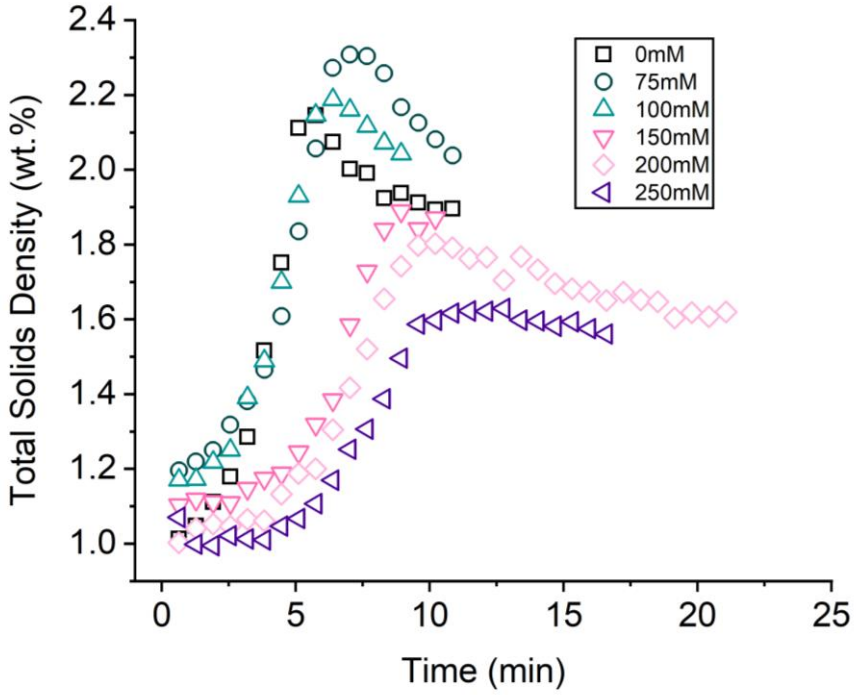

Figure 45 - Total solids density (Bassanite + Gypsum) for the experiments under mixed (50 vol.%) ethanol / aqueous solvent environment and varying concentrations of Mg2+ (shown in the legend). Solids density varies over time, indicative of a dissolution-reprecipitation process.

The variation in the individual sizes of the Bassanite (101) and Gypsum (020) peaks were also considered, in order to quantitatively describe the relative masses of each hydrate at different points in the reaction. The variation in the conversion ($X_{d,B}$ – equation 34) of Bassanite over time for each concentration of Mg^{2+} is presented in Figure 46, with a linear fit indicating zero-order dissolution kinetics (equation 35, $0.1 < X_{d,B} < 0.9$). Parameter values associated with the fits are given in the inset table. A

reasonable fit to the relationship is indicated by the high R^2 values. Qualitatively, there is a longer time period for which Bassanite is stable at higher concentrations of Mg^{2+} additive. This presents an additional kinetic barrier, as Mg^{2+} molecules have to be re-solvated having adsorbed to the surface of the Bassanite crystal before solvation of the Bassanite can proceed. The increase in the gradient of the slope across Mg^{2+} concentrations is indicative of a decrease in dissolution rate as Mg^{2+} concentration increases.

$$X_{d,B} = \frac{Area\ (101)}{Area\ (101)_{intial}} \quad 34$$

$$X_{d,B} = -kt \quad 35$$

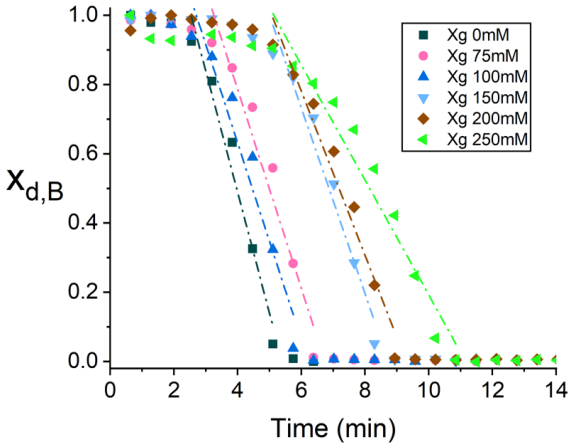

Mg^{2+} Conc. (mM)	Intercept	Slope	R^2
0	1.88833	-0.3498	0.958
75	1.93441	-0.28723	0.93405
100	1.76836	-0.28429	0.92682
150	2.33938	-0.26791	0.95329
200	2.20108	-0.23679	0.95811
250	1.8525	-0.16605	0.94935

Figure 46 – Variation of dissolution conversion of Bassanite, $X_{d,B}$, over time. Zero-order fits are shown by the dashed lines, with parameters of the fits given in the inset table.

Figure 47 (a) shows the variation in the conversion of Gypsum ($X_{g,G}$) over time for the different concentrations of Mg^{2+}. An attempt was made to fit these to a first-order growth rate, as shown in Figure 47(b) by the dashed lines (on a plot corresponding to equation 35). The data showed a poorer fit to the first-order growth relationship compared to the purely aqueous case. This is indicated both visually and by the R_2 values shown in Table 9 (alongside values of $K_{g,G}$). This could be a result of a fluctuating supply of ions from the dissolution of the bassanite, compounded by the effect of the Mg^{2+} on the nucleation of new Gypsum crystals. At low values of $X_{g,G}$, there is a distinct non-linearity, where this relationship with time corresponds well (qualitatively) with the equivalent time points for the dissolution of Bassanite. This shows that the transformation is likely limited by the dissolution of the Bassanite

phase. A reduction in values of $K_{g,G}$ is observed with increasing additive concentration. This is indicative of the Mg^{2+} ions binding to the growing surface of the crystal, and providing an additional barrier to growth.

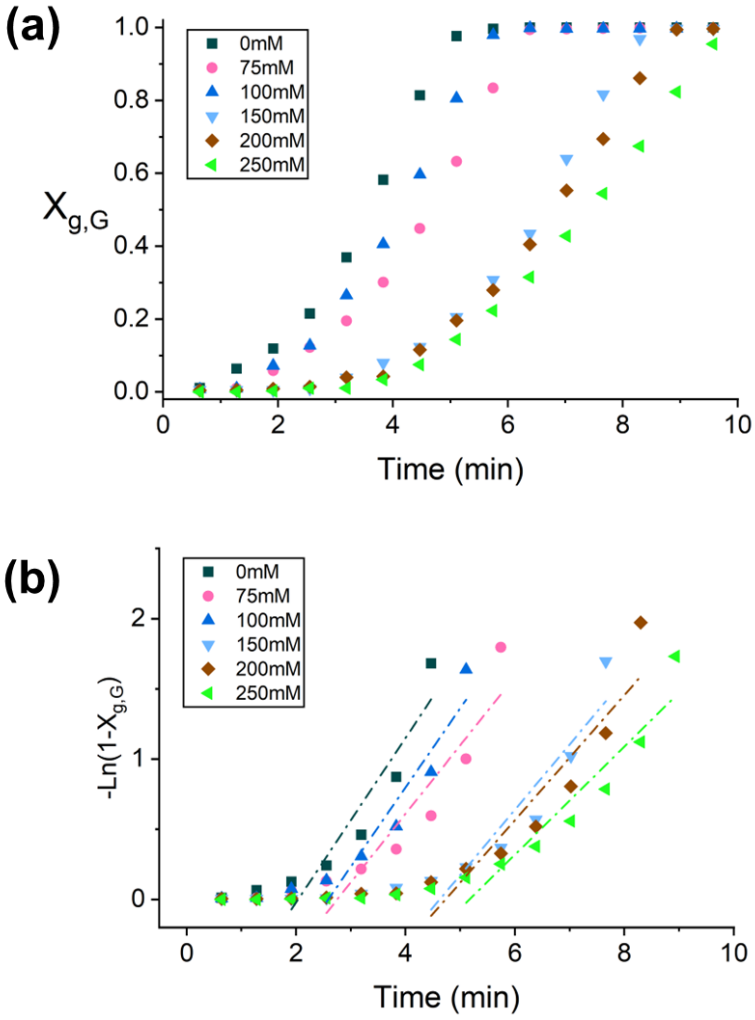

Figure 47 - (a) Conversion of Gypsum (b) First-order growth rate.

Table 9 – First-order growth rate parameters ($K_{g,G}$) and R^2 values for the growth of Gypsum following conversion from Bassanite in a mixed ethanol / aqueous solution with different concentrations of Mg^{2+} additive.

Mg^{2+} Concentration	$K_{g,G}$	R^2
0	0.58591	0.84278
75	0.48855	0.82753
100	0.56426	0.88012
150	0.46532	0.84632
200	0.44540	0.84697
250	0.38468	0.88413

2.4. Discussion and Significance

2.4.1. Monitoring Growth Kinetics

In relating the intensity of diffraction to the amount of material present in the sample, the previously reported linear relationship between peak area and solids content was observed. However, this instrument enables much lower (an order of magnitude) mass fractions to be detected than previous reports [194, 195]. This enables a wider range of experimental conditions to be monitored. Furthermore, the acquisition times for this instrument are much lower than the same previous reports (up to one frame every ~20s), enabling greater time resolution in batch crystallisations. This allows for a high degree of accuracy in measuring fast-growing crystals *in situ*. Fewer diffraction reflections were observed compared with a typical off-line PXRD acquisition of either $CaSO_4$ phase. Four diffraction peaks were easily observed even at low solids content, with a small peak beginning to form at the highest solid content representing the (040) peak at 23.1°. Because of the typical anisotropic morphology of Gypsum, the diffractions that are observed are related to the long axis of gypsum, as opposed to the smaller capping faces. A much higher signal to noise would be required to get signal from reflections associated with relatively smaller diffraction planes.

In attempting to fit the growth rate data to kinetic models, first-order kinetics were found to fit the data better than second order kinetics. This indicated that the integration of monomers onto the growing crystal surface is the rate-limiting step as opposed to the diffusion of crystals to the crystal surface. In the presence of Mg^{2+} additives at varying concentrations, first-order kinetics were also found to accurately model the growth rates. The obtained kinetic profiles facilitated comparison of the effect of process parameters (concentration, additive profile) on the overall growth rate (on a mass basis). In the case of the effect of varying additive concentration, this allowed for a mechanistic insight to be suggested as to the means by which growth kinetics were reduced with additive concentration. The increase in induction times with additive concentration was likely a result of solution complexation, which has previously been shown to affect nucleation rates [30]. The Mg^{2+} additives were not found to induce the precipitation of Bassanite initially, as has previously been reported, demonstrating the value of accurate *in situ* characterisation of crystal structure for determining crystallisation pathways. The overall experimental apparatus has shown to be a valuable methodology for assessing the effect of process parameters on crystal growth, and as such could be used in future work to design crystallisation protocols to obtain particles of a desired size.

2.4.2. Monitoring Phase Transformations

Under a mixed ethanol and aqueous solvent environment, the precipitation of Bassanite occurs initially, before undergoing a transformation to Gypsum under all studied conditions. This can be readily monitored using the experimental apparatus. This represents the first such example of this experiment, wherein the Ca^{2+} is directly dissolved in ethanol prior to the crystallisation, rather than being combined first in an all-aqueous crystallisation [14]. This is also the first example of tracking the evolution of the hydrates present during the mixed organic / aqueous crystallisation in a time-resolved manner. It was observed that Bassanite instantaneously nucleates, before undergoing a transformation to the stable Gypsum form. This suggests that the precipitation under these conditions proceeds via an Ostwald ripening process. The increase in stability of Bassanite with increasing ethanol content suggests that the transformation is kinetically inhibited by the increasingly low solubility at higher ethanol contents. This, along with the differing kinetics of dissolution and growth rate of the Gypsum, suggests a dissolution – reprecipitation process is occurring, as opposed to a solid-state transformation. The excellent time-resolution that can be obtained with the instrumental set-up allowed for the short-lived Bassanite precursor phase to be identified, as well as the dissolution kinetics of this phase to be distinguished from the growth kinetics of the Gypsum phase. This in turn was crucial in providing a mechanistic insight into the nature of the transformation.

2.5. Conclusions

In-line PXRD has been used successfully to measure the crystal growth kinetics and phase transformation kinetics for the reactive crystallisation of CaSO4. A quantitative correlation was developed between the measured diffraction peak area and the crystalline phase content for the gypsum and bassanite crystallisation system. This allowed for the kinetics of crystal growth to be obtained, where the fitting of a first-order rate equation best described the measured growth data of the stable Gypsum phase. Under different precursor concentrations (supersaturations) growth rate kinetics showed a reduction in rate with an increase in additive (Mg2+) concentration and under the influence of an inorganic additive (Mg2+), the kinetics of growth showed the expected variations. The in-line PXRD system could also be used to monitor the evolution of the crystalline phases under a mixed ethanol / water solvent system. The kinetics of the transformation from the metastable hydrate (Bassanite) to the stable hydrate (Gypsum) could be quantified through the fitting of an Avrami function. By

examining the individual contributions of Bassanite and Gypsum to the overall diffraction pattern, a dissolution – reprecipitation process was suggested. The effect of Mg2+ additives on the transformation process was shown to slow down the dissolution of Bassanite and the growth of the Gypsum phase.

Overall, the laboratory-based in-line PXRD apparatus showed excellent utility as a methodology of rapidly obtaining kinetic information relating to reactive crystallisations. This novel set-up represents the first study of reactive crystallisation kinetics using in situ laboratory-based PXRD acquisitions of a flowing-slurry. This has been enabled by step-change improvement in time-resolution and signal-to-noise relative to previous laboratory-based XRD instruments. This apparatus partially-alleviates the need for synchrotron-sources for *in situ* studies, and allows for a rapid, detailed understanding as to the effects of reaction parameters on crystallisations. We have demonstrated how this apparatus can enable quantitative studies of crystallisations processes, leading to a furthering of our understanding of the mechanics of such phenomena. Further work could involve the extension of the types of crystallisations that can be characterised in this manner and observing amorphous to crystalline transformations.

3. Continuous Reactive Crystallisation of $CaSO_4$

3.1. Introduction

3.1.1. Background Science

Within the literature, a gap exists in the application of laboratory-based *in situ* PXRD analysis to small-scale continuous crystallisations. There have been demonstrations of the coupling of such platforms with synchrotron radiation and analysis [108, 181, 185], which has the same positives and drawbacks as previously discussed. But the use of laboratory based XRD instruments has been largely limited to batch crystallisers. This may be down to familiarity of operation of batch crystallisations, operational flexibility, industrial applicability, or the lack of requirement to consider residence time distribution (RTD). Furthermore, there may be practical issues with respect to the coupling of a continuous-flow platform with an XRD instrument. How can analysis be performed without disrupting the delicate balance of flow conditions achieved at steady-state? How can one operate a continuous crystallisation that on the one hand is small enough to be practical, and on the other provides enough material such that a sufficient signal-to-noise can be obtained?

The combination of in-line analysis techniques and continuous-flow platforms has proven to be useful for the study of homogeneous or heterogeneous chemical reactions. Analysis at a steady-state allows for acquisition time to be decoupled from reaction time, making such a combination of analysis technique and reaction platform ideal for the study of rapid processes. These techniques may allow for self-optimisation algorithms to be applied, wherein steady-state reaction conditions are autonomously changed to optimise a reaction. This has been extensively demonstrated for chemical reactions, but rarely for reactions involving solids or for crystallisations. This is a result of two issues: development of analysis techniques for *in situ* analysis of solids (specifically the coupling of X-ray diffraction techniques), and the development of a small-scale (i.e. reasonable materials usage) continuous crystallisation platform with a wide range of operation.

3.1.2. Goals and Rationale

The aim of this study is to characterise crystallisation kinetics in a continuous-flow platform with a laboratory-based X-ray diffraction device. Achieving this would confer a number of benefits. Firstly, successfully applying laboratory-based *in situ* XRD to a

continuous crystallisation platform would demonstrate how laboratory-based instruments may be able to supplement or replace experiments previously performed in a synchrotron source. Secondly, the ability to study transient crystallisation processes (such as structural transformations) with excellent time-resolution in a continuous-flow platform may allow for efficient and accurate quantitative screening of the effect of reaction parameters on crystallisation processes. Finally, the combination of in situ XRD and a continuous crystallisation platform may have future applicability to automated optimisation and control, in a similar manner to aforementioned reports for homogeneous reactions.

Firstly, a continuous crystallisation route was to be developed, with a platform selected that would facilitate well controlled crystallisations at a wide-range of experimental conditions. Specifically, it would need to be able to handle a high enough solids density that sufficient signal-to-noise could be obtained when in situ XRD characterisation was applied, as well as enable facile adaption to the XRD instrument. Previous reports have demonstrated that continuous crystallisation devices operating on the microfluidic scale may not yield sufficient signal with the laboratory-based XRD instrument as to allow for quantitively studies of crystallisation processes [144]. As such, continuous crystallisers that operate on the millifluidic scale were to be considered, which strike a balance between sufficient solids material as to allow for a reasonable signal-to-noise, without excessive material usage and space requirements. Secondly, adaptions were to be made to the continuous crystallisation device to allow for in-line XRD analysis to be applied at different points along the device, allowing for time-resolved steady-state analysis.

A model crystallisation processes was to selected for demonstration in this combined platform, in order to assess its utility. In considering the batch results discussed in the previous chapter, the reactive crystallisation of $CaSO_4$ in mixed ethanol / aqueous environments was chosen. This was shown to induce the nucleation of Bassanite, which underwent a subsequent transformation to the stable hydrate Gypsum over a time period on the order of minutes. The rapid nucleation and attainment of a high yield of crystals makes analysis with in-line PXRD applicable, as there should be a high signal to noise across the fReactor cascade. As such, the aim was to replicate the batch experiments with the fReactor cascade.

3.2. Methods

3.2.1. Apparatus and Reactor Design

Modifications to the fReactor cascade

The fReactor cascade was modified to enable operation in a linear fashion, in turn allowing for *in situ* XRD measurements to be taken between the fReactor units. Two additional ¼-28 ports were drilled on each fReactor base, each being directly opposite each other. To provide stirring of the magnetic fleas, a custom-made stirring unit was used, as created by a previous student (Carlos Gonzales Nino) [246]. This consisted of a length of square drainpipe, within which were 5 small computer fans mounted on a 3D-printed holder, with the fans adjacent to the inside upper side of the drainpipe. A 10 pence coin was glued to each of the computer fans and on each of these two small neodymium magnets were glued. The computer fans were wired in series, and power was supplied by a power supply unit (operating at 5V). This entire design means that, with the fReactors placed directly above each of the computer fans, the magnetic fleas would be stirred by the rotating computer fans.

Modifications to the transfer tubing

The transfer tubing between the fReactor units was modified to allow for in-line PXRD measurements to be carried out. Kapton tubing (ID = 0.0578”, OD = 0.0615”, Cole-Parmer, IL, USA) was used in lieu of PFA tubing, due to it’s lower X-ray attenuation and diffraction [185]. Because the available sizes of the Kapton mean that it can’t directly interface with commercial ferrules and nuts, short lengths of PFA tubing (ID = 1/16”, OD = 1/8”, Cole-Parmer, IL, USA) were used at the interface with the fReactors. Superflangeless ferrules (ID = 1/8”, Cole-Parmer, IL, USA) and PEEK nuts (size ¼”-28) were used directly on the PFA tubing, with the Kapton inside of this, running the length between the two fReactor units (the kapton tubing length was 70mm). Because the Kapton tubing was approximately 3x the length of the PFA tubing, this resulted in an area of exposed Kapton tubing in the middle of the tubing apparatus, where X-ray diffraction measurements could take place. Small amounts of silicone sealant (Kwik-Cast™, World Precision Instruments (WPI), FL, USA) were used at the end of the PFA lengths, resulting in flowing material only traversing through the Kapton tubing. A diagram showing the tubing apparatus is shown in Figure 48.

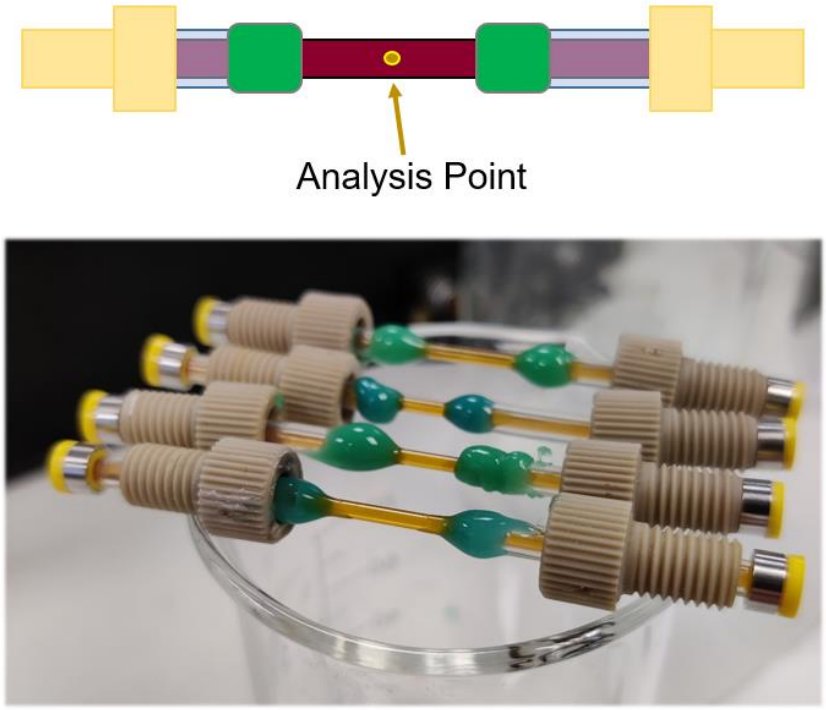

Figure 48 – Transfer tubing used between fReactors for in-line PXRD analysis. Kapton tubing is sealed in place with ferrules and 1/8" OD PFA tubing. Nuts allow for sealing the tubing between the fReactor units. Analysis takes place at the exposed Kapton tubing at the centre of the tubing.

XYZ-Stage

To enable manipulation of the fReactor cascade in front of the beam, and multi-directional stage was created by a laboratory technician (Samuel Flint). This consisted of two stages allowing vertical and horizontal movement positioned parallel to each other, with a linear-movement stage bridging the two. A photograph of the apparatus is shown in Figure 49. The stage was controlled via a custom-made programme. The stage allowed for millimetre-level movement precision, enabling the positioning of samples into the beam.

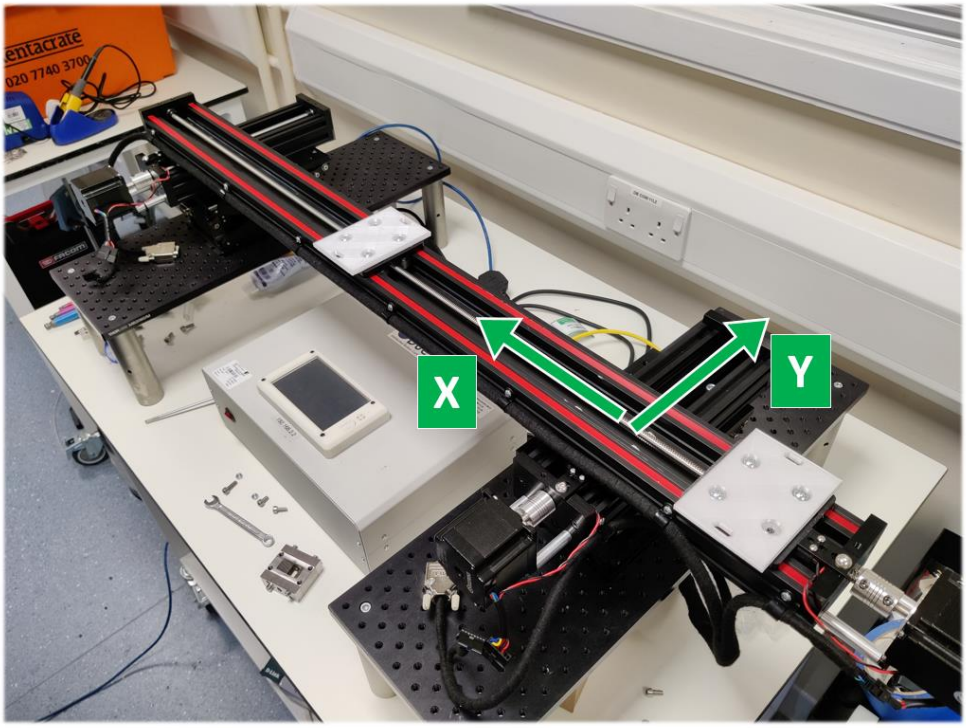

Figure 49 - XYZ stage outside of the X-ray enclosure. Samples can be mounted on one of two moveable brackets (white squares). The X and Y directions are shown by the arrows – the Z direction is represented by movement in and out of the plane of the page (I.E. raising and lowering the stage).

The custom-made stirring unit was positioned on the linear stage to enable movement in the 'X' direction. The cascade was adjusted in both the 'X' and 'Z' direction to ensure the Kapton windows were positioned in front of the beam. The 'Y' direction was kept at its minimum value, resulting in the windows being as close of the beam as possible. Likewise, a detector distance of 80mm was used, which was the minimum practical sample to detector distance, ensuring maximum diffracted intensity at the widest range of diffraction angles. This is shown for the example of window 4 positioned in front of the beam in Figure 50.

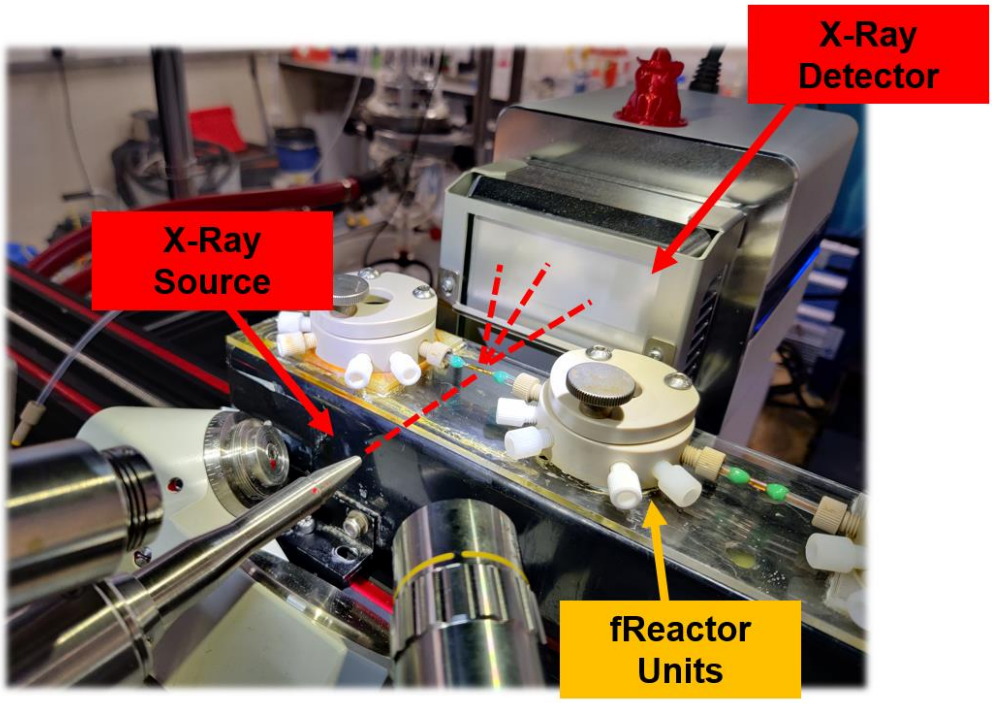

Figure 50 – Image of in-line X-Ray diffraction taking place at window 4 of the fReactor. The Kapton windows used for analysis are shown between the fReactor units. The detector is in the minimum possible distance from the analysis point.

3.2.2. Continuous Crystallisation Experiments

Reagents and Apparatus

Two syringe pumps (Harvard PHD Ultra™; Harvard Apparatus, MA, USA) were used to deliver reagents to the fReactor cascade. Two syringes (50mL, Terumo Japan) were used in parallel with one another on each syringe pump to extend the range of residence times that could be accessed. T-junctions were used to combine the flow from the syringes to form one stream for each reagent prior to introduction to the first fReactor unit. One syringe was used to pump ethanolic Ca^{2+} solution, and the other aqueous SO_4^{2-} solution, with the two streams initially mixing in the first fReactor. PFA tubing was used to transport material from the syringes to the fReactor cascade, and a short length (20cm) of tubing was used following the final fReactor to deliver material to a waste container.

Similar to the batch crystallisation experiments, $CaCl_2.2H_2O$ was dissolved in ethanol, and Na_2SO_4 was dissolved in water to form an aqueous solution. In order to adjust ethanol content, but maintain the same final concentration of $CaSO_4$, the concentrations of the individual precursor ions were changed between ethanol

fractions, as shown in Table 10. Upon mixing, the final concentration of the precursor ions Ca^{2+} and SO_4^{2-} was thus 100mM each.

Table 10 – Experimental conditions for the continuous crystallisation monitoring experiments at different ethanol fractions.

Ethanol Vol. Fraction (%)	Ca^{2+} conc., mM	SO_4^{2-} conc., mM
40	250	167.7
50	200	200
60	167.7	250

In Situ XRD Experiments

Before each experiment, the fReactor cascade was degassed by removing the lids of the fReactors, blocking the exit tubing at the final fReactor, and pumping water through the cascade. This resulted in the liquid level of the fReactors gradually increasing – at the point before water was about to flow over the top, the flow was stopped. The lids where then replaced, and the exit tubing unblocked. For each of the four windows, alignment of the windows was performed by manipulating the XYZ stage controls until the window was visually estimated to be in front of the beam. XRD measurements were then made, and the stage was manipulated in the Z-direction in order to minimise the height of the peak from Kapton, present at $2\theta = 4.1°$. This would be indicative of measurement taking place at the centre of the tubing, wherein attenuation from the Kapton is minimised, and attenuation from the sample is maximised. A schematic of the continuous crystallisation experiments set-up is shown in Figure 51.

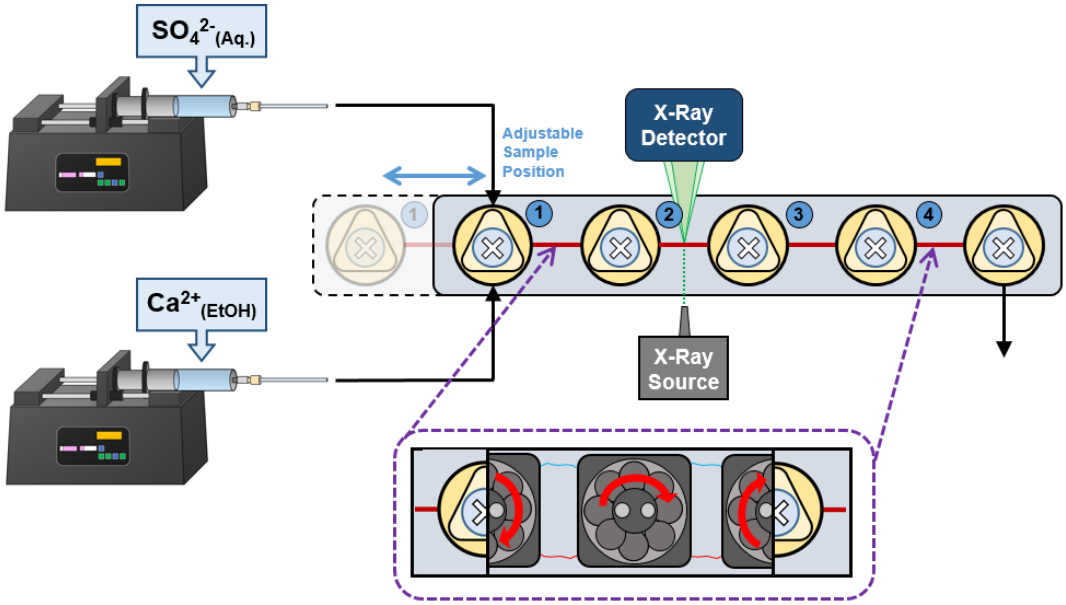

Figure 51 – Apparatus used for continuous-flow crystallisations of $CaSO_4$ within the fReactor cascade, with in-line PXRD analysis. Acquisitions are undertaken at the Kapton tubing present between the fReactor units. The fReactors are mounted on the stirring device (shown inset), which in turn is mounted on a moveable stage. The figure is not to scale.

A 3-minute residence time was initially selected - considering the volume of the reactor cascade is 7.8mL, this resulted in a total flowrate of 2.6mL.min^{-1}. For different ethanol volume fractions, the individual flowrates of the $Ca^{2+}_{(EtOH)}$ and $SO_4^{2-}_{(Aq.)}$ streams could then be set to match the required ethanol volume fraction. For the case of the 3-minute residence time, four experiments were carried out for each volume fraction, with the X-ray incident on each of the four windows. X-ray diffraction patterns were acquired at an acquisition time of 20s following the pumping of a volume of material equal to 3-times the volume of the cascade (a *residence volume (RV)*, ~23.4mL). Subsequent acquisitions were obtained for each RV up to 8 RVs, giving 6 acquisitions for each experiment. For the case of 40 and 50 vol.%, a few other residence times were used in order to extend the range of times acquired. A complete list of the experiments performed is shown in Table 11.

The time point represented by the window / residence time used was estimated based on residence time distribution experiments, as carried out with liquid dyes. RTD behaviour was previously shown to emulate that of continuous stirred-tank reactors (CSTRs) in series [126]. As such, the equation for the F-curve (the frequency distribution of residence times) for *N* CSTRs in series was used to calculate the mean time at steady state (wherein F = 0.5). This is given in equation 36, where θ_i is the ratio of time (t) over mean-time per tank ($\bar{t}$) for N tanks. The mean time for each experiment at steady-state is shown in Table 11.

$$\boldsymbol{F} = 1 - e^{-\theta_i}\left[1 + \theta_i + \frac{{\theta_i}^2}{2!} + \cdots + \frac{{\theta_i}^{N-1}}{(N-1)!} + \cdots\right] = 0.5 \qquad 36$$

Table 11 – Experiments carried out on the fReactor cascade with in-line PXRD monitoring of the reactive crystallisation of $CaSO_4$ under different ethanol fractions. The mean time points represented by steady-state analysis at a given window and residence time are shown, as calculated from the F-curve equation 36.

Exp. Number	EtOH Vol. Fraction (%)	Ca^{2+} Flowrate (mL.min-1)	$SO4^{2-}$ Flowrate (mL.min-1)	Total Flowrate (mL.min-1)	Residence time (min)	Window	Mean Time (min)
1	40	4.68	3.120	7.80	1	1	0.139
2	40	1.56	1.040	2.60	3	1	0.416
3	40	1.56	1.040	2.60	3	2	1.008
4	40	2.34	1.560	3.90	2	4	1.336
5	40	1.56	1.040	2.60	3	3	1.603
6	40	1.56	1.040	2.60	3	4	2.138
7	40	1.17	0.780	1.95	4	4	1.469
1	50	1.56	1.040	2.60	3	1	1.836
2	50	1.56	1.040	2.60	3	2	2.203
3	50	1.56	1.040	2.60	3	3	2.570
4	50	1.56	1.040	2.60	3	4	2.938
5	50	1.34	0.891	2.23	3.5	4	3.672
6	50	1.87	1.248	3.12	2.5	4	0.139
7	50	1.17	0.780	1.95	4	4	0.277
8	50	1.87	1.248	3.12	2.5	3	0.416
9	50	1.17	0.780	1.95	4	3	1.008
10	50	0.94	0.624	1.56	5	4	1.336

Reactor Flow-regime Analysis

A key tenet of the fReactor is the fact that the mixing is supposedly deconvoluted from the flowrate. To analyse this, Reynold's numbers were calculated for the Kapton tubing used in the experiments, at a range of flow-rates inclusive of those used in the experiments (0.5-10 mL/min). Reynold's number (Re) is given by the equation Re = ρud / μ, where ρ is the density, u is average speed of the fluid perpendicular to the diameter of the tubing, and μ is the kinematic viscosity of the fluid. A Re value of below 2000 is indicative of operation in the laminar regime, a value between 2000-4000 is indicative of the transition region, and a value above 4000 is indicative of the

turbulent regime. Flow in the laminar regime can be modelled based on a maximum axial velocity at the centre of the tubing, and zero velocity at the walls. This effectively results in a wide residence time distribution. Flow in the turbulent regime results in radial mixing and eddies resulting in backmixing. This is more analogous to active mixing from for example an overhead stirrer operating at a high speed.

Table 12 provides details regarding the Kapton tubing used in the experiments, and the volume of the fReactor units (minus the volume taken up by magnetic fleas). This shows that the volume of the actively stirred parts is 16.45 times the volume inside the tubing.

Table 12 – Specification of the Kapton tubing used in the fReactor experiments.

Length of Kapton (mm)	70
ID of Kapton (mm)	1.46812
Cross-sec. area Kapton (mm2)	1.693048111
Cross-sec. area Kapton (m2)	1.69305E-06
Volume of Kapton (mm3)	118.5133677
Volume of Kapton (m3)	1.19E-07
Volume of single fReactor (mL)	1.56
Volume of single fReactor (m3)	1.56E-06
Ratio fReactor vol / tubing vol	16.45

Using these measures contained in the table, the Reynold's number across a range of range of flow-rates inclusive of those used in the experiments (0.5-10 mL/min) was calculated, as shown in Figure 52 – Calculated Reynold's Number (Re) against flowrate for the Kapton tubing.. This assumes the fluid is water at 20°C (ρ = 998.2 kg/m3, μ = 1.0023E-06 m2/s). The calculated values of Re are always comfortably above 4000. This shows that throughout the experiments carried out, at the total flowrates used, the flow regime in the non-actively mixed tubing remains in the turbulent regime. This offers evidence that the flow-regime is always decoupled from the flowrates used. Although the mixing will change based on the flowrates used, the vast majority of the volume of the fReactor cascade is accounted for by the fReactor chambers themselves, and thus there will only be very minor differences in mixing between experiments (as the magnetic fleas are always run at the same intensity).

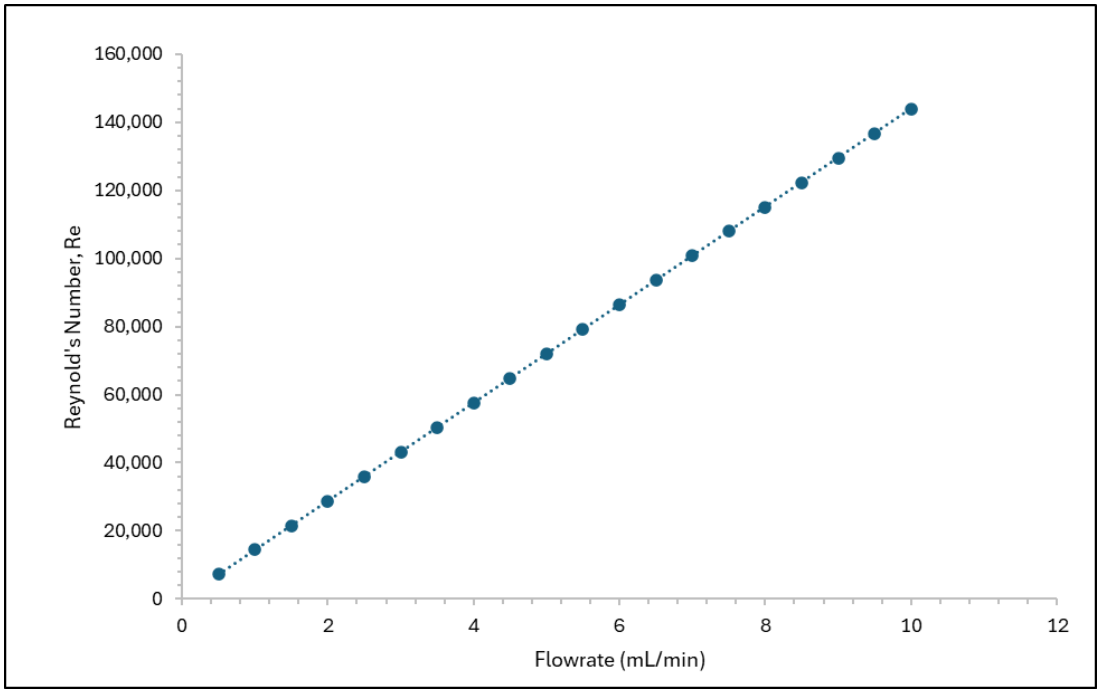

Figure 52 – Calculated Reynold's Number (Re) against flowrate for the Kapton tubing.

3.3. Results

3.3.1. In-line PXRD Characterisation

In-line PXRD Acquisitions

Figure 53 shows a typical 2D diffraction pattern from the XRD experiments (in this case the frame corresponds to a mixture of Bassanite and Gypsum). Diffraction rings can be seen around the centre of the beam, indicating scattering from many different individual crystals in different orientations during the acquisition. A few bright spots can be seen in the rings, as indicated by the red box – this is where crystals are stuck to the inside wall of the Kapton window. Crystals that are stuck to the inside window at the sampling point may provide an excessive intensity to the measurements, disrupting the expected relative intensities of the diffraction peaks. The measurements may not be representative of the estimated time point of crystals in the bulk, and as such may distort the results. However, the spots observed are not high in intensity relative to the diffraction from the rest of the ring, and as such were not presumed to have a large effect on the measurements of the phases present. It shows that crystals were rarely sticking to the inside of the tubing, a validation of the excellent performance of the fReactor in this regard. The stirring unit does preclude a large proportion of the diffraction from being detected by the detector, as can be seen by the lack of any kind of signal in the lower half of the acquisition.

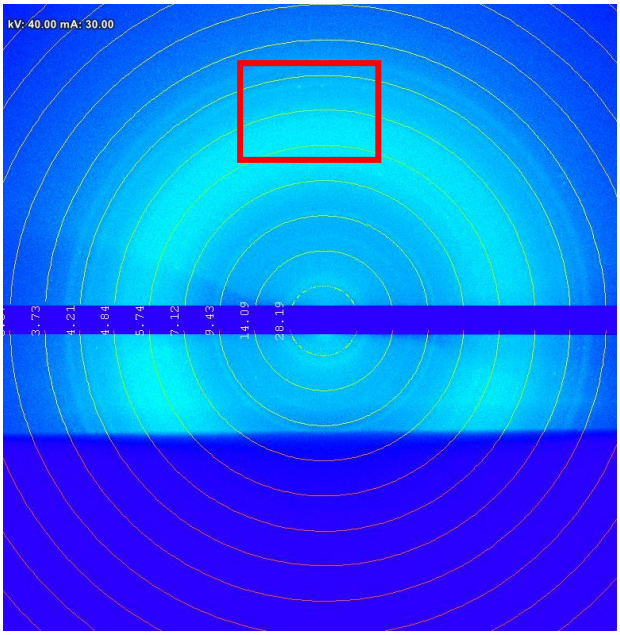

Figure 53 – Example of a typical 2D diffraction pattern obtained from the fReactor during continuous crystallisation of CaSO4 under a mixed ethanol and aqueous environment. Some small spots of high diffraction intensity (red box) were occasionally present, but the majority of solids diffraction originates from the bulk crystals, as indicated by the smooth powder diffraction rings. Window 4, 50% ethanol, 4-minute residence time.

Figure 54 shows the 1D diffraction pattern obtained following azimuthal integration of the 2D pattern shown in Figure 53, accomplished with CrysAlis Pro software. The instrument is calibrated with respect to the XtalCheckS module previously used for the batch crystallisation experiments. The fReactor cascade could not be mounted close enough to the X-ray source such that it was the same distance as the XtalCheckS module would have been (this was removed to accommodate the fReactor cascade). As such, the instrument makes incorrect assumptions during integration, resulting in diffraction peaks appearing at slightly lower values than would be expected. This can be seen by the identified diffraction reflections of Bassanite and Gypsum shown in Figure 54, all of which are at lower 2θ values. A linear correction was developed by identifying the four peaks associated with Bassanite and comparing their measured positions with their known positions (Figure 55). This was applied in future experiments to correct the 2θ positions.

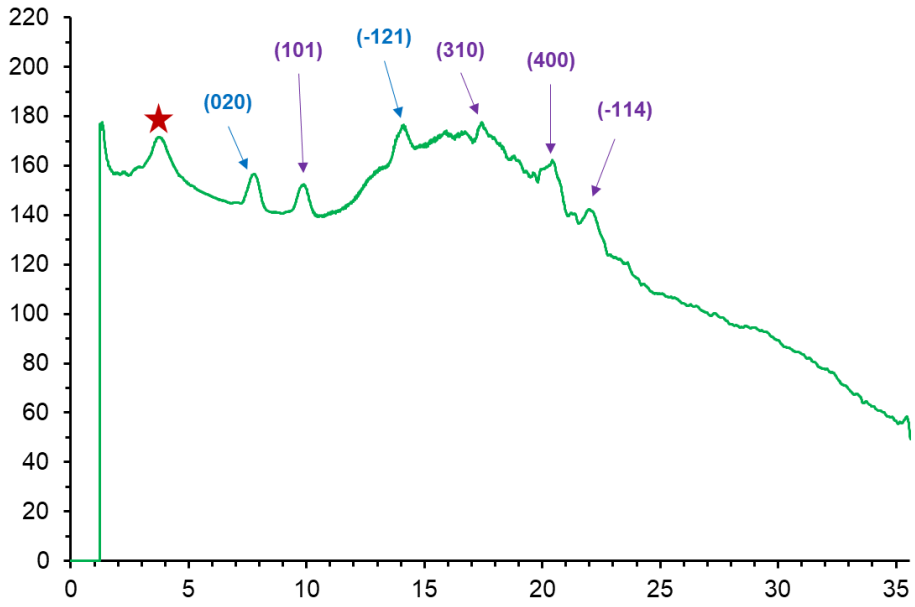

Figure 54 - Azimuthual integration of the 2D diffraction pattern shown previously. Peaks corresponding with the Gypsum phase are shown in blue, Bassanite in purple, and the red star represent diffraction associated with Kapton tubing. Due to an error in the integration process, the 2θ position of the peaks are slightly lower than expected.

(hkl)	Expected Position (°)	Actual Position (°)	Difference (°)
(101)	14.72	9.73	4.99
(310)	25.56	17.18	8.38
(400)	29.56	20.23	9.33
(-114)	31.62	21.97	9.65

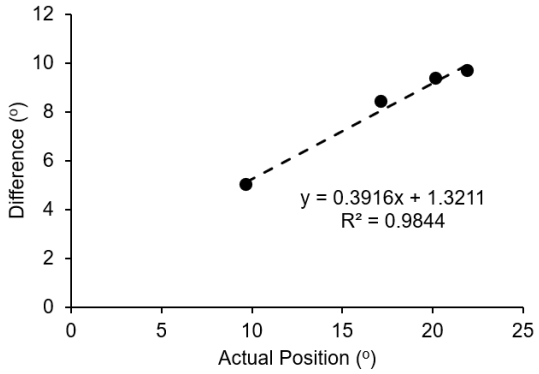

Figure 55 - Correction developed to correct measured (actual) values of 2θ to the desired values. Based on measured positions of four reflections associated with Bassanite. The linear equation shown in the graph was used to correct future experiments.

Figure 56 shows the same diffraction pattern following the application of the 2θ correction and following background subtraction. OriginPro software (version 2023b, OriginLabs, MA, USA) was used to accomplish the background subtraction using Asymmetric Least Squares regression (Asymmetric factor = 0.001, Threshold = 0.03, Smoothing factor = 4, number of iterations = 10). A number of peaks are clearly visible beyond the background, particularly the distinguishing peaks in the region 10-15.5°, where there was relatively less background scattering.

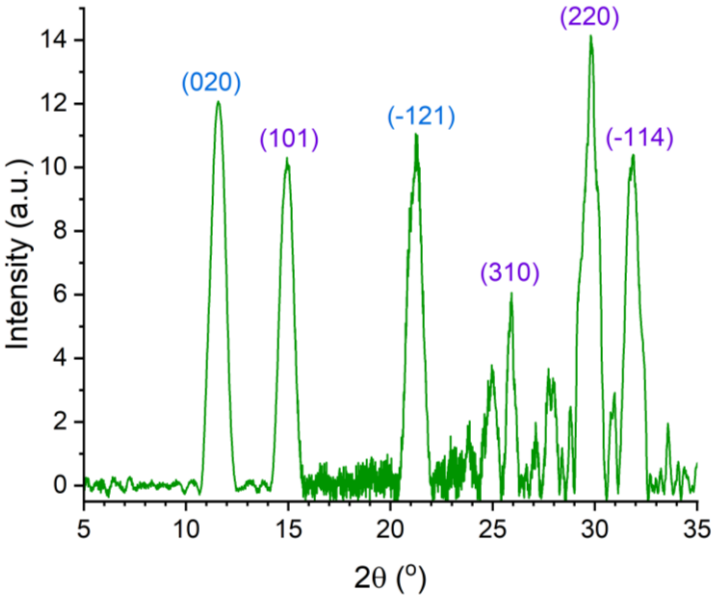

Figure 56 – Background subtraction of the 1D diffraction pattern, showing observed reflections associated with CaSO4 (Gypsum in blue, Bassanite in purple).

Assessing Steady-State

Steady-state is a key aspect of operation of continuous crystallisation devices. To assess the ability of the fReactor cascade to maintain a steady-state with respect to time, the intensity of diffractions obtained for experiment 4 (as an example) were assessed across different residence volumes. A residence volume is defined as the time taken to pump a volume equal to the total volume of the reactor up to the point of analysis. So, for experiment 4, where acquisitions were taken at window 2 (volume 3.12mL) with a 3-minute total residence time (total flow-rate 2.6mL.min^{-1}), a residence volume has a time of 1.2 minutes. Figure 57 shows a series of diffraction patterns for experiment 4 for the range 2θ = 10-16° obtained across 3-8 residence volumes. Within this range of 2θ values, the (020) peak of Gypsum and (101) peak of Bassanite can be observed in all the patterns.

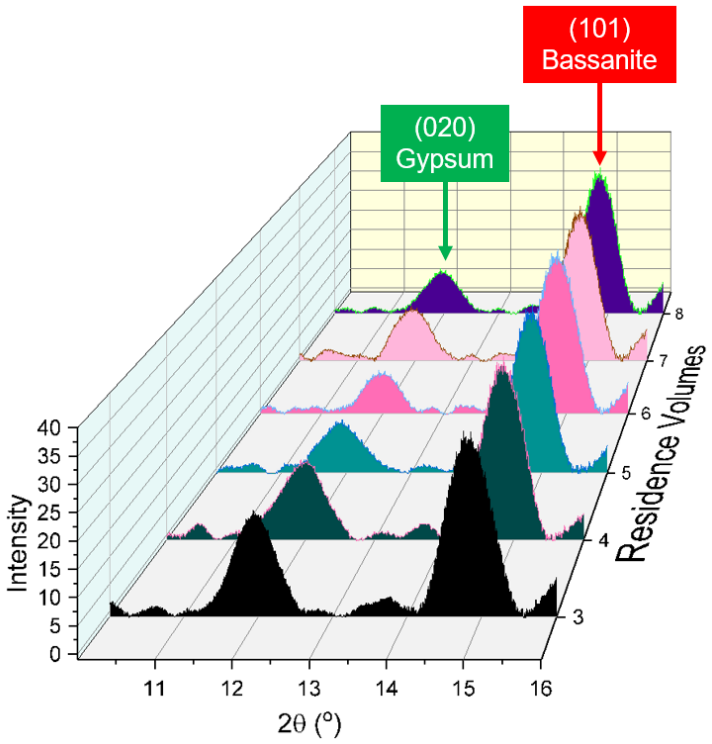

Figure 57 – Diffraction patterns obtained for different residence volumes at the 2nd window of the fReactor cascade during 40% ethanol experiment at a three minute residence time. The size of the (020) peak of Gypsum at 11.6° relative to the (101) peak of Bassanite at 14.8° remains constant, indicative of a steady-state of operation being achieved.

The relative sizes of the peaks in Figure 58 are seen to be similar across the residence volumes. This indicates that the relative proportion of Gypsum and Bassanite present is not changing over real time, indicative of steady-state. Figure 58 shows the relative size of the (020) peak compared with the (101) peak, as captured by the relationship β, given by equation 37. Steady-state can be assumed to have been reached following 5 RVs. This is because there is a relatively insignificant standard deviation (±0.030) from mean values between 5-8 RVs. The time taken to reach steady-state is a little longer than a theoretical CSTR cascade, which can reach steady-state within 2-3 RVs [103]. This is likely because of the inherently more complicated heterogenous crystallisation system. Other reports of continuous crystallisation in cascades of CSTRs have shown steady-state to be achieved following 3-7 RVs [247-249], which matches well with these experiments. Furthermore, relative errors in measured values at steady-state of around 2% have previously been reported [248, 250], which is again comparable.

$$\beta = \frac{Area\ (020)\ Peak}{Area\ (020)\ Peak\ +\ Area\ (101)\ Peak} \qquad 37$$

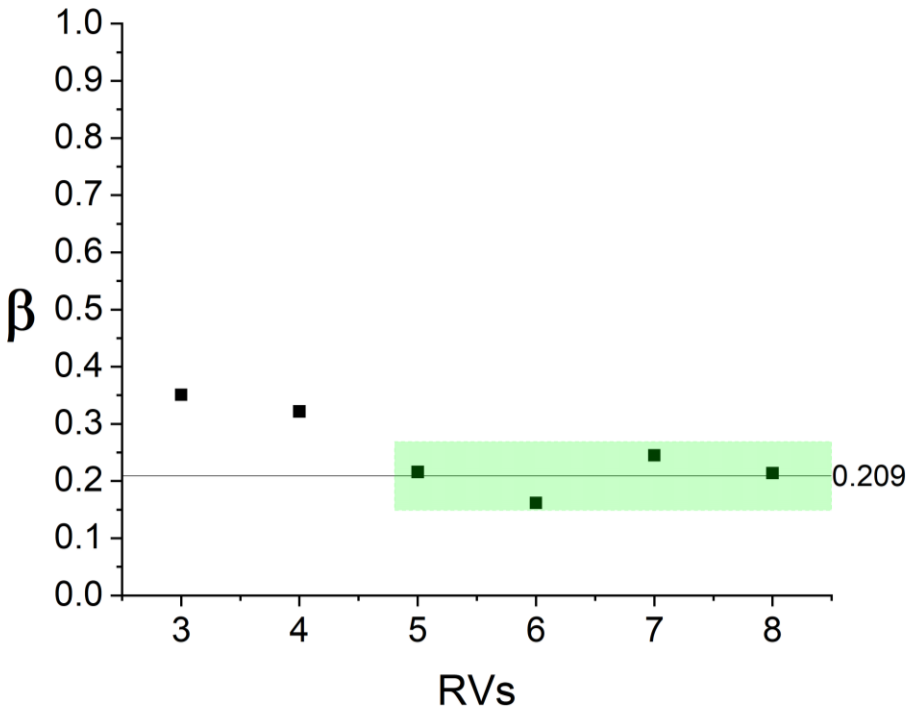

Figure 58 – Values of β (relative size of the (020) peak compared with the overall area) over residence volumes (RVs). The green area represents 2 standard deviations (±0.06) from the mean of the values between 5-8 RVs. Because of the insignificant deviation from the mean value across this range, steady-state is deemed to have been reached.

3.3.2. Continuous Crystallisation Characterisation

Figure 59 shows the results (in terms of conversion, α, equation 33 in chapter 2) of the monitoring of the continuous reactive crystallisation of $CaSO_4$ under (a) 40 and (b) 50 vol.% ethanol. Different time-points were accessed through manipulation of the fReactor cascade to monitor different windows and by adjusting the overall flow-rate of material. The error bars represent a standard deviation from the mean of three acquisitions at 6, 7 and 8 residence volumes. Avrami relationships have been fitted to each set of results, as shown by the dashed line (parameters are shown in the inset table).

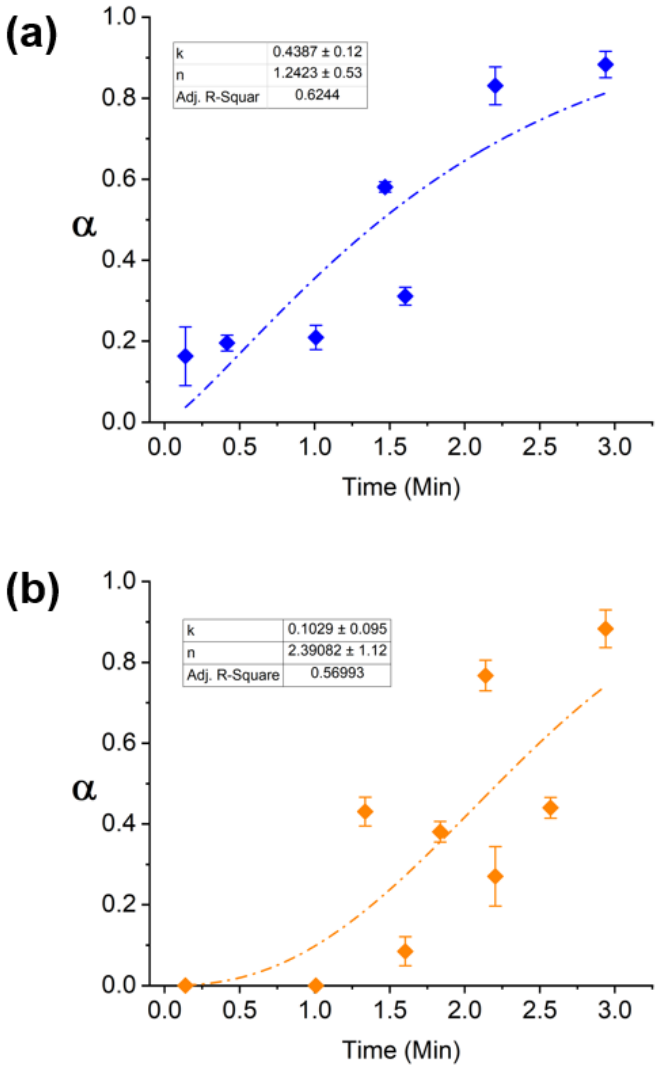

Figure 59 – Conversion (α) over time of Bassanite to Gypsum, measured using the in-line PXRD characterisation within the fReactor cascade. Avrami relationships are fitted to each dataset, as indicated by the dashed lines, and the inset tables. (a) 40 vol.% (b) 50 vol.% ethanol.

For all the experiments, there is a relatively low deviation from steady-state behaviour as indicated by the tight error bars. Residence volumes beyond 8 could not be accessed due to the syringes on the syringe pumps running out of material. For both experiments, the general trend present is that of a hydrate conversion from Bassanite to Gypsum occurring over the length of the fReactor cascade. However, there is a great degree of fluctuation between repeated experiments. As an example, consider the experiments 3 and 4 at 50% Ethanol. In the case of the former, conversion has approached 50%, whereas in the case of the latter, conversion is at practically zero. Similar behaviour is presented at most of the intermediate residence times. This is indicative of a potential pitfall of this approach – an inherent lack of repeatability between experiments. This could somewhat be remedied by running an experiment

at a single residence time and simply moving the analysis window. However, this was not immediately practical, due to the requirement to move the waste bin as the analysis window changed, and because of the limited supply of precursor solutions from the syringes. Furthermore, this would be limited to just four time-points.

The fluctuation in experimental results from the expected is not merely down to changing the mean residence time. Consider experiments 2, 3, 5 and 6 in the case of 40% Ethanol, where the residence time is fixed at 3 minutes and only the analysis window is changed. The first two show a similar value of conversion (~0.2) and this is similar for the latter two (~0.85), whereas a more gradual change between the experimental conditions would be expected. This shows that there is an inherent stochasticity in the kinetics of the transformation between repeated equivalent experiments. Unfortunately, repeats of the equivalent batch experiments were not undertaken, so no comparisons of the repeatability between experiments could be made.

Avrami relationships were fitted to the results of the experiments in the same manner as the equivalent batch experiments (chapter 2, equation 33 and Figure 43). Although (qualitatively) these captured the overall trend fairly well, they show poor agreement with the experimental data points, as shown by the relatively low R^2 values. This is a result of the aforementioned stochasticity in the observed values of conversion, particularly in intermediate residence times. Figure 60 shows comparisons of the obtained Avrami relationships for the batch and continuous experiments for (a) 40 and (b) 50 vol.% Ethanol. Overall, the trends are fairly similar, with the notable finding of the transformation appearing to begin earlier in the continuous fits. This could be down to significant back mixing appearing in the continuous set-up, leading to the presence of Gypsum at earlier time-points. It could also be a result of the higher specific surface area (i.e. relative to volume) in the fReactor, which may provide alternative nucleation sites for Gypsum. This shows how, despite the overall stochasticity of conversion results, the averaged values over time begin to approximate the transformation rates observed in batch. Furthermore, it is a validation of the RTD model that has been assumed and used to estimate the reaction time-point of the different windows and the residence times used.

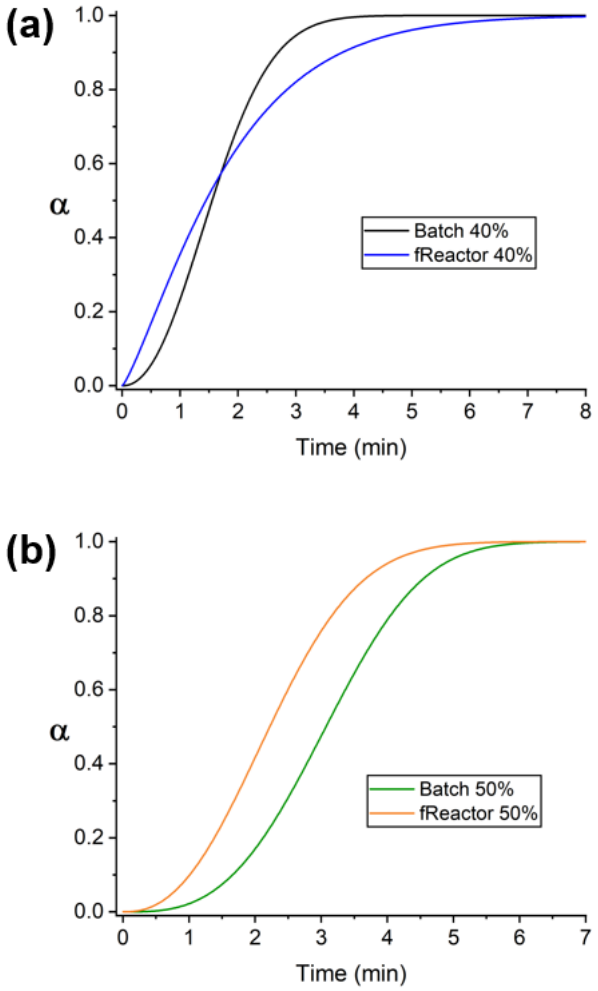

Figure 60 – Comparison of Avrami fits to batch and continuous data for (a) 40 (b) 50 vol.% ethanol experiments. Hydrate conversion is observed to start earlier in the fReactor compared to the batch reactor. There is reasonably good general agreement between the fits.

3.4. Conclusions

The fReactor millilitre-scale CSTR cascade successfully enabled the continuous crystallisation of $CaSO_4$ from mixed ethanol and water solutions under different solvent fractions and with residence times on the order of minutes. Crystallizations are notorious for being difficult to carry out in continuous flow, owing to blockages and encrustations – problems which can typically be exacerbated by operation at small (i.e. millilitre) scales. As such, the successful demonstration of the reactive precipitation of this important mineral system within the fReactor represents a novel and important advance. The modular design of the fReactor cascade allowed for in-line PXRD analysis of the crystallisation to take place between CSTR units, allowing for reaction-time evolution to be accounted for by measurements across the cascade.

Furthermore, the active stirring provided by the fReactor units resulted in the decoupling of overall flow-rate and mixing intensity, conferring further operational flexibility.

In attempting to replicate the batch experiments (tracking of hydrate transformation under different ethanol and water fractions), calculated values of conversion showed a great degree of fluctuation between time-points, although the general trend of Bassanite transforming to Gypsum could be observed. It is presumed that these fluctuating values of conversion at intermediate time-points are due to the way the experiments were carried out. Repeats of the equivalent experiment were carried out at different windows or with different residence times. This means there could be a slightly different reaction pathway in terms of the stability of the Bassanite phase or the nucleation of the subsequent Gypsum phase. Effectively, this captures the inherent randomness of some of the processes in this complicated crystallisation process, such as the seemingly random induction time for the dissolution of metastable phases [251] or the nucleation of stable phases [241]. The actual stability of the system once at a steady-state is good – between 5 to 8 residence times, there was generally very little fluctuation in the measured values of the intensity of Bassanite and Gypsum peaks. This is a positive reflection of the ability of the fReactor system to provide a consistent environment for continuous crystallisations to take place.

Future work may focus on the automation of the process. Autonomous, transient measurement of homogeneous chemical reactions in continuous flow has allowed for the automated fitting of kinetic models [252]. Self-optimisation algorithms have also been used to enable rapid optimisation of process parameters such as space-time yield or process selectivity [252-258]. Techniques such as these have not yet been demonstrated for continuous crystallisations in the same manner as liquid-phase chemical reactions, due to the limitations of previous solid-phase analysis techniques and the generally poor solids handling abilities of continuous flow reactors. The fReactor – PXRD platform is flexible enough as to provide a wide operational range for algorithmic exploration of reaction parameters, and the signal to noise from the laboratory-based instrument allows for a wide range of solids densities to be measured. More immediately, automation could be beneficial in fitting kinetic profiles to data acquired at a steady-state. It is clear from the experiments that have been undertaken that measurements at steady-state require a large number of repeats across different residence times and window to allow kinetic information to be accurately extracted. Automation could allow for the minimum number of experiments

to be performed to facilitate an accurate fit. Being able to carry out these experiments away from the synchrotron allows for better experimental flexibility and less of a time-pressure. This is further beneficial for complex and novel experiments such as in the development of automated platforms of this nature.

4. Continuous Antisolvent Crystallisation of ROY

4.1. Introduction

4.1.1. Background Science

Antisolvent crystallisation processes are widely used in industrial production of crystalline products [31, 259, 260]. They are particularly beneficial for heat-sensitive materials, for usage in conditions in which there is a relatively small difference in solubility of a solute between low and high temperatures, and when additional yield of crystals is required following a cooling crystallisation [261-263]. The high supersaturation generated during antisolvent crystallisation can also be used in a 'bottom-up' approach to producing nano-sized crystals [264, 265]. Such an approach for accessing crystals at the nanoscale has several benefits over 'top-down' (attrition) approaches, including a lower energy requirement and a higher degree of control over crystal properties [266]. Recent reports have demonstrated that antisolvent crystallisations in a continuous-flow environment may show superior performance in terms of crystal quality attributes compared to the equivalent batch process [124, 139, 267]. Because of the inherent sensitivity of antisolvent crystallisations to mixing conditions [268], a suitable continuous crystallisation device should provide efficient, consistent mixing across different flow-rates, limiting the spatio-temporal variation of supersaturation [269].

ROY (5-Methyl-2-[(2-nitrophenyl)amino]-3-thiophenecarbonitrile) is a small organic molecule which has been widely studied, due to its extraordinary propensity towards the formation of many different polymorphic forms. In total, 12 fully characterised forms of ROY have been reported - a record for an organic molecule [270]. Recent literature has demonstrated the isolation of several of these polymorphs through antisolvent crystallisation of ROY from acetone with water as the antisolvent. Ziemecka and co-workers previously reported the generation of a variety of ROY polymorphs through the injection of ROY solution into water in a Hele-Shaw cell [271]. This out-of-equilibrium approach, however, exhibits poor mixing and an inherent concentration gradient away from the injection site. Consequently it is difficult to study the specific effect of concentration and antisolvent content on the polymorph that forms. Van Nerom and co-workers reported the same antisolvent crystallisation with the use of a microfluidic chip with induced acoustic mixing provided by a piezoelectric element [272]. However, this was only demonstrated at a single antisolvent content and at a very small scale.

4.1.2. Goals and Rationale

The main goal of these experiments is to assess the capabilities of the fReactor as a device that can facilitate and allow for the study of antisolvent crystallisations over a wide range of experimental conditions. This could demonstrate the utility of the fReactor cascade as a platform for the rapid screening of antisolvent crystallisation conditions, as well as demonstrating solids handling within a CSTR cascade. The antisolvent crystallisation of ROY from acetone with water was chosen as a model system. This is because ROY is analogue of an industrially relevant small organic molecule (it is a closely-related precursor to the drug Olanzapine [273]) which has been shown to produce a number of different polymorphs. A common challenge for the fine chemical industry is control over crystal structures and polymorphs during crystallisations [57]. As such, there exists a driver for methods of rapidly screening the effect of processing conditions on polymorphs for industrially relevant compounds.

The initial goal is to be able to screen across different conditions at which the antisolvent crystallisation takes place within the fReactor set-up. To this end, a solubility study was conducted on ROY across different acetone / water mixtures in order to quantitatively rationalise the driving force for the ROY crystallisation. Then, continuous flow antisolvent crystallisations of ROY were conducted in the fReactor cascade at several different antisolvent ratios and residence times, at two different starting ROY solute concentrations. Samples were taken to determine the polymorphs produced across different experimental conditions. The fReactor was also coupled with in-line PXRD characterisation to assess if such a combination of reactor and analysis technique could be used to monitor transient crystallisation phenomena.

4.2. Methods

4.2.1. Initial crystallisation characterisation

Solubility of ROY across solvent mixtures

Solubility assessment of ROY in different acetone and water mixtures was carried out using off-line UV-vis analysis (Shimadzu UV-2600i). For each UV-vis experiment, 0.7mL samples were run in a quartz cuvette. A calibration of peak absorbance with ROY concentration is required to measure how the concentration varies with peak UV-vis absorbance, such that ROY concentrations can be determined. Since various solvent mixtures were found to have a slight variation in the wavelength at which peak absorbance occurred, as well as a different relationship between ROY concentration and absorbance, calibrations were carried out at several different acetone volume fractions (relative to water): 30, 70, and 100%. For each acetone volume fraction, solutions of 0.005, 0.01, and 0.02g.L^{-1} were created, with UV-vis spectra being taken for each. For each experiment, the peak UV-vis absorbance was recorded, along with the wavelength of peak absorbance.

Following the creation of a calibration curve, saturated solutions were created in 15mL glass vials at a 10mL scale for a range of water fractions (relative to acetone) through the addition of an excess of ROY (Flurorochem Ltd., Glossop, UK). The slurries in the glass vial were left stirring for 24hr at room temperature, before being transferred to centrifuged at 5000RPM for 3 minutes. The supernatant was subsequently removed from the centrifuge tube using pipettes, and vacuum filtered to remove any remaining solids, using a 0.45µm membrane filter (MF Millipore™; Merck KGaA, Darmstadt, Germany). The filtrate was then diluted down such that the resultant solution was approximately within the range of the calibration.

Generation and characterisation of different ROY polymorphs

Following methods described in the literature [271], two different ROY polymorphs were produced and isolated for characterisation: Yellow Prisms (YP) and Orange Needles (ON). YP was produced through the addition of 20mL of deionised water to 20mL of 10g.L^{-1} ROY in Acetone, which was subsequently left for 1 hour to ensure complete selectivity of the YP-form. The solids were then vacuum filtered using the 0.45µm membrane filters and left to dry in an oven set at 40°C overnight. ON was produced by adding 40mL of deionised water to 20mL of 10g.L^{-1} ROY in Acetone under stirring with a stirrer bar. This was filtered after 1 minute and left to dry in the same manner.

The solids produced were examined with a variety of characterisation techniques. Optical Microscopy (Nikon Eclipse LV100D) was used to visualise the crystals. A small spatula of crystals was added to 1.5mL of 0.1g.L^{-1} aqueous TWEEN® 20 solution (Sigma Aldrich®, Merck KGaA, Darmstadt, Germany), shaken briefly, sonicated for 5 minutes, and then shaken again. The use of the TWEEN 20 surfactant would allow for the solids to become suspended in the solution and for clumps of solids to be broken up (with the assistance of the sonication). 30µL was then dispersed on a glass slide, which was left to dry in an oven set at 40°C. Raman spectroscopy (Horiba Labram HR Evolution, λ = 532nm) and Off-line Powder X-Ray Diffraction (PXRD, Bruker D2 Phaser, Cu-Kα, λ = 1.54Å) were carried out to confirm the polymorphs produced. Raman spectroscopy was carried out on the same samples used for optical microscopy using a 50x objective (532nm laser, edge filter, 10% power, 30s acquisition). PXRD samples were prepared by first grinding each of the powders using a pestle and mortar, then creating the same dispersions using TWEEN 20. Dispersions were then drop-cast onto a 40mm silicon disc for use with the PXRD instrument. Diffractions were taken with a range of $2\theta^{o}$ angles from 5-50°. Predicted PXRD patterns were generated using CrystalMaker X software [274] (CrystalMaker Software Ltd, Begbroke, UK) for comparison with the measured PXRD patterns, making use of previously reported unit cell data from single-crystal X-Ray diffraction experiments, as shown in Table 13 [275].

Table 13 – Unit cell parameters used for simulated diffraction patterns of two forms of ROY: the YP- and ON-forms. Parameters taken from [275].

Polymorph	**YP-form**	**ON-form**
Space Group	$P2_1/n$	$P2_1/c$
***a*, Å**	8.5001	3.9453
***b*, Å**	16.413	18.685
***c*, Å**	8.5371	16.3948
***α*, deg.**	90	90
***β*, deg.**	91.767	93.830
***γ*, deg.**	90	90

4.2.2. Continuous Antisolvent Crystallisation

Residence Time Distribution (RTD) experiments

Residence time distribution (RTD) experiments have previously been carried out on the fReactor cascade using one, three, and five units [126]. To extend this to include two and five units, further experiments were carried out using a similar methodology. A small mass of water-soluble dye (Sunset Yellow FCF, Sigma, USA) was mixed into

1L of DI water, and stirred to dissolve. The fReactor cascade was prepared by removing the units not in use and using the transfer tubing of either the second or fourth unit as the exit of the cascade. A syringe pump was connected to the first fReactor unit using a length of PFA tubing (ID = 1/16”, OD = 1/8”, Cole-Parmer, IL, USA). DI water was added to a 50mL syringe, and the syringe placed on the syringe pump. The syringe pump was switched to 10mL/min and was left running until the cascade was full, ensuring any bubbles present were removed by tilting the cascade as necessary. The tubing leading from the final fReactor was then capped using a PTFE union adaptor and PTFE blocking screw to seal the fReactor cascade, and the syringe was then swapped for one containing the dye solution. The tubing leading to the first fReactor was then removed from the first fReactor, and the syringe was then switched on, flowing at 1mL/min. The syringe was then left running until the solution containing the dye had reached the end of the tubing, before being stopped. This tubing was then re-connected to the first fReactor, and the blocking screw removed from the end of the final fReactor.

Flow-rates of the dye solution of 2mL/min was used during the RTD experiments using two or four fReactor units in series. As soon as the syringe pump was started at this rate during a single experiment, samples at the end of the cascade were collected using small glass vials. The solution at the end of the cascade was left to drip into a single vial for 30s before another vial was instantaneously swapped in. Following the conclusion of the experiment, aliquots of the solution were deposited into cuvettes, and subjected to UV/vis absorption spectroscopy using a Shimadzu UV-2600i instrument. The peak absorption was then recorded.

fReactor Continuous Antisolvent Crystallisations

Continuous crystallisations were carried out in the fReactor system using 5 individual CSTR units in series. The fReactors were placed on the standard metal holder and in turn placed on a hot-plate stirrer (IKA Plate RCT digital; IKA-Werke GmbH, Staufen, Germany). For off-line tests, short lengths of PFA tubing (1/8” O.D., 1/16” I.D.; Upchurch Scientific, IL, USA) were used to connect the fReactor units using standard-sized PEEK Flangeless ferrules and nuts (Upchurch Scientific, IL, USA). The input of reagents was provided by syringe pumps (Harvard PHD Ultra™; Harvard Apparatus, MA, USA) through the same PFA tubing, with all reagents being mixed initially in the first fReactor unit. The fReactors were operated at a constant stirring rate to provide consistent mixing intensity. The total volume of the fReactor cascade (accounting for the volume in the fReactors and the transfer tubing, and the volume taken up by the

stirrer bars) was 7.8mL. A schematic of the fReactor cascade used for the experiments is shown in Figure 61.

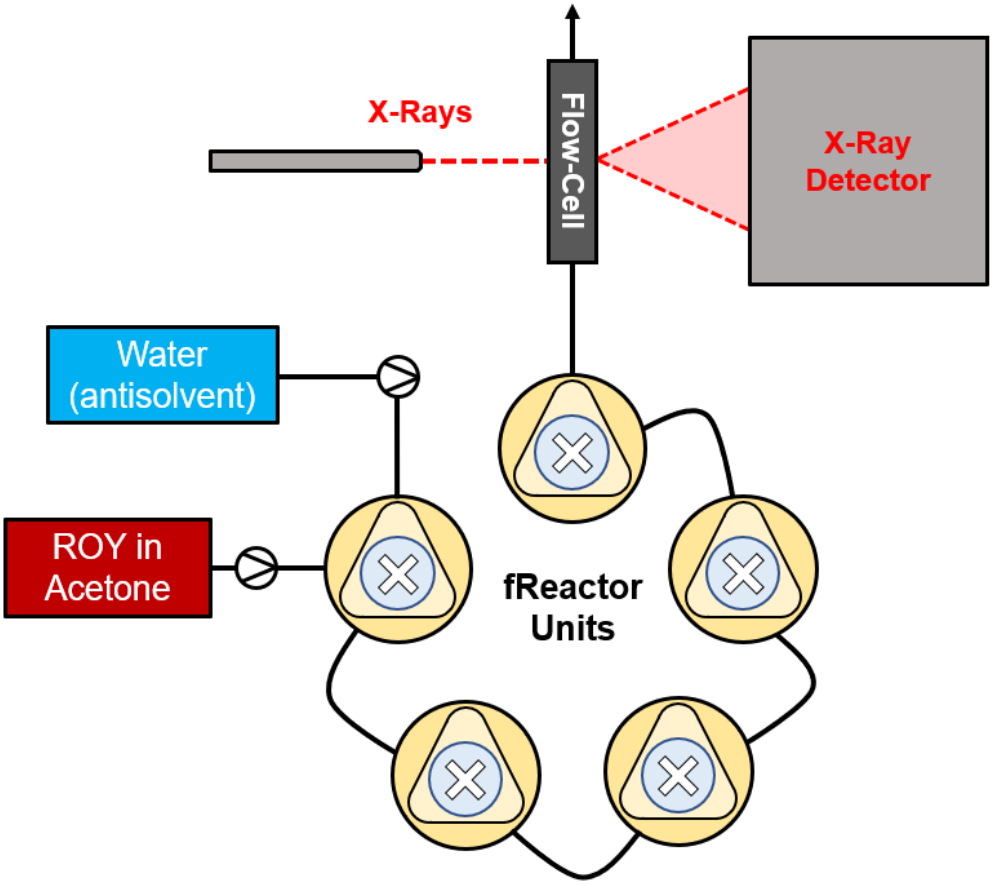

Figure 61 – Top-down schematic of the fReactor apparatus used for the continuous antisolvent crystallisations. Water (antisolvent) and ROY in acetone solutions are pumped into the cascade using syringe pumps. The 5 fReactor units are arranged in series and connected with short lengths of tubing. For in-line PXRD characterisation, a flow-cell was attached in series following the 5th fReactor unit, as shown.

Initial screen of operating conditions

Initial fReactor experiments sought to determine both the solid handling capabilities of the fReactor, and the optimal operating range for further in-line PXRD analysis. Initially, acetone was pumped through the cascade until a volume equivalent to 3-times the volume of the cascade (23.4mL) had been pumped through. The cascade was tilted upwards during this process to facilitate de-gassing. The pure acetone stream was switched to ROY dissolved in acetone, at one of either two concentrations (10 or 20g.L^{-1}). For each concentration, a range of residence times was screened, from 30s to 3 minutes, which determined the overall flowrate of the two streams. A range of antisolvent ratios was also screened, which represented the ratio of the

flowrate of the antisolvent to the solution. 2mL samples were collected from a short outlet stream from the final fReactor unit, and immediately filtered through a vacuum-driven Millipore 0.22µm PVDF membrane filter arrangement to retain the solids. These were then left to dry overnight in a drying oven set at 40°C. Optical microscopy was carried out on the samples produced, and a qualitative evaluation of the morphologies and colours of the crystals was undertaken to determine the polymorphs present. A table presenting the flowrates used for the fReactor experiments is shown in Table 14.

Table 14 - Flowrates used for the fReactor experiments.

Residence Time (s)	Antisolvent Ratio	Water Flowrate (mL/min)	ROY Flowrate (mL/min)
120.000	0.700	1.606	2.294
180.000	0.700	1.071	1.529
30.000	1.000	7.800	7.800
60.000	1.000	3.900	3.900
120.000	1.000	1.950	1.950
180.000	1.000	1.300	1.300
30.000	1.500	9.360	6.240
60.000	1.500	4.680	3.120
120.000	1.500	2.340	1.560
180.000	1.500	1.560	1.040
10.000	2.000	31.200	15.600
30.000	2.000	10.400	5.200
60.000	2.000	5.200	2.600
120.000	2.000	2.600	1.300
10.000	3.000	35.100	11.700
30.000	3.000	11.700	3.900
60.000	3.000	5.850	1.950
120.000	3.000	2.925	0.975

In-line PXRD characterisation

In-line PXRD diffraction experiments were performed with a XtaLAB Synergy-R custom single-crystal diffractometer, comprising of a microfocus rotating anode X-Ray source (Cu Kα, λ ≈ 1.54Å, PhotonJet-R) and a HPC detector (Rigaku HyPix 6000HE). The resultant beam size is approximately 140x140µm. Initially, a calibration

experiment was performed on the in-line PXRD, using a batch reactor (500mL), a peristaltic pump (Masterflex L/S, Easyload II head, L/S 15 tubing), and the custom-made flow-cell previously described in chapter 2. The goal was to quantitatively determine how the size of the diffraction peaks change with the added, solid, ROY. To this end, a saturated solution of equal volumes of acetone and water was prepared by the addition of 5g of solid YP-form ROY to 500mL of acetone and water (50% vol. each), which was left to stir at 20°C overnight with a magnetic flea. The suspension was then filtered using vacuum filtration and 0.45µm membrane filters and the filtrate was retained as the saturated solution. 200g of the solution was added to the batch reactor and continuously pumped through the flow-cell in a loop back to the batch reactor. After several minutes to ensure equilibrium, a 30s acquisition was made with the PXRD. A small mass (0.2g) of solid YP-form ROY was added to the saturated solution, and another acquisition was completed. This was repeated with sequential additions of solid ROY up to 2 wt.% of solids (4g).

For in-line monitoring of continuous antisolvent crystallisations, the fReactor cascade was mounted on two adjustable stands next to the diffractometer. The XtalCheckS module was mounted in front of the beam, and the flow-cell was mounted into the XtalCheckS. A short length of PFA tubing (20cm, ID = 1.59mm, OD = 3.18mm) was used to connect the final fReactor unit to the flow-cell – this was the minimum practical length that could be used, in order to minimise the time between the end of the fReactor cascade and the flow-cell. After the flow-cell, another short length of PFA tubing lead from the flow-cell to a waste container. Reactants were pumped into the fReactor cascade using the same syringe pumps at variable flowrates, in order to access different residence times.

4.3. Results

4.3.1. Initial crystallisation characterisation

Solubility of ROY across solvent mixtures

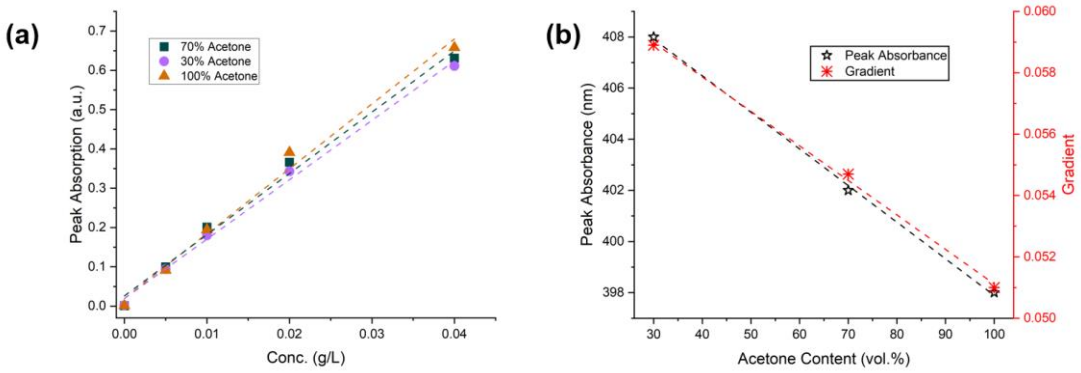

Figure 62 – (a) Calibration curves obtained for the three values of acetone (30-70 vol.%) by plotting peak UV-vis absorbance against concentration of ROY. A linear fit has been applied to each data set. (b) Variation in values of gradient and peak absorbance value (nm) for the three acetone content values, with linear fits for each.

Figure 62 (a) shows the resulting calibration curves for the three different values of acetone volume fraction used: 30, 70, and 100%. Peak absorption values were plotted against the known concentration values, and a linear fit was applied to the data series. This fitted well to the data points. There is a slight discrepancy between the obtained gradients for each of the acetone contents, as well as a difference in the peak absorption values caused by the different solvent environments. To account for this, plots were made of the values of gradient and peak absorption position across acetone content, as shown in Figure 62(b). Linear fits were applied to each of these data sets to facilitate extrapolation between acetone values, meaning that a prediction of concentration of a sample could be made for any acetone volume fraction.

The obtained calibration was then used to calculate concentration values of the samples for the solubility experiments. The solubility across different acetone / water content is shown in Figure 63, with solubility plotted as a log-scale. This shows a steep decrease in solubility as the water content is increased, from 107.9 $g.L^{-1}$ within pure acetone, to 2.1 x 10^{-3} $g.L^{-1}$ within pure water. The vast difference in solubility of ROY in pure acetone and water results in a large supersaturation being generated upon the introduction of a sufficient amount of water to a ROY solution in acetone. This forms the driving force for antisolvent crystallisation to occur.

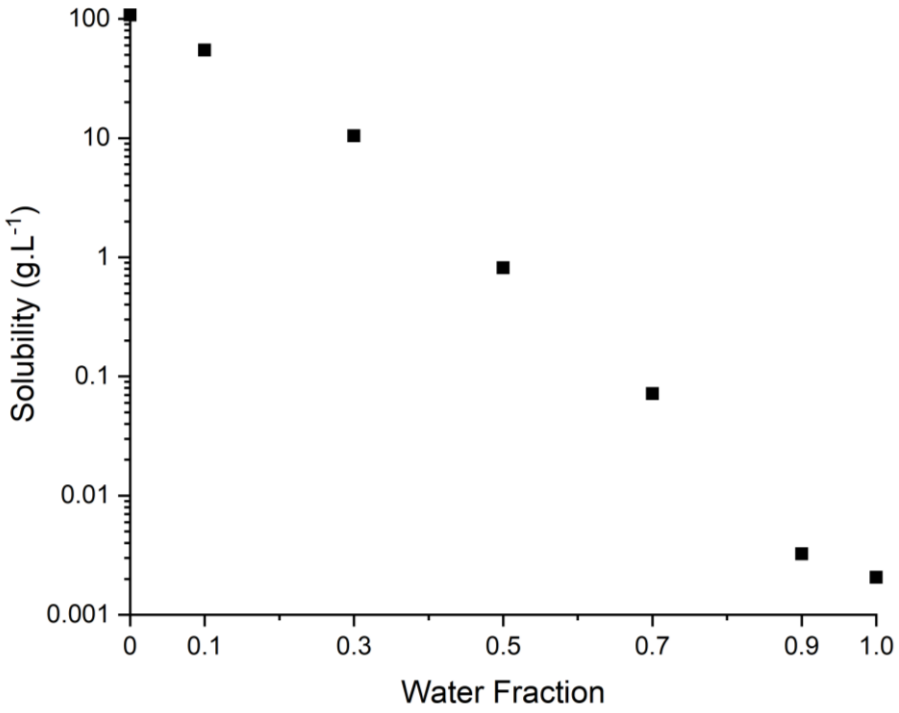

Figure 63 – Solubility of ROY in different acetone / water mixtures, as represented by water fraction. Solubility was calculated from UV-vis absorption spectra and from the previously determined calibration of absorption to concentration.

Generation of different ROY polymorphs

Optical microscopy images of the YP and ON forms of ROY obtained following filtration and drying are shown in Figure 64(a) and (b) respectively. They reveal the expected morphologies and colours of the two polymorphs. The PXRD patterns of the isolated ON- and YP-form crystals are shown below in Figure 65, alongside the simulated diffraction patterns. A key differential peak is the (013) peak present in the ON-form of ROY at 2θ = 16.96°, where no peak is present in the YP-form diffractogram. The good match between the measured and predicted PXRD patterns confirms the identity of the two formed polymorphs, and the comparison with the optical microscopy images shows that their underlying crystal structure matches the expected morphologies. Raman spectroscopy (results shown in Figure 66) further confirmed differences in crystal structure, with key differences at wavenumbers of 17.7254, 373.002, and between ~2215-2243cm^{-1}.

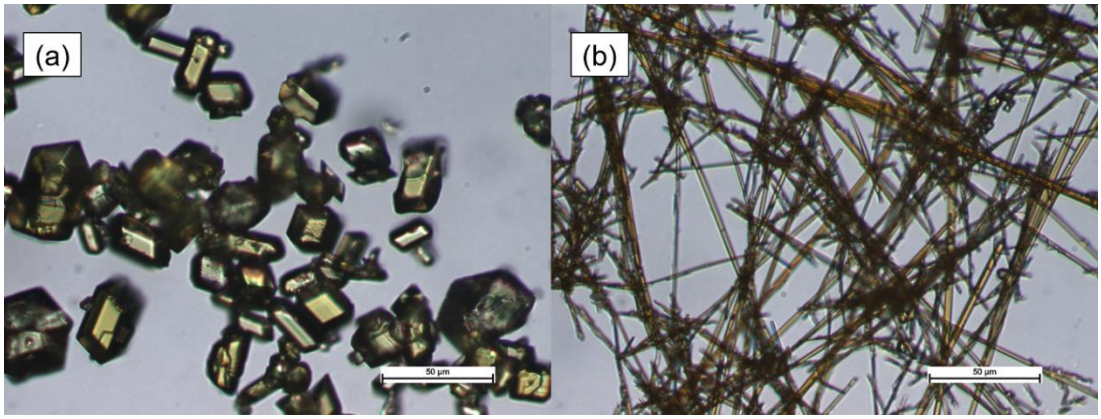

Figure 64 - Optical Microscopy images of the two obtained ROY polymorphs. (a) The YP form, showing the expected yellow prism morphology. (b) The ON form, showing the expected orange needle morphology.

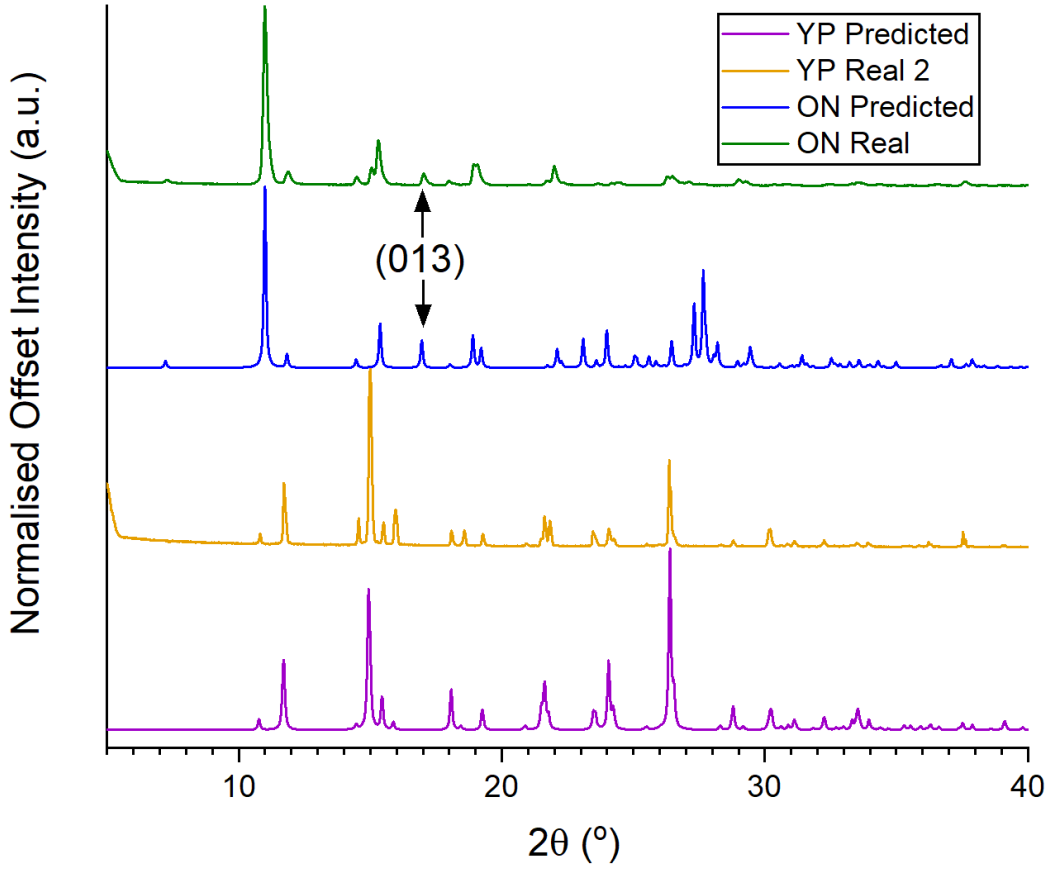

Figure 65 - Predicted PXRD diffractograms of the YP- and ON-forms of ROY, as well as off-line PXRD diffractograms of samples of the two forms. The peak (013) for the ON-form (2θ = 16.96° is labelled)

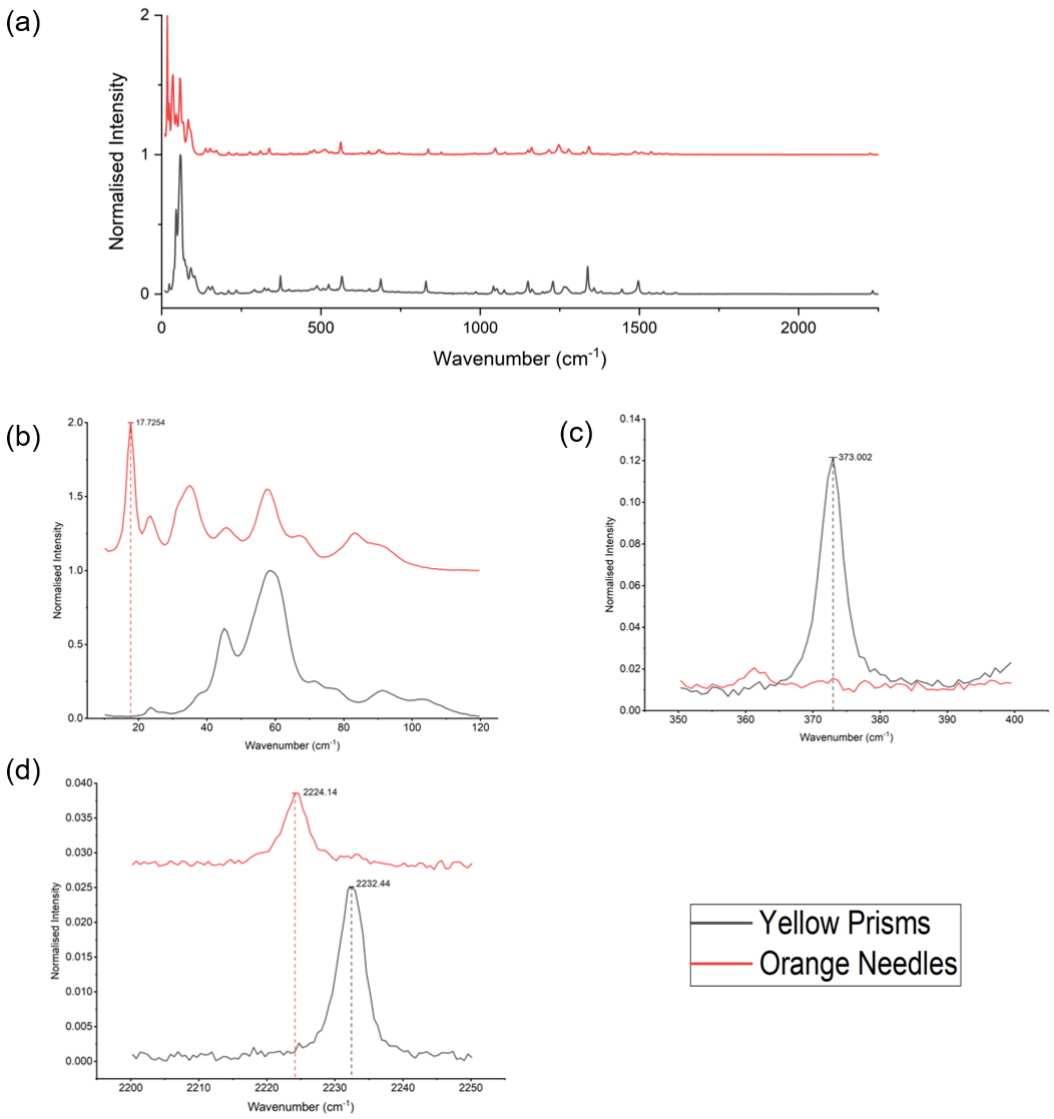

Figure 66 - Raman spectra of the orange needle (ON) and yellow prism (YP) forms of ROY. (a) Within a wavenumber range 10-2000cm-1. (b) Showing differences in spectra in the wavenumber range 350-400cm-1 (c) 2200-2250cm-1 (d) 10-120cm-1.

Residence Time Distribution (RTD) Experiments

Figure 67 shows a graph of the results of the RTD experiments for both 2 and 4 units. This is presented as θ on the x-axis, which is equal to the product of the volumetric flow rate and the time over the reactor cascade volume, and normalised absorption on the y-axis (normalised to the sum of all individually measured absorption values). Normalised absorption values are plotted as markers, and the lines in between serve as guides for the eye. Further line graphs are plotted for equivalent, theoretical data points, calculated using equation 20. The data shows that the experimental data matches reasonably well with the theoretical model for CSTRs in series. This was found to be the case for previous investigations of the fReactor cascade [126].

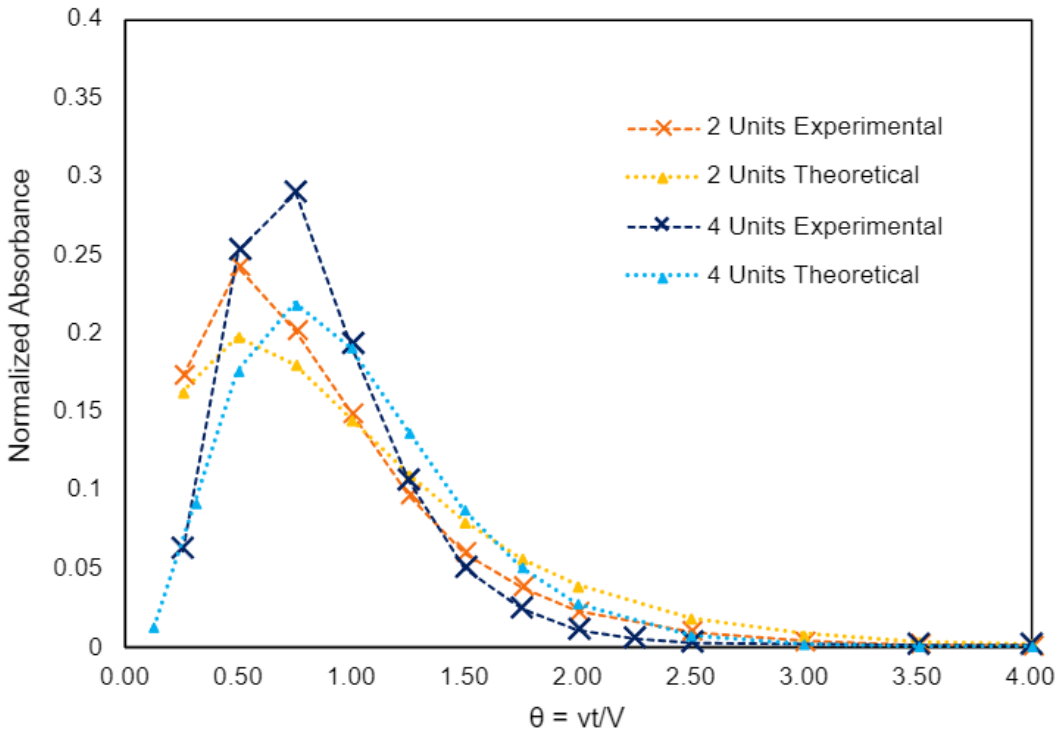

Figure 67 - RTDs for 2 and four units, showing both experimental data and that calculated using the tanks in series model.

4.3.2. Continuous Antisolvent Crystallisation

Initial Screen of Operating Conditions

The results of the screening experiments are shown in Figure 68 for (a) 10g.L^{-1} and (b) 20g.L^{-1}. Solids handling was good in the case of the lower initial concentration, with all attempted experiments showing that a steady-state of operation could be maintained. A range of polymorphs were produced, depending on both residence time and antisolvent ratio. At lower antisolvent ratios, YP was produced exclusively, irrespective of residence time. At an antisolvent ratio of 1.5, ON was produced exclusively at a 30s residence time. At longer residence times of 60s and 120s, a mixture of ON and YP was produced, and at the longest tested residence time (180s), the sample collected showed only YP. This indicates a possible polymorphic transformation that occurs within the span of 3 minutes at an antisolvent ratio of 1.5. Higher antisolvent ratios resulted in either the exclusive production of ON or of a mixture of polymorphs. Residence times longer than 3 minutes were not tested, due to the possibility of insufficient velocity through the transfer tubing, which could result in blockages occurring through the settling of solids.

In the case of the 20g.L^{-1} initial concentration, antisolvent ratios above 1.5 and residence times above 30s resulted in blockages occurring within the fReactor. Blockages began to occur between approximately 1-2 residence times, starting off as a repeated, visible fluctuations in flowrate before the pumps began to stall. Through the windows in the fReactor CSTR units, significant agglomerations of orange crystals could be seen, which was determined to be orange needles upon extraction and optical microscopy analysis. At a residence time of 30s, a mixture of ON and crystals with a yellow needle (YN) morphology was observed. The yellow needles had a similar morphology to the yellow needles polymorph previously reported [276]. Although further analysis was not undertaken to confirm the identity of this polymorph, it was presumed to match that of the reported form due to the identical morphology, colour, and the fact that YN can be obtained from this antisolvent crystallisation in similar circumstances [271, 272].

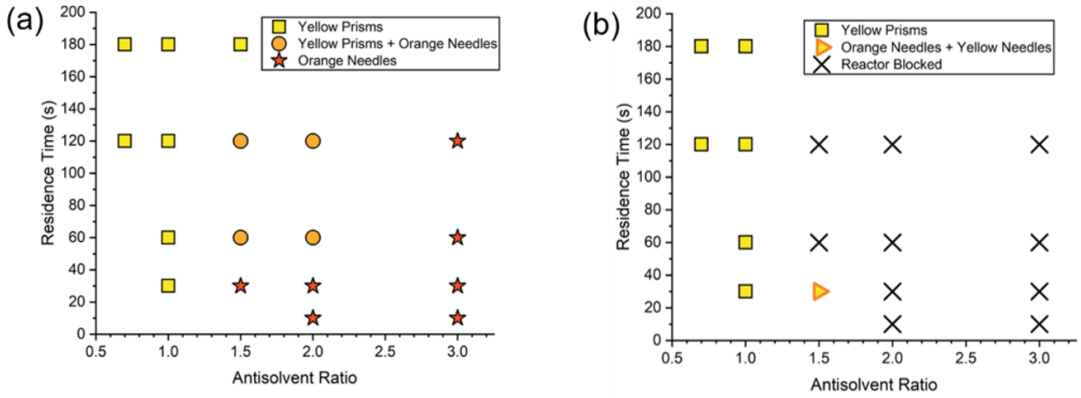

Figure 68 – Results of the antisolvent continuous crystallisation of ROY on the fReactor set-up. (a) 10g.L-1 concentration of ROY, showing blockage-free performance and the production of different ROY polymorphs. (b) 20g.L-1 showed blockages at higher antisolvent ratios and higher residence times.

Microscopy images pertaining to results of the antisolvent fReactor experiments with a 10g.L^{-1} concentration is given in Figure 69.

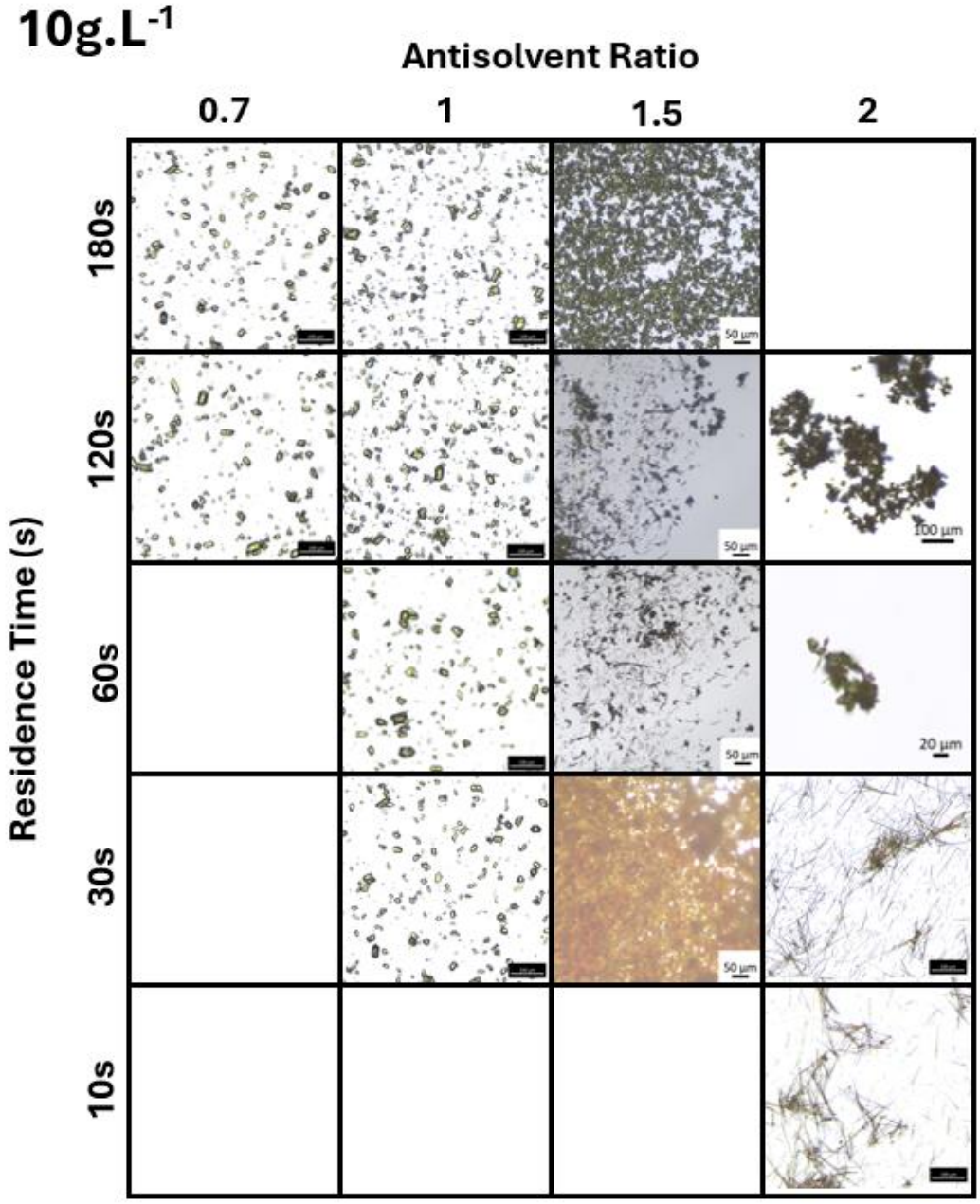

Figure 69 - Microscopy images for the fReactor antisolvent experiment at a ROY concentration of 10g.L^{-1}

Microscopy images pertaining to results of the antisolvent fReactor experiments with a 20g.L^{-1} concentration is given in Figure 70.

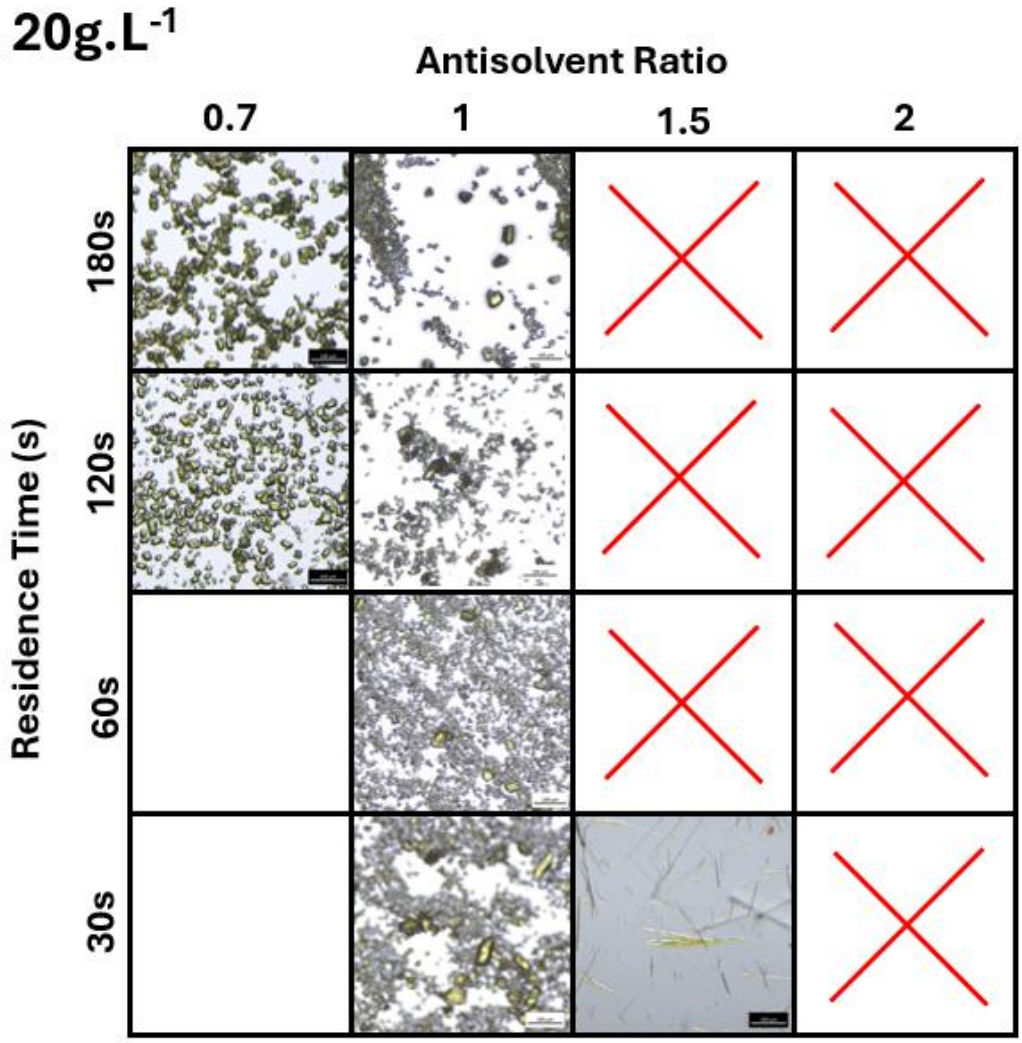

Figure 70 - Microscopy images for the fReactor antisolvent experiment at a ROY concentration of 20g.L^{-1}

The blockages at the higher concentration occurring under the visible presence of needle morphology crystals is potentially indicative of a morphology-dependent blocking propensity. The morphology of crystals is known to be a factor that can affect the extent of agglomeration [277-279]. Agglomeration has previously been considered to take place in three stages: collision of crystals, adhesion of crystals due to attractive forces (forming aggregates), and finally the growth of aggregates into polycrystalline agglomerates [280, 281]. A mechanism by which the blockages can occur now be proposed. Under initial low solids loading, ROY solids nucleate as the ON-form, and subsequently undergo collisions and adhesion to form initial agglomerates. These then undergo growth to form agglomerates large enough to disrupt the magnetic fleas present inside the fReactor units. Slowing down the

magnetic fleas results in a reduction in the shear forces present within the fReactor unit, allowing for settling of ROY crystals within the exit and entrance ports of the fReactor unit. These continue to grow with the constant input of fresh solution and antisolvent, resulting in eventual blockage. It is proposed that at lower concentrations (as in the 10g.L^{-1} experiment) there may not be sufficient solids loading to initially disrupt the stirring provided by the magnetic fleas, hence the lack of blockages even during the production of needle-like crystals.

Maintaining a high rate of stirring is vital to the prevention of blockages. An experiment was carried out with a residence time of 60s and an antisolvent ratio of 1 within the fReactor cascade without stirring present. Previously, the fReactor could operate seemingly indefinitely without blockages occurring with stirring switched on. However, blockages were found to rapidly occur without stirring. Together, this shows the importance of a combination of morphology and stirring on the prevention of blockages within the fReactor cascade. As such, the performance of the fReactor in alleviating blockages during continuous crystallisations could be improved by including more robust agitation techniques, such as overhead, mechanical stirrers as opposed to magnetic fleas. Sonication has also been previously applied to successfully alleviate blockages in small-scale continuous crystallisers [282, 283]. Applying this to the fReactor cascade, particularly focussing on regions of low hydrodynamic intensity (such as the transfer tubing between fReactor units) could help to prevent blockages occurring.

In-line PXRD characterisation

Results of the calibration experiments are shown in Figure 71. Following the collection of raw diffraction data, baseline correction was applied to the region of 2θ = 14-16°, isolating the (120) peak of YP-form ROY, as shown in Figure 71(a). Clearly, there is a visible increase in the size of the peak with an increase in solids fraction. This is expected - a higher solids fraction results in more diffraction planes for X-rays to diffract off for a single acquisition. Each (120) peak was integrated to get the peak area, which were subsequently plotted against the known cumulative solids fraction, as shown in Figure 71(b). A linear fit was applied to the data, with a high R^2 value (0.98857) indicating a good fit. This lends evidence to the linear scaling of peak area with solids fraction as observed previously with $CaSO_4$ (chapter 2) and in previous publications [195].

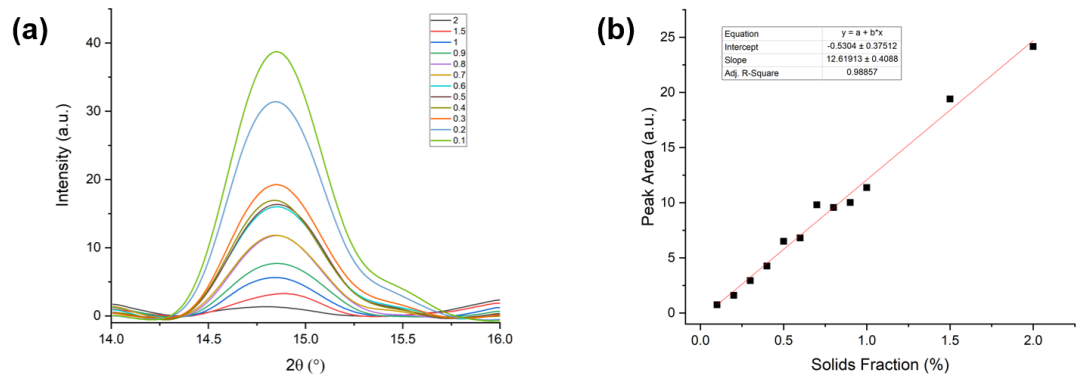

Figure 71 – Results of the calibration experiment for ROY with the in-line PXRD apparatus. (a) Baseline-corrected diffraction data for the range 14-16°, showing the (120) reflection for different weight fractions of YP-form ROY. (b) Integrated (120) peak area across different solids fractions, with a linear fit applied to the discrete data points.

As noted in the results of the initial screen of fReactor conditions, with a starting concentration of 10g.L^{-1}, a polymorphic transformation seems to occur within three minutes at an antisolvent ratio of 1.5. As such, in-line PXRD experiments were carried out at this antisolvent ratio, with only the residence time being changed. The total volume of the cascade was assumed to be 8.1mL (including the 0.3mL volume of the small length of tubing at the end of the cascade). The flowrates used for the four residence times is shown in Table 15.

Table 15 – Flowrates used for the antisolvent crystallisation of ROY carried out in the fReactors with subsequent in-line PXRD characterisation.

Residence Time *(min)*	**Total Flowrate** *(mL.min^{-1})*	**Antisolvent Flowrate** *(mL.min^{-1})*	**Solution Flowrate** *(mL.min^{-1})*
0.5	16.2	9.72	6.48
1	8.1	4.86	3.24
2	4.05	2.43	1.62
3	2.7	1.62	1.08

Figure 72 shows the obtained diffraction patterns for the four different residence times explored. Some differences are immediately noticeable within the peak intensities, particularly for peaks that are specific to one polymorph of ROY. At 2θ = 16.7°, the (013) peak which is exclusively found for the ON-form of ROY is present at a near identical intensity at 30s- and 1-minute residence times. Under a 2-minute residence time, the size of the peak is seen to diminish, and at a 3-minute residence time it has almost disappeared. However, there are other peaks in each of the four residence

times screened that are associated with each of the forms of ROY. For YP, these are: (101) @ 14.96°, (011) @ 11.8°, (130) @ 21.61°. For ON, there is the (**1**11) at 24.1° present in all three samples. This indicates the presence of both polymorphs in all four samples, contradicting the off-line experiments. This can perhaps be explained by considering the 2D diffraction data, pre-integration, an example of which is shown in Figure 73.

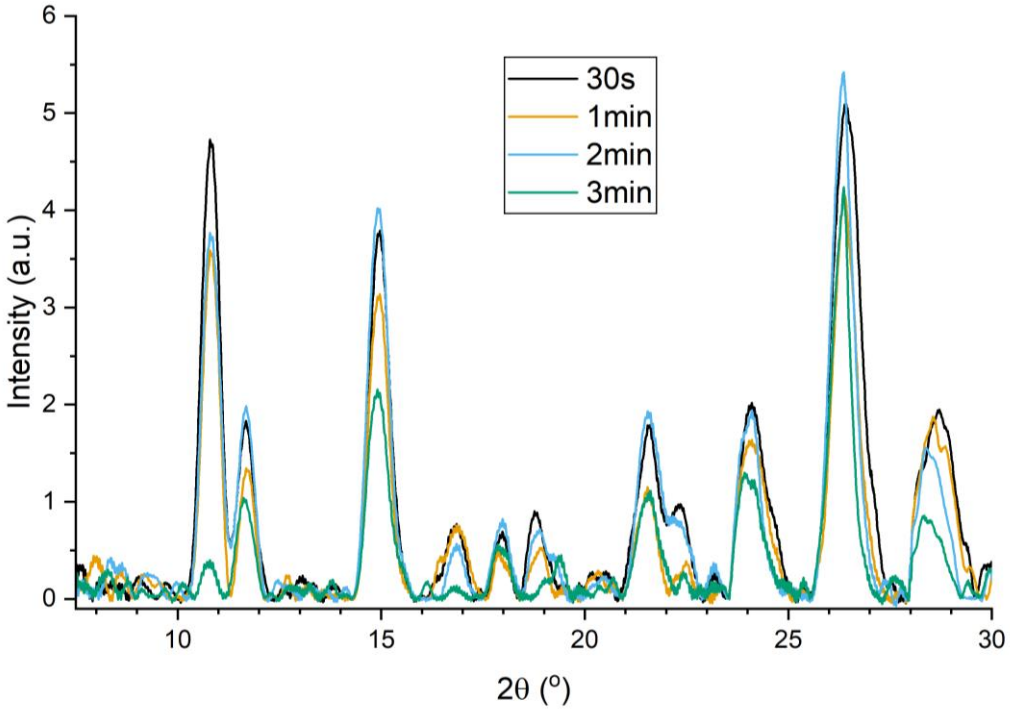

Figure 72 – Obtained PXRD patterns for the antisolvent crystallisation of ROY in the fReactor cascade at four different residence times, with in-line characterisation taking place in the flow-cell.

Figure 73 shows the 2D diffraction data obtained for the 1 minute experiment. Although powder rings can be seen towards the centre of the diffraction pattern, there are also significant bright spots around the image. These bright diffraction spots are the result of particles sticking to the window, and the same particle being scanned with the X-ray source throughout the course of a single acquisition. As such, these particles are not representative of the assumed residence time of the system, and dominate the obtained X-Ray diffraction data. Most likely, particles begin to stick to the window from a time before the system has reached a steady-state, when there is often a visible and variable mixture of polymorphs present in the system. The presence of YP form particles at the 30s residence time experiments suggest that even fast flow-rates are not sufficient to provide enough shear force to prevent particles from attaching to the window walls. Interestingly, this issue was not observed

for the $CaSO_4$ system (which used a similar range of residence times) with the Kapton tubing referred to in chapter 3. This suggests that the sticking of particles to the analysis windows could be a function of the window material and / or the crystal system being studied.

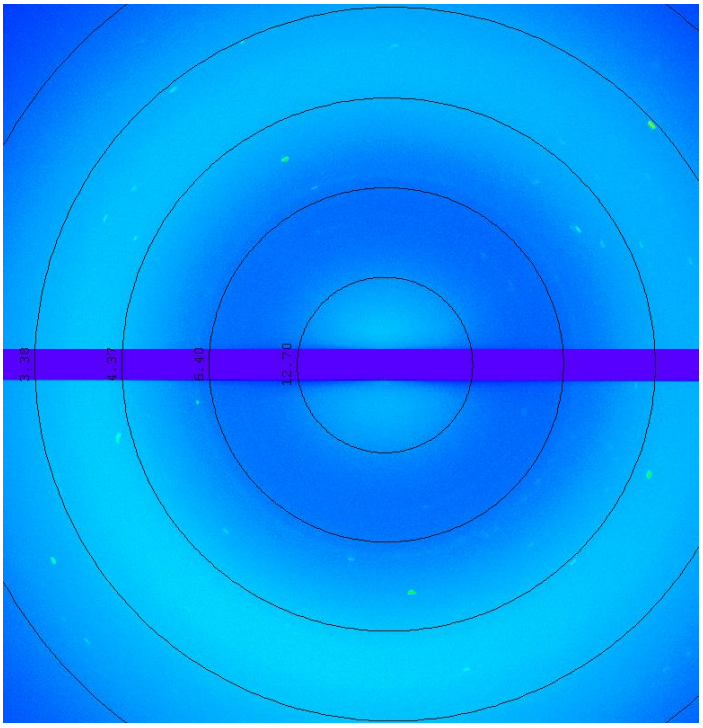

Figure 73 - 2D raw PXRD acquisition from the flow-cell following the fReactor, for the crystallisation of ROY. Small dots indicate sticking of material to the flow-cell walls.

4.4. Conclusions

The antisolvent crystallisation of ROY was carried out in the fReactor continuous flow reactor at different solute concentrations, antisolvent ratios, and residence times. At the lower solute concentration, two different polymorphs could be produced at a steady-state: the yellow-prism (YP) form and orange-needle (ON) form of ROY, both of which were previously characterised using off-line PXRD and Raman spectroscopy. At an antisolvent ratio of 1.5, varying the residence times of the fReactor cascade led to the metastable ON-form being produced at lower residence times and the more stable YP-form being produced at higher residence times. This is indicative of a polymorphic transformation taking place and highlights the ability of the fReactor to facilitate the screening of experimental conditions and the identification of transient crystallisation processes occurring. At the higher solute concentration, blockages began to occur during the production of the needle morphology ON-form of ROY. A proposal for the mechanism underpinning the blockages is made, wherein the needle-like morphology results in agglomerates which disrupt the magnetic stirring fleas, resulting in rapid build-up of material in the fReactors and blockages. No such blockages occurred when producing YP-form ROY at lower antisolvent ratios, lending evidence to the suggestion that this blocking mechanism is morphology-dependent. The transformation that seems to occur was studied using in-line PXRD and a custom-made flow-cell placed in series after the fReactor cascade. Solids sticking to the walls of the flow-cell resulted in unreliable data being gathered, as shown by the bright spots in the 2D diffraction data.

Although the fReactor cascade does show promise for facilitating and studying antisolvent crystallisations (potentially with in-line characterisation techniques), several improvements could be made to assure performance. Firstly, more robust methods of stirring should be introduced to handle greater solids loads and difficult to process crystals (such as those that extensively agglomerate or possess needle morphologies). To allow for crystallisation monitoring to take place with in-line PXRD, a better designed flow-cell should be considered that does not allow for encrustation at the point of analysis. This would allow for crystals to only be measured in the bulk flow, which would give more reliable and accurate time-resolved data. This could be achieved either through the use of a smaller diameter (which would result in a faster velocity and could result in the detachment of crystals from the window walls) or an alternate material or coating that shows a lower affinity to the crystals in order to prevent sticking.

5. Development of a Seeded Continuous Crystallisation route for Succinic Acid

5.1. Introduction

5.1.1. Cooling Crystallisations for Industrial Processes

Cooling crystallisations are useful for industrial processes where there is a large difference in solubility between two temperatures. This allows for economically viable extraction of the solute from the solution as a solid form, which can then be filtered out. The generation of supersaturation can easily be controlled through manipulation of the cooling rate. This in turn leads to control of the relative nucleation and growth rates, which in turn facilitates control of the end size of the crystals. Combined with techniques such as seeding and *in situ* monitoring of the crystallisation process, model-free or model-based approaches have been demonstrated to control crystal size distribution (CSD). The CSD is effectively the range of crystal sizes of a powder sample of crystals expressed as a frequency distribution. The size can be expressed as either a 1D length measurement (measuring a single length of the crystal), a 2D length measurement (capturing two different length measurements of a single crystal), or a 3D length measurement (capturing three different lengths). Furthermore, a distribution can be expressed of the volume of crystals, which can easily be converted to mass by accounting for the density [284].

Population balance modelling (PBM) can be used to account for how the different individual rates of crystal growth, nucleation, agglomeration and attrition change the CSD over time during a crystallisation [285]. Because of the mathematics involved in this (requiring the solving of partial differential equations through either numeric of arithmetic means), software is typically used to solve the population balance equations (PBE) underpinning the model. In the sequential parameter estimation approach of Perez-Calvo and co-workers, individual, well-designed experiments are undertaken to individually measure the rates of growth, primary and secondary nucleation, attrition, and agglomeration of a small organic molecule undergoing cooling crystallisation [286]. Accounting for the effect of supersaturation on the rate of these processes allowed them to be combined into a single model on PBM software, allowing for supersaturation profiles to be designed to achieve the desired end CSD. This methodology is showcased graphically in Figure 74.

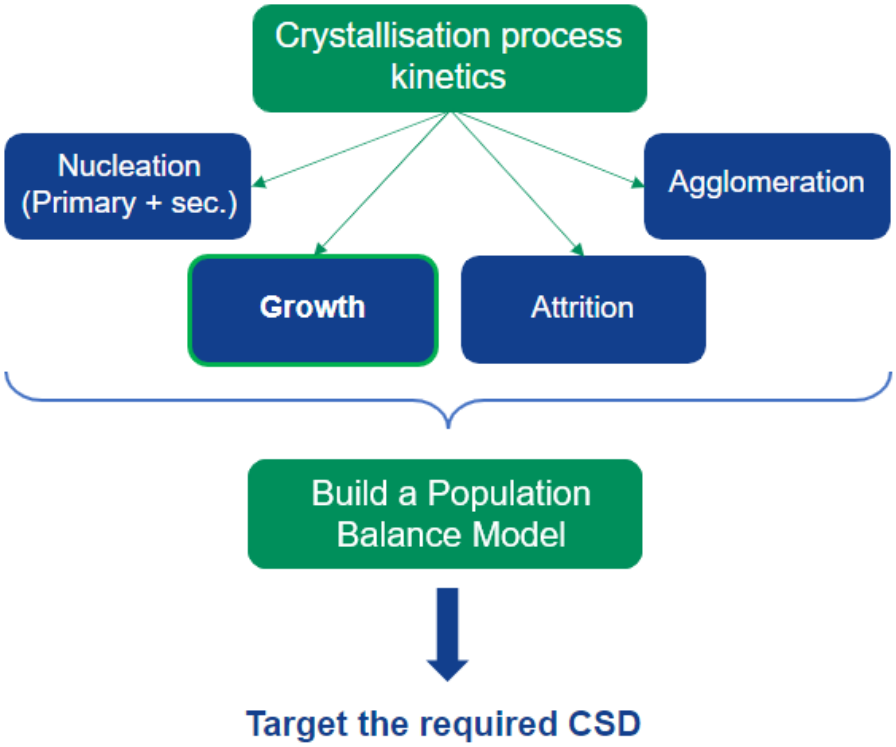

Figure 74 - Illustration of the sequential parameter estimation technique of Perez-Calvo et al., wherein individual, well-designed experiments are performed to measure nucleation, growth, attrition, and agglomeration kinetics. These rates can then be used to create a PBM of the process, allowing the targeting of desired CSD.

5.1.4. Seeded continuous cooling crystallisations

Seeded crystallisations are challenging to replicate in a continuous-flow platform owing to the inherent complications associated with particulate handling. Seeding in a continuous crystallisation will typically rely on either the spontaneous generation of seed crystals followed by the application of a cooling gradient [117, 287] or the input of a suspension of seed crystals as a slurry [288]. Seeded continuous cooling crystallisations have shown the ability to operate with fewer blockages than the equivalent non-seeded crystallisation [289]. This is due to the reduced supersaturation present during seeded crystallisations, supressing primary nucleation on the walls of the crystalliser, reducing the risk of encrustation. Seeding in a continuous crystallisation platform has also proven to be beneficial in enhancing polymorph control [290], in much the same way as in batch processes.

Eder and co-workers made use of a coiled tubular crystalliser with a small internal diameter of 2mm for the continuous seeded crystallisation of acetylsalicylic acid

(ASA) [48]. Two input streams were used – an undersaturated stream at a high temperature, and a seed crystal suspension at a lower temperature. With the crystalliser itself kept at ambient temperature, this results in a cooling gradient being present across the length of the crystalliser. Schematically, this is shown in Figure 75. Besenhard and co-workers extended the concept of using a suspension of seed crystals to a segmented-flow continuous crystalliser [288]. Passing the tubing through alternate heating and cooling baths, and in combination with in-line analysis techniques such as image analysis and laser diffraction, enabled control of CSD through the dissolution of fine crystals and control of growth - a technique which had previously been confined to batch crystallisations [291]. This demonstrates how advances in continuous crystallisation platform design and operation can enable even complicated crystallisation control techniques to be replicated in continuous flow.

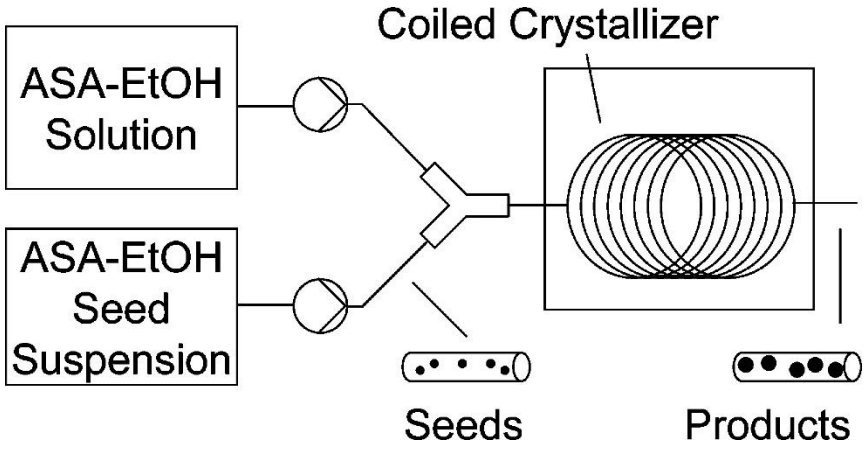

Figure 75 - Schematic of the continuous tubular crystalliser used by Eder and co-workers to enable the seeded crystallisation of ASA [287].

5.1.5. Proposal and Plan

The proposal for this set of experiments is to use the sequential parameter estimation method of Perez-Calvo and co-workers [286], specifically the extraction of growth rate, within a continuous flow platform. This is to be done by performing a continuous seeded crystallisation under isothermal conditions, and tracking the growth rate across the length of the crystalliser using an appropriate PAT technique. This would represent the first such transfer of this growth rate estimation methodology to a continuous flow platform, as well as one of the few examples of a continuous flow seeded cooling crystallisation occurring isothermally. The results of the continuous-flow experiments will be compared to the equivalent experiment in batch through comparison of measured CSDs. PBM will be used to extract growth rate parameters

in both experimental cases. The fReactor system will be used as the continuous crystallisation platform, which will extend the demonstration of this platforms capabilities to cover seeded continuous cooling crystallisations. A successful demonstration of these experiments will more broadly serve as a proof of concept that crystallisation kinetics can be acquired using small-scale continuous-flow apparatus, via analysis at a steady-state with respect to time. This will prove useful in terms of future automation of such experiments. Succinic Acid (SA) was chosen as the model crystallisation compound for these experiments.

5.2. Methods

Most of the work completed as part of this project took place within the laboratories of the Process Studies Group located at Syngenta Group's Jealott's Hill research and development site in Berkshire, UK. This included work involving the use of the Technobis Crystalline instrument, Mettler-Toledo EasyMax synthesis platform, ReactIR and FBRM probes, Malvern Morphologi G3, and the use of the fReactor for continuous seeded crystallisations. Furthermore, modelling and analysis was also completed at this site using Siemens gPROMS formulated products software.

5.2.1. CSD Measurements

Measurements of CSD of both seed crystals and crystals recovered following experiments was completed on a Malvern Morphologi G3 instrument (Malvern Instruments, Malvern, UK). This makes use of automated image analysis to determine the size of particles dispersed onto a flat glass plate. The dry powder sample is first dispersed onto the plate using a burst of dry air. Next, objective lenses are used to scan over the powder on the plate, taking images. Particles are automatically identified through the contrast between the bright background and dark particles. The software then makes a 'fit' to the outer bound of the particles, and can thus provide detail on the area , circumference, and circular-equivalent diameter of the particles. This has advantages over scattering-based approaches, as it does not rely on an approximation to a sphere and is thus better suited for crystals with highly isotropic morphologies (such as needles). It does require, however, efficient sample dispersion to break-up unwanted aggregates of crystals which may form upon drying.

5.2.2. Solubility

Solubility of Succinic Acid in water was measured using a *Crystalline* instrument (Technobis Crystallization Systems, Alkmaar, Netherlands). This instrument (shown Figure 76(a)) consists of 8 different 'wells' within which 8mL silanised glass vials

(containing the compound and solvent of choice in known amounts) can be placed. These can be heated and cooled according to user-specified heating and cooling cycle(s), and a camera and turbidity probe present within each vial captures the images and turbidity data across these cycles. The point of nucleation (observed during cooling) can be determined from when transmission drops, measured through turbidity, or by simply observing when crystals appear with the camera. Likewise, the point of maximum solubility (observed during heating) can be placed at the point where no crystals are present, according to the images captured by the camera. The lids of the glass vials can contain either a 'hook' or 'impeller' stirrer (the former is shown in Figure 76(b)), to stir slurries within the vials, resulting in a homogeneous distribution of both the material within the vial and the temperature of the material. Selecting different concentrations of material within the vials, then subsequently measuring the points of nucleation and maximum solubility, allows for both the solubility and MSZW to be tracked across concentration and temperature (giving up to 8 data points at a time). Although it is good practice to find solubility within the reaction vessel where crystallisations will be taking place (typically in an *in situ* manner), initial experiments with the Crystalline instrument should provide a guide for calibration of the *in situ* IR probe and give an idea as to the feasibility of future seeded crystallisations (i.e. is the MSZW wide enough to provide sufficient operational flexibility).

Figure 76- (a) Technobis Crystalline instrument used for solubility determination. (b) Silanised vial and hook impeller used within the instrument.

Five concentrations of SA in water were used for the solubility experiments, as shown in Table 16. These were selected (based on previous literature solubility data [292]) to give solubility points approximately across a temperature range of 10-80°C. For each solubility experiment, a heating rate of 0.2°C / min was applied to the vials in the crystalline from a temperature of 22-90°C. A one-hour hold was then used to

ensure complete dissolution of the crystals, before a cooling rate of 0.2°C / min was used to take the temperature back down to 22°C.

Table 16 – Concentrations of SA in water used for the solubility experiments in the Technobis Crystalline instrument. Concentrations are expressed as a mass of SA per total mass of SA and solvent.

Vial	Concentration (g_{SA}/g_{total})
1	0.1023
2	0.1556
3	0.2019
4	0.2990
5	0.5475

5.2.3. Modelling of Seeded Batch Crystallisations of Succinic Acid

Principles and Apparatus

The aim of the seeded batch crystallisations was to add seed crystals within the metastable zone under isothermal conditions, resulting in purely growth occurring to consume the supersaturation. In monitoring the drop in concentration following the addition of seeds (as growth occurs) over time, a mass-weighted growth rate can be regressed using population balance modelling. In combination with data regarding the seed CSD and total mass, as well as physical property data such as density of solid crystals, a prediction can be made as to the final product CSD. This process can be shown on a plot of temperature vs concentration (Figure 77). The temperature is reduced at a fixed concentration (red line) before being held isothermally. Seed crystals are then added to the batch reactor (at the 'star' position) and supersaturation is thus consumed by growth, resulting in a drop in concentration until the point of solubility is reached. This process assumes that primary and / or secondary nucleation, agglomeration, aggregation, or breakage are not occurring (which would result in errors in the prediction of end CSD).

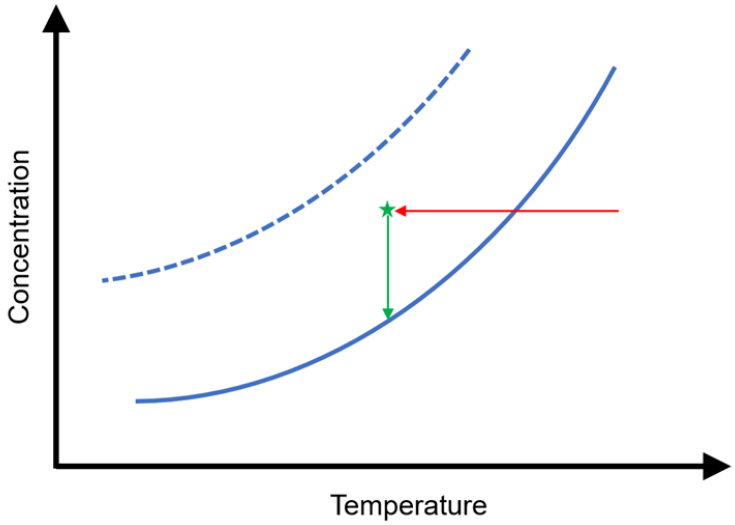

Figure 77- Principle behind seeded isothermal desupersaturation as expressed on a graph of temperature and concentration. The temperature is reduced to cause the system to become supersaturated, but within the metastable zone, meaning nucleation does not occur. Seed crystals are introduced at a certain isothermal temperature, and supersaturation is consumed.

The seeded batch crystallisations were carried out with a Mettler Toledo EasyMax 102 synthesis platform (Mettler Toledo, Grieffensee, Swizerland) – the apparatus is shown in Figure 78. This consists of a temperature-controlled heating jacket surrounding a 100mL glass reaction vessel with a motorised overhead impeller. A temperature probe was connected to Mettler Toledo iControl software allowing for temperature control of the reactor. A Mettler Toledo ReactIR ATR-FTIR probe was included in dedicated ports in the top of the reactor vessel. This took in situ IR spectroscopy measurements of the reaction mixture. A calibration was developed between the concentration of SA and IR spectroscopy measurements, enabling quantitative assessment of concentration. A Mettler Toledo FBRM probe was also included, which took chord length distribution and particle count measurements.

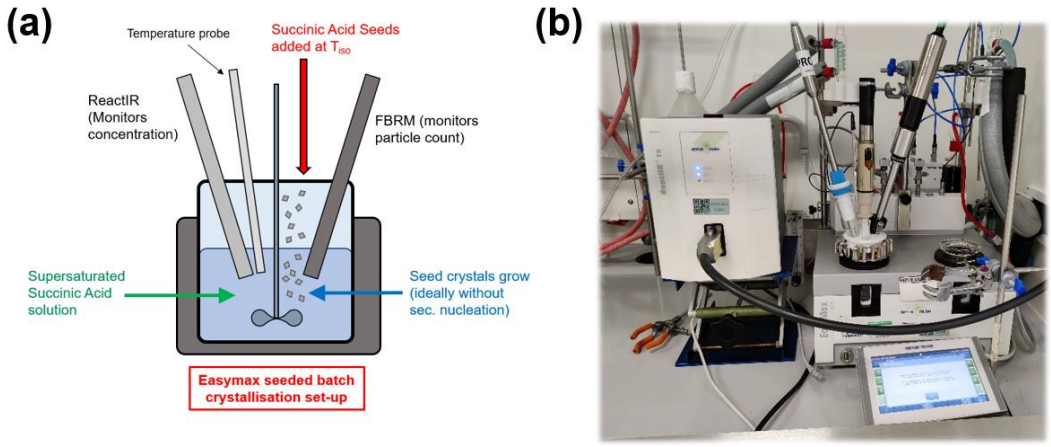

Figure 78 - Apparatus used for the seeded isothermal batch crystallisations. (a) Schematic of the apparatus showing various probes used to monitor the crystallisation within the EasyMax reactor. (b) Photograph of the set-up.

Population Balance Modelling

Population balance modelling of the crystallisation was accomplished using gPROMS FormulatedProducts software [293]. This software solves the PBEs numerically using the high-resolution finite volume scheme with flux limiting function (HRFVS-FL), the specifics of which have been discussed in the literature [294]. The goal of the use of the software was to solve the PBEs to regress growth kinetics from the input time-resolved concentration data from the IR probe. The crystal growth rate was assumed to be surface-integration limited (as opposed to volume diffusion limited) due to the high mixing intensity in the crystallisation environments. This can thus be expressed using the Mersmann equation shown in equation 38, where the parameters shown in bold are those to be fitted.

$$G(L) = \boldsymbol{k_g} exp\left(-\frac{\boldsymbol{E_{A,g}}}{RT}\right)\left[\frac{c_l(L) - c^*}{\rho_c}\right]^{\boldsymbol{g}} \quad 38$$

Where G(L) is the growth rate for a dimension L, k_g is a rate constant, $E_{A,g}$ is activation energy, c_L is the concentration at the face of the crystal, c* is the solubility at a temperature T, ρ_c is the density of the crystal solids, and g is the supersaturation dependency of the surface controlled growth. A material database entry was used which had previously been constructed by another user (Jennifer Webb) {Webb, 2022 #319}. This specified chemical-physical properties of SA, such as melting point, heat capacity, and density, among other parameters. Solubility was specified within the software as a 3rd order polynomial model regressed from solubility experiments.

Calibration of ReactIR spectroscopy measurements to Succinic Acid concentration

Calibrations can be constructed to relate variations in intensity of IR spectroscopy measurements at different wavenumbers to concentration of solutes. IR spectroscopy probes represent a useful way of continuously characterising solute concentration, but require an accurate calibration model to be constructed. This must account for temperature as well as concentration of solute, as the former also affects the intensity of spectra.

As such, the ReactIR probe was calibrated under different concentrations at four different temperatures, with conditions specified in . A background was first taken in the empty reactor vessel, before solvent and solute at known masses were discharged into the vessel. Stirring was engaged at 300RPM and the solids were left to dissolve. FBRM counts in the chord length range 10-100μm were monitored to gauge the point of complete dissolution, which was presumed to occur once the counts had plateaued. An IR spectrum was then acquired. More solids were then added, and the process was repeated, increasing temperature after four concentrations at a particular temperature.

Table 17 – Temperatures and concentrations of SA in water (on a mass per total mass basis) used for the calibration of the ReactIR probe within the EasyMax reactor platform.

Temperature (oC)	Concentration (g_{SA}/g_{total})
20	0.01261
20	0.02515
20	0.03766
20	0.05010
40	0.07515
40	0.07515
40	0.10019
40	0.12497
40	0.13746
50	0.17498
50	0.17498
50	0.18753
50	0.19997
50	0.21248
60	0.23757
60	0.23757
60	0.26258
60	0.28767
60	0.31269

The concentration of SA was calibrated to the relationship between the band associated with the stretching of the carbonyl group of SA at 1806-1675cm^{-1}, and the water peak at 1671-1494cm^{-1} (illustrated in Figure 79 [295]). Integrating between these wavenumbers and taking the quotient of the former against the latter gives a Peak Area Ratio (PAR), shown in equation 39. This calibration has previously been used to monitor the concentration of SA in water using an *in situ* FTIR probe [295].

$$PAR = \frac{Peak\ Area\ 1806{:}1675\ cm^{-1}}{Peak\ Area\ 1671{:}1495\ cm^{-1}} \qquad 39$$

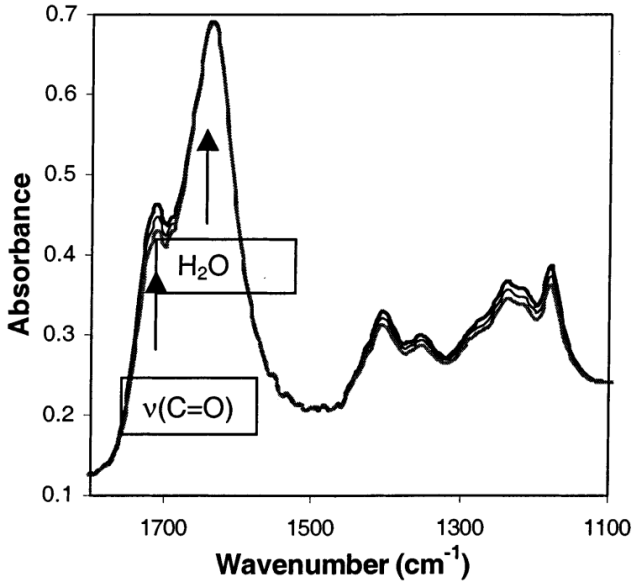

Figure 79– IR spectroscopy bands used for the calibration of SA concentration. The stretching of the Cabonyl (C=O) band of SA was calibrated against the water peak at the lower wavenumbers. Taken from [295].

Monitoring of Seeded Batch Crystallisations of Succinic Acid

Seeded batch crystallisations of SA were carried out at an isothermal temperature of 40°C. A concentration of SA was selected – based on the solubility and MSZW data – such that the system would be in the metastable zone at this temperature. The solution was first heated to 70°C with stirring engaged at 350 RPM, in order to ensure complete dissolution of the SA. Dissolution was judged to be complete once the FBRM counts in the size range of 10-100µm reached a constant minimum value for at least 60 mins. Cooling was then applied to reduce solution temperature down to 40°C at a rate of 0.7°C/min. Once the isothermal temperature was reached, seed crystals were added at a mass equivalent to 3 wt.% of the total mass of the solution. The IR spectra from the ReactIR probe was then monitored to determine the point of complete consumption of supersaturation (that is, when the predicted concentration reached a constant minimum value).

5.2.4. Continuous-flow Seeded Crystallisations of Succinic Acid

A schematic of the apparatus used for the monitoring of seeded crystallisations in continuous flow is shown in Figure 80, and a photo of the same set-up is shown in Figure 81. The fReactor system will be used as a continuous crystalliser in a linear fashion (additional ¼-28 threaded ports were drilled into the sides of each CSTR unit to facilitate this). Short (approximately 30mm) lengths of PFA tubing (ID = 1/12”, OD = 1/8”) were used to connect 5 fReactor units in series using standard PEEK fittings

and ferrules. These were places on an IKA RT 5 linear hot-plate stirrer (IKA-Werke GmbH, Staufen, Germany), containing 5 individually heated and stirred positions on which each fReactor unit sat. Two solutions were pumped into the first fReactor unit using Peristaltic pumps (323du, Watson Marlow, Marlow, UK). The first is the higher temperature 'hot' stream, containing SA solution at a high temperature. The second is a low temperature 'cold' stream, containing a saturated solution and seed crystals of SA. Each of these was stored in a round-bottomed flask, placed on top of a hotplate stirrer (stirring engaged at 300RPM).

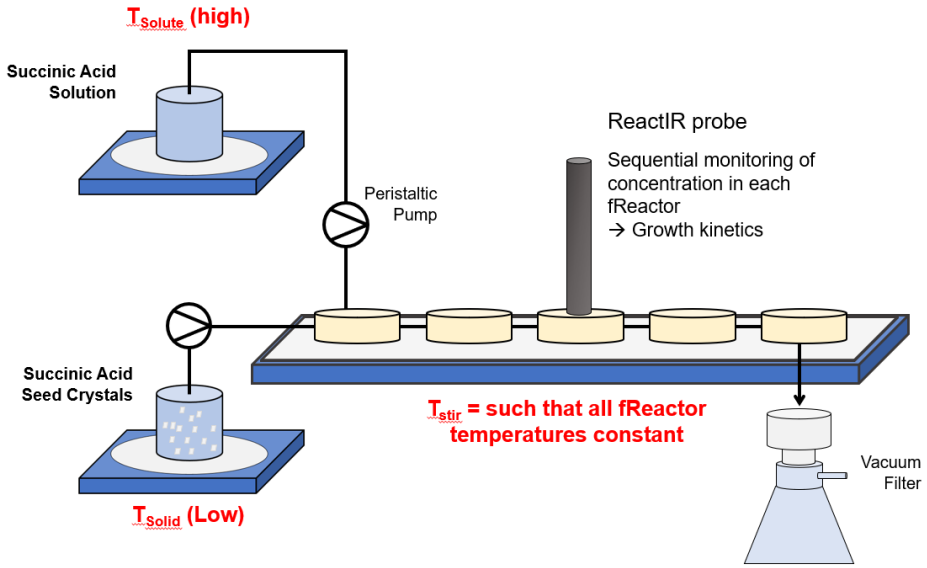

Figure 80 - Schematic of the apparatus used for the continuous seeded crystallisation experiments in the fReactor cascade. Two input solutions are used – seed crystals of SA at a low temperature, and a SA solution at a high temperature. The fReactor cascade is temperature controlled such that all the fReactors are at the same temperature. A ReactIR probe is used to monitor SA concentration.

Figure 81 – Photograph of the apparatus used for the continuous seeded crystallisation experiments, showing the fReactor, pumps, and storage vessels.

To replicate the batch experiments in continuous-flow, the flow-rates and concentrations of the solutions, and temperatures of the three hot-plate stirrers must be carefully selected to ensure that SA is supersaturated, with seed crystals present, in the first fReactor, and that all the fReactors are at the same temperature. This is the equivalent of the red star in Figure 82, where T_{solid} is the temperature of the hot stream, T_{solute} is the temperature of the cold stream, C is the concentration within the first fReactor, and C' is the solubility at the temperature of the fReactor cascade. Because of the connection between the temperature of the fReactors and the flow rate from the hot and cold streams, and the requirement to keep the fReactors at an identical temperature, the residence time within the fReactor cascade is constrained to a single value.

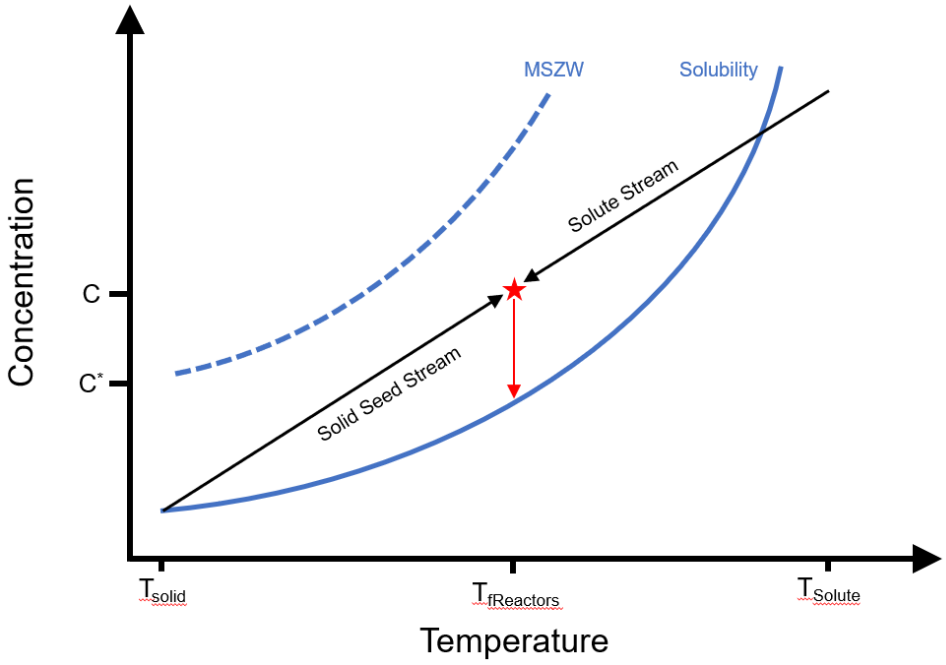

Figure 82 - Graph of temperature vs concentration showing the operating principal behind the use of the fReactor cascade for continuous isothermal seeded crystallisations. The input streams meet at the first fReactor unit – equivalent to the red star – and the concentration drops as supersaturation is consumed.

Two temperature probes were installed within the second and fifth fReactor units. A series of trial-and-error experiments, using just water, were undertaken to determine the correct mixture of flow-rates and temperatures which would result in the desired, consistent temperature within the cascade. The temperature of one stream was fixed at 25°C, and the temperature of the other stream and the hotplate stirrers were varied during these experiments. The flowrates of the two streams were kept equal, but were adjusted, again to adjust the temperature within the fReactor cascade. Once the correct temperatures and flowrates had been found, the concentration of the hot stream could be calculated, in order to result in the SA present in the first fReactor being supersaturated.

To monitor concentration of SA, a custom-made lid for the fReactor was developed to allow a ReactIR probe to be inserted into the fReactor from the top. This sealed the probe in place such that the tip of the probe was in contact with the contents of the reactor, without disturbing the stirrer bar inside. It consists of two parts, both constructed out of PEEK: a lid with a hole in it which attaches to the top of the fReactor with screws, and a threaded collar with rubber o-rings on the inside, which screws

into the lid and forms a seal around the probe. A photo of the fReactor with the ReactIR probe sealed in place is shown in Figure 83.

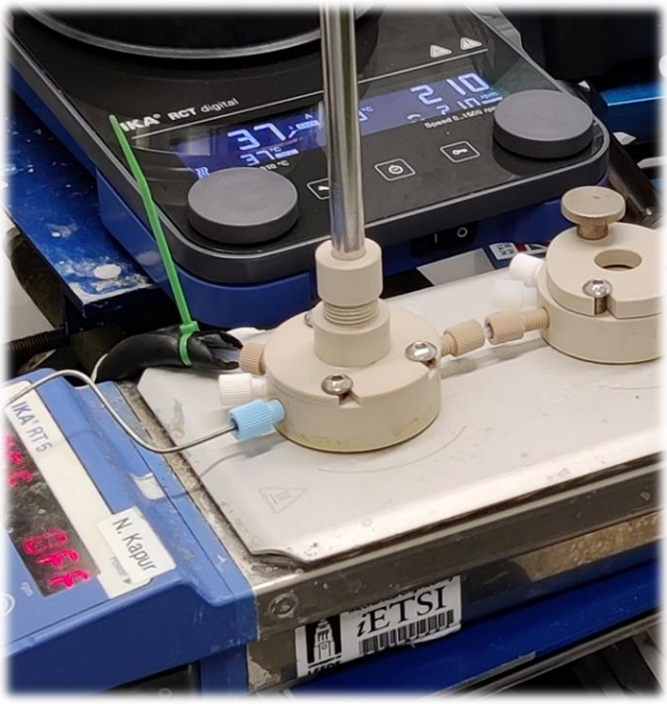

Figure 83 – ReactIR probe sealed in place in the fReactor using the custom-made lid.

5.3. Results and Discussion

5.3.1. Solubility Assessment in Water

Solubility was assessed using the *in situ* imaging function on the crystalline instrument, with typical images from the experiments shown in Figure 84. Below the point of solubility during heating, crystals can be seen clearly in the images. These gradually begin to dissolve as the temperature increases during heating, until no more crystals can be seen. The frame at which the final crystal can be seen is judged to be the point of dissolution, and the corresponding temperature is used for that concentration. Note that some dust particles are present which do not dissolve, which can make it difficult to judge solubility (but these particles will be present at all temperatures, and can be distinguished from SA in terms of morphology). During cooling, the point of nucleation is very clearly established – the solution is typically completely clear during one frame, and nearly saturated with crystals in the next (the equivalent of Figure 84 (c) and (d)). The temperature of the frame with the crystals was used as the value of MSZW.

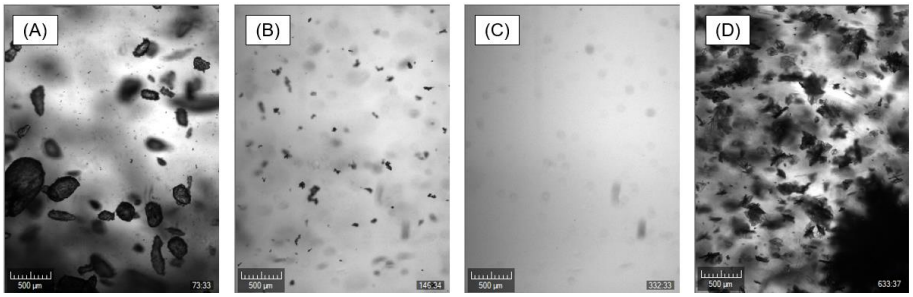

Figure 84 - Camera captures during a typical crystalline experiment. (a) Crystals of SA well below the point on solubility (b) just before dissolution (c) just after the point of complete dissolution, showing dust present (d) immediately after nucleation during cooling.

Measured solubility and MSZW values of the experiment are shown in Figure 85, alongside solubility values from the literature [292]. The solubility data shows a general agreement with the literature data, indicating reasonably accurate estimates of solubility. The MSZW data shows a slightly larger gap between the point of nucleation and solubility at lower temperatures than higher temperatures. Generally, the MSZW appears to be wide enough to allow for reasonable supersaturation to be achieved without spontaneous nucleation, which would in turn allow for seeded crystallisations to be undertaken.

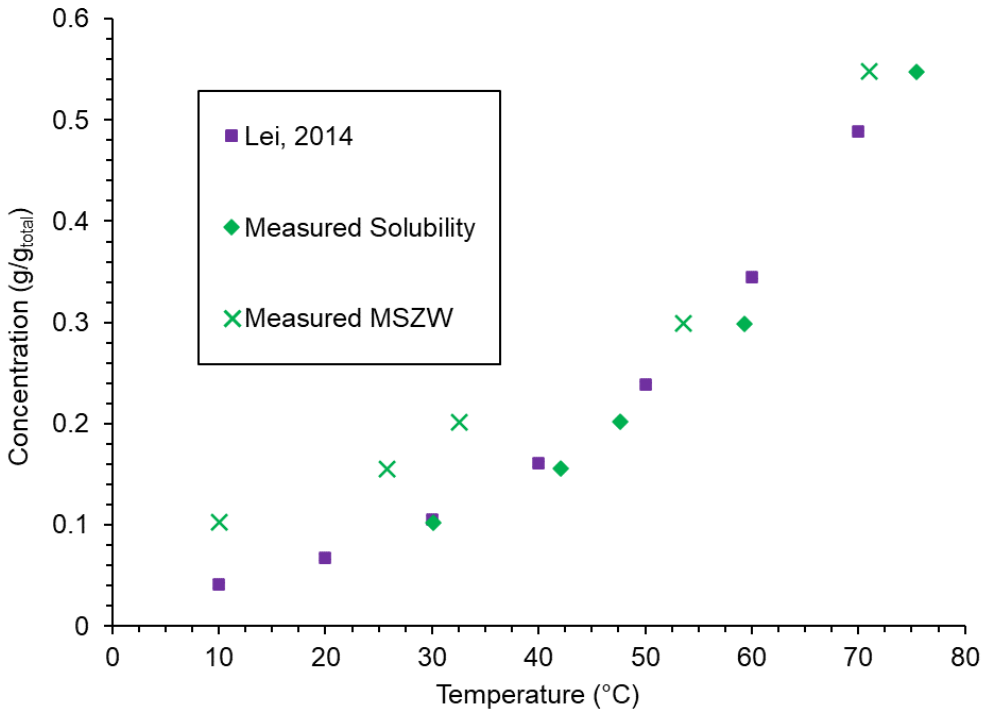

Figure 85 - Measured solubility (squares and diamonds) and MSZW data (crosses) for SA in water across different temperatures as derived from Technobis Crystalline experiments (shown in green). Solubility data taken from the literature is shown in purple [292].

5.3.2. Seeded Batch Crystallisations of Succinic Acid

Calibration of IR spectra to Succinic Acid Concentration

Results of the calibration of the IR spectra from the ReactIR probe are shown in Figure 86. Linear calibrations were drawn for the concentration values at each of the four temperatures studied, with their equation and R^2 values shown in the figure. There is a slight decrease in the steepness of the calibrations with an increase in temperature, highlighting the need to calibrate against temperature as well as concentration. For each, the R^2 values indicate a very tight relationship, showing the applicability of the calibration model for further predictive use.

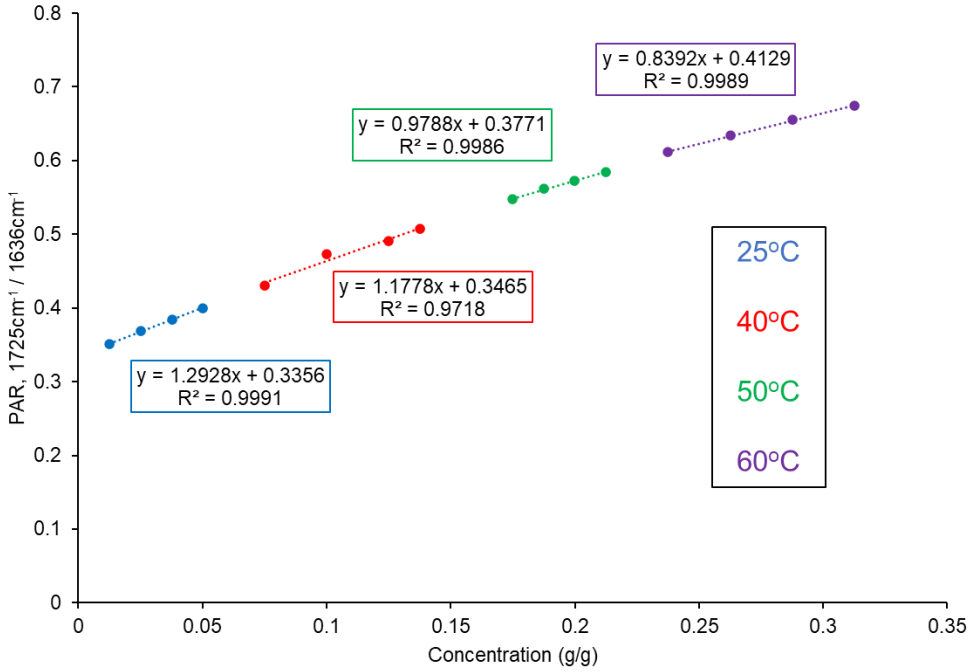

Figure 86 - Calibration of SA concentration to peak area ratio (PAR) taken from the ReactIR spectra. The calibration was performed at different temperatures, as shown in the inset legend.

Characterisation of CSD of Seed Crystals

The CSD of the Seed crystals of SA were characterized using a Malvern Morphologi G3, with the resultant CSD shown in Figure 87. The CSD represents, in this case, the frequency distribution of sizes of crystals weighted relative to their volume, with size represented by the circular equivalent (CE) diameter (that is, the diameter of a circular crystal with an equal area to the measured crystals). The decision to use a volume-weighted frequency expression (as opposed to a number-weighted frequency distribution) accounts for the fact that the majority of the mass in the sample is

accounted for by a relatively small amount of large crystals, as opposed to the many fine crystals. This means that modelling will better account for the effects of crystal growth on size for the crystals which carry the majority of the mass of sample, conferring greater practical benefits.

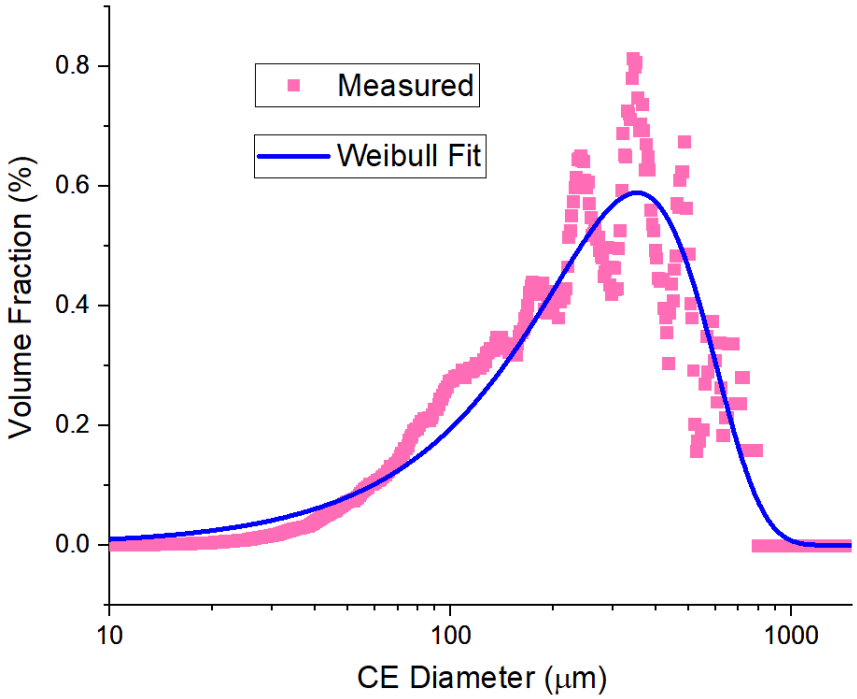

Figure 87 – Measured CSD of the seed crystals of SA from the Morphologi G3 instrument. A Weibull fit is included, which shows a good agreement with the data. The values of the two fitted Weibull parameters are α = 2.3 and β = 452.

A Weibull fit was fitted to the measured CSD data, using FormulatedProducts software. A Weibull fit was chosen over alternative commonly-used fitting models (such as the Lognormal model) due to its ability to better account for the large, visible fines tail at low CE diameter values (even plotted on a log-scale). The equation for the Weibull distribution (for x ≤ 0) is given by equation 40, where x is the variable to be fitted (in this case CE diameter), α is the shape parameter, and β is the scale parameter. Regressed values of α = 2.3 and β = 452 were found to result in the closest fit to the data.

$$f(x;\,\alpha,\beta) = \frac{\alpha}{\beta}\left(\frac{x}{\beta}\right)^{\alpha-1} e^{-(x/\beta)^{\alpha}} \qquad 40$$

Population Balance Modelling of Batch Seeded Desupersaturation of Succinic Acid

Based on the solubility data, an experiment temperature of 40°C was selected, as this gives quite a wide metastable zone width of approximately 10°C. The solubility at this temperature is approximately 0.129g/g_{tot}. In selecting the initial concentration of SA in solution, a consideration was made of the need to have a sufficient amount of solute that would grow out of solution onto the seed crystals that could practically be measured with the IR probe. This should not, however, risk unwanted nucleation occurring at too high a concentration. An initial concentration of 0.149 g/g_{tot} was thus chosen, equivalent to the approximate solubility at 43°C, giving an effective mszw of 3°C.

Figure 88 shows the measured values of concentration of SA over the time following the addition of the seed crystals (t = 0s), as obtained from IR spectroscopy measurements using the calibration previously developed. Qualitatively, it shows a significant decrease in concentration at the point of seeding, which begins to level off before plateauing after approximately 800s. FormulatedProducts software was used to fit the data to the growth rate shown in equation 40. Table 18 gives the fitted parameters to equation 21. The fitted, predicted values of concentration are shown in Figure 88Figure 88.

Table 18 – Regressed growth kinetics parameters (relating to equation 21) taken from the simulation of the batch crystallisation.

Parameter	Units	Value
kg	J/mol	50003.0
Ea,g	m/s	45772.5
g	-	2.40892

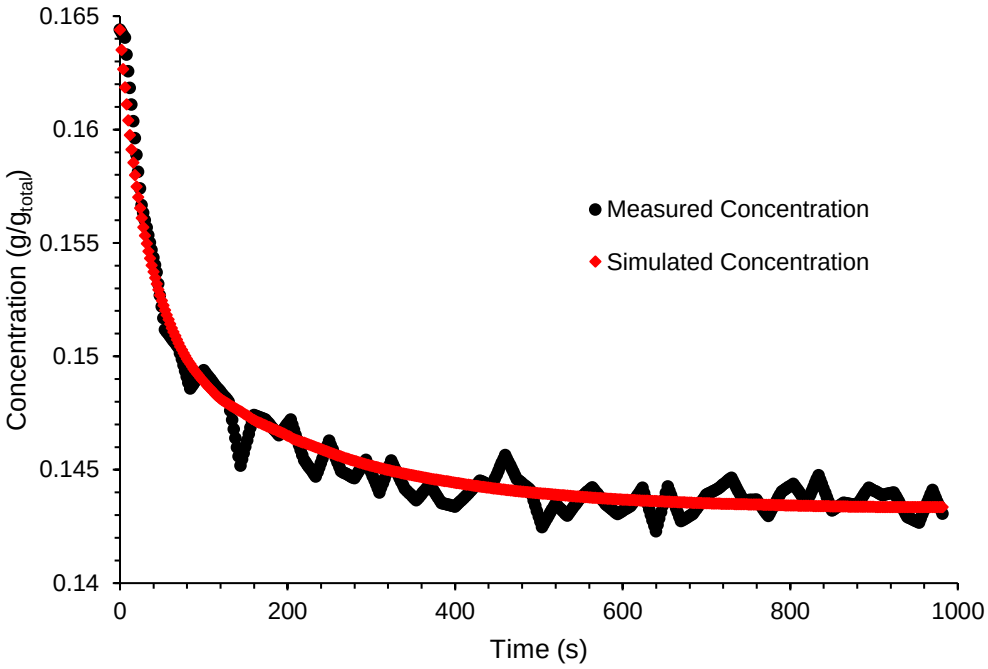

Figure 88 – Measured and simulated concentrations of SA during the seeded batch crystallisation. Measured concentrations were taken from ReactIR measurements using the calibration developed previously. Simulated concentrations were fitted using FormulatedProducts software.

Once the state of equilibrium was reached at 1000s, a pipette was used to quickly take a sample from the batch crystalliser, which was immediately vacuum filtered. This was left to dry, before the CSD of the sample was measured using the Morphologi G3 instrument. The results are shown in Figure 89, alongside measured values of seed crystals and the Weibull fit to the seed crystals (the same as shown in Figure 87). This shows a small shift in the CSD at lower sizes to higher values (from approximately 20-100µm). This is as expected – because it is a volume-weighted size distribution, a greater shift in size values will occur at lower crystal sizes compared to higher crystal sizes for a given supersaturation.

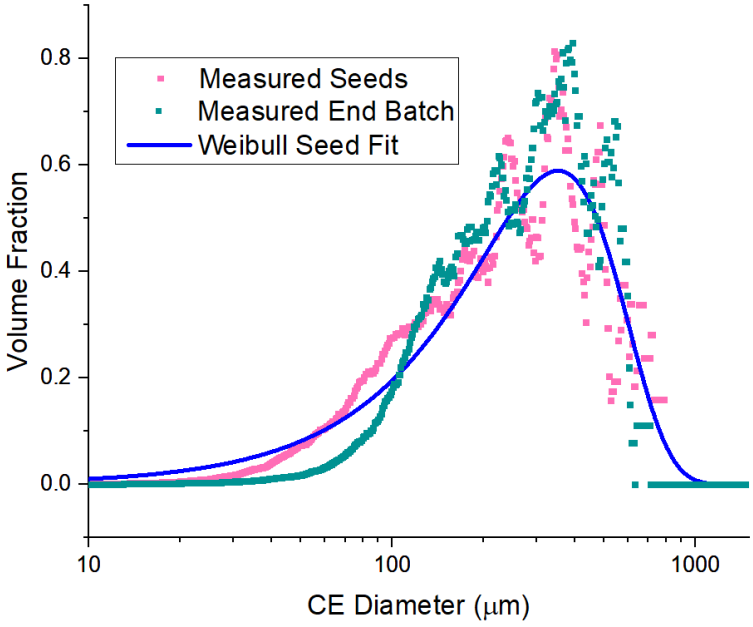

Figure 89 – Measured CSDs of seed crystals and the crystals taken as a sample from the batch crystallisation. For comparison, the Weibull fit to the seed CSD is shown.

FormulatedProducts software was used to simulate the batch crystallisation experiment using the fitted parameters described in Table 18. A prediction of the final CSD was fitted to a Weibull distribution, as shown in Figure 90 alongside a comparison with the measured final CSD. Due to an unresolved software issue, a peak at lower sizes was observed. A second peak at the expected size range was also observed. Because the peak at the lower size ranges would account for only a small proportion of the total volume present, it is assumed that the error caused by this is minimal. As such, a comparison can be made with the peak at higher size values. This shows a broad agreement with the measured values, although there is a slight error in the 100-200µm. This perhaps suggest that there are other, unwanted processes occurring within the crystalliser which would reduce the CSD slightly whilst consuming supersaturation. This could include crystal breakage or secondary nucleation.

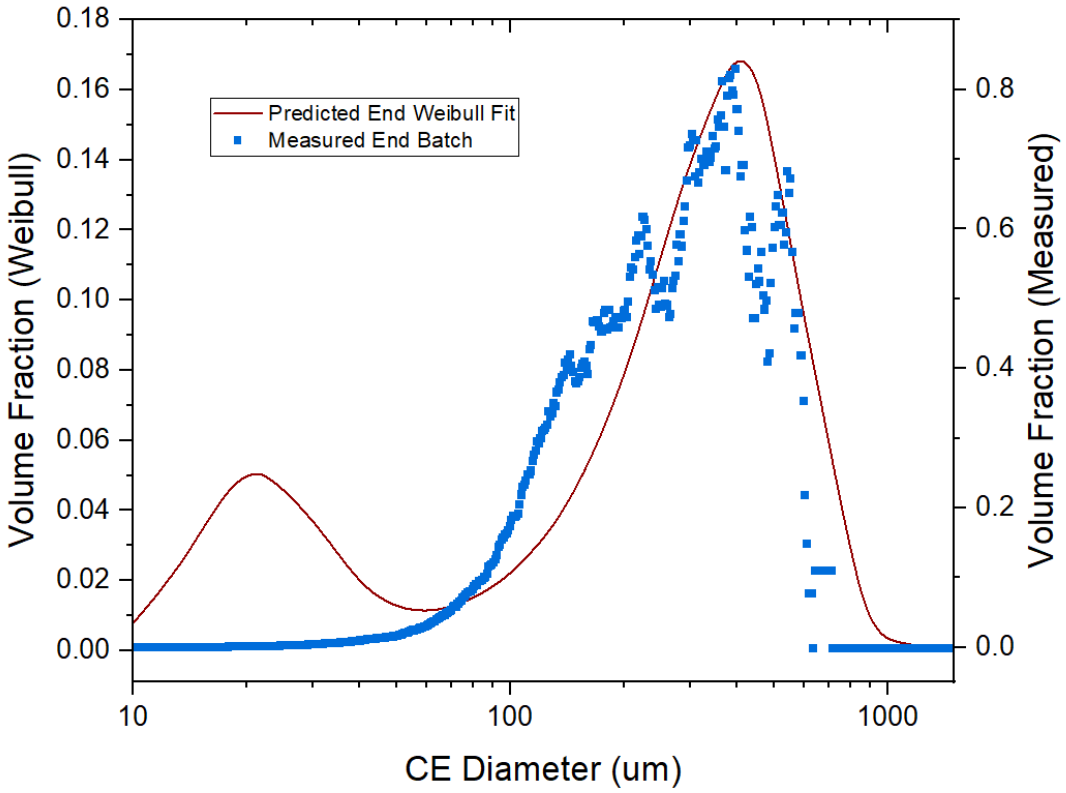

Figure 90 – Predicted Weibull CSD of the crystals from the batch experiment, simulated using the regressed growth rate parameters, alongside the measured CSD.

5.3.3. Continuous-flow Seeded Crystallisations of Succinic Acid

Table 19 shows the temperatures of the hotplate stirrers, flow rates of pumps, and concentrations of SA used for the continuous-flow seeded crystallisations of SA. The flow-rate and temperatures were found using water, and the concentration was determined based on these values and the requirement to be operating within the MSZW. Based on the flowrates used and assuming a cascade volume of 10mL, an average, theoretical residence time of 38s was calculated. This is relatively short compared to the time taken for the system to desupersaturate in the batch experiment (over 10 minutes), which could cause errors in the use of the steady-state measurements of concentration at different positions across the cascade. Also included in Table 19 are measured temperatures of fReactor 2 and 5. This was the closest approximation to the desired temperature of 40°C that could be obtained with this complex system.

Table 19 – Optimised operating conditions for the continuous seeded crystallisation of SA using the fReactor cascade

Parameter	Value	Units
Hot stream holding Temperature	67	°C
Hot stream flow rate	7.9	mL/min
Hot stream concentration	0.290	g / g_{tot}
Cold stream holding temperature	25	°C
Cold stream flow rate	7.9	mL/min
Cold stream seed weighting	6	wt.%
fReactor hot plate stirrer temperature	47	°C
Measured temperature fReactor 2	41.2	°C
Measured temperature fReactor 5	40.5	°C

At these conditions, the fReactor could run without blockages for approximately 5-10 minutes. During all of the runs undertaken at these conditions, a blockage would invariably occur, but only after a period where the system operated at what seemed to be a steady state. The blockages seemed to occur at the tubing, based on observations of the tubing following blockages which showed excessive amounts of crystalline material stuck inside. This is expected, as the point where the tubing meets the fReactor is the narrowest part of the fReactor cascade (1/16th inch).

To assess whether a steady state had been achieved, a ReactIR probe was inserted into the third fReactor unit, and IR spectroscopy measurements were taken during the run. The calibration between the IR spectra and the concentration of SA was used to determine the concentration of SA during the experiment. The results of this are plotted in Figure 91 – a graph of calculated SA concentration against residence time. This shows an increase in the predicted concentration of SA over time, levelling off after approximately 6 residence times. Unfortunately, a blockage occurred after the spectra taken at 6.7 residence times, meaning the experiment was stopped. However, the similarity in the predicted concentration of the final two acquired spectra suggests a steady state had been achieved. The value of 6 residence times taken to achieve steady state is similar to the experiments with $CaSO_4$ presented in chapter 3, and suggests that a slightly longer period of time to achieve steady state compared with the theoretical time for a homogeneous, well-mixed CSTR cascade (2-3 residence times). This may be due to the solids moving at a slower rate through the reactor than the liquid phase.

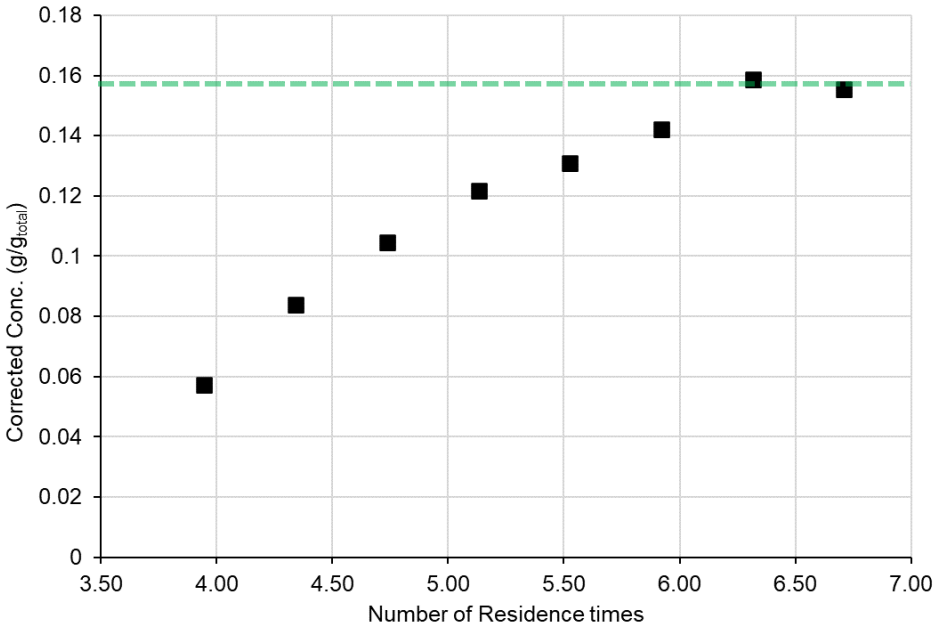

Figure 91 – Concentration values of SA in the third fReactor unit during continuous crystallisation experiments, as measured using the ReactIR probe and the previously developed calibration.

Figure 92 shows the predicted concentration of 0.157 g/g_{total} on a graph of the measured and predicted concentration values over time from the batch crystallisation. The concentration is marked at 22.8s, which represents the predicted residence time (assuming plug flow) at the 3rd fReactor (that is, three-fifths of the total residence time of 38s). This shows the measured concentration lines up well with the concentration at the same time in the batch crystallisation. This shows evidence for both the plug-flow assumption being valid at these fast flow rates, and that the growth rate appears to be similar in both the batch and continuous flow environments. It also suggests that the use of the ReactIR probe in this manner is valid for monitoring concentrations within the fReactor at a steady-state. Due to experimental time-constraints (the work having been carried out by necessity during an industrial placement), only one repeat could be carried out with the ReactIR at the third fReactor. Repeating the continuous crystallisation with the ReactIR probe in all five fReactors would effectively give time-resolved concentration values (as theoretically desupersaturation should occur across the length of the fReactor cascade operating at steady-state). This should form the basis of future experiments.

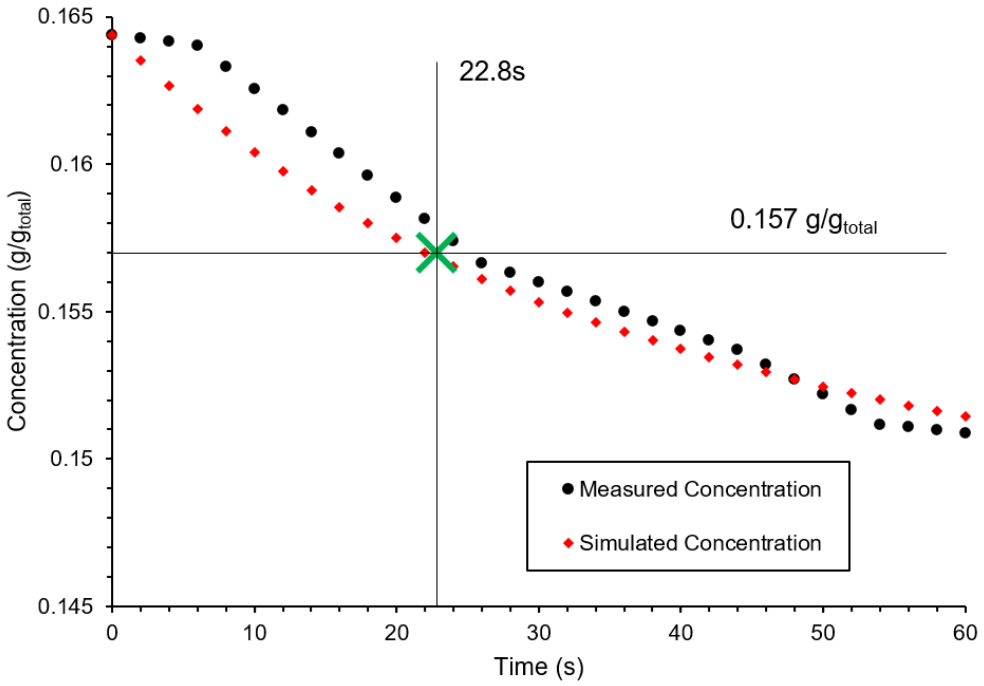

Figure 92 - Measured concentration at the third fReactor during the continuous crystallisation of SA (green cross), compared to the measured and predicted concentration values from the batch crystallisation. The predicted value of residence time at the third fReactor (based on a plug-flow model) is 22.8s.

Seed crystals were retained from the continuous crystallisation, and subjected to CSD analysis using the Morphologi G3 instrument, with the results shown in Figure 93. The CSD of the crystals following the continuous crystallisation seems to show a significant increase in size, particularly in the size range 30-120μm. However, there was significant aggregation of particles observed within the microscopy images taken during CSD measurement, as shown in Figure 94. Although during CSD measurement, care was taken to eliminate aggregated particles (likely from the filtration and drying process), it was not possible to do so with the samples from the continuous crystallisation, as there were very few images of single crystals, without aggregation.

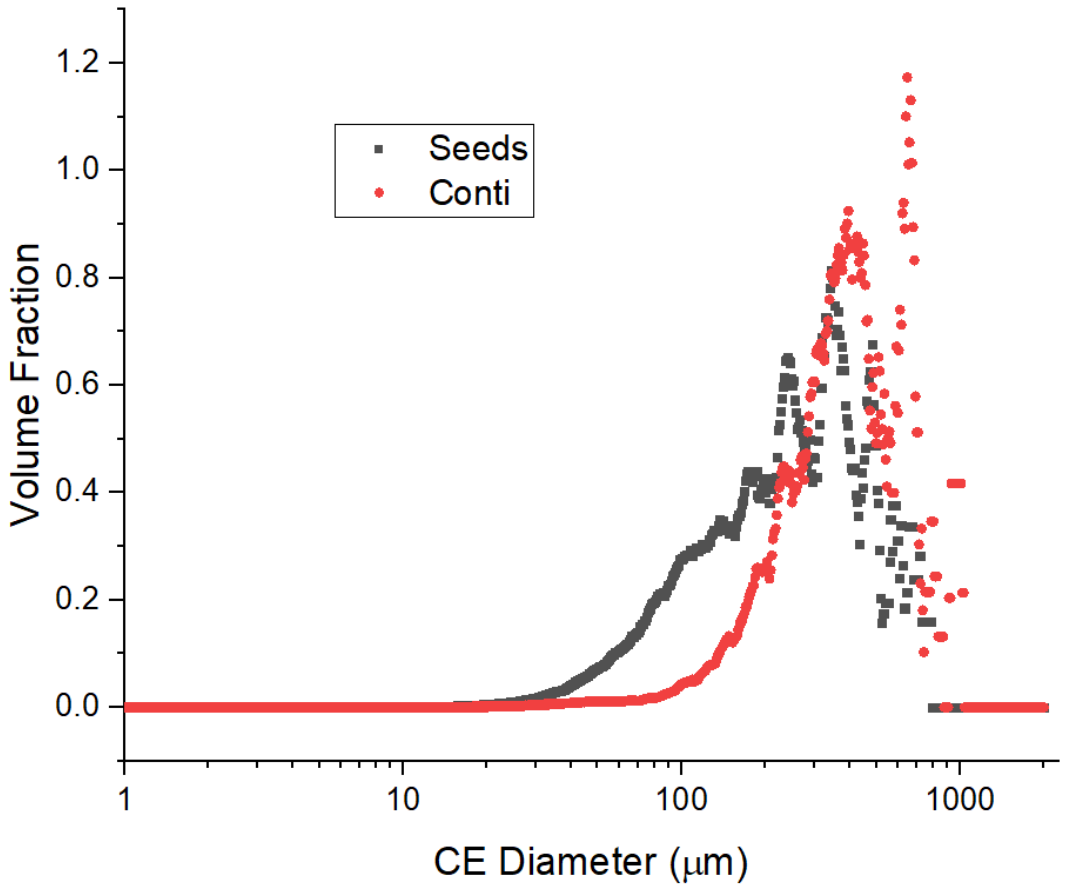

Figure 93 – Comparison of measured size distributions of the seed crystals and crystals taken from continuous-flow crystallisations of SA within the fReactor cascade.

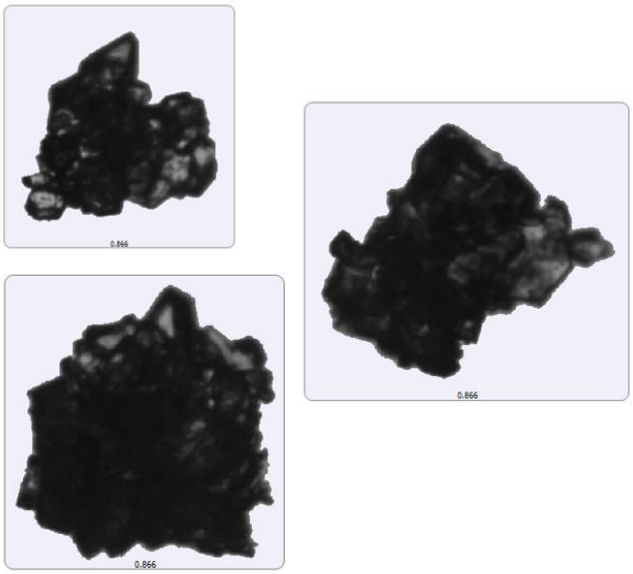

Figure 94 - Examples of significant aggregation of crystals from the continuous crystallisation experiments in the fReactor cascade.

It is unclear whether the visibly increase population of crystals showing states of aggregation was induced by the fReactor or simply by the particular drying filtration and drying method used (although this was the same vacuum-filtration method used for the batch crystallisations). A potential route whereby the fReactor could cause aggregation could be due to the fast-moving stirrer bars. These could induce secondary nucleation, resulting in the birth of small crystalline nuclei. The high surface area to volume ratio of these particles could cause aggregation to become favourable. However, it is unclear as to the exact mechanism at play, and further experimentation is required to determine if growth mechanisms are different within the different crystallisation environments (batch and fReactor).

5.4. Conclusions

Methodologies to characterise crystal growth under different extents of supersaturation are vital for designing crystallisation processes to achieve the correct size of crystals. The combination of population balance modelling and *in situ* has shown to be useful for studying the batch crystallisation of SA. Solubility of SA in water was characterised, which showed good agreement with existing literature data. Seeded batch crystallisations of SA were carried out isothermally at 40°C, with an *in situ* FTIR (ReactIR) probe being used to characterise concentration throughout the experiment. The data from this was used to fit a power law growth rate equation using population balance modelling software. This showed a good agreement with the predicted concentration values.

The seeded batch crystallisation experiments were carried out in continuous flow using the fReactor CSTR cascade. Conditions were found wherein the temperature across the fReactor cascade would remain isothermal at 40°C, and flowrates and temperatures were specified to result in supersaturation being present at the first fReactor unit. Significant aggregation of crystals occurred within the fReactor cascade (compared to the equivalent batch crystallisation). This could be a result of the unique, intense mixing behaviour within the fReactor system. A single concentration measurement within the third fReactor unit suggested a concentration drop due to supersaturation consumption that was broadly equivalent to the same predicted time point in the equivalent batch experiment. Further work is required to determine the exact utility of the fReactor to enable seeded continuous cooling crystallisations, and whether the use of *in situ* monitoring across the length of the fReactor cascade can

enable position-dependent monitoring of concentration, leading in turn to the extraction of crystal growth rates.

6. Report Conclusions

6.1. Summary and Significance

Overall, the *in situ* X-ray diffraction instrument has proven to be useful for the monitoring of crystallisation processes. *In situ* characterisation of the contents of a batch reactor was carried out by developing a sampling loop apparatus, which pumped the contents of the reactor through a custom-made flow-cell where PXRD samples could be continuously acquired. Initially, a calibration was drawn between the intensity of PXRD patterns obtained and the solids content of the gypsum and bassanite forms of $CaSO_4$. This allowed for quantification of the kinetics of crystallisation processes in a time-resolved manner across different operating conditions, with supersaturation, additive concentration, and solvent system being varied. This study represents the first use of a laboratory-based PXRD instrument to characterise reactive crystallisation growth kinetics. It also provided evidence for the role of ethanol in inducing the formation of the metastable form of $CaSO_4$ (Bassanite) and represents the first study of its subsequent transformation into Gypsum. In terms of the effect of additives, the use of Mg^{2+} was found to not impact the hydrate pathway, in contrast to previous work, instead only impacting the growth rate. This is a poignant example of the benefits that can be drawn, in a general sense, from the development of *in situ* techniques to supplement or replace existing *ex situ* methods of characterisations.

An existing millifluidic-scale continuous-flow device (the *fReactor*) was adapted for use as a continuous crystallisation platform. Continuous crystallisations are desirable due to the potential for more efficient performance and the ability to monitor processes at a steady-state with respect to time. The fReactor device was interfaced with the PXRD instrument using X-ray transparent tubing, enabling *in situ* monitoring across the length of the device. As a proof-of-concept, the reactive crystallisation of $CaSO_4$ under mixed ethanol and aqueous solutions was carried out in this platform. Taking steady-state PXRD patterns at different points along the reactor and under different residence times enabled the kinetics of the metastable to stable hydrate transformation to be monitored. This represents a novel method of monitoring transient crystallisation processes.

Antisolvent crystallisations of a small organic molecule (ROY) were carried out in batch and in the fReactor system. Changing the antisolvent content was found to selectively induce the formation of either a metastable form or the stable form, the

results of which could be easily screened using the fReactor platform. However, in coupling the platform to the flow-cell for *in situ* PXRD analysis, it was found that significant sticking of crystals to the walls of the flow-cell occurred. This gave data biased towards these crystals as opposed to the crystals in the bulk (information from which is desired). This shows that there are still significant challenges in the application of continuous crystallisation platforms as crystallisation analysis platforms.

6.2. Outlook

This report only scratches the surface of the capabilities of the *in situ PXRD* instrument, and there is a wealth of information that can be gathered from the data. This includes information regarding morphology, gathered by comparing the relative heights of diffraction peaks, and analysis of peak shapes (such as Reitveld analysis), which can provide information regarding crystal size and strain. There are many other types of crystallisations which can be explored with the instrument, notably cooling crystallisations, which find extensive industrial applicability. In terms of the systems reported here, the exploration of a wider range of conditions could yield other polymorphs or hydrates beyond those reported, as could the inclusion of additives such as polymers, which have previously shown a stark effect on crystal structures and properties. The application of different continuous crystallisation platforms may result in the ability to explore a different operational envelope in continuous flow, or they may be better suited to alternative methods of generating supersaturation.

The advances in this report are largely driven by the step-change in capabilities of laboratory-based XRD instrumentation in recent years. From a user standpoint, the accessibility of such instruments relative to synchrotron sources could allow for greater experimentation and flexibility of experiments to be developed. This could include those which require months of development in terms of analysis techniques, experimental set-up, and the iterative trial-and-error process of optimising operating conditions. A pertinent example of where this could be beneficial is in the application of experimental automation and screening, which is increasingly prevalent in optimising chemical reactions and processes. Experiments would be run and then results analysed autonomously, then experimental conditions are changed using an algorithm, with the process being repeated iteratively until optimum conditions are reached. This could be useful, in the case of crystallisations, in optimising the yield of a particular crystal polymorph, or autonomously discovering crystallisation pathways

through different crystalline (or amorphous) forms. The laboratory-based instrument may, alternatively, be used as a ‘practice’ device to optimise experimental conditions prior to beamline trips, resulting in greater time efficiency.

7. References

1. Lee, A.Y., D. Erdemir, and A.S. Myerson, *Crystals and Crystal Growth*, in *Handbook of Industrial Crystallization*. 2019. p. 32-75.
2. Aitipamula, S. and V.R. Vangala, *X-Ray Crystallography and its Role in Understanding the Physicochemical Properties of Pharmaceutical Cocrystals.* Journal of the Indian Institute of Science, 2017. **97**(2): p. 227-243.
3. Mullin, J.W., *Crystallization*. 2001, Oxford: Elsevier Science & Technology.
4. Byrn, S.R., *Solid-state properties of pharmaceutical materials*, ed. G. Zografi and X. Chen. 2017, Hoboken, NJ, USA: Wiley.
5. Nespolo, M., *International Tables for Crystallography, Volume A, Space-group symmetry. 6th edition. Edited by Mois I. Aroyo. Wiley, 2016. Pp. xxi + 873. Price GBP 295.00, EUR 354.00 (hardcover). ISBN 978-0-470-97423-0.* Acta Crystallographica Section A, 2017. **73**(3): p. 274-276.
6. Kitaigorodsky, A.I., *Particle Packing in a Crystal*, in *Mixed Crystals*, A.I. Kitaigorodsky, Editor. 1984, Springer Berlin Heidelberg: Berlin, Heidelberg. p. 49-84.
7. Yu, L. and S.M. Reutzel-Edens, *CRYSTALLIZATION | Basic Principles*, in *Encyclopedia of Food Sciences and Nutrition (Second Edition)*, B. Caballero, Editor. 2003, Academic Press: Oxford. p. 1697-1702.
8. Erdemir, D., A.Y. Lee, and A.S. Myerson, *Crystal Nucleation*, in *Handbook of Industrial Crystallization*. 2019. p. 76-114.
9. Kashchiev, D. and G.M. van Rosmalen, *Review: Nucleation in solutions revisited.* Crystal Research and Technology, 2003. **38**(78): p. 555-574.
10. Schall, J.M., G. Capellades, and A.S. Myerson, *Methods for estimating supersaturation in antisolvent crystallization systems.* CrystEngComm, 2019. **21**(38): p. 5811-5817.
11. Sadeghi, M. and Å.C. Rasmuson, *On the estimation of crystallization driving forces.* CrystEngComm, 2019. **21**(34): p. 5164-5173.
12. Oxtoby, D.W., *Nucleation of First-Order Phase Transitions.* Accounts of Chemical Research, 1998. **31**(2): p. 91-97.
13. De Yoreo, J.J. and P.G. Vekilov, *Principles of Crystal Nucleation and Growth.* Reviews in Mineralogy and Geochemistry, 2003. **54**(1): p. 57-93.
14. Doran, P.M., *Chapter 11 - Unit Operations*, in *Bioprocess Engineering Principles (Second Edition)*, P.M. Doran, Editor. 2013, Academic Press: London. p. 445-595.
15. Kashchiev, D., *Nucleation : basic theory with applications*. 1999, Oxford: Butterworth-Heinemann.
16. Agrawal, S.G. and A.H.J. Paterson, *Secondary Nucleation: Mechanisms and Models.* Chemical Engineering Communications, 2015. **202**(5): p. 698-706.
17. Jun, Y.S., et al., *Classical and Nonclassical Nucleation and Growth Mechanisms for Nanoparticle Formation.* Annu Rev Phys Chem, 2022. **73**: p. 453-477.
18. Kelton, K.F. and A.L. Greer, *Heterogeneous Nucleation*, in *Nucleation in Condensed Matter - Applications in Materials and Biology*. 2010. p. 165-226.
19. Vekilov, P.G., *Nucleation.* Cryst Growth Des, 2010. **10**(12): p. 5007-5019.
20. Vekilov, P.G., *The two-step mechanism of nucleation of crystals in solution.* Nanoscale, 2010. **2**(11): p. 2346-57.
21. Richardson, J.F., J.H. Harker, and J.R. Backhurst, *Crystallisation*, in *Chemical Engineering*. 2002. p. 827-900.
22. Garside, J., *Industrial crystallization from solution.* Chemical Engineering Science, 1985. **40**(1): p. 3-26.

23. Garside, J. and R.J. Davey, *Invited Review Secondary Contact Nucleation: Kinetics, Growth and Scale-Up.* Chemical Engineering Communications, 2007. **4**(4-5): p. 393-424.
24. Nahi, O., et al., *Solvent-Mediated Enhancement of Additive-Controlled Crystallization.* Crystal Growth & Design, 2021. **21**(12): p. 7104-7115.
25. Wu, K., et al., *Measurement of Crystal Face Specific Growth Kinetics.* Crystal Growth & Design, 2016. **16**(9): p. 4855-4868.
26. Myerson, A.S. and R. Ginde, *2 - Crystals, crystal growth, and nucleation*, in *Handbook of Industrial Crystallization (Second Edition)*, A.S. Myerson, Editor. 2002, Butterworth-Heinemann: Woburn. p. 33-65.
27. Burton, W.K., et al., *The growth of crystals and the equilibrium structure of their surfaces.* Philosophical Transactions of the Royal Society of London. Series A, Mathematical and Physical Sciences, 1951. **243**(866): p. 299-358.
28. Uwaha, M., *Introduction to the BCF theory.* Progress in Crystal Growth and Characterization of Materials, 2016. **62**(2): p. 58-68.
29. Chernov, A.A., *THE SPIRAL GROWTH OF CRYSTALS.* Soviet Physics Uspekhi, 1961. **4**(1): p. 116-148.
30. Pritula, I. and K. Sangwal, *29 - Fundamentals of Crystal Growth from Solutions*, in *Handbook of Crystal Growth (Second Edition)*, P. Rudolph, Editor. 2015, Elsevier: Boston. p. 1185-1227.
31. Nagy, Z.K., M. Fujiwara, and R.D. Braatz, *Modelling and control of combined cooling and antisolvent crystallization processes.* Journal of Process Control, 2008. **18**(9): p. 856-864.
32. Irisawa, T., *2 - Theory of Crystal Growth from Vapor and Solution*. 2002, Elsevier Inc. p. 25-54.
33. Nielsen, A. *Transport Control in Crystal Growth from Solution*. 2018.
34. Wilcox, W.R., *Transport phenomena in crystal growth from solution.* Progress in Crystal Growth and Characterization of Materials, 1993. **26**: p. 153-194.
35. Garside, J., J.W. Mullin, and S.N. Das, *Growth and Dissolution Kinetics of Potassium Sulfate Crystals in an Agitated Vessel.* Industrial and Engineering Chemistry Fundamentals, 1974. **13**(4): p. 299-305.
36. Garside, J., V.R. Phillips, and M.B. Shah, *On Size-Dependent Crystal Growth.* Industrial and Engineering Chemistry Fundamentals, 1976. **15**(3): p. 230-233.
37. Garside, J. and S.J. Jančić, *Growth and dissolution of potash alum crystals in the subsieve size range.* AIChE Journal, 1976. **22**(5): p. 887-894.
38. Rousseau, R.W., *Crystallization Processes☆*, in *Reference Module in Chemistry, Molecular Sciences and Chemical Engineering*. 2014.
39. Nokhodchi, A., N. Bolourtchian, and R. Dinarvand, *Crystal modification of phenytoin using different solvents and crystallization conditions.* International Journal of Pharmaceutics, 2003. **250**(1): p. 85-97.
40. Davey, R.J., J.W. Mullin, and M.J.L. Whiting, *Habit modification of succinic acid crystals grown from different solvents.* Journal of Crystal Growth, 1982. **58**(2): p. 304-312.
41. Sangwal, K., *Effects of impurities on crystal growth processes.* Progress in Crystal Growth and Characterization of Materials, 1996. **32**(1): p. 3-43.
42. Harner, R.S., et al., *Use of a Fiber-Optic Turbidity Probe to Monitor and Control Commercial-Scale Unseeded Batch Crystallizations.* Organic Process Research & Development, 2009. **13**(1): p. 114-124.
43. Wu, Z., S. Yang, and W. Wu, *Application of temperature cycling for crystal quality control during crystallization.* CrystEngComm, 2016. **18**(13): p. 2222-2238.
44. Nagy, Z.K., et al., *Recent advances in the monitoring, modelling and control of crystallization systems.* Chemical Engineering Research and Design, 2013. **91**(10): p. 1903-1922.

45. Parambil, J.V. and J.Y.Y. Heng, *Seeding in Crystallisation*, in *Engineering Crystallography: From Molecule to Crystal to Functional Form*. 2017. p. 235-245.
46. Nagy, Z.K., E. Aamir, and C.D. Rielly, *Internal Fines Removal Using Population Balance Model Based Control of Crystal Size Distribution under Dissolution, Growth and Nucleation Mechanisms.* Crystal Growth & Design, 2011. **11**(6): p. 2205-2219.
47. Erum, A., N. Zoltan, and R. Chris, *Systematic design of supersaturation controlled crystallisation processes*. 2009.
48. Eder, R.J.P., et al., *Continuously Seeded, Continuously Operated Tubular Crystallizer for the Production of Active Pharmaceutical Ingredients.* Crystal Growth & Design, 2010. **10**(5): p. 2247-2257.
49. Eder, R.J.P., et al., *Seed loading effects on the mean crystal size of acetylsalicylic acid in a continuous-flow crystallization device.* Crystal Research and Technology, 2011. **46**(3): p. 227-237.
50. Chung, S.H., D.L. Ma, and R.D. Braatz, *Optimal seeding in batch crystallization.* The Canadian Journal of Chemical Engineering, 1999. **77**(3): p. 590-596.
51. Haleblian, J. and W. McCrone, *Pharmaceutical applications of polymorphism.* J Pharm Sci, 1969. **58**(8): p. 911-29.
52. Nicoud, L.H. and A.S. Myerson, *The Influence of Impurities and Additives on Crystallization*, in *Handbook of Industrial Crystallization*. 2019. p. 115-135.
53. Di Martino, P., et al., *A new pure paracetamol for direct compression: The orthorhombic form.* International Journal of Pharmaceutics, 1996. **128**(1): p. 1-8.
54. Momma, K., et al., *New silica clathrate minerals that are isostructural with natural gas hydrates.* Nature Communications, 2011. **2**(1): p. 196.
55. Burley, J.C., et al., *Enforcing Ostwald's rule of stages: Isolation of paracetamol forms III and II.* European Journal of Pharmaceutical Sciences, 2007. **31**(5): p. 271-276.
56. Evans, T., P.F. James, and R.W. Ditchburn, *A study of the transformation of diamond to graphite.* Proceedings of the Royal Society of London. Series A. Mathematical and Physical Sciences, 1964. **277**(1369): p. 260-269.
57. Lee, E.H., *A practical guide to pharmaceutical polymorph screening & selection.* Asian Journal of Pharmaceutical Sciences, 2014. **9**(4): p. 163-175.
58. Hodnett, B.K. and V. Verma, *Thermodynamic vs. Kinetic Basis for Polymorph Selection.* Processes, 2019. **7**(5).
59. Roelands, C.P.M., et al., *Antisolvent Crystallization of the Polymorphs of l-Histidine as a Function of Supersaturation Ratio and of Solvent Composition.* Crystal Growth & Design, 2006. **6**(4): p. 955-963.
60. Bernstein, J., R.J. Davey, and J.-O. Henck, *Concomitant Polymorphs.* Angewandte Chemie International Edition, 1999. **38**(23): p. 3440-3461.
61. Dunitz, J.D. and J. Bernstein, *Disappearing Polymorphs.* Accounts of Chemical Research, 1995. **28**(4): p. 193-200.
62. Sato, K., *Polymorphic transformations in crystal growth.* Journal of Physics D: Applied Physics, 1993. **26**(8B): p. B77-B84.
63. Miyazaki, S., M. Nakano, and T. Arita, *Effect of Additives on the Polymorphic Transformation of Chlortetracycline Hydrochloride Crystals.* CHEMICAL & PHARMACEUTICAL BULLETIN, 1976. **24**(9): p. 2094-2101.
64. Mukuta, T., et al., *Influence of Impurities on the Solution-Mediated Phase Transformation of an Active Pharmaceutical Ingredient.* Crystal Growth & Design, 2005. **5**(4): p. 1429-1436.
65. Parambil, J.V., et al., *Template-induced nucleation for controlling crystal polymorphism: from molecular mechanisms to applications in pharmaceutical processing.* CrystEngComm, 2019. **21**(28): p. 4122-4135.

66. Singh, A., et al., *Crystal growth on self-assembled monolayers.* CrystEngComm, 2011. **13**(1): p. 24-32.
67. Beckmann, W., *Seeding the Desired Polymorph: Background, Possibilities, Limitations, and Case Studies.* Organic Process Research & Development, 2000. **4**(5): p. 372-383.
68. McGinty, J., et al., *Chapter 1 - Nucleation and Crystal Growth in Continuous Crystallization*, in *Handbook of Continuous Crystallizations*, Z. Nagy and N. Yazdanpanah, Editors. 2020.
69. Cui, Y. and A.S. Myerson, *Experimental Evaluation of Contact Secondary Nucleation Mechanisms.* Crystal Growth & Design, 2014. **14**(10): p. 5152-5157.
70. Bobrovs, R., L. Seton, and N. Dempster, *The reluctant polymorph: investigation into the effect of self-association on the solvent mediated phase transformation and nucleation of theophylline.* CrystEngComm, 2015. **17**(28): p. 5237-5251.
71. Newman, A., *Specialized Solid Form Screening Techniques.* Organic Process Research & Development, 2012. **17**(3): p. 457-471.
72. Muller, F.L., M. Fielding, and S. Black, *A Practical Approach for Using Solubility to Design Cooling Crystallisations.* Organic Process Research & Development, 2009. **13**(6): p. 1315-1321.
73. Su, Q., Z.K. Nagy, and C.D. Rielly, *Pharmaceutical crystallisation processes from batch to continuous operation using MSMPR stages: Modelling, design, and control.* Chemical Engineering and Processing: Process Intensification, 2015. **89**: p. 41-53.
74. Kubota, N., et al., *Seeding policy in batch cooling crystallization.* Powder Technology, 2001. **121**(1): p. 31-38.
75. Estroff, L.A., *Introduction: Biomineralization.* Chemical Reviews, 2008. **108**(11): p. 4329-4331.
76. Jiang, M. and X.-W. Ni, *Reactive Crystallization of Paracetamol in a Continuous Oscillatory Baffled Reactor.* Organic Process Research & Development, 2019. **23**(5): p. 882-890.
77. Van Alsten, J.G., et al., *Continuous Reaction/Crystallization Process for Production of a Hazardous Intermediate.* Organic Process Research & Development, 2008. **12**(5): p. 989-994.
78. McDonald, M.A., et al., *Reactive crystallization: a review.* Reaction Chemistry & Engineering, 2021. **6**(3): p. 364-400.
79. Kelkar, V.V. and K.M. Ng, *Design of reactive crystallization systems incorporating kinetics and mass-transfer effects.* AIChE Journal, 1999. **45**(1): p. 69-81.
80. Teychené, S., I. Rodríguez-Ruiz, and R.K. Ramamoorthy, *Reactive crystallization: From mixing to control of kinetics by additives.* Current Opinion in Colloid & Interface Science, 2020. **46**: p. 1-19.
81. Barrett, M., et al., *In Situ Monitoring of Supersaturation and Polymorphic Form of Piracetam during Batch Cooling Crystallization.* Organic Process Research & Development, 2011. **15**(3): p. 681-687.
82. Sangwal, K., E. Mielniczek-Brzóska, and S. Barylska, *Solubility of ammonium oxalate in water–acetone mixtures and metastable zone width of their solutions.* Chemical Engineering Research and Design, 2014. **92**(3): p. 491-499.
83. Black, S.N., *Crystallization in the Pharmaceutical Industry*, in *Handbook of Industrial Crystallization*. 2019. p. 380-413.
84. Karpiński, P.H. and J. Bałdyga, *Batch Crystallization*, in *Handbook of Industrial Crystallization*. 2019. p. 346-379.
85. ter Horst, J.H., C. Schmidt, and J. Ulrich, *Fundamentals of Industrial Crystallization*, in *Handbook of Crystal Growth*. 2015. p. 1317-1349.

86. Woo, X.Y., et al., *Simulation of Mixing Effects in Antisolvent Crystallization Using a Coupled CFD-PDF-PBE Approach.* Crystal Growth & Design, 2006. **6**(6): p. 1291-1303.
87. Barrett, M., et al., *The role of meso-mixing in anti-solvent crystallization processes.* Chemical Engineering Science, 2011. **66**(12): p. 2523-2534.
88. Alvarez, A.J. and A.S. Myerson, *Continuous Plug Flow Crystallization of Pharmaceutical Compounds.* Crystal Growth & Design, 2010. **10**(5): p. 2219-2228.
89. Wood, B., et al., *Progress to Date in the Design and Operation of Continuous Crystallization Processes for Pharmaceutical Applications.* Organic Process Research & Development, 2019. **23**(2): p. 122-144.
90. Chen, J., et al., *Pharmaceutical Crystallization.* Crystal Growth & Design, 2011. **11**(4): p. 887-895.
91. Baumann, M. and I.R. Baxendale, *The synthesis of active pharmaceutical ingredients (APIs) using continuous flow chemistry.* Beilstein Journal of Organic Chemistry, 2015. **11**: p. 1194-1219.
92. Gutmann, B., D. Cantillo, and C.O. Kappe, *Continuous-Flow Technology—A Tool for the Safe Manufacturing of Active Pharmaceutical Ingredients.* 2015. **54**(23): p. 6688-6728.
93. Cole, K.P., et al., *Kilogram-scale prexasertib monolactate monohydrate synthesis under continuous-flow CGMP conditions.* Science, 2017. **356**(6343): p. 1144.
94. Mascia, S., et al., *End-to-End Continuous Manufacturing of Pharmaceuticals: Integrated Synthesis, Purification, and Final Dosage Formation.* 2013. **52**(47): p. 12359-12363.
95. Reizman, B.J., et al., *Small-Volume Continuous Manufacturing of Merestinib. Part 2. Technology Transfer and cGMP Manufacturing.* Organic Process Research & Development, 2019. **23**(5): p. 870-881.
96. Rogers, L. and K.F. Jensen, *Continuous manufacturing – the Green Chemistry promise?* Green Chemistry, 2019. **21**(13): p. 3481-3498.
97. Zhang, P., et al., *Advanced Continuous Flow Platform for On-Demand Pharmaceutical Manufacturing.* Chemistry, 2018. **24**(11): p. 2776-2784.
98. McGlone, T., et al., *Oscillatory Flow Reactors (OFRs) for Continuous Manufacturing and Crystallization.* Organic Process Research & Development, 2015. **19**(9): p. 1186-1202.
99. Sans, V. and L. Cronin, *Towards dial-a-molecule by integrating continuous flow, analytics and self-optimisation.* Chemical Society Reviews, 2016. **45**(8): p. 2032-2043.
100. Calabrese, G.S. and S. Pissavini, *From batch to continuous flow processing in chemicals manufacturing.* AIChE Journal, 2011. **57**(4): p. 828-834.
101. Poechlauer, P., et al., *Continuous Processing in the Manufacture of Active Pharmaceutical Ingredients and Finished Dosage Forms: An Industry Perspective.* Organic Process Research & Development, 2012. **16**(10): p. 1586-1590.
102. Plumb, K., *Continuous Processing in the Pharmaceutical Industry.* Chemical Engineering Research and Design, 2005. **83**(6): p. 730-738.
103. Levenspiel, O., *Chemical Reaction Engineering*. 1999: Wiley.
104. Méndez del Río, J.R. and R.W. Rousseau, *Batch and Tubular-Batch Crystallization of Paracetamol: Crystal Size Distribution and Polymorph Formation.* Crystal Growth & Design, 2006. **6**(6): p. 1407-1414.
105. Sang-Il Kwon, J., et al., *Crystal shape and size control using a plug flow crystallization configuration.* Chemical Engineering Science, 2014. **119**: p. 30-39.

106. Savvopoulos, S.V., et al., *A Mathematical Model of the Ultrasound-Assisted Continuous Tubular Crystallization of Aspirin.* Crystal Growth & Design, 2019. **19**(9): p. 5111-5122.
107. Benitez-Chapa, A.G., K.D.P. Nigam, and A.J. Alvarez, *Process Intensification of Continuous Antisolvent Crystallization Using a Coiled Flow Inverter.* Industrial & Engineering Chemistry Research, 2019.
108. Levenstein, M.A., et al., *Evaluation of microflow configurations for scale inhibition and serial X-ray diffraction analysis of crystallization processes.* Lab Chip, 2020. **20**(16): p. 2954-2964.
109. Robertson, K., et al., *Design and Evaluation of a Mesoscale Segmented Flow Reactor (KRAIC).* Crystal Growth & Design, 2016. **16**(8): p. 4759-4764.
110. Zheng, B., L.S. Roach, and R.F. Ismagilov, *Screening of Protein Crystallization Conditions on a Microfluidic Chip Using Nanoliter-Size Droplets.* Journal of the American Chemical Society, 2003. **125**(37): p. 11170-11171.
111. Termühlen, M., et al., *Continuous slug flow crystallization: Impact of design and operating parameters on product quality.* Chemical Engineering Research and Design, 2021. **170**: p. 290-303.
112. Robertson, K., P.H. Seeberger, and K. Gilmore, *Rapid optimisation of API crystallisation in a segmented flow reactor with a continuous, variable temperature gradient.* Reaction Chemistry & Engineering, 2023. **8**(1): p. 77-83.
113. Hadiwinoto, G.D., et al., *Integrated Continuous Plug-Flow Crystallization and Spray Drying of Pharmaceuticals for Dry Powder Inhalation.* Industrial & Engineering Chemistry Research, 2019. **58**(36): p. 16843-16857.
114. Brown, C.J. and X.-W. Ni, *Evaluation of Growth Kinetics of Antisolvent Crystallization of Paracetamol in an Oscillatory Baffled Crystallizer Utilizing Video Imaging.* Crystal Growth & Design, 2011. **11**(9): p. 3994-4000.
115. Fitch, A.W., H. Jian, and X. Ni, *An investigation of the effect of viscosity on mixing in an oscillatory baffled column using digital particle image velocimetry and computational fluid dynamics simulation.* Chemical Engineering Journal, 2005. **112**(1-3): p. 197-210.
116. Lawton, S., et al., *Continuous Crystallization of Pharmaceuticals Using a Continuous Oscillatory Baffled Crystallizer.* Organic Process Research & Development, 2009. **13**(6): p. 1357-1363.
117. Siddique, H., et al., *Establishment of a Continuous Sonocrystallization Process for Lactose in an Oscillatory Baffled Crystallizer.* Organic Process Research & Development, 2015. **19**(12): p. 1871-1881.
118. Agnew, L.R., et al., *Continuous Crystallization of Paracetamol (Acetaminophen) Form II: Selective Access to a Metastable Solid Form.* Crystal Growth & Design, 2017. **17**(5): p. 2418-2427.
119. Zhao, L., et al., *From discovery to scale-up: α-lipoic acid : nicotinamide co-crystals in a continuous oscillatory baffled crystalliser.* CrystEngComm, 2014. **16**(26): p. 5769-5780.
120. Ferguson, S., et al., *Use of Continuous MSMPR Crystallization with Integrated Nanofiltration Membrane Recycle for Enhanced Yield and Purity in API Crystallization.* Crystal Growth & Design, 2013. **14**(2): p. 617-627.
121. Moschou, P., et al., *Advances in continuous crystallization: toward microfluidic systems.* Reviews in Chemical Engineering, 2014. **30**(2).
122. Alvarez, A.J., A. Singh, and A.S. Myerson, *Crystallization of Cyclosporine in a Multistage Continuous MSMPR Crystallizer.* Crystal Growth & Design, 2011. **11**(10): p. 4392-4400.
123. Li, J., B.L. Trout, and A.S. Myerson, *Multistage Continuous Mixed-Suspension, Mixed-Product Removal (MSMPR) Crystallization with Solids Recycle.* Organic Process Research & Development, 2015. **20**(2): p. 510-516.

124. Ferguson, S., et al., *Characterization of the anti-solvent batch, plug flow and MSMPR crystallization of benzoic acid.* Chemical Engineering Science, 2013. **104**: p. 44-54.
125. Levenspiel, O., *Chemical Reaction Engineering.* Industrial & Engineering Chemistry Research, 1999. **38**(11): p. 4140-4143.
126. Chapman, M.R., et al., *Simple and Versatile Laboratory Scale CSTR for Multiphasic Continuous-Flow Chemistry and Long Residence Times.* Organic Process Research & Development, 2017. **21**(9): p. 1294-1301.
127. Mo, Y. and K.F. Jensen, *A miniature CSTR cascade for continuous flow of reactions containing solids.* Reaction Chemistry & Engineering, 2016. **1**(5): p. 501-507.
128. Pomberger, A., et al., *A Continuous Stirred-Tank Reactor (CSTR) Cascade for Handling Solid-Containing Photochemical Reactions.* Organic Process Research & Development, 2019. **23**(12): p. 2699-2706.
129. Nandiwale, K.Y., et al., *Continuous stirred-tank reactor cascade platform for self-optimization of reactions involving solids.* Reaction Chemistry & Engineering, 2022. **7**(6): p. 1315-1327.
130. Lignos, I., et al., *Continuous Multistage Synthesis and Functionalization of Sub-100 nm Silica Nanoparticles in 3D-Printed Continuous Stirred-Tank Reactor Cascades.* ACS Appl Mater Interfaces, 2020. **12**(5): p. 6699-6706.
131. Lignos, I., et al., *A high-temperature continuous stirred-tank reactor cascade for the multistep synthesis of InP/ZnS quantum dots.* Reaction Chemistry & Engineering, 2021. **6**(3): p. 459-464.
132. Norby, P., *In-situ XRD as a tool to understanding zeolite crystallization.* Current Opinion in Colloid & Interface Science, 2006. **11**(2-3): p. 118-125.
133. Acevedo, D., et al., *Raman Spectroscopy for Monitoring the Continuous Crystallization of Carbamazepine.* Organic Process Research & Development, 2018. **22**(2): p. 156-165.
134. Févotte, G., *In Situ Raman Spectroscopy for In-Line Control of Pharmaceutical Crystallization and Solids Elaboration Processes: A Review.* Chemical Engineering Research and Design, 2007. **85**(7): p. 906-920.
135. Simone, E., A.N. Saleemi, and Z.K. Nagy, *In Situ Monitoring of Polymorphic Transformations Using a Composite Sensor Array of Raman, NIR, and ATR-UV/vis Spectroscopy, FBRM, and PVM for an Intelligent Decision Support System.* Organic Process Research & Development, 2015. **19**(1): p. 167-177.
136. Bakar, M.R.A., Z.K. Nagy, and C.D. Rielly, *Seeded Batch Cooling Crystallization with Temperature Cycling for the Control of Size Uniformity and Polymorphic Purity of Sulfathiazole Crystals.* Organic Process Research & Development, 2009. **13**(6): p. 1343-1356.
137. Powell, K.A., et al., *Monitoring Continuous Crystallization of Paracetamol in the Presence of an Additive Using an Integrated PAT Array and Multivariate Methods.* Organic Process Research & Development, 2016. **20**(3): p. 626-636.
138. Rehman, G.U., T. Vetter, and P.A. Martin, *Design, Development, and Analysis of an Automated Sampling Loop for Online Monitoring of Chiral Crystallization.* Org Process Res Dev, 2022. **26**(4): p. 1063-1077.
139. Ferguson, S., et al., *In-situ monitoring and characterization of plug flow crystallizers.* Chemical Engineering Science, 2012. **77**: p. 105-111.
140. Liu, W., H. Wei, and S. Black, *An Investigation of the Transformation of Carbamazepine from Anhydrate to Hydrate Using in Situ FBRM and PVM.* Organic Process Research & Development, 2009. **13**(3): p. 494-500.
141. Brown, C.J. and X. Ni, *Online Evaluation of Paracetamol Antisolvent Crystallization Growth Rate with Video Imaging in an Oscillatory Baffled Crystallizer.* Crystal Growth & Design, 2011. **11**(3): p. 719-725.

142. Yu, W. and K. Erickson, *Chord length characterization using focused beam reflectance measurement probe - methodologies and pitfalls.* Powder Technology, 2008. **185**(1): p. 24-30.
143. Hammond, R.B., et al., *Application of In-Process X-ray Powder Diffraction for the Identification of Polymorphic Forms during Batch Crystallization Reactions.* Crystal Growth & Design, 2004. **4**(5): p. 943-948.
144. Levenstein, M.A., et al., *Serial small- and wide-angle X-ray scattering with laboratory sources.* IUCrJ, 2022. **9**(Pt 5): p. 538-543.
145. Nagy, Z.K. and R.D. Braatz, *Advances and new directions in crystallization control.* Annu Rev Chem Biomol Eng, 2012. **3**: p. 55-75.
146. Levenstein, M.A., et al., *Droplet Microfluidics XRD Identifies Effective Nucleating Agents for Calcium Carbonate.* Advanced Functional Materials, 2019. **29**(19).
147. Sima, F., et al., *3 - Laser thin films deposition and characterization for biomedical applications*, in *Laser Surface Modification of Biomaterials*, R. Vilar, Editor. 2016, Woodhead Publishing. p. 77-125.
148. Chatterjee, A.K., *8 - X-Ray Diffraction*, in *Handbook of Analytical Techniques in Concrete Science and Technology*, V.S. Ramachandran and J.J. Beaudoin, Editors. 2001, William Andrew Publishing: Norwich, NY. p. 275-332.
149. Buschow, K.H.J., et al., *X-ray Diffraction*, in *Encyclopedia of Materials - Science and Technology, Volumes 1-11*. Elsevier.
150. Girolami, G.S., *X-Ray Crystallography*. University Science Books.
151. Hasegawa, K., *Introduction to single crystal X-ray analysis.* The Rigaku Journal, 2012. **28**(1): p. 14-18.
152. Zhang, H., et al., *Application of Continuous Crystallization in an Integrated Continuous Pharmaceutical Pilot Plant.* Crystal Growth & Design, 2014. **14**(5): p. 2148-2157.
153. Holder, C.F. and R.E. Schaak, *Tutorial on Powder X-ray Diffraction for Characterizing Nanoscale Materials.* ACS Nano, 2019. **13**(7): p. 7359-7365.
154. Chadwick, K., et al., *Molecular Modeling Applications in Crystallization*, in *Handbook of Industrial Crystallization*. 2019. p. 136-171.
155. Binns, J., et al., *Preferred orientation and its effects on intensity-correlation measurements.* IUCrJ, 2022. **9**(Pt 2): p. 231-242.
156. Nagy, Z.K., M. Fujiwara, and R.D. Braatz, *Monitoring and Advanced Control of Crystallization Processes*, in *Handbook of Industrial Crystallization*. 2019. p. 313-345.
157. Jendrzejewska, I., et al., *X-ray and Thermal Analysis of Selected Drugs Containing Acetaminophen.* Molecules, 2020. **25**(24).
158. Law, D. and D. Zhou, *Solid-State Characterization and Techniques*, in *Developing Solid Oral Dosage Forms*. 2017. p. 59-84.
159. Seeck, O.H. and B.M. Murphy, *X-ray diffraction : modern experimental techniques*, ed. O.H. Seeck and B.M. Murphy. 2014, Boca Raton, Florida: CRC Press.
160. Cats, K.H. and B.M. Weckhuysen, *Combined Operando X-ray Diffraction/Raman Spectroscopy of Catalytic Solids in the Laboratory: The Co/TiO(2) Fischer-Tropsch Synthesis Catalyst Showcase.* ChemCatChem, 2016. **8**(8): p. 1531-1542.
161. Grillo, I., *Applications of stopped-flow in SAXS and SANS.* Current Opinion in Colloid & Interface Science, 2009. **14**(6): p. 402-408.
162. Inada, Y., S. Funahashi, and H. Ohtaki, *In-laboratory stopped-flow extended x-ray absorption fine structure apparatus in the dispersive mode for determination of the structure of short-lived intermediates.* Review of Scientific Instruments, 1994. **65**(1): p. 18-24.

163. Jensen, G.V., et al., *Direct observation of the formation of surfactant micelles under nonisothermal conditions by synchrotron SAXS.* J Am Chem Soc, 2013. **135**(19): p. 7214-22.
164. Abécassis, B., et al., *Probing in situ the Nucleation and Growth of Gold Nanoparticles by Small-Angle X-ray Scattering.* Nano Letters, 2007. **7**(6): p. 1723-1727.
165. Pontoni, D., et al., *Crystallization of Calcium Carbonate Observed In-situ by Combined Small- and Wide-angle X-ray Scattering.* The Journal of Physical Chemistry B, 2003. **107**(22): p. 5123-5125.
166. Cravillon, J., et al., *Fast nucleation and growth of ZIF-8 nanocrystals monitored by time-resolved in situ small-angle and wide-angle X-ray scattering.* Angew Chem Int Ed Engl, 2011. **50**(35): p. 8067-71.
167. Polyzoidis, A., et al., *Revealing the Initial Reaction Behavior in the Continuous Synthesis of Metal-Organic Frameworks Using Real-Time Synchrotron X-ray Analysis.* Inorg Chem, 2017. **56**(10): p. 5489-5492.
168. Lafleur, J.P., et al., *Automated microfluidic sample-preparation platform for high-throughput structural investigation of proteins by small-angle X-ray scattering.* Journal of Applied Crystallography, 2011. **44**(5): p. 1090-1099.
169. Chen, X., et al., *Simultaneous SAXS/WAXS/UV-Vis Study of the Nucleation and Growth of Nanoparticles: A Test of Classical Nucleation Theory.* Langmuir, 2015. **31**(42): p. 11678-91.
170. BioLogic. *Stopped-flow/quench flow*. 2023 [cited 2023; Available from: https://www.biologic.net/product_category/stopped-flow-quench-flow/.
171. Stawski, T.M., et al., *Formation of calcium sulfate through the aggregation of sub-3 nanometre primary species.* Nat Commun, 2016. **7**: p. 11177.
172. Quayle, M.J., et al., *In situ monitoring of rapid crystallisation processes using synchrotron X-ray diffraction and a stopped-flow cell.* Physical Chemistry Chemical Physics, 2002. **4**(3): p. 416-418.
173. Alison, H.G., et al., *Using a novel plug flow reactor for the in situ, simultaneous, monitoring of SAXS and WAXD during crystallisation from solution.* Physical Chemistry Chemical Physics, 2003. **5**(22).
174. Andrade, M.A.B., N. Pérez, and J.C. Adamowski, *Review of Progress in Acoustic Levitation.* Brazilian Journal of Physics, 2017. **48**(2): p. 190-213.
175. Barbosa, E.J., et al., *Acoustic levitation and high-resolution synchrotron X-ray powder diffraction: A fast screening approach of niclosamide amorphous solid dispersions.* Int J Pharm, 2021. **602**: p. 120611.
176. Wolf, S.E., et al., *Early Homogenous Amorphous Precursor Stages of Calcium Carbonate and Subsequent Crystal Growth in Levitated Droplets.* Journal of the American Chemical Society, 2008. **130**(37): p. 12342-12347.
177. Gnutzmann, T., et al., *Solvent-Triggered Crystallization of Polymorphs Studied in Situ.* Crystal Growth & Design, 2014. **14**(12): p. 6445-6450.
178. Levenstein, M.A., et al., *Dynamic Crystallization Pathways of Polymorphic Pharmaceuticals Revealed in Segmented Flow with Inline Powder X-ray Diffraction.* Anal Chem, 2020. **92**(11): p. 7754-7761.
179. Zheng, B., et al., *A droplet-based, composite PDMS/glass capillary microfluidic system for evaluating protein crystallization conditions by microbatch and vapor-diffusion methods with on-chip X-ray diffraction.* Angew Chem Int Ed Engl, 2004. **43**(19): p. 2508-11.
180. Stehle, R., et al., *Small-angle X-ray scattering in droplet-based microfluidics.* Lab Chip, 2013. **13**(8): p. 1529-37.
181. Pham, N., et al., *Coupling High Throughput Microfluidics and Small-Angle X-ray Scattering to Study Protein Crystallization from Solution.* Anal Chem, 2017. **89**(4): p. 2282-2287.
182. Lopez, C.G., et al., *Microfluidic devices for small-angle neutron scattering.* J Appl Crystallogr, 2018. **51**(Pt 3): p. 570-583.

183. Scott, C.D., et al., *Integrated plug flow synthesis and crystallisation of pyrazinamide.* Reaction Chemistry & Engineering, 2018. **3**(5): p. 631-634.
184. Pallipurath, A.R., et al., *In situ non-invasive Raman spectroscopic characterisation of succinic acid polymorphism during segmented flow crystallisation.* Molecular Systems Design & Engineering, 2020. **5**(1): p. 294-303.
185. Levenstein, M.A., *Micro- and Milli-fluidic Systems for X-Ray Scattering Analysis of Crystallization Processes*. 2019, University of Leeds.
186. Skarzynski, T., *Collecting data in the home laboratory: evolution of X-ray sources, detectors and working practices.* Acta Crystallogr D Biol Crystallogr, 2013. **69**(Pt 7): p. 1283-8.
187. Turner, T.D., et al., *Flow-Xl: A New UK Facility for the Analysis of Crystallisation in Flow Systems*. 2023.
188. Gesswein, H., et al., *A multipurpose laboratory diffractometer for operando powder X-ray diffraction investigations of energy materials.* J Appl Crystallogr, 2022. **55**(Pt 3): p. 503-514.
189. Wansleben, M., et al., *Photon flux determination of a liquid-metal jet X-ray source by means of photon scattering.* Journal of Analytical Atomic Spectrometry, 2019. **34**(7): p. 1497-1502.
190. Förster, A., S. Brandstetter, and C. Schulze-Briese, *Transforming X-ray detection with hybrid photon counting detectors.* Philosophical Transactions of the Royal Society A: Mathematical, Physical and Engineering Sciences, 2019. **377**(2147): p. 20180241.
191. Donath, T., et al., *EIGER2 hybrid-photon-counting X-ray detectors for advanced synchrotron diffraction experiments.* J Synchrotron Radiat, 2023. **30**(Pt 4): p. 723-738.
192. Grön, H., A. Borissova, and K.J. Roberts, *In-Process ATR-FTIR Spectroscopy for Closed-Loop Supersaturation Control of a Batch Crystallizer Producing Monosodium Glutamate Crystals of Defined Size.* Industrial & Engineering Chemistry Research, 2003. **42**(1): p. 198-206.
193. Dharmayat, S., et al., *Polymorphic transformation of l-glutamic acid monitored using combined on-line video microscopy and X-ray diffraction.* Journal of Crystal Growth, 2006. **294**(1): p. 35-40.
194. Dharmayat, S., et al., *An Examination of the Kinetics of the Solution-Mediated Polymorphic Phase Transformation between α- and β-Forms of l-Glutamic Acid as Determined Using Online Powder X-ray Diffraction.* Crystal Growth & Design, 2008. **8**(7): p. 2205-2216.
195. Turner, T.D., et al., *Kinetics of the Aqueous-Ethanol Solution Mediated Transformation between the Beta and Alpha Polymorphs of p-Aminobenzoic Acid.* Crystal Growth & Design, 2018. **18**(2): p. 1117-1125.
196. Polte, J., et al., *SAXS in combination with a free liquid jet for improved time-resolved in situ studies of the nucleation and growth of nanoparticles.* Chem Commun (Camb), 2010. **46**(48): p. 9209-11.
197. Herbst, M., E. Hofmann, and S. Forster, *Nucleation and Growth Kinetics of ZnO Nanoparticles Studied by in Situ Microfluidic SAXS/WAXS/UV-Vis Experiments.* Langmuir, 2019. **35**(36): p. 11702-11709.
198. Ossorio, M., et al., *Physicochemical and Additive Controls on the Multistep Precipitation Pathway of Gypsum.* Minerals, 2017. **7**(8).
199. Amathieu, L. and R. Boistelle, *Crystallization kinetics of gypsum from dense suspension of hemihydrate in water.* Journal of Crystal Growth, 1988. **88**(2): p. 183-192.
200. Van Driessche, A.E.S., T.M. Stawski, and M. Kellermeier, *Calcium sulfate precipitation pathways in natural and engineered environments.* Chemical Geology, 2019. **530**.

201. Shen, L., et al., *Thermodynamic Modeling of Calcium Sulfate Hydrates in the CaSO(4)-H(2)O System from 273.15 to 473.15 K with Extension to 548.15 K.* J Chem Eng Data, 2019. **64**(6): p. 2697-2709.
202. Wang, W., et al., *Experimental determination and modeling of gypsum and insoluble anhydrite solubility in the system CaSO4–H2SO4–H2O.* Chemical Engineering Science, 2013. **101**: p. 120-129.
203. Raju, K.U.G. and G. Atkinson, *The thermodynamics of "scale" mineral solubilities. 3. Calcium sulfate in aqueous sodium chloride.* Journal of Chemical & Engineering Data, 1990. **35**(3): p. 361-367.
204. Gurgul, S.J., G. Seng, and G.R. Williams, *A kinetic and mechanistic study into the transformation of calcium sulfate hemihydrate to dihydrate.* J Synchrotron Radiat, 2019. **26**(Pt 3): p. 774-784.
205. Shen, Z., et al., *Effect of Potassium Sodium Tartrate and Sodium Citrate on the Preparation of α-Calcium Sulfate Hemihydrate from Flue Gas Desulfurization Gypsum in a Concentrated Electrolyte Solution.* Journal of the American Ceramic Society, 2009. **92**(12): p. 2894-2899.
206. Schmid, T., R. Jungnickel, and P. Dariz *Insights into the CaSO4–H2O System: A Raman-Spectroscopic Study*. Minerals, 2020. **10**, DOI: 10.3390/min10020115.
207. Schmidt, H., et al., *Water channel structure of bassanite at high air humidity: crystal structure of CaSO4.0.625H2O.* Acta Crystallogr B, 2011. **67**(Pt 6): p. 467-75.
208. Jia, C., et al., *Structural Characteristics of Amorphous Calcium Sulfate: Evidence to the Role of Water Molecules.* The Journal of Physical Chemistry C, 2021. **125**(6): p. 3415-3420.
209. Anduix-Canto, C., et al., *Exploiting Confinement to Study the Crystallization Pathway of Calcium Sulfate.* Advanced Functional Materials, 2021. **31**(50).
210. Galloway, J.M., et al., *Electron transparent nanotubes reveal crystallization pathways in confinement.* Chem Sci, 2023. **14**(24): p. 6705-6715.
211. Wang, Y.W., et al., *A new precipitation pathway for calcium sulfate dihydrate (gypsum) via amorphous and hemihydrate intermediates.* Chem Commun (Camb), 2012. **48**(4): p. 504-6.
212. Van Driessche, A.E.S., et al., *Calcium Sulfate Precipitation Throughout Its Phase Diagram*, in *New Perspectives on Mineral Nucleation and Growth*. 2017. p. 227-256.
213. Tritschler, U., et al., *Controlling the selective formation of calcium sulfate polymorphs at room temperature.* Angew Chem Int Ed Engl, 2015. **54**(13): p. 4083-6.
214. Tritschler, U., et al., *A simple strategy for the synthesis of well-defined bassanite nanorods.* CrystEngComm, 2015. **17**(20): p. 3772-3776.
215. Liu, S.-T. and G.H. Nancollas, *The kinetics of crystal growth of calcium sulfate dihydrate.* Journal of Crystal Growth, 1970. **6**(3): p. 281-289.
216. Nancollas, G.H., M.M. Reddy, and F. Tsai, *Calcium sulfate dihydrate crystal growth in aqueous solution at elevated temperatures.* Journal of Crystal Growth, 1973. **20**(2): p. 125-134.
217. Barcelona, M.J. and D.K. Atwood, *Gypsum-organic interactions in natural seawater: Effect of organics on precipitation kinetics and crystal morphology.* Marine Chemistry, 1978. **6**(2): p. 99-115.
218. Meer Siese, D.E., J. Spiers Christopher, and J. Peach Colin, *Kinetics of precipitation of gypsum and implications for pressure-solution creep.* Journal of the Geological Society, 2000. **157**(2): p. 269-281.
219. Van Driessche, A.E.S., et al., *The Role and Implications of Bassanite as a Stable Precursor Phase to Gypsum Precipitation.* Science, 2012. **336**(6077): p. 69-72.

220. Ilett, M., et al., *Evaluation of correlated studies using liquid cell and cryo-transmission electron microscopy: Hydration of calcium sulphate and the phase transformation pathways of bassanite to gypsum.* J Microsc, 2022. **288**(3): p. 155-168.
221. Hand, R.J., *The kinetics of hydration of calcium sulphate hemihydrate: A critical comparison of the models in the literature.* Cement and Concrete Research, 1994. **24**(5): p. 885-895.
222. Avrami, M., *Kinetics of Phase Change. II Transformation-Time Relations for Random Distribution of Nuclei.* The Journal of Chemical Physics, 2004. **8**(2): p. 212-224.
223. Gualtieri, A.F., *Synthesis of sodium zeolites from a natural halloysite.* Physics and Chemistry of Minerals, 2001. **28**(10): p. 719-728.
224. Buckley, H.E., *Habit modification in crystals as a result of the introduction of impurities during growth.* Discussions of the Faraday Society, 1949. **5**(0): p. 243-254.
225. Prasad, K.V.R., et al., *Crystallization of paracetamol from solution in the presence and absence of impurity.* International Journal of Pharmaceutics, 2001. **215**(1): p. 29-44.
226. Sun, Y., et al., *Solubility Measurement and Correlation of Isobutane with Two Pentaerythritol Tetraalkyl Esters between (293.15 and 348.15) K.* Journal of Chemical & Engineering Data, 2015. **60**(5): p. 1504-1509.
227. Poon, G.G. and B. Peters, *Accelerated Nucleation Due to Trace Additives: A Fluctuating Coverage Model.* J Phys Chem B, 2016. **120**(8): p. 1679-84.
228. Heffernan, C., et al., *Influence of Structurally Related Impurities on the Crystal Nucleation of Curcumin.* Crystal Growth & Design, 2018. **18**(8): p. 4715-4723.
229. Ruiz-Agudo, E., et al., *A non-classical view on calcium oxalate precipitation and the role of citrate.* Nat Commun, 2017. **8**(1): p. 768.
230. Green, D.C., et al., *3D visualization of additive occlusion and tunable full-spectrum fluorescence in calcite.* Nat Commun, 2016. **7**: p. 13524.
231. Kim, Y.-Y., et al., *Tuning hardness in calcite by incorporation of amino acids.* Nature Materials, 2016. **15**(8): p. 903-910.
232. Lang, A., et al., *Bioinspired Molecular Bridging in a Hybrid Perovskite Leads to Enhanced Stability and Tunable Properties.* Advanced Functional Materials, 2020. **30**(42).
233. Wang, Y.-W. and F.C. Meldrum, *Additives stabilize calcium sulfate hemihydrate (bassanite) in solution.* Journal of Materials Chemistry, 2012. **22**(41).
234. Wang, C., et al., *Stable Bassanite Bulk Phase Formed in Aqueous Solution under the Control of Polymer-Mediated Water Activity.* Crystal Growth & Design, 2023. **23**(2): p. 1172-1178.
235. Fu, H., et al., *Insights into the Role of Na(+) on the Transformation of Gypsum into alpha-Hemihydrate Whiskers in Alcohol-Water Systems.* ACS Omega, 2022. **7**(18): p. 15570-15579.
236. Guan, B., L. Yang, and Z. Wu, *Effect of Mg2+ Ions on the Nucleation Kinetics of Calcium Sulfate in Concentrated Calcium Chloride Solutions.* Industrial & Engineering Chemistry Research, 2010. **49**(12): p. 5569-5574.
237. Rabizadeh, T., et al., *The Effects of Inorganic Additives on the Nucleation and Growth Kinetics of Calcium Sulfate Dihydrate Crystals.* Crystal Growth & Design, 2017. **17**(2): p. 582-589.
238. Meldrum, F.C. *Flow-Xl: A New UK Facility for Analysis of Crystallisation in Flow Systems*. 2021 24-07-2023]; Available from: https://eps.leeds.ac.uk/dir-record/facilities/4391/flow-xl-a-new-uk-facility-for-analysis-of-crystallisation-in-flow-systems.

239. Le Magueres, P., et al., *The Rigaku Oxford Diffraction XtaLAB Synergy: from Powder Analysis to Charge Density Studies and Protein Structure Solution.* Acta Cryst, 2019. **75**: p. a163.
240. Corporation, O. *Origin 2023b Feature Highlights*. 2023 24-03-2023]; Available from: https://www.originlab.com/index.aspx?go=Products/Origin/2023b&pid=4460.
241. Jiang, S. and J.H. ter Horst, *Crystal Nucleation Rates from Probability Distributions of Induction Times.* Crystal Growth & Design, 2011. **11**(1): p. 256-261.
242. Mullin, J.W., *6 - Crystal growth*, in *Crystallization (Fourth Edition)*, J.W. Mullin, Editor. 2001, Butterworth-Heinemann: Oxford. p. 216-288.
243. Liendo, F., et al., *Nucleation and growth kinetics of CaCO3 crystals in the presence of foreign monovalent ions.* Journal of Crystal Growth, 2022. **578**: p. 126406.
244. Wu, X., et al., *Solubility of Calcium Sulfate Dihydrate in Ca−Mg−K Chloride Salt Solution in the Range of (348.15 to 371.15) K.* Journal of Chemical & Engineering Data, 2010. **55**(6): p. 2100-2107.
245. Gomis, V., M.D. Saquete, and J. García-Cano, *CaSO4 solubility in water–ethanol mixtures in the presence of sodium chloride at 25°C. Application to a reverse osmosis process.* Fluid Phase Equilibria, 2013. **360**: p. 248-252.
246. Gonzalez Nino, C., *Optimisation of flow chemistry: tools and algorithms*. 2019, University of Leeds.
247. Onyemelukwe, I.I., et al., *The Role of Residence Time Distribution in the Continuous Steady-State Mixed Suspension Mixed Product Removal Crystallization of Glycine.* Crystal Growth & Design, 2018. **19**(1): p. 66-80.
248. Capellades, G., et al., *Characterization of a Multistage Continuous MSMPR Crystallization Process Assisted by Image Analysis of Elongated Crystals.* Crystal Growth & Design, 2018. **18**(11): p. 6455-6469.
249. Acevedo, D., et al., *A continuous multi-stage mixed-suspension mixed-product-removal crystallization system with fines dissolution.* Chemical Engineering Research and Design, 2018. **135**: p. 112-120.
250. Powell, K.A., et al., *Periodic steady-state flow crystallization of a pharmaceutical drug using MSMPR operation.* Chemical Engineering and Processing: Process Intensification, 2015. **97**: p. 195-212.
251. Juilland, P., et al., *Dissolution theory applied to the induction period in alite hydration.* Cement and Concrete Research, 2010. **40**(6): p. 831-844.
252. Taylor, C.J., et al., *Rapid, automated determination of reaction models and kinetic parameters.* Chemical Engineering Journal, 2021. **413**: p. 127017.
253. Sans, V., et al., *A self optimizing synthetic organic reactor system using real-time in-line NMR spectroscopy.* Chemical Science, 2015. **6**(2): p. 1258-1264.
254. Amar, Y., et al., *Machine learning and molecular descriptors enable rational solvent selection in asymmetric catalysis.* Chemical Science, 2019. **10**(27): p. 6697-6706.
255. Clayton, A.D., et al., *Automated self-optimisation of multi-step reaction and separation processes using machine learning.* Chemical Engineering Journal, 2020. **384**: p. 123340.
256. Clayton, A.D., et al., *Bayesian Self-Optimization for Telescoped Continuous Flow Synthesis.* Angewandte Chemie International Edition, 2023. **62**(3): p. e202214511.
257. Cortes-Borda, D., et al., *An Autonomous Self-Optimizing Flow Reactor for the Synthesis of Natural Product Carpanone.* J Org Chem, 2018. **83**(23): p. 14286-14299.
258. Schweidtmann, A.M., et al., *Machine learning meets continuous flow chemistry: Automated optimization towards the Pareto front of multiple objectives.* Chemical Engineering Journal, 2018. **352**: p. 277-282.

259. Brown, C.J., J.A. Adelakun, and X.-w. Ni, *Characterization and modelling of antisolvent crystallization of salicylic acid in a continuous oscillatory baffled crystallizer.* Chemical Engineering and Processing: Process Intensification, 2015. **97**: p. 180-186.
260. Di Profio, G., et al., *Antisolvent membrane crystallization of pharmaceutical compounds.* J Pharm Sci, 2009. **98**(12): p. 4902-13.
261. Jia, S., et al., *Recent progress in antisolvent crystallization.* CrystEngComm, 2022. **24**(17): p. 3122-3135.
262. McGinty, J., et al., *Effect of Process Conditions on Particle Size and Shape in Continuous Antisolvent Crystallisation of Lovastatin.* Crystals, 2020. **10**(10).
263. Yang, Y. and Z.K. Nagy, *Advanced control approaches for combined cooling/antisolvent crystallization in continuous mixed suspension mixed product removal cascade crystallizers.* Chemical Engineering Science, 2015. **127**: p. 362-373.
264. Kakran, M., et al., *Preparation of nanoparticles of poorly water-soluble antioxidant curcumin by antisolvent precipitation methods.* Journal of Nanoparticle Research, 2012. **14**(3).
265. Wu, C.Y. and W. Wang, *Application of Antisolvent Precipitation Method for Formulating Excipient-Free Nanoparticles of Psychotropic Drugs.* Pharmaceutics, 2022. **14**(4).
266. Kumar, R., et al., *Liquid antisolvent crystallization of pharmaceutical compounds: current status and future perspectives.* Drug Deliv Transl Res, 2023. **13**(2): p. 400-418.
267. Blandin, A.F., et al., *Kinetics identification of salicylic acid precipitation through experiments in a batch stirred vessel and a T-mixer.* Chemical Engineering Journal, 2001. **81**(1): p. 91-100.
268. Marchisio, D.L., L. Rivautella, and A.A. Barresi, *Design and scale-up of chemical reactors for nanoparticle precipitation.* AIChE Journal, 2006. **52**(5): p. 1877-1887.
269. Pandit, A.V. and V.V. Ranade, *Fluidic Oscillator as a Continuous Crystallizer: Feasibility Evaluation.* Industrial & Engineering Chemistry Research, 2020. **59**(9): p. 3996-4006.
270. Beran, G.J.O., et al., *How many more polymorphs of ROY remain undiscovered.* Chem Sci, 2022. **13**(5): p. 1288-1297.
271. Ziemecka, et al., *Polymorph Selection of ROY by Flow-Driven Crystallization.* Crystals, 2019. **9**(7).
272. Van Nerom, M., et al., *The Effect of Controlled Mixing on ROY Polymorphism.* Crystals, 2022. **12**(5).
273. Yu, L., *Polymorphism in Molecular Solids: An Extraordinary System of Red, Orange, and Yellow Crystals.* Accounts of Chemical Research, 2010. **43**(9): p. 1257-1266.
274. *CrystalMaker X*. 2022, CrystalMaker Software Ltd.
275. Stephenson, G.A., et al., *Conformational and Color Polymorphism of 5-Methyl-2-[(2-nitrophenyl)amino]-3-thiophenecarbonitrile.* Journal of Pharmaceutical Sciences, 1995. **84**(11): p. 1385-1386.
276. Yu, L., et al., *Thermochemistry and Conformational Polymorphism of a Hexamorphic Crystal System.* Journal of the American Chemical Society, 2000. **122**(4): p. 585-591.
277. Saleemi, A.N., et al., *Enhancing crystalline properties of a cardiovascular active pharmaceutical ingredient using a process analytical technology based crystallization feedback control strategy.* Int J Pharm, 2012. **430**(1-2): p. 56-64.
278. Simone, E., et al., *Preventing Crystal Agglomeration of Pharmaceutical Crystals Using Temperature Cycling and a Novel Membrane Crystallization Procedure for Seed Crystal Generation.* Pharmaceutics, 2018. **10**(1).

279. Ochsenbein, D.R., et al., *Agglomeration of Needle-like Crystals in Suspension. II. Modeling.* Crystal Growth & Design, 2015. **15**(9): p. 4296-4310.
280. Abramov, Y.A., *Understanding the Risk of Agglomeration of Polar Pharmaceutical Crystals.* Crystal Growth & Design, 2017. **17**(5): p. 2873-2880.
281. Brunsteiner, M., et al., *Toward a Molecular Understanding of Crystal Agglomeration.* Crystal Growth & Design, 2005. **5**(1): p. 3-16.
282. Vancleef, A., et al., *Continuous Crystallization Using Ultrasound Assisted Nucleation, Cubic Cooling Profiles and Oscillatory Flow.* Processes, 2021. **9**(12).
283. Ezeanowi, N., et al., *Monitoring the Dynamics of a Continuous Sonicated Tubular Cooling Crystallizer.* Crystal Growth & Design, 2020. **20**(3): p. 1458-1466.
284. Erdemir, D., A.Y. Lee, and A.S. Myerson, *Crystals and Crystal Growth*, in *Handbook of Industrial Crystallization*, D. Erdemir, A.Y. Lee, and A.S. Myerson, Editors. 2019, Cambridge University Press: Cambridge. p. 32-75.
285. Rasmuson, Å.C., *Crystallization Process Analysis by Population Balance Modeling*, in *Handbook of Industrial Crystallization*, D. Erdemir, A.Y. Lee, and A.S. Myerson, Editors. 2019, Cambridge University Press: Cambridge. p. 172-196.
286. Pérez-Calvo, J.-F., S.S. Kadam, and H.J.M. Kramer, *Determination of kinetics in batch cooling crystallization processes—A sequential parameter estimation approach.* AIChE Journal, 2016. **62**(11): p. 3992-4012.
287. Eder, R.J.P., et al., *Continuous Sonocrystallization of Acetylsalicylic Acid (ASA): Control of Crystal Size.* Crystal Growth & Design, 2012. **12**(10): p. 4733-4738.
288. Besenhard, M.O., et al., *Crystal Engineering in Continuous Plug-Flow Crystallizers.* Crystal Growth & Design, 2017. **17**(12): p. 6432-6444.
289. Wu, W.-L., et al., *Continuous In Situ Seed Generation through the Integration of a Mixed Suspension Mixed Product Removal and an Oscillatory Baffled Crystallizer for the Control of Crystal Size Distribution and Polymorphic Form.* Crystal Growth & Design, 2021. **21**(12): p. 6684-6696.
290. Lai, T.-T.C., et al., *Control of Polymorphism in Continuous Crystallization via Mixed Suspension Mixed Product Removal Systems Cascade Design.* Crystal Growth & Design, 2015. **15**(7): p. 3374-3382.
291. Seki, H., N. Furuya, and S. Hoshino, *Evaluation of controlled cooling for seeded batch crystallization incorporating dissolution.* Chemical Engineering Science, 2012. **77**: p. 10-17.
292. Lei, F., et al., *Solubilities of Succinic Acid in Acetic Acid + Water Mixtures and Acetic Acid + Cyclohexane Mixtures.* Journal of Chemical & Engineering Data, 2014. **59**(5): p. 1714-1718.
293. Seimens, *gPROMS FormulatedProducts.* 2022.
294. Davidson, S., *Antisolvent Crystallisation in Oscillatory Baffled Crystallisers*, in *Strathclyde Institute of Pharmacy and Biomedical Sciences*. 2019, University of Strathclyde.
295. Feng, L. and K.A. Berglund, *ATR-FTIR for Determining Optimal Cooling Curves for Batch Crystallization of Succinic Acid.* Crystal Growth & Design, 2002. **2**(5): p. 449-452.